

# Computational Methods for Cognitive and Cooperative Robotics

**Dissertation**

der Mathematisch-Naturwissenschaftlichen Fakultät  
der Eberhard Karls Universität Tübingen  
zur Erlangung des Grades eines  
Doktors der Naturwissenschaften  
(Dr. rer. nat.)

vorgelegt von

Albert Mukovskiy  
aus Elektrostal, Russland

Tübingen  
2018

Gedruckt mit Genehmigung der Mathematisch-Naturwissenschaftlichen Fakultät der Eberhard Karls Universität Tübingen.

Tag der mündlichen Qualifikation:	12 September 2018
Dekan:	Prof. Dr. Wolfgang Rosenstiel
1. Berichterstatter:	Prof. Dr. Martin Giese
2. Berichterstatter:	Prof. Dr. Andreas Schilling



# Abstract

In the last decades design methods in control engineering made substantial progress in the areas of robotics and computer animation. Nowadays these methods incorporate the newest developments in machine learning and artificial intelligence. But the problems of flexible and online-adaptive combinations of motor behaviors remain challenging for human-like animations and for humanoid robotics. In this context, biologically-motivated methods for the analysis and re-synthesis of human motor programs provide new insights in and models for the anticipatory motion synthesis.

This thesis presents the author's achievements in the areas of cognitive and developmental robotics, cooperative and humanoid robotics and intelligent and machine learning methods in computer graphics. The first part of the thesis in the chapter "Goal-directed Imitation for Robots" considers imitation learning in cognitive and developmental robotics. The work presented here details the author's progress in the development of hierarchical motion recognition and planning inspired by recent discoveries of the functions of mirror-neuron cortical circuits in primates. The overall architecture is capable of 'learning for imitation' and 'learning by imitation'. The complete system includes a low-level real-time capable path planning subsystem for obstacle avoidance during arm reaching. The learning-based path planning subsystem is universal for all types of anthropomorphic robot arms, and is capable of knowledge transfer at the level of individual motor acts.

Next, the problems of learning and synthesis of motor synergies, the spatial and spatio-temporal combinations of motor features in sequential multi-action behavior, and the problems of task-related action transitions are considered in the second part of the thesis "Kinematic Motion Synthesis for Computer Graphics and Robotics". In this part, a new approach of modeling complex full-body human actions by mixtures of time-shift invariant motor primitives is presented. The online-capable full-body motion generation architecture based on dynamic movement primitives driving the time-shift invariant motor synergies was implemented as an online-reactive adaptive motion synthesis for computer graphics and robotics applications.

The last chapter of the thesis entitled "Contraction Theory and Self-organized Scenarios in Computer Graphics and Robotics" is dedicated to optimal control strategies in multi-

---

agent scenarios of large crowds of agents expressing highly nonlinear behaviors. This last part presents new mathematical tools for stability analysis and synthesis of multi-agent cooperative scenarios.

# Zusammenfassung

In den letzten Jahrzehnten hat die Forschung in den Bereichen der Steuerung und Regelung komplexer Systeme erhebliche Fortschritte gemacht, insbesondere in den Bereichen Robotik und Computeranimation. Die Entwicklung solcher Systeme verwendet heutzutage neueste Methoden und Entwicklungen im Bereich des maschinellen Lernens und der künstlichen Intelligenz. Die flexible und echtzeitfähige Kombination von motorischen Verhaltensweisen ist eine wesentliche Herausforderung für die Generierung menschenähnlicher Animationen und in der humanoiden Robotik. In diesem Zusammenhang liefern biologisch motivierte Methoden zur Analyse und Resynthese menschlicher motorischer Programme neue Erkenntnisse und Modelle für die antizipatorische Bewegungssynthese.

Diese Dissertation präsentiert die Ergebnisse der Arbeiten des Autors im Gebiet der kognitiven und Entwicklungsrobotik, kooperativer und humanoider Robotersysteme sowie intelligenter und maschineller Lernmethoden in der Computergrafik. Der erste Teil der Dissertation im Kapitel “Zielgerichtete Nachahmung für Roboter” behandelt das Imitationslernen in der kognitiven und Entwicklungsrobotik. Die vorgestellten Arbeiten beschreiben neue Methoden für die hierarchische Bewegungserkennung und -planung, die durch Erkenntnisse zur Funktion der kortikalen Spiegelneuronen-Schaltkreise bei Primaten inspiriert wurden. Die entwickelte Architektur ist in der Lage, ‘durch Imitation zu lernen’ und ‘zu lernen zu imitieren’. Das komplette entwickelte System enthält ein echtzeitfähiges Pfadplanungssystem zur Hindernisvermeidung während der Durchführung von Armbewegungen. Das lernbasierte Pfadplanungssystem ist universell und für alle Arten von anthropomorphen Roboterarmen in der Lage, Wissen auf der Ebene einzelner motorischer Handlungen zu übertragen.

Im zweiten Teil der Arbeit “Kinematische Bewegungssynthese für Computergrafik und Robotik” werden die Probleme des Lernens und der Synthese motorischer Synergien, d.h. von räumlichen und räumlich-zeitlichen Kombinationen motorischer Bewegungselemente bei Bewegungssequenzen und bei aufgabenbezogenen Handlungsübergängen behandelt. Es wird ein neuer Ansatz zur Modellierung komplexer menschlicher Ganzkörperaktionen durch Mischungen von zeitverschiebungsinvarianten Motorprimitiven vorgestellt. Zudem wurde ein online-fähiger Synthesealgorithmus für Ganzkörperbewegungen entwickelt, der

---

auf dynamischen Bewegungsprimitiven basiert, die wiederum auf der Basis der gelernten verschiebungsinvarianten Primitive konstruiert werden. Dieser Algorithmus wurde für verschiedene Probleme der Bewegungssynthese für die Computergrafik- und Roboteranwendungen implementiert.

Das letzte Kapitel der Dissertation mit dem Titel “Kontraktionstheorie und selbstorganisierte Szenarien in der Computergrafik und Robotik” widmet sich optimalen Kontrollstrategien in Multi-Agenten-Szenarien, wobei die Agenten durch eine hochgradig nichtlineare Kinematik gekennzeichnet sind. Dieser letzte Teil präsentiert neue mathematische Werkzeuge für die Stabilitätsanalyse und Synthese von kooperativen Multi-Agenten-Szenarien.

# Acknowledgements

I thank Prof. Martin A. Giese for his dedicated supervision of my scientific work in the last ten years. I am thankful for his guidance of my scientific research direction, and I thank him for his perpetual teaching of researching and writing skills of his students. I gratefully acknowledge financial support of my research positions at the University of Tübingen, which were supported by the DFG Forschergruppe “Perceptual Graphics” and European Commission grants: ArteSImit (IST-200-29689), JAST (IST-2-003747-IP), EC FP6-43403 project “COBOL”, FP7-ICT-249858 project “TANGO”, EC FP7-ICT-248311 project “AMARSi”, FP7 project “KoroiBot” (No. 611909 ICT-2013.2.1) and H2020 ICT-644727 project “CogIMon”.

I also thank my colleagues and collaborators at the Computational Sensomotorics Laboratory of the University of Tübingen during my work in 2007-2016 for all the years of our productive work on computer graphics and on experimental studies of motor control: Lars Omlor, Aee-ni Park, Enrico Chiovetto, Nick Taubert, Andrea Christensen, Winfried Ilg, Karsten Rohweder.

I thank Prof. Wolfram Erlhagen and Prof. Estela G. S. Bicho-Erlhagen, my supervisors in the EC ArteSImit project group of University of Minho (Portugal), for perpetual support and guidance on the way to the new frontiers of developmental robotics. I also thank my colleagues in the EC ArteSImit project in 2003-2005 for the fruitful collaboration: C. Gregorio (Univ. of Minho), G. Panin, Prof. A. Knoll (Techn. Univ. München) and Prof. H. Bekkering.

I am greatly thankful to all my co-authors and the colleagues from other universities all around the world for the collaboration and their expertise in our robotics projects in the last ten years: Prof. J.J.E. Slotine, Prof. T. Flash, Prof. A. Ijspeert, Prof. P. Soueres, Prof. O. Stasse, Prof. T. Schack, Prof. D. Endres, Prof. N. Tsagarakis, Prof. D. Sternad, M. Karklinsky, M. Naveau, C. Vassallo, W. Land, F. Reinhart, M. Ajallooeian and H. Dalali. I thank Tjeerd Dijkstra, my colleague at the Section for Computational Sensomotorics of the Werner Reichardt Center for Integrative Neuroscience (CIN), University of Tübingen for his generous helping hand during my work on this thesis and for his restless correction

---

work of my written English.

I am grateful to Prof. Werner von Seelen, Prof. Martin A. Giese and Danil Gorinevski for inviting me to the Neuroinformatik Institute at the Ruhr University in Bochum to boost my science researcher career in the newly developing research areas of computational neuroscience, cognitive modelling, machine learning and robotics. In the years 1999-2001 of wonderful collaborative work I learned most of the new theoretical directions and practical methods in modern statistical learning theory, control theory, numerical optimization and algorithms, applied mathematics and programming. I would like to express my sincere acknowledgments to the director of the Neuroinformatik Institute during my visit, Prof. Werner von Seelen for the scientific encouragement and inspiration, for letting free research spirit float and for his generosity in offering opportunities in theoretical, experimental and applied sciences.

I thank my parents for letting me find my way in life and always supporting me on the way.

# Contents

<b>1</b>	<b>Introduction</b>	<b>1</b>
1.1	Thesis Overview . . . . .	1
1.2	Overview of Chapter 2 . . . . .	3
1.3	Overview of Chapter 3 . . . . .	4
1.4	Overview of Chapter 4 . . . . .	6
<b>2</b>	<b>Goal-directed Imitation for Robots</b>	<b>9</b>
2.1	Introduction and Experimental Paradigm . . . . .	9
2.1.1	Experimental Paradigm . . . . .	10
2.2	System Architecture . . . . .	11
2.2.1	Vision Module . . . . .	11
2.2.2	Cognitive Module . . . . .	13
2.3	Path Planning . . . . .	18
2.3.1	Path Planners and their Role in Sensory-motor Planning . . . . .	18
2.3.2	Path Planning Algorithm . . . . .	21
2.4	Results . . . . .	33
2.4.1	Copying the Means . . . . .	33
2.4.2	Discerning Motor Intention . . . . .	37
2.4.3	Goal Directed Imitation . . . . .	37
2.4.4	Learning Color Cues . . . . .	41
2.4.5	The Biological Relevance of the Results . . . . .	41
2.5	Extension of the Learning Rule . . . . .	43
<b>3</b>	<b>Kinematic Motion Synthesis for Computer Graphics and Robotics</b>	<b>51</b>
3.1	Introduction . . . . .	51
3.2	Related Work . . . . .	53
3.2.1	Kinematic Primitives for the Adaptive Synthesis of Multi-action Sequences . . . . .	53
3.2.2	Related Approaches in Humanoid Robotics . . . . .	54

3.3	Kinematic Motion Synthesis Architecture . . . . .	56
3.3.1	Data Sets . . . . .	57
3.3.2	Kinematic Angle Trajectories Representations and Retargeting . . .	62
3.3.3	Learning of Kinematic Movement Primitives . . . . .	67
3.3.4	The DMP Architectures for the Online Synthesis of Kinematic Motion Trajectories . . . . .	79
3.4	Motion Style Morphing by Anechoic Mixture Parameter Blending . . . . .	86
3.4.1	Event-based Transitions between Actions in Multi-action Sequences	87
3.4.2	Learning of Behavior Specific Mappings between Action Parameters and Mixing Weights . . . . .	88
3.4.3	Semi-supervised Learning for <i>Style</i> vs <i>Content</i> Separation . . . . .	89
3.5	Navigation . . . . .	98
3.6	Computer Graphics Applications . . . . .	101
3.7	Modelling and Online-reactive Simulations of Walking-and-reaching Sequential Behaviors . . . . .	108
3.8	Adaptive Synthesis of Feasible Full Body Movements for HRP-2 . . . . .	110
3.8.1	Overview of Robot Control Architecture . . . . .	111
3.8.2	WPG based on Optimal Predictive Control . . . . .	112
3.8.3	Approximation of Dynamically Feasible Training Trajectories by Robot Movements . . . . .	113
3.8.4	Further Experiments on the Open-HRP Simulator and the real HRP-2117	
<b>4</b>	<b>Contraction Theory and Self-organized Scenarios in Computer Graphics and Robotics</b>	<b>123</b>
4.1	Introduction and Related Work . . . . .	123
4.2	Contraction Theory for Analysis of Stability of Nonlinear Systems . . . . .	125
4.2.1	General Theorems of Contraction Analysis . . . . .	126
4.2.2	Partial Contraction and Flow-invariant Manifolds . . . . .	128
4.3	Linear Coupling of Nonlinear DMPs . . . . .	130
4.3.1	The Andronov-Hopf Oscillator . . . . .	132
4.3.2	Symmetric Diffusive Coupling of Linear Phases of Multiple Oscillators	133
4.3.3	All-to-all Symmetric Linear Diffusive Coupling of Multiple DMPs . .	134
4.3.4	Symmetric Linear Diffusive Couplings with more General Structure	136
4.3.5	Simulations of Collective Behavior of the Networks of Coupled Oscillators . . . . .	139
4.3.6	Theoretical vs. Empirical Convergence Rates . . . . .	140
4.3.7	Leader-group Asymmetric Interaction . . . . .	141
4.4	Stability Conditions for Crowd Control . . . . .	143



---

4.4.1	Crowd Control Architecture . . . . .	144
4.4.2	Analysis of Scenarios of Crowd Formation Control . . . . .	147
4.4.3	Analysis of Schöner-Dose Dynamics of Heading Direction Control . . . . .	151
4.5	Warped Limit Cycle Attractors for Robotics Applications . . . . .	154
4.5.1	Equi-affine Transform Preserving “Power Laws” and Partial Contraction for the Modeling and Control of Walking . . . . .	156
<b>5</b>	<b>Conclusions and Outlook</b>	<b>161</b>
<b>A</b>	<b>Some Facts from Algebraic Graph Theory</b>	<b>167</b>
A.1	Definitions and Facts from Algebraic Graph Theory . . . . .	167
A.2	Some Examples . . . . .	171
<b>B</b>	<b>Stability Conditions for Non-linear Dynamical Systems</b>	<b>173</b>
B.1	Some Definitions and Facts from Matrix Analysis . . . . .	173
B.2	Lur’e-Persidskii Systems . . . . .	175
B.3	Partial Contraction and its Necessary and Sufficient Stability Conditions . . . . .	176
B.3.1	The <i>Necessary Conditions</i> for Positive Definiteness of the Anticommutator of two Positive Definite Symmetric Real Matrices . . . . .	180
B.3.2	The <i>Sufficient Conditions</i> for Positive Definiteness of the Anticommutator of two Positive Definite Symmetric Real Matrices . . . . .	181
B.3.3	The <i>Necessary and Sufficient Conditions</i> for Positive Definiteness of the Anticommutator of two Positive Definite Symmetric Real Matrices	184
B.3.4	The Role of the Sufficient Conditions for Partial Contraction in Design of Convergent Multi-agent Behavior . . . . .	185
	<b>Bibliography</b>	<b>186</b>



# Chapter 1

## Introduction

### 1.1 Thesis Overview

The flexible modelling of human motion becomes an increasingly important problem for technological applications. This problem is important for computer vision where the tracking and analysis of human movements and activities is necessary for many applications in video analysis, e.g. for communication devices or for driver assistance systems (<sup>41,89,113,296</sup>). An important recent problem for internet applications is also the automatic labelling and searching of videos with human actions and activities (<sup>3,134</sup>). Another technical domain where the simulation of human movements with high degree of realism is central is computer graphics. Recent animation movies such as Lord of the Rings (<sup>4,280</sup>) or Valerian (<sup>317</sup>) (VFX: Weta Digital Ltd.) achieve a degree of realism of the simulation of human motion that makes it almost indistinguishable from real motion. Another domain, where the realization of human-like motor behavior becomes increasingly important is humanoid robotics. Human-like motor behavior of robots is important for two reasons: first, because the flexibility and versatility of human motor behavior is still unachieved by present humanoid robots. This makes it interesting to transfer concepts from flexible human motor control to humanoid robots in order to realize complex highly adaptive behaviors for such systems. The second reason is that humanoid robots are built increasingly for direct interaction with humans. For many applications, this makes it necessary to implement human-like motion in order to increase the acceptance of such systems for human users (<sup>43</sup>). A further argument is that humanoids will be used increasingly with humans in joint tasks (<sup>31,83,84,289</sup>). This makes it necessary to integrate human and robot behavior in terms of a smooth interaction, which likely is more similar if the robot behaves in a human-like manner, making its actions easier to predict.

The transfer of human-like characteristics from humans to technical systems is a non-trivial problem. First, no unified theory about the organization and control principles of

human motor behavior exist. This makes it a challenge to find flexible and adaptive frameworks for the modeling of complex human behavior. While a huge number of approaches exist to generate human-like motion kinematics based on recorded data by interpolation or retrieval of trajectory segments (<sup>12,106,107,256,340</sup>), e.g. exploiting motion capture, the challenge for many applications is to generate complex and structured human motion online and in an adaptive manner. For applications in robotics, in addition the problem emerges that human motion typically violates the physical constraints of humanoid robot systems. In this case it is a nontrivial problem to decide which aspects of the human motion should be reproduced by the technical system to improve its performance. This is even more so as technical implementations of human-like behaviors can be accomplished exploiting technology that is not biologically inspired. An example is the impressive performance of the robots by Boston Dynamics (<sup>73</sup>), which exploits high-energy effector technology and standard control approaches using extremely fast control loops rather than biologically-inspired concepts.

In this thesis I present work on the development of flexible motion representations in different domains: cognitive and developmental robotics, humanoid robotics, and machine learning methods in computer graphics. This work has been realized at the University do Minho, Portugal, and at the Eberhard Karls Universität Tübingen, Germany. The thesis is based on a series of papers which are specified in detail below. The work has been accomplished as part of the EU projects ArteSImit (FP6), the projects AMARSi and KoroBot (FP7), and the project CogIMon (H2020).

The Thesis consists of the three main chapters. Chapter 2 covers topics in cognitive and developmental robotics, proposing a brain-inspired architecture that realizes a robotics system for imitation learning. Chapter 3 covers a new approach for online kinematic motion synthesis for reactive motion synthesis in computer graphics as well as for the synthesis of movements for humanoid robots. The approach integrates this synthesis algorithm in the full control architecture that guarantees dynamic balance during walking. Chapter 4 finally treats new mathematical tools for the synthesis of human-like multi-agent motion and stability analysis of the underlying complex nonlinear dynamics.

The major innovations of this thesis can be characterized as follows: 1) online reactive architecture for the kino-dynamic motion planning of goal-directed reaching movements with a robot arm, capable of online imitation of motion and imitative learning of new motor skills; 2) online reactive kinematic synthesis algorithm for complex full body motion, which is based on learned Dynamic Movement Primitives (DMPs), and which is implemented in two ways: as generative architecture for motion in a computer animation system, and as a part of a general control architecture for the humanoid biped robot HRP-2; 3) new meth-

ods for nonlinear stability methods in the framework of Contraction Theory implemented both for the design of the networks of coupled DMPs that control agent motion, and as a nonlinear control synthesis framework, a design tool applied to the multi-agent control scenarios.

All chapters of the thesis treat the problem of learning motor features from examples of human behavior. This includes the problems of transfer of motor features at the level of individual motor acts (geometric correspondence problem, cf. <sup>222,258</sup>), as well as transfer at a higher level: the learning and synthesis of motor synergies, which define spatial and spatio-temporal combinations of motor features. Also this thesis considers the problems of synthesis of sequential multi-action behavior, both in goal-directed and spontaneous activities, and the problems of task-related action transitions. A further problem treated in this thesis is the implementation of multi-agent control strategies for crowds of agents that realize human full-body motion, and which are characterized by highly nonlinear agent models. Basic control strategies for navigation of individual agents are derived from simplified models of human navigation. The flexible combinations of behaviors, navigation and the synthesis of complex transient behaviors requires elaborated tools from modern theories of nonlinear control in order to guarantee stable system behavior.

In the following, I give a more detailed overview of the contents of the individual chapters. Each chapter starts with an overview of its research area and with the review of the literature. References to the current literature are given in the main text of the chapters.

## 1.2 Overview of Chapter 2

**Chapter 2** presents work in the area of cognitive and developmental robotics. It addresses problems of hierarchical motor planning and online control of complex sequential behaviors. A biologically plausible motion synthesis architecture is proposed for the learning-for-imitation, learning-to-imitate, and learning-by-imitation problems. My approach combines ideas of optimal path planners in configurational space with ideas of pre-selection of motor action sub-goals and means. The pre-selections take place on high levels of general sub-summation architecture (<sup>39</sup>). The robotics architecture presented in this chapter is inspired by recent finding in biological motor control, the discovery of mirror neurons in cortical areas F5 and PFG of primates (<sup>93,253,318</sup>). The top levels of motor feature selections are realized by interconnected populations of Neural Fields, building up to a ladder-type hierarchy of pairwise coupled sensor and motor representations of actions. I propose a new modified Hebb-like learning rule for the Neural Fields, which allows automatic spatial and

temporal fusion and splitting of concept representations. This conceptually new approach was successfully implemented by me as a robotics architecture, controlling a real KUKA robot arm in the framework of EU project ArteSimit (FP6) at the University do Minho, Portugal. My main contributions to this work include the development of the low-level connectionist motion planning paradigm, based on learned and online refined probabilistic road maps in configuration space. This paradigm resulted in a universal path planning algorithm, realized in C/C++ capable of real time optimal planning. This algorithm is transferable to any robotics arm with up to 8 degrees of freedom, admitting arbitrary static and kinematic constraints. The other main achievements include the design of a hierarchical architecture for the representation of motion features, capable of online motion planning and re-planning, flexibly combining sub-goals and means of a motor action. This architecture is capable of learning new motor skills from a demonstrator for motor imitation.

The results presented in **Chapter 2** are published in the following papers:

W. Erlhagen, **A. Mukovskiy**, E. Bicho, G. Panin, C. Kiss, A. Knoll, H. van Schie and H. Bekkering. *Action Understanding and Imitation Learning in a Robot-Human Task*. In: “Artificial Neural Networks: Biological Inspirations, ICANN, 2005”. Duch, W. et al. editors. LNCS 3696, pp.: 261-268. Springer-Verlag, Berlin, Heidelberg, 2005. <sup>(78)</sup>

W. Erlhagen, **A. Mukovskiy**, E. Bicho, G. Panin, C. Kiss, A. Knoll, H. van Schie and H. Bekkering. *Goal-Directed Imitation for Robots: A Bio-Inspired Approach to Action Understanding and Skill Learning*. *Journal of Robotics and Autonomous Systems*, 54(5): 353-360, 2006. <sup>(79)</sup>

W. Erlhagen, **A. Mukovskiy** and E. Bicho. *A Dynamic Model for Action Understanding and Goal-directed Imitation*. *Brain Research*, 1083(1): 174-188, 2006. <sup>(76)</sup>

W. Erlhagen, **A. Mukovskiy**, F. Chersi and E. Bicho. *On the Development of Intention Understanding for Joint Action Tasks*. In IEEE 6th Int. Conf. on Development and Learning, ICDL 2007, pp.: 140-145, 2007. <sup>(80)</sup>

They were presented at the following conference:

W. Erlhagen, **A. Mukovskiy**, E. Bicho and H. Bekkering. *Development of Action Understanding in Imitation Tasks*. Proc. Of IEEE Int. Conf. on Robotics and Automation, ICRA'2005, April, 2005, Barcelona, Spain. <sup>(77)</sup>

### 1.3 Overview of Chapter 3

**Chapter 3** presents work in computer graphics and robotics. It solves the problem of learning motion control primitives from examples of human motion, including both goal-directed and free performed actions, where motion data was acquired by motion

capture techniques. During the project many datasets were collected for free walking with different styles, dancing, navigational walking, walking with arm reaching at different phases of gait cycle, arm reaching towards perturbed targets, goal-directed walking and arm reaching. The flexible models for the generation of motion are based on unsupervised learning techniques, including unconstrained and constrained anechoic mixture models, and methods of shift-invariant ICA and PCA. The estimation techniques developed by me include approaches for the hierarchical step-wise estimation of anechoic mixtures of source signals, defining spatio-temporal time-shift-invariant and non-invariant kinematic motor primitives. I developed a general multilayer architecture for the online-reactive generative synthesis of realistic human motion based on anechoic mixture models. The main control module of the architecture is a network of interconnected canonical dynamical systems, which define dynamic motion primitives (DMPs). To test the approach I developed a computer animation architecture that was used for the online generation of adaptive motion in diverse scenarios, e.g. collective dancing, crowd navigation, goal directed walking and arm reaching. During the work, a number of machine learning techniques were proposed to establish online behavioral control of the animation by external variables. These methods include the learning of mappings from task parameters of goal-directed actions onto the manifold of weights and delays of kinematic motion primitives defined by anechoic mixtures, which participate in the synthesis.

This developed architecture, which was originally tested in computer graphics, was extended to a kinematic control synthesis block that then was embedded in the control architecture of a walking humanoid robot. The proposed solution guaranteed dynamic stability during walking. It was tested successfully on a robot physics simulator as well as on the real HRP-2 humanoid robot, realizing the online control of walking combined with arm reaching and other tasks performed with the upper body. I show the feasibility of the proposed embedded kinematic control not only for the flexible instantaneous multi-action behaviors, but also for the online control of transitional multi-action sequences. Additionally, I used a Contraction Theory framework for the design of the stable networks of DMPs in the proposed kinematic pattern synthesis architecture.

The results presented in **Chapter 3** are published in the following papers, conference papers, and book chapters:

A. Park, **A. Mukovskiy**, L. Omlor and M. A. Giese. *Synthesis of Character Behaviour by Dynamic Interaction of Synergies Learned from Motion Capture Data*. Skala, V. (ed): Proceedings of the 16th Int. Conf. in Central Europe on Computer Graphics, Visualization and Computer Vision (WSCG), Plzen, Czech Republic, pp.: 9-16. 2008. <sup>(236)</sup>

A. Park, **A. Mukovskiy**, L. Omlor and M. A. Giese. *Self-organized Character Animation based on Learned Synergies from Full-body Motion Capture Data*. Int. Conf. on Cognitive

Systems (CogSys), Springer-Verlag, Berlin. 2008. <sup>(235)</sup>

**A. Mukovskiy**, A. Park, L. Omlor, J. J. E. Slotine and M. A. Giese. *Self-organization of Character Behavior by Mixing of Learned Movement Primitives*. Proc. of the 13th Fall Workshop on Vision, Modeling, and Visualization (VMV 2008), October 8-10, Konstanz, Germany. 2008. <sup>(210)</sup>.

M. A. Giese, **A. Mukovskiy**, A. Park, L. Omlor and J. J. E. Slotine. *Real-Time Synthesis of Body Movements based on Learned Primitives*. Book chapter. In Cremers D, Rosenhahn, B., Yuille, A. L. (eds): “Statistical and Geometrical Approaches to Visual Motion Analysis”, Springer Verlag, Lecture Notes in Computer Science 5604, pp.: 107-127. 2009. <sup>(103)</sup>

**A. Mukovskiy**, W. M. Land, T. Schack and M. A. Giese. *Modeling of Predictive Human Movement Coordination Patterns for Applications in Computer Graphics*. Journal of WSCG, 23(2), pp.: 139-146. 2015. <sup>(209)</sup>

**A. Mukovskiy**, C. Vassallo, M. Naveau, O. Stasse, P. Souères and M. A. Giese. *Adaptive Synthesis of Dynamically Feasible Full-body Movements for the Humanoid Robot HRP-2 by Flexible Combination of Learned Dynamic Movement Primitives*. Robotics and Autonomous Systems, Vol.91, pp.: 270-283. 2017. <sup>(215)</sup>

**A. Mukovskiy**, N. Taubert, D. Endres, C. Vassallo, M. Naveau, O. Stasse, P. Souères and M. A. Giese. *Modeling of Coordinated Human Body Motion by Learning of Structured Dynamic Representations*. In: Laumond, J. P., et al. (Eds.): “Geometric and Numerical Foundations of Movements,” Springer STAR Series, Springer-Verlag Berlin Heidelberg. Vol.117 of the series Springer Tracts in Advanced Robotics, pp.: 237-267. 2017. <sup>(214)</sup>

## 1.4 Overview of Chapter 4

The final **Chapter 4** is dedicated to computer animation applications and mathematical problems related to the development of new stability analysis and synthesis tools exploiting the framework of Contraction Theory <sup>(183)</sup>. Here, I developed a number of control scenarios for crowds of walking avatars, including multiple-feedback controls for the individual avatars based on their instantaneous positions, velocities, walking directions and gait phases. All these control feedbacks are inherently non-linear. Contraction theory is a tool for the stability analysis of essentially nonlinear systems, developed by Prof. J. J. E. Slotine and his colleagues at M.I.T. This tool, when applied as a synthesis principle, allows the composability of control blocks in parallel or hierarchical schemes. In this project I developed a number of mathematical tools guaranteeing the sufficient contraction conditions for composite nonlinear systems. The derivations of these tools are presented in the main text and in the appendix of this thesis. The mathematical results



obtained were successfully implemented for the control of interacting crowds of multiple agents driven by nonlinear DMPs. The results are illustrated by a number of videos, while performance measures are evaluated and compared with the theoretical results. The scientific impact of this work extends beyond applications in computer graphics and robotics, as it also has a general impact on the methods of nonlinear control of multi-agent scenarios.

The results of this chapter are published in the following full papers, conference papers, and book chapters:

A. Park, **A. Mukovskiy**, J. J. E. Slotine and M. A. Giese. *Design of Dynamical Stability Properties in Character Animation*. In: The 6th Workshop on Virtual Reality Interaction and Physical Simulation. VRIPHYS'09, Nov. 5-6, Karlsruhe, Germany, pp.: 85-94. 2009. <sup>(237)</sup>

**A. Mukovskiy**, J. J. E. Slotine and M. A. Giese. *Design of the Dynamic Stability Properties of the Collective Behavior of Articulated Bipeds*. Proc. of 10th IEEE-RAS Int. Conf. on Humanoid Robots, Humanoids, 2010. Dec. 6-8, 2010, Nashville, TN, USA, pp.: 66-73, 2010. <sup>(213)</sup>

**A. Mukovskiy**, J. J. E. Slotine and M. A. Giese. *Analysis and Design of the Dynamical Stability of Collective Behavior in Crowds*. Journal of WSCG. Skala V. (ed): Proc. of the 19th Int. Conf. on Computer Graphics, Visualization and Computer Vision 2011 (WSCG'2011), Jan.31-Febr.3, 2011, Plzen, Czech Republic. 2011. <sup>(211)</sup>

**A. Mukovskiy**, J. J. E. Slotine and M. A. Giese. *Dynamically Stable Control of Articulated Crowds*. Journal of Computational Science, 4(4), pp.: 304-310, 2013. <sup>(212)</sup>

M. Ajallooeian, J. van den Kieboom, **A. Mukovskiy**, M. A. Giese and A. J. Ijspeert. *A General Family of Morphed Nonlinear Phase Oscillators with Arbitrary Limit Cycle Shape*. Physica D: Nonlinear Phenomena, 263, pp.: 41-56. 2013. <sup>(5)</sup>

M. Karklinsky , M. Naveau, **A. Mukovskiy**, O. Stasse, T. Flash and P. Souères. *Robust Human-Inspired Power Law Trajectories for Humanoid HRP-2 Robot*. In Proc. Of 6th IEEE Conf. Biomedical Robotics and Biomechatronics, pp.: 106-113. 2016. <sup>(148)</sup>



## Chapter 2

# Goal-directed Imitation for Robots

### 2.1 Introduction and Experimental Paradigm

There has been a growing interest in creating autonomous robots which are capable of developing motor and cognitive skills through real-time interactions with their environment. Research in movement learning suggests that trying to imitate an experienced teacher (e.g., a human) is a powerful means of speeding up the learning process (for reviews see<sup>275,276</sup>). This form of social learning in robots is not restricted to movements. It may be complemented by acquiring more abstract knowledge such as, for instance, structurally new motor behaviors composed of a set of parametrized motor primitives.

In this part I summarize results of an interdisciplinary project which aimed at exploring new ways of imitation and imitation learning in artefacts based on recent discoveries in cognitive psychology and neuroscience. The basic idea was to get new insights into the relevant functional mechanisms underlying imitation from behavioral and neuronal data. Central questions for robot imitation that I have addressed in my work concern “what to imitate” and how to solve the correspondence problem across dissimilar embodiments and task constraints<sup>222</sup>. Often these differences do not allow for a matching at the level of movement trajectory or path. In the goal-directed theory of imitation proposed by H. Bekkering and colleagues<sup>22,341</sup> imitative behavior can be considered successful whenever the goal of an action in terms of the desired outcome of the movement is reproduced. The action means, on the other hand, may or may not coincide with the observed one. The focus on the consequences of the movement requires that the imitator understands the demonstrator’s behavior as an intentional motor act directed at a specific goal (e.g., placing an object at a certain position). The “matching hypothesis” forwarded by Rizzolatti and colleagues<sup>253</sup> based on their discovery of the mirror system states that an action is understood if its observation activates the motor representations controlling the execution

of a similar goal-directed action (“motor simulation”).

Here I present a dynamic model, which aims at substantiating the idea of a distributed neuronal network in which action understanding and goal-directed imitation occurs within a continuous dynamic process. In its architecture, the model reflects the basic functionality of neuronal population of distinct but anatomically connected areas in the frontal, temporal and parietal cortex, which are known to be involved in action observation and action execution. Contextual information, action means and action goals are explicitly represented as dynamic activity patterns of localized pools of neurons.

Specifically, I apply an imitation paradigm consisting of a grasping-placing sequence to show how the mapping from perception to action may contribute to the inference of the action goal. I also simulate how knowledge about the action goal can be used to flexibly change between different means to reproduce the witnessed action effect. A second objective of the present modeling study is to illustrate how learning within the network can be exploited for skill growth. The focus is on changes in environmental constraints and on observed means not in the motor repertoire of the imitator. To directly illustrate the functionality of the dynamic model I use a simulator of robot arm. The model implements a cognitive “decision module” which decides about the means the artifact uses to reproduce the observed or inferred action effect. Since our approach is focused on the goal of the action and do not assume that demonstrator and imitator share the same embodiment, the implementation may be seen as a contribution to solving the correspondence problem. The proposed controller implements action understanding and goal-directed imitation as a continuous process which combines sensory evidence, contextual information, and a goal-directed mapping of action observation onto action execution. As a theoretical framework, the implementation is based on dynamic neural fields<sup>9</sup> previously used to endow autonomous robots with cognitive capabilities (e.g., memory, decision making,<sup>30,75,247</sup>).

The complete control architecture including vision, cognition and path planning is validated in variations of a paradigm in which the robot system learns to imitate a grasping and placing sequence displayed by a human model. The learning is accompanied by structural changes in the controller representing knowledge transferred from the human to the robot during imitation.

### 2.1.1 Experimental Paradigm

To test the idea of a goal-directed organization of imitative behavior in a robot-human task, a paradigm was adopted, which has been originally developed for experiments with

human subjects (<sup>324</sup>). The paradigm employs an object that must be grasped and then placed at one of two laterally presented targets that differ in height. Importantly, the grasping and transporting behaviors are constrained by an obstacle in form of a bridge (see Fig. 2.1). Depending on the height of the bridge, the lower target may only be reached by grasping the object with a full grip and transporting it below the bridge. Placing the object at the higher target, on the other hand, may require combining a precision grip and a hand trajectory above the bridge.

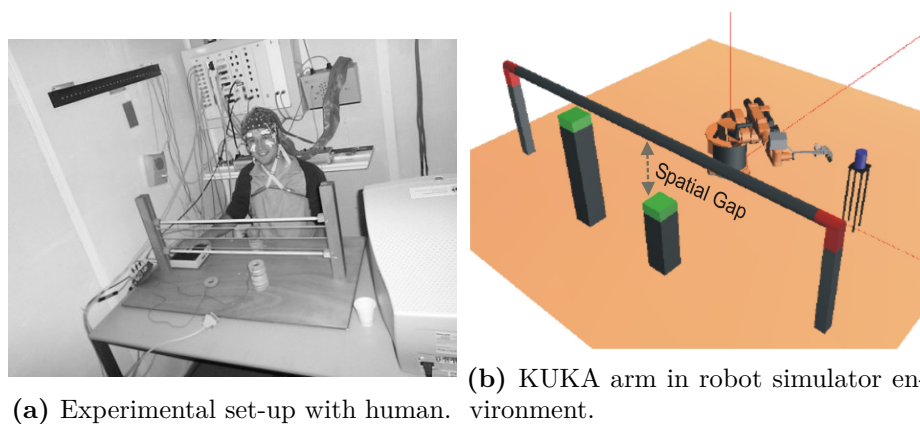


**Figure 2.1:** Bridge Paradigm. The robot has to imitate a human grasping an object and placing it at one of the two targets behind the bridge obstacle.

The robot had to reproduce the observed or inferred action consequence (placed object). The work was conducted on a robot platform consisting of an industrial 6-Degrees-of-Freedom robot arm (KUKA, Germany) on which a four-fingered anthropomorphic robot hand (GRAALTECH, University of Genova, Italy) was mounted. A real-time vision system provided information about the scene parameters and the human hand motion.

## 2.2 System Architecture

Three interconnected modules (vision, cognition, path planning) define the robot control architecture (see Fig. 2.2).

### 2.2.1 Vision Module

The *vision module* provides the environmental variables of the task setting (Cartesian position of bridge, object and goals) by means of a semi-automatic calibrated stereo camera system. All outputs are stored in the general configuration structure, globally available for

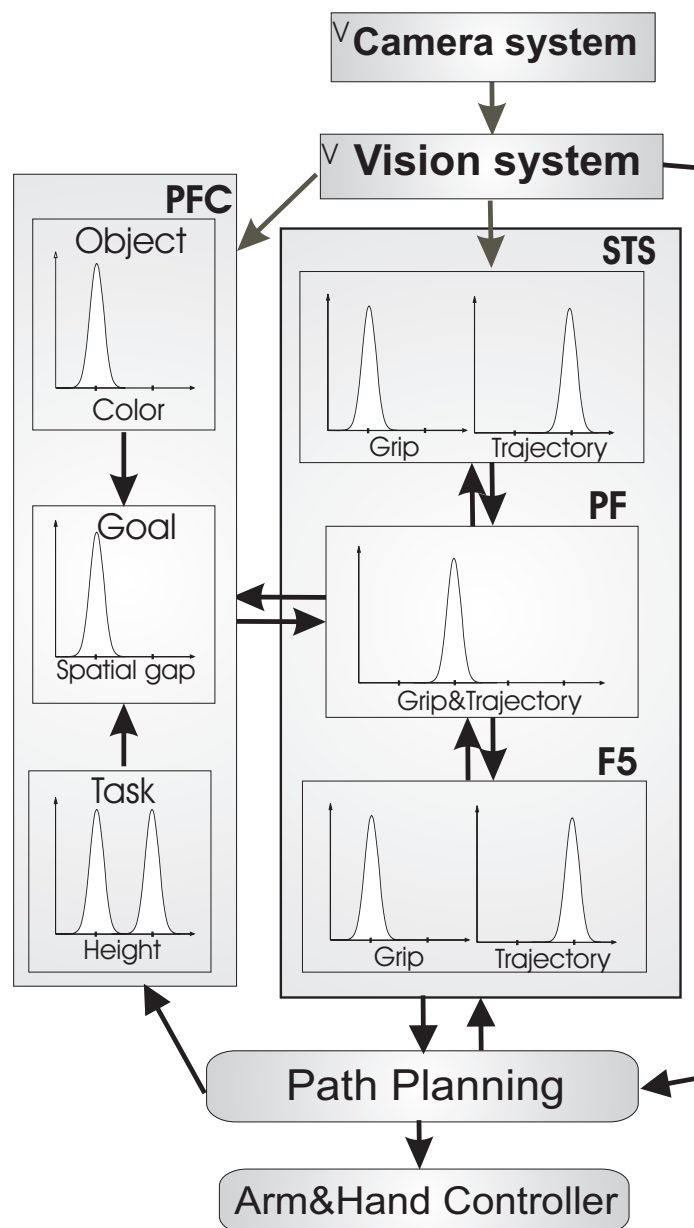


**Figure 2.2:** Schematic diagram of the control architecture. The central part responsible for the selection of means and goals in the imitation task reflects recent neurophysiological findings in 4 interconnected brain areas. The functionality of the STS-PF-F5 pathway is to match action observation and action execution. The matching is controlled by the goal representations in area PFC. The figure is adopted from<sup>79</sup>.

the other modules of the controller. The demonstrator's hand and the object are identified and tracked in real time on the basis of a chroma-space blob segmentation in the YUV color space using a monocular camera view. The hand tracking algorithm is based on a

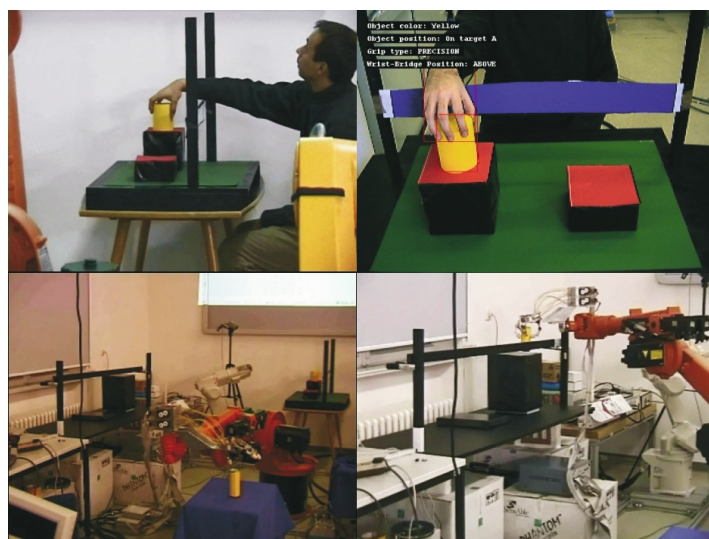


**Figure 2.3:** Snapshots from the experimental set-up. The upper row depicts the visual analysis of teacher’s world configuration and of the teacher’s action. The right inset displays the view from the robot camera. The vision module detects the color of the object and the target height relative to the bridge (blue bar). With a fixed height of the bridge, the higher target is classified as *small spatial gap*. The vision module also detects the features of teacher’s action as grip type (PG) and arm trajectory type (AT), the last is estimated from the wrist position relative to the bridge. Bottom row shows two snapshots of the robot in action. The figure is adopted from<sup>78</sup>.

mutual information optimization approach<sup>327</sup> which maximizes the consistency between an observed image and postures of a hypothetic hand model (26-degrees-of-freedom). The hand trajectory (above or below the bridge) and the placing goal (high or low) are classified on the basis of a distance measure relative to the respective object. The categorization of the grasping behavior (full or precision) is based on the orientation of the palm relative to the object.

Fig. 2.3 demonstrates snapshots from a real experimentation scene with KUKA robot arm. The snapshots on the upper row show two views of the teacher’s table. The upper right inset displays the view from the robot camera. In all imitation tasks, the exact geometrical parameters of the teacher’s scene are different from the task parameters of the KUKA environment. The Vision module extracts only the symbolic, categorized information from the teacher’s scene and actions. Bottom left inset also shows a view on teacher’s table at the back near the wall and its frontal robot camera observing the table.

## 2.2.2 Cognitive Module

In the *cognitive module* decisions about the action goal and the means to achieve that goal are made. Its layered architecture is biologically inspired, as it represents the basic

functionality of neuronal populations in brain areas known to be involved in action observation/execution tasks (for details see<sup>76</sup>). The STS-PF-F5 pathway is believed to represent the neural basis for matching between the visual description of an action in area STS and its motor representation in area F5. Direct physiological evidence for this hypothesis comes from the existence of “mirror neurons” in F5 that become active both when the animal makes a particular action and when it observes another individual making a similar action. The fundamental idea here is that the matching takes place on the level of motor primitives that represent complete goal-directed motor behaviors such as, for instance, “grasping an object with a full grip”<sup>253</sup>, see also<sup>275</sup> for an excellent overview in the context of robotics research. Motor primitives do not encode the fine details of the movement and thus provide a sufficiently abstract level of description for imitation learning across dissimilar embodiments.

Subpopulations of neurons in the premotor area F5 are thought to represent distinct goal-directed motor acts such as for instance grasping, holding or placing an object. Perrett and colleagues described neurons with strikingly similar firing characteristics with respect to hand-object interactions in the superior temporal sulcus (STS) of macaque (for review see<sup>50</sup>). The major difference to the mirror neurons in F5 is that the goal-related neurons in STS do not discharge during active movements. With respect to the direct matching hypothesis this suggests that neuronal populations in STS may provide a visual description of a goal-directed action, which is then mapped onto a similar motor representation in F5. For the modeling, separate action observation and action execution layers are proposed, in which neuronal populations encode abstract motor primitives. Concretely for the bridge paradigm, we distinguish two types of grasping primitives (precision grip (PG) and full grip (FG)) and two types of transporting primitives for avoiding the obstacle (below (BT) or above (AT) the bridge).

The representations in the intermediate layer PF reflect recent neurophysiological findings in brain area PF that suggest a goal-directed organization of action means. Using a grasping-placing task, Fogassi and colleagues<sup>93</sup> described a population of grasping mirror neurons which showed a selective response in dependence of the final goal of the action (placing vs. eating) to which the grasping act belongs. For the bridge paradigm, this finding is abstracted by assuming representations of specific combinations of primitives (e.g., PG-AT) which allow achieving a specific placing goal. Possible goals parameterized by their height relative to the bridge (spatial gap, Fig. 2.1), are assumed to be encoded in neuronal populations of the “prefrontal area” PFC. The reciprocal connections between PFC and PF are learned during the imitation experiments. Functionally, they allow to override a direct matching between primitives in STS and F5 if necessary. Beside the



direct stimulation by the vision system (placed object), the goal representations in PFC may be influenced by two additional information sources: *i)* The task input represents memorized information about the number, identity (height) and probability of goals (for details of a computational implementation see<sup>81</sup>). It reflects the fact that in a known task setting the robot may engage in partial motor preparation even before the observation of the human model. *ii)* The second input represents object cues (e.g. color) which may become associated with the goal during imitation.

### Dynamics of Decision Making and Learning

Each individual layer of the cognitive module is formalized by a dynamic field. The particular form as employed here was originally introduced by Amari<sup>9</sup> as a mathematical model for the dynamics of pattern formation in neuronal tissue. The main idea is that the interplay between excitatory and inhibitory interactions in local populations of neurons may sustain the population activity for extended periods of time. The build-up of self-sustained activity patterns in populations encoding action goal and means may thus be seen as the process of stabilizing and maintaining the task relevant information.

In the modified Amari model<sup>139</sup>, the activity  $u(x, t)$  of a neuron at field location  $x$  at time  $t$  is governed by the following integro-differential equation:

$$\begin{aligned} \tau \frac{\delta}{\delta t} u(x, t) = & -u(x, t) + h + \sum_i S_i(x, t) + \\ & + f_1(u(x, t)) \left[ \int w(x - x') f_2(u(x', t)) dx' - w_{inhib} \int f_2(u(x', t)) dx' \right] \end{aligned} \quad (2.1)$$

where  $\tau > 0$  defines the time scale of the dynamics and  $h < 0$  the resting level to which the field activity relaxes without external stimulation. The non-linear functions  $f_i(u)$ ,  $i=1,2$ ; are of sigmoid shape,

$$f_i(u) = \frac{1}{1 + \exp(-\beta_i(u - \theta_i))} \quad (2.2)$$

with threshold  $\theta_1 > \theta_2$  and slope parameter  $\beta_1 = \beta_2$  (cf.<sup>139</sup>). The strength of the excitatory connections  $w$  to field neighbors is expressed in terms of the distance between locations, that is,  $w(x, x') = w(x - x')$ . We used gaussian profiles with standard deviation  $\sigma_s$  and amplitude  $A_s$ . The feedback inhibition depends on the overall activity in the field and is controlled by the constant  $w_{inhib} > 0$ . Since the excitatory process is spatially restricted, the globally inhibitory process dominates at larger distances. Finally, the term  $\sum_i S_i(x, t)$  represents the summed external input to the field which consists of excitation from connected layers and input from the vision module. The latter is modeled as gaussian functions of adequate intensity.

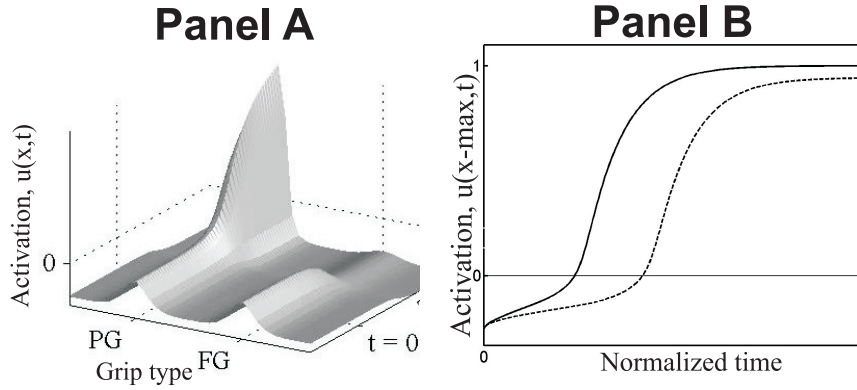


**Figure 2.4: Panel A:** The temporal evolution of a self-stabilized activation pattern representing a decision for a PG-grip. Note that at the time of stimulus onset,  $t = 0$ , the field appears to be already pre-activated by the constant input from the task layer in PFC. **Panel B:** The time course of the maximally excited field element is compared for the case with pre-activation (solid line) and without pre-activation (dashed line). The figure is adopted from<sup>79</sup>.

Here the model parameters were adapted to guarantee a bistable regime of the dynamics in which a transient input may act as a switch between a homogeneous rest state and a localized activity profile<sup>9</sup>. In Fig. 2.4, Panel A, we exemplify the evolution of such a profile in response to an input to a neuronal population representing the precision grip (PG). The build-up of excitation is accompanied by an increase in lateral inhibition which causes a suppression of activation in the population representing the grip alternative (FG). There is a threshold,  $u_{TH}=0$ , for triggering a self-sustained pattern. Weak external inputs (e.g., task input) may only bring the activation close to that threshold. As shown in Panel B, this “preshaping” mechanism may nevertheless drastically alter the time course of the suprathreshold response triggered by a sufficiently strong input<sup>81</sup>. The observed speed-up of processing may, in turn, affect the decision processes in connected layers.

The learning of synaptic connections between neuronal populations in any two layers of the model network is based on Hebbian learning (for discussion of theoretical aspects see<sup>67</sup>). Keysers and Perrett<sup>153</sup> have suggested that a correlation-based learning rule within the STS-PF-F5 circuit may explain how mirror properties may evolve. In addition, we propose that also the synaptic links of area PF to the goal representations in PFC may develop using such biologically plausible rules.

A basic assumption is that the time scale of the synaptic modification is small compared to the time scale of the neuronal dynamics. The synaptic efficiency can thus be treated as constant on the fast time scale of the pattern formation. When the network has relaxed to a stable state, a Hebb rule is applied during a developmental period defined by a

internal reinforcement signal. Note that the transient phase of the dynamics could have been included in the learning process as well without qualitatively changing the results presented here. Fig. 2.5 sketches the connections  $a(x, y)$  between neurons in two distinct network layers which are modified during practice and the connections  $w(x, x')$  between two neurons within the same layer which are assumed to remain fixed and are chosen to guarantee the bistable behavior of the layer dynamics.

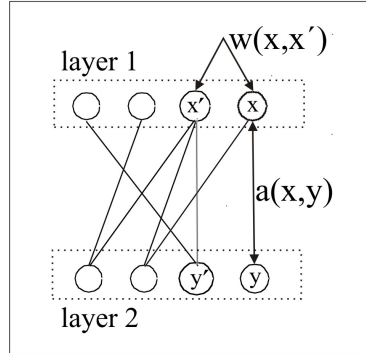


**Figure 2.5:** Sketch of the connectivity within layers,  $w(x, x')$ , and between layers,  $a(x, y)$ , of the model network. The figure is adopted from<sup>76</sup>.

The equation for the correlation-based synaptic modification between neuron  $x$  in layer 1 and neuron  $y$  in layer 2 is given by (Fig. 2.5):

$$\tau_s \frac{\delta}{\delta t} a(x, y, t) = -a(x, y, t) + \eta f_2(\bar{u}_1(x)) f_2(\bar{u}_2(y)) \quad (2.3)$$

where  $\bar{u}_1, \bar{u}_2$  denote the equilibrium solutions of the relaxation phase in layer 1 and layer 2, respectively,  $\eta > 0$  defines a scaling parameter,  $\tau \ll \tau_s$  denotes the time scale and  $f$  is the sigmoidal threshold function. Note that the activity patterns coding for the distinct, categorical choices in each network layer are assumed to be non-overlapping such that the strength  $a(x, y, t)$  is not affected by the representation of alternative means or goals. The time window for learning is defined by an internally generated reinforcement signal representing a successful path planning. Technically we implement the monitoring process by multiplying the right hand side of equation 2.3 with a function that takes on for simplicity the value 1 during the learning period and the value 0 otherwise. At the end of the learning process, the synaptic strength  $a(x, y, t)$  becomes the time-independent  $A(x, y)$ :

$$A(x, y) = \eta f_2(\bar{u}_1(x)) f_2(\bar{u}_2(y)) \quad (2.4)$$

Since the self-stabilized activity patterns  $\bar{u}_1$  and  $\bar{u}_2$  are symmetric and bell-shaped, also the evolving connection profile is symmetric with maximum connection strength to the maxi-

mum excited neuron in the other layer. The equilibrium solution in layer 1 (equivalently for layer 2) is then given by:

$$\bar{u}_1(x) = \int w(x - x')f(\bar{u}_1(x'))dx' + h + S_2(x) \quad (2.5)$$

with the input from layer 2

$$S_2(x) = \int A(x, y')f(\bar{u}_2(y'))dy'$$

For the model simulations, the strength of the learned synaptic connections between layers is adjusted using the parameter. Depending on whether or not an existing activation pattern should drive the evolution of suprathreshold activity in a subsequent layer or should only preshape neuronal representations, its effective input strength is chosen above or slightly below the threshold  $A_{TH}$  for the ignition of an active response.

## 2.3 Path Planning

### 2.3.1 Path Planners and their Role in Sensory-motor Planning

The path planning module plays a central role in my architecture, despite its position as the lowest motion planning level producing the detailed kinematic trajectories to be followed by the robot PD controllers. The main motivation for the connectionist path planning module is not only to have a system capable of the reliable real time motion planning for the systems with many degrees of freedom (like standard robot arms with 7-9 DoFs), but also to have a system for constrained or prioritized planning, with pre-selection and prioritization of the motor acts as specified by higher levels of my architecture.

Another important feature of the proposed design is its capacity for “learning for imitation”. When the low-level planing is performed without pre-selection and prioritization from the higher motion-planing levels, then the resulting solutions in form of bundles of trajectories can be clustered and categorized in an unsupervised way or be associated with important, behavior-related features of the environment. Thus, the autonomous performance of the low-level planning system itself is providing the motor repertoire, which is categorized by the higher levels. In my system, the next level above the path planning module, called F5, is associating the stereotypical bundles of trajectories with discrete motor features. These bundles or beams of trajectories are described as subsets of states in configuration space (C-space), where kinodynamic planning takes place. These subsets (or areas in C-space), once learned and represented in F5, can be pre-selected from F5 in the form of state-prioritization, by lowering the cost function of states falling into the intersections of the multiple pre-selections. The reduction of the state cost function

shifts the resulting planned path towards areas of such preferential pre-selections.

Related methods of planning with pre-selections in C-space were developed by<sup>157</sup> for the sequential planning of multiple concatenated motion clips. A similar approach of combining low-level geometric and high-level semantic planners was proposed by<sup>46,47,111</sup>. The inspiration for the hybrid multi-level planners roots in earlier work of R. Brooks on the *subsumption architecture*. The subsumption architecture couples sensory information to action selection in an intimate and bottom-up fashion<sup>13</sup>. It does this by decomposing the complete behavior into sub-behaviors. These sub-behaviors are organized into a hierarchy of layers. Each layer implements a particular level of behavioral competence, and higher levels are able to *subsume* lower levels in order to create viable behavior. The layers, which all receive only pieces of sensory information in ranges of their behavioral competence, all work in parallel and generate outputs affecting the lower layers. The higher layers may utilize the lower-level competencies as constraints resulting from planning trials of lower layers (similar to<sup>111</sup>).

In a similar way, my system architecture is based on a hierarchy of planning levels for motor action representations. The whole sensory-motor architecture has a ladder hierarchy: the motor action representations at each layer of the motor hierarchy are connected to the corresponding scene parameter representations of the visual hierarchy<sup>95</sup>. This structure assumes also a hierarchical organization of skill learning. The connections from the lower layers of visual representations of simple geometric scene features are linked to simple motor-acts representations. These connections are learned earlier relative to those in-between the higher visual-motor layers.

I call this hierarchical approach to sensory-motor learning “learning to imitate”. It is intended to solve the motion features *transfer problem* in imitation learning (known also as the *correspondance problem*, see<sup>222</sup>). The critical geometric motion features cannot be copied from one actor (teacher) to another actor (student) directly due to the difference in body geometries and variable environmental constraints<sup>263</sup>. So, motion features need to be categorized and abstracted, and such categorization as result of learning is dependent on the individual experience of each actor. An abstraction, as a result of categorization, leads to the formation of motor representations on the higher levels, which in their turn, are associated with more abstract sensory-derived concepts describing the scene geometry<sup>96</sup>. For the lower level C-space planner, the chosen combined motor features are affecting the planning while acting as constraints and pre-selection in the space of trajectories.

Optimal kinodynamic planners in configuration space (C-space planners) are very common in robotics, for motion planning involving a few degrees-of-freedom (DoFs), e.g. see the robotics books<sup>48,167,195</sup>. Extensions of C-space planners for higher dimensional C-spaces have been proposed recently<sup>20,49,151</sup>. This research resulted in stochastic algorithms for off-

line and online C-space re-sampling during planning, an approach known as Probabilistic Road Maps (PRMs)<sup>152,170,290</sup>. The suboptimal online re-sampling method called Rapidly-exploring Random Trees<sup>169,171</sup> became popular in the last years (e.g.<sup>7,118,138,140,239,320</sup>). Recently, the interest of scientists is directed towards integration of such approaches with stochastic identification and control frameworks<sup>37,146,147,219,311,312</sup>, Dynamic Bayesian Networks (DBNs)<sup>101,315</sup> and POMDPs<sup>297,310</sup>. Some researchers employ the game-theoretic approach for the local optimization for planners<sup>204</sup> and for the optimal controllers<sup>233</sup>. Substantial research efforts were invested in the design of multi-resolution C-space and policy space refining methods<sup>200,201,264</sup>.

C-space shortest path planners for low-dimensional configuration spaces can be realized on regular lattices representing the discrete configurations. The nodes of the lattices are assumed to be connected regularly with the nearest neighbors. In this case, with an appropriate regularization of the connection weights, the shortest path finding algorithm can be reformulated as breadth-first search, (e.g.<sup>114,173,265</sup>). The last can be realized in the connectionist paradigm as a wave expansion neural network (e.g.<sup>149</sup>). Multiple models of such neural networks were proposed with applications in robotics<sup>42,172,176,177,216</sup>. In a series of papers from the 1990s, David A. Rosenbaum and colleagues proposed a C-space kinodynamic planner for arm reaching and grasping tasks, where the connection structure of the C-space sampling PRM can be learned by trial-and-error. Here, the robot practices the reaches in different environments, in the presence of gravitational and dynamic-reactive forces<sup>259-263</sup>. Our approach explores similar ideas for learning the connection structure. Other approaches similar to ours were also realized by<sup>119,120,172</sup>.

In the last half century path integration models similar to PRMs (or potential field models,<sup>224</sup>) became also popular in computational neuroscience as connectionist models for decision making and action planning in subcortical areas as the hippocampus, the basal ganglia and the nucleus caudate in the striatum. E.g. a model of striatum as a state-space planner was presented in series of papers<sup>58-60</sup>. Those were based on old physiological findings, e.g.<sup>168,191</sup> and later resulted in a kinodynamic planning and control architecture for robots<sup>129</sup>. Exemplary state-space based models of dynamic planning in hippocampal place-cells system are presented in<sup>194,197,224,270</sup>.

### 2.3.2 Path Planning Algorithm

#### Wave-expansion breadth-first search algorithm. Connectionist implementation

For generating overt behavior, the abstract motor primitives represented in layer F5 have to be translated into the right kinematics. We employ a global planning method in C-space (posture space)<sup>79</sup>, which is inspired by biologically plausible network models (see subsection 2.3.1). In this C-space covering sparsely connected network, which can be regarded as PRM, each of the locally interconnected nodes represents a stored posture, that is an array of joint angle values. It is assumed, that a model for the forward kinematics of the arm/hand system exists, that is, the nodes are associated with the arm/hand location in Cartesian workspace. Each node  $i$  of the C-space covering network is connected with its  $k$  nearest neighbors. The connection weights  $w_{ij} = w(i, j)$  are assumed to decrease exponentially with normalized euclidean distance in C-space, as  $w(i, j) = \exp(-d(i, j))$ .

Starting with an external activation of a set of goal postures  $P_G$ , activation spreads in each time step to inactive nodes by summing the excitation,  $v_j$  from the active neighbors multiplied by the respective connection weight,  $v_i(t) = \sum_{j=1}^k v_j(t-1) * w(i, j)$  and  $v_{P_G}(0) = 1$  (there is no interaction between already activated units). This wave-propagation in the network realizes a breadth-first search algorithm. When the wavefront reaches the node corresponding to the initial posture, the activation dynamics stops. The sequence of postures defining a path from the initial state to the goal state is then found by local backward search of the maximally excited neighboring nodes. The last operation of backward search by local maximization is an analogue of Viterbi's algorithm in Dynamic Programming. In our case, the wave-expansion method realizes the breadth-first search variant of this algorithm. Posture nodes which are impossible due to obstacles are inhibited. The forbidden set  $P_O$  of all inhibited nodes is found by explicitly testing for spatial overlap in Cartesian space between the to-be-assumed arm posture and the environmental obstacles using forward kinematics. The complement of the forbidden set  $P_O$  in the set of all nodes is denoted as  $P_{free}$ . Additional information from the vision and the cognitive module of the control architecture is integrated before starting the wavefront operations (similar to the pre-selection method of<sup>157</sup>). Moreover, the ensemble of nodes which can become part of the wavefront is further constrained by the motor primitives in F5. For instance, we use again forward kinematics to check whether a particular node represents "the elbow link of the robot arm in a high position" as required by a trajectory above the bridge. This pre-selection of a set of compatible postures,  $P_{F5}$ , restricts the global planning process to the subset  $P_{F5} \cap P_{free}$ .

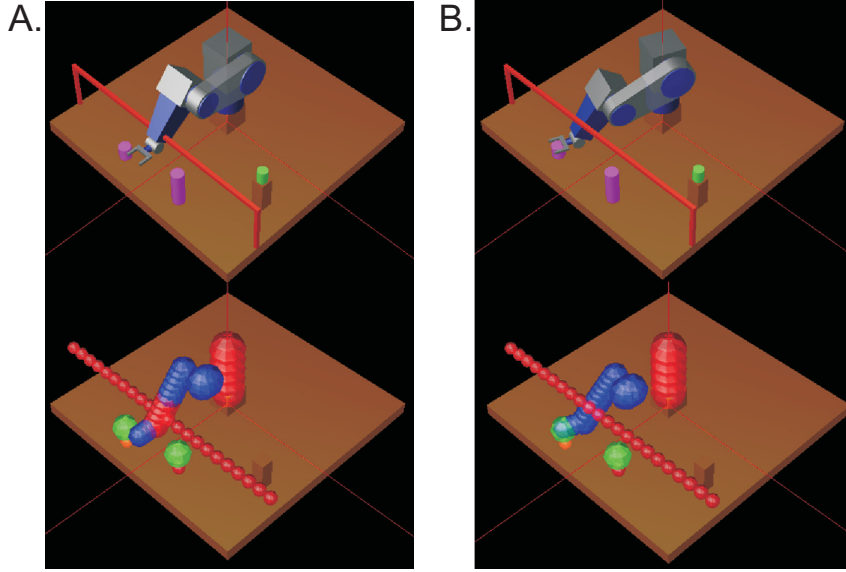


**Figure 2.6:** Kinematic model of the RX-90 robot arm in a modeled scene of the experimental workspace. Panel A depicts the prohibited arm configuration, where the arm-obstacle collision is detected. Panel B depicts the target arm configuration, when the gripper reached the target goal position with a collision-free posture. The lower pictures in each panel show the distributions of the ‘safety balls’ along the arm links (blue balls). The arm safety balls that collide with the bridge safety balls in Panel A are highlighted red.

### Forward kinematics for collision detection in the workspace

Obstacles are taken into account by using forward maps: nodes representing postures that imply arm-body self-collisions or arm-obstacle collisions are checked by forward mapping from C-space to Cartesian workspace. The procedure works as follows. Each link of the robot arm, the robot body and each part of an obstacle is covered by a union of virtual safety balls. Each ball is represented by its center point (*safety point*) and its radius (*safety radius*). The forward kinematics produces the robot arm configuration in workspace, which gives the 3d positions of all safety points. For all pairs of safety points (one belonging to an arm link and the other one belonging to an obstacle, to another not neighboring arm link or to a body part), we check, if the pair is closer than the sum of their safety radii. If they are, the node representing the arm configuration is considered to be inhibited.

The architecture was designed for many different geometries of the robot arms. For illustrating the different C-space sampling techniques, I implemented the architecture for 2DoF and 3DoF planar arm kinematic models. The final architecture was produced for the robot arms of Amtec with 7 DoF (in different mounting configurations), for a Staubli RX90 with 6 DoF and for a KUKA arm with 7 DoF<sup>79</sup>. As an example, the kinematic model of a 6 DoF RX90 arm is depicted in Fig. 2.6. Panel A demonstrates the collision



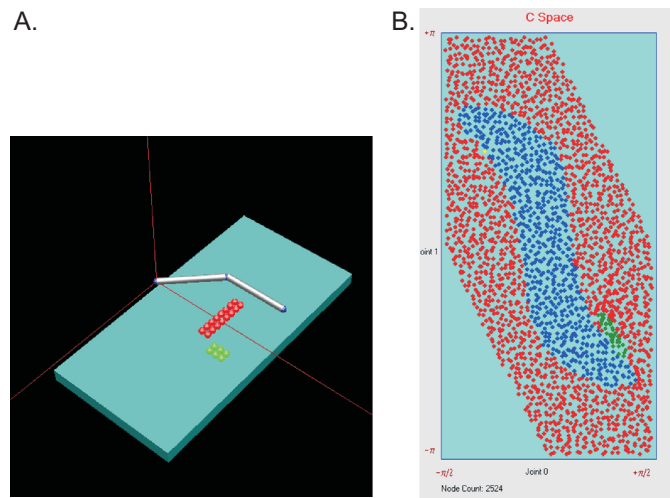


**Figure 2.7:** A. Kinematic model of 2-DoF planar arm placed in a virtual environment with an obstacle (red balls) and a target positions for the arm end-effector (green balls). B. C-space of 2-DoF planar arm covered with the posture-nodes. Freely available 'active nodes' are red. The nodes inhibited by obstacle-collisions are blue. The nodes corresponding to the arm configurations, when the end-effector reaches the target area, are green.

detection: the arm safety balls in collision with the bridge safety balls are highlighted red. Panel B demonstrates one of the target postures, when the end-effector of the hand reaches the object placement target.

Panel A in Fig. 2.7 displays a 2 DoF planar arm kinematic model in its workspace. The arm links are covered by safety cylinders (instead of balls), and the planar obstacle is covered by a union of 16 safety balls (red). The blue ball is covering the end-effector of the actuator, and the union of 6 green balls is covering the target. When the end-effector safety ball (blue in Fig. 2.7) collides with a green target ball then the posture is considered as target posture (target arm configuration). Panel B (Fig. 2.7) depicts the random coverage of C-space of the planar arm model with the posture nodes. "Joint 0" axis represents the "shoulder" joint angle and the "Joint 1" axis corresponds to the "elbow" angle. Red dots are the free, 'active' nodes, while the blue ones are 'inhibited' by arm-obstacle collisions. The green dots correspond to the target arm configurations, regarded as the end-goals for the path planning algorithm. The single yellow dot near the border of the red and blue clouds represents the initial configuration of the arm. The parts of the C-space free of any nodes are not sampled due to the constraints in configuration space imposed on by the actuator angles. This depicted example of the C-space of a 2 DoF planar arm is used until the end of this section for illustration of the stages of pre-selection and path planning.

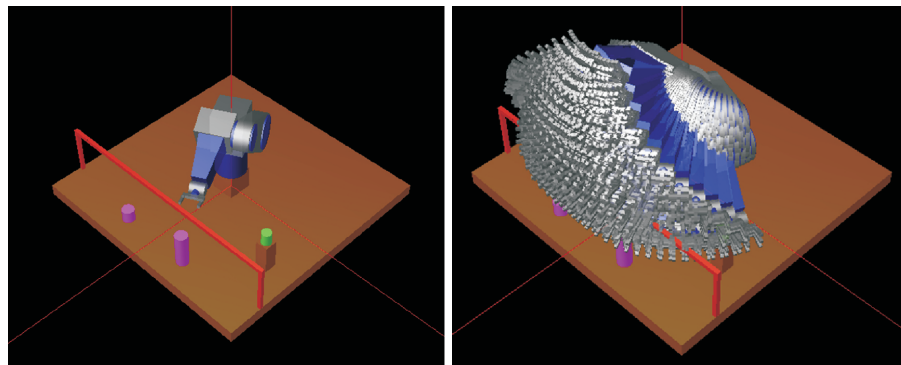


**Figure 2.8:** Left panel: kinematic model of the RX-90 robot arm with two-finger gripper. The obstacle bridge is red, the object to grasp is green and the two target positions are the tops of two magenta cylinders. Right panel: multiple snapshots of IK-generated trajectories of the robot arm starting from several initial positions towards the goals placed in the half-circular area above the table.

### Selection and representation of the task specific trajectories

The path planning starts with a distribution of posture nodes covering the whole workspace of the artifact. For the 7 DOFs KUKA arm about two to three thousand initial nodes are sufficient, since the refinement procedure described below guarantees, that new nodes can be introduced when needed (e.g. in the vicinity of obstacles). Then, Inverse Kinematics (IK) produces the ensemble of posture sequences that move the gripper from a random starting position towards the target position. This IK-based sampling of the C-space is running in the kinematic robot arm simulator and does not care about obstacle avoidance.

Inverse kinematics produces a set of postures
---

Start with a small random subset taken from the initial set of postures, sparsely representing the whole joint space.
---

<i>Cycle</i> (for all feasible targets):
--

For each posture move the hand toward the target by inverse kinematics and obtain the sequence of postures along the path sampled with an appropriate time interval.
--

For example, in the simulations of the 7 DOFs KUKA robot arm, I used 10 initial configurations for each target leading to 10 paths each consisting of a sequence of 15 postures.

An example of posture sets produced by IK, depicted in the workspace, is presented in Fig. 2.8. The time-steps for the iterative IK are chosen to obtain a uniformly spaced

distribution of the sampled nodes in C-space. The IK can be based on prioritization (e.g.<sup>17</sup>) taking into account the gravitational potential energy of the arm postures. We use Berkinblit's model of parallelized IK for the goal directed arm reaching movements<sup>26</sup>. Alternatively, a similar approach by G. Hinton can be used<sup>122</sup>. Also, quasi-stationary dynamical models were exploited in other work<sup>217,282</sup>, using naturalistic arm stiffness and damping.

### **Reduction of the search space: off-line refinement of the C-space representation network**

Real-time path planning for artifacts with higher degrees of freedom is possible with a technique known in the literature as the refinement procedure (first introduced in<sup>201,264</sup>). The goal of the refinement is to sample densely only for the task-relevant regions in C-space. Starting with a distribution of posture nodes sparsely covering free C-space, new nodes are introduced whenever needed. This is necessary, for instance, in vicinity of obstacle borders in C-space. Below, I describe the two types of refinements used in my path planning. The *off-line* refinement is performed before the first planning trial. It includes 1) the refinement of the C-space network done specifically for each type of robot (operating in the C-space areas free from self-collisions), and also 2) the pre-planning off-line refinement done when the robot is first presented with the environment with new objects and obstacles. The *online* refinement of the C-space network in the vicinity of a planned path is an iterative procedure, which includes re-planning of a planned path.

### **Pre-planning refinement**

On the first stage of off-line re-sampling of C-space, the nodes produced by random sampling and by IK-based production and inhibited by self-collisions are shifted towards the areas of C-space which are free and in the vicinity of the self-collision areas. The algorithm for this procedure is the same as the one for the re-sampling of the C-space in presence of obstacles, which is described below. The result of this first stage of re-sampling is specific to the particular robot geometry and independent from the path planning task and its environmental constraints. Thus, this first stage procedure has to be done only once for each robot and the result can be stored for future tasks.

The IK-based posture set production described above gives multiple sets of postures sampled from trajectories produced with different preferences for motion features. These sets are stored in my system as remembered pre-selections. They represent the regions in C-space associated with different motion preferences. Given a new task with its preferences,

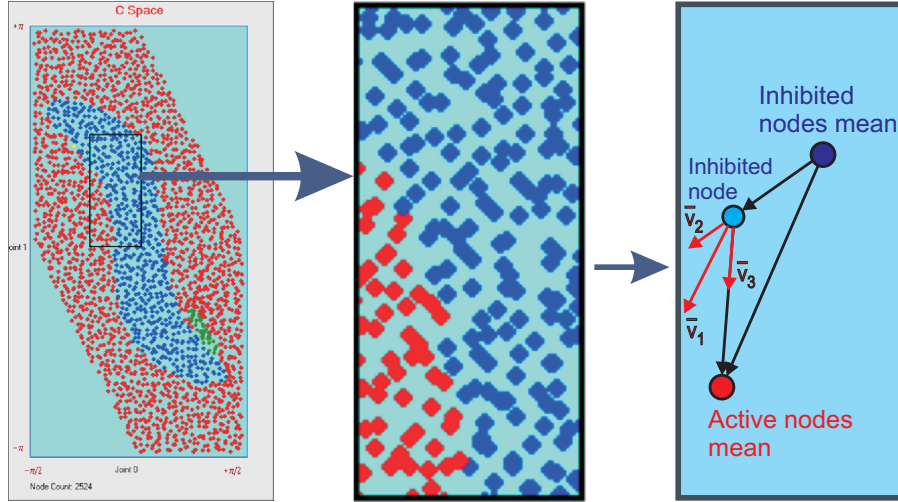


**Figure 2.9:** Left panel depicts the whole C-space for 2 a DoF planar arm model (see Fig. 2.7) and a rectangular testing window. Middle panel shows zoom-in of the testing window. The right panel presents the positions of the mean postures in the testing window: blue and red for the mean 'inhibited' and mean 'active' postures. The light blue node is a randomly chosen inhibited node to be shifted. Shift vectors are explained in the text.

the corresponding sub-set of posture nodes is added to the default posture set (which is pre-stored for every robot). Next, in the following stages of re-sampling and refinement in C-space, the nodes from this additional subset are treated just as the other nodes. This subset creates a preference for certain areas of C-space only by increasing the density of posture nodes in that area. Only later, during the building of the connected network of nodes, the explicit pre-selection affects the weights of the node links, reducing these weights for the nodes placed in pre-selected regions of C-space.

The *off-line* re-sampling in the presence of obstacles starts when the robot is presented with the task environment. A sketch of this proposed re-sampling algorithm is presented in Fig. 2.9. We choose a fixed-size rectangular testing window in C-space and positioned it such that it contains at least one inhibited node. For a fixed window position, for all inhibited nodes inside the window, perform the following cycle: consider each inhibited node (tested node) and compute the mean position of the other inhibited nodes in the window and the mean position of the rest of the free 'active' nodes (if there are any in the window); compute the vectors  $\bar{v}_2$  and  $\bar{v}_3$  (see Fig. 2.9), in absence of the active nodes  $\bar{v}_3 = 0$ ; then, the shift of the tested inhibited node will be in the direction of  $\bar{v}_1 = \bar{v}_2 + \bar{v}_3$ . Here we don't assign the new shifted positions to the inhibited nodes, but remember them. After the testing window scanned all its admissible positions, we finish the default iteration by assignment of all the new shifted positions to the tested inhibited nodes. Next, we

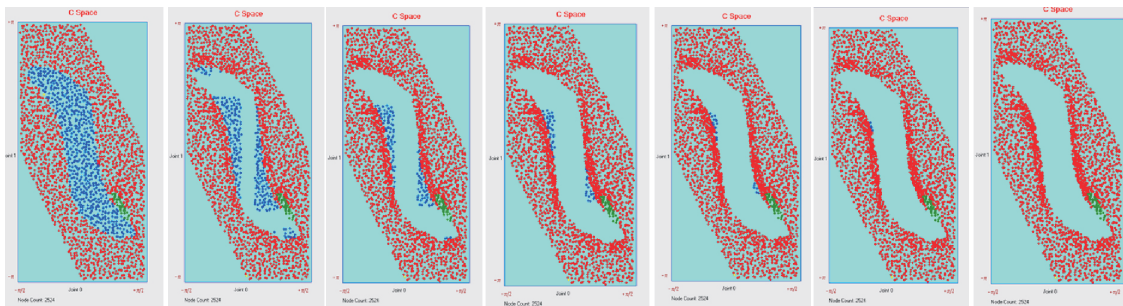


**Figure 2.10:** The initial (first panel), the final (last panel) and intermediate distributions of nodes in C-space during six iterations of the offline re-sampling procedure.

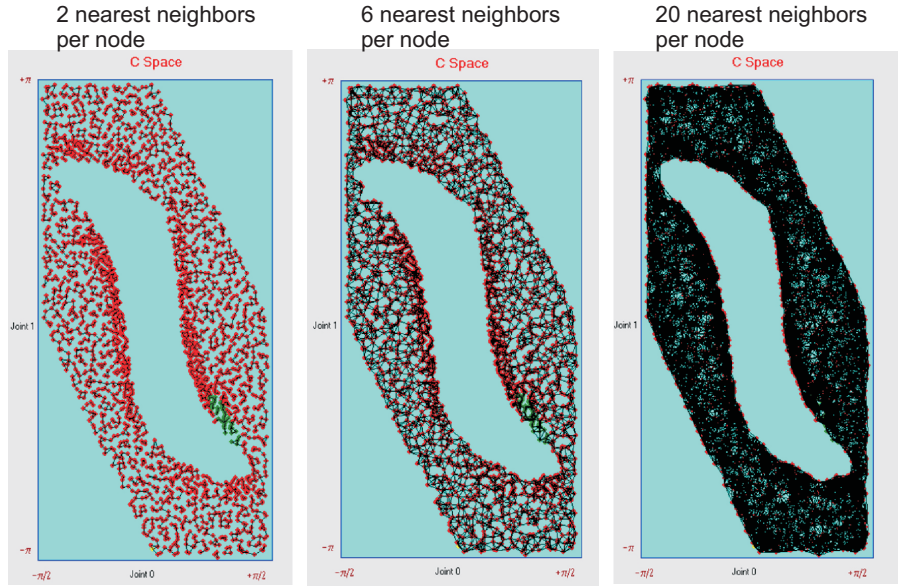
check the forward maps of the shifted nodes, which results in turning some of them into the 'active' set. Then, a new cycle of the new scanning path of testing window starts.

Fig. 2.10 displays the initial (first panel), the final (last panel) and intermediate distributions of nodes (in C-space of a 2 DoF planar arm) during six iterations of the off-line re-sampling procedure. The iterations stop when less than 2 percent of the nodes remain inhibited. Usually, just few iterations are needed, when the spatial range of the testing window is about the characteristic range of the obstacles. The larger the window size, the fewer the number of iterations needed and the more time each iteration takes. I optimized the total computation time of this procedure by choosing the testing window size to be about the same as smallest diameter of the typical obstacle in C-space.

All these re-sampling steps are called *refinement*, because the density of the sampled nodes increases in vicinity of the obstacle borders in C-space, while the total number of nodes remains the same as most of them change from the inhibited to the active state. After this procedure, I drop the remaining nodes which still stay inhibited ( $< 2\%$ ).

### Learning the connection structure for the network of C-space nodes

I define an Euclidian metric in C-space (which is joint angle space) and the number  $k$  of nearest neighbors (NN). For the 7 DoF KUKA arm with 2-3 thousands sample nodes I choose  $k = 4$ . Then, I run the  $k$ -nearest neighbors (kNN) algorithm which results in the  $k$  nearest neighbors for the given metric for all the active nodes. For this purpose we use "Ranger", an algorithm for nearest neighbor search in higher dimensions<sup>291,292</sup>, based on refined kd-trees<sup>25</sup> using median cuts and bucketing<sup>94</sup>. In detail, I run the kNN algorithm producing  $2k$  NN-lists, order them and store them for re-use as extended lists in the cluster connecting stage. Next, for the symmetrization, if node  $i$  is in the list of node  $j$ , I add node  $j$  to the list for node  $i$ . Thus, the symmetrized list enumerates all bi-directional



**Figure 2.11:** Examples of bi-directional symmetric linkage. Left panel depicts symmetrized linkage based on 2-NNs search. Middle panel demonstrates 6-NNs symmetrized linkage. Right panel: 20-NNs.

symmetric links of that node.

Three examples of bi-directional symmetric linkage are presented in Fig. 2.11. The left panel corresponds to  $k = 2$ , symmetrized linkage based on 2-NNs search. The middle panel depicts the link density for  $k = 6$  and the right panel the same for  $k = 20$ . In the left panel one sees many mutually disconnected clusters of nodes.

As the next step I check all triangles of links. A link  $[i, j]$  in a triangle of nodes  $(i, j, k)$  is a candidate for removal if  $d_{ij}^2 > d_{jk}^2 + d_{ki}^2$ . After finding all the candidates, I remove all these links from the lists. The result of the link removal for a symmetrized linkage based on 4-NNs search is depicted in Fig. 2.12. Link removal is performed to obtain a smoother path in breadth-first search for the shortest path.

The smaller number of NNs in the linkage procedure described above, the smoother the planned shortest path is. But with a smaller number of nearest neighbors, the linkage results in multiple disconnected clusters of nodes. As the next step, I reconnected the clusters (constellations) by shortest inter-cluster links. I search for single-connected disjoint clusters using a breadth-first search, which can be regarded as a modification of the Floyd-Warshall transitive closure algorithm. Next, for each pair of clusters I find the closest pair of nodes and connect this pair of nodes with a bi-directional link. Here one can use faster algorithms for the bichromatic closest pair search (e.g.<sup>2</sup>), but I use the pre-stored lists of  $2k$ -NNs (from the extended Ranger search), and search for the nearest bichromatic connection using these lists only. An illustration of these newly introduced inter-cluster



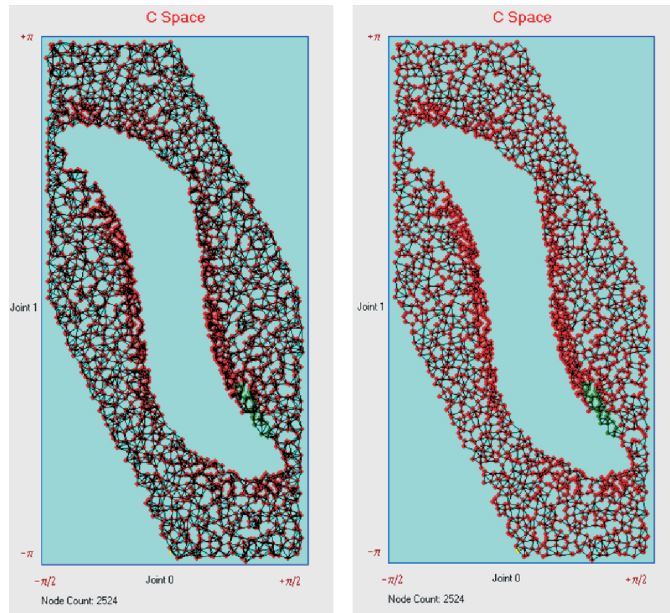


**Figure 2.12:** Left panel: the symmetrized linkage based on 4-NNs search. Right panel: the result of the removal of the long links.

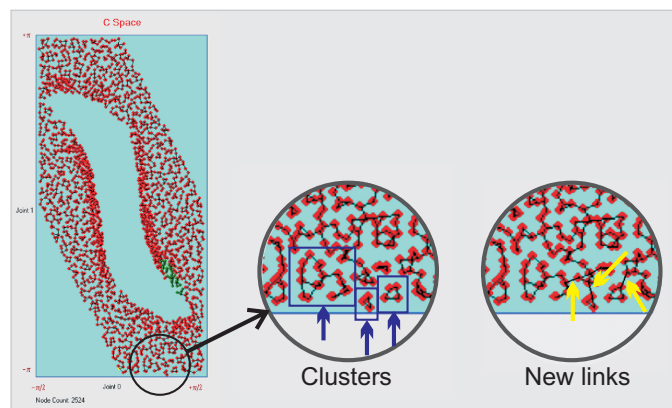


**Figure 2.13:** The newly introduced inter-cluster connections.

connections is depicted in Fig. 2.13.

The multi-stage procedure of linkage structure production, as described above, is specific for a particular robot in a particular fixed environment with all obstacle positions given and the node sets are re-sampled for the given obstacles. Thus, the connection structure can be stored together with the sampled set of nodes for the future use. A new task introduces new pre-selected nodes and only an update of the connection structure is needed. The last also includes the introduction of new nodes in the kd-tree structures to be re-used in updates of the  $k$ -NN lists by Ranger.

As a last step in connection building procedure, I assign the weights of the links  $w(i, j) = w(j, i)$  as decreasing exponentially with euclidian distance between the nodes in C-space, as  $w(i, j) = \exp(-d(i, j))$ . If motion feature preferences are introduced, they result in weight reduction for all the links connected to the nodes in the preference regions of the C-space.

The goal of these stages of off-line refinement and re-sampling is to reduce the computational time when the task instructions are given to the robot. On receiving the instruction about the motion preferences, only fast updates of node sets, their link structure and link weights are needed. At this moment, with the selection of the set of target nodes, the fast breadth-first search wave-expansion algorithm produces the first template solution for the shortest path. The next iterations, which I call *online* refinement are done with iterative re-planning of this path.

### **Online refinement of the planned path**

After the first template planning, I add more nodes around and in between path nodes for refinement of the planned shortest path.



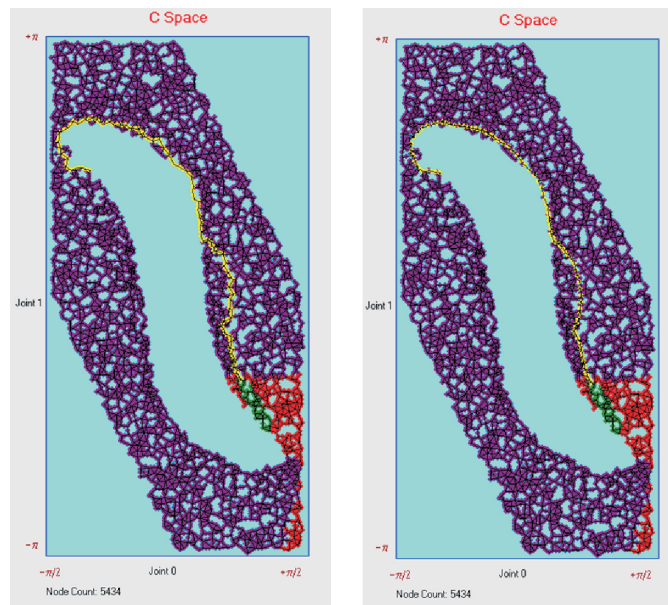


**Figure 2.14:** Left panel: the initially found template path. Right panel: the result of path refinement after the first iteration.

”Refinement of the generated trajectory. Single iteration”

- Take all nodes that represent the planned path.
- Refinement in the vicinity of the path:  
Add all nodes from the active set that are linked to the path nodes.
- Cycle:*  
For each path node:  
*Cycle:*  
For each pair of nodes linked to it:  
introduce a new node whose corresponding posture is a linear combination of the three postures.
- Refinement along the path:  
Add new nodes representing the linear combination of any two postures of neighboring path nodes.
- Find newly inhibited nodes and define the new active set.
- Update the connection structure of the network.
- Re-run the path planning algorithm.

Each iteration of the refinement procedure increases the size of the active set approximately by a factor 2. Usually, it is sufficient to repeat the path refinement only 2-3 times.

Fig. 2.14 presents the result of path refinement after the first iteration.

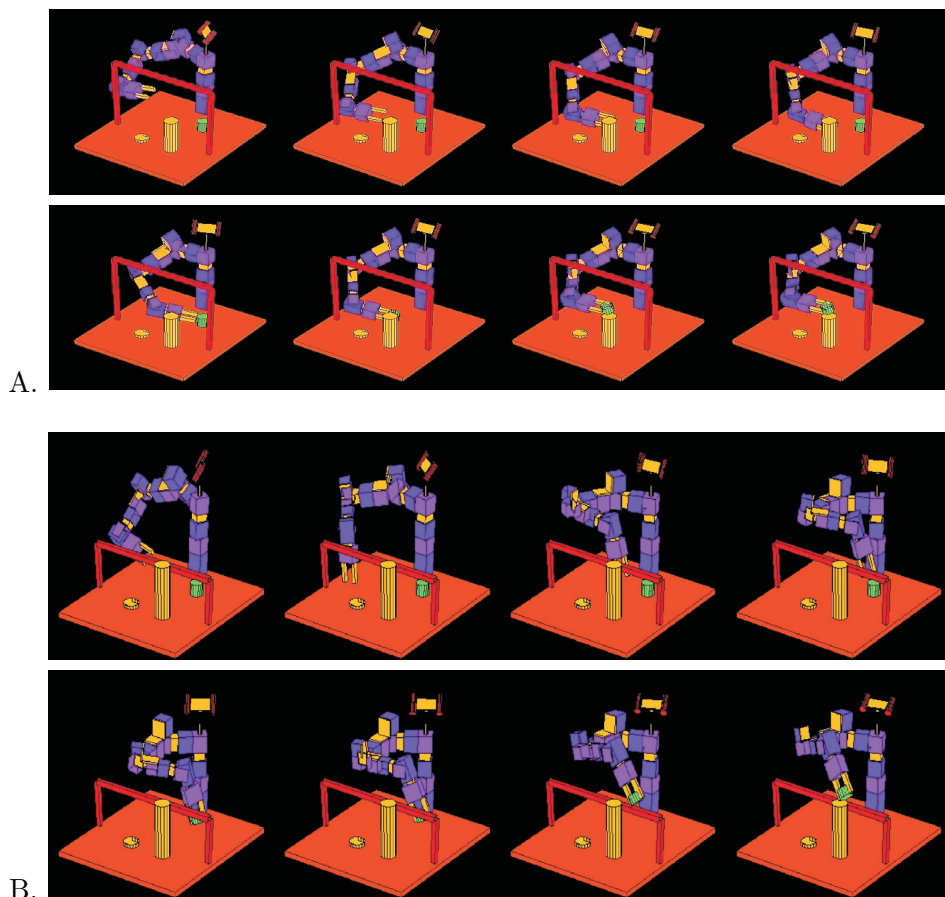


**Figure 2.15:** A. Two rows of snapshots: the AmTec robot arm is transporting the object below the bridge using a full (side) grip. B. Two rows of snapshots: the AmTec robot arm is transporting the object above the bridge using a precision (top) grip.

In some cases, the obtained planned path requires additional smoothing. For this purpose I use the "Elastic band" technique based on virtual local potential forces<sup>246</sup>.

Two examples of the AmTec robot arm simulator performing full (A.) or precision grip (B.) are shown in Fig. 2.15.

An example of the KUKA robot arm simulator (<sup>79</sup>) performing full grip and transporting the object below the bridge to the low target position is shown in Fig. 2.16. This exemplary obstacle avoidance motion is presented in [video<sup>1</sup>].

<sup>1</sup><https://goo.gl/LEz3BK> ([tiny.cc/9b715y](http://tiny.cc/9b715y))

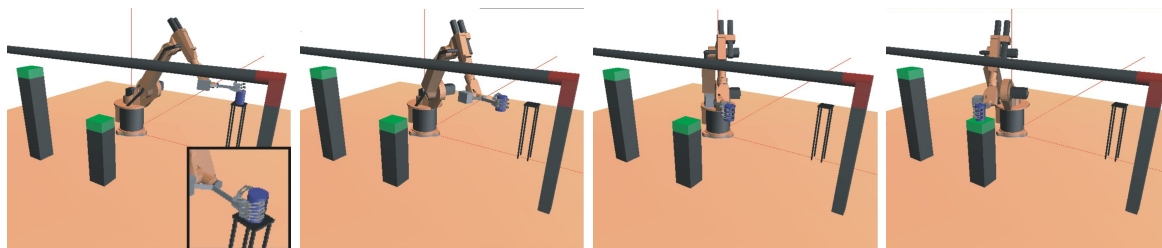


**Figure 2.16:** KUKA robot arm is transporting the object below the bridge to the low target position using full grip. The snapshots show postures generated by the path planning system.

## 2.4 Results

A set of imitation experiments with the bridge paradigm was performed which differ in the amount of visual information available to the robot and in the task constraints. The aims were 1) to exemplify what kind of knowledge may be transferred from the human to the robot by autonomously developing new representations, and 2) to illustrate the advantages of the goal-directed organization of the control architecture in terms of robustness, compared to more traditional via-point matching models.

### 2.4.1 Copying the Means

In the first set of experiments, a complete visual description of the teacher's grasping and transporting behavior exists and the vision system identifies the placing goal. Although the robot has the knowledge how to grasp, transport and place objects in its motor repertoire, it does not know how to combine the specific motor primitives to achieve the same end state under the constraints of the bridge paradigm. One strategy could be to copy the primitives displayed by the human demonstrator. The visual description of the observed motion in layer STS resonates via the matching mechanism in the mirror circuit with the congruent motor representations of the robot. If the covert path planning toward the desired posture necessary to achieve the action goal turns out to be successful, the observed action sequence becomes associated with the goal representation in layer PFC by the learning procedure described above. Fig. 2.17 illustrates the result of this learning by imitation in an example in which the robot copies the demonstrated precision grip and the trajectory above the bridge to place the object at the higher goal. In the various layers of the neural field model, the task specific information is encoded by activity profiles representing a steady state of the dynamics. Fig. 2.18 displays an example in which the robot copies the full grip and the trajectory below the bridge (for the lower goal).

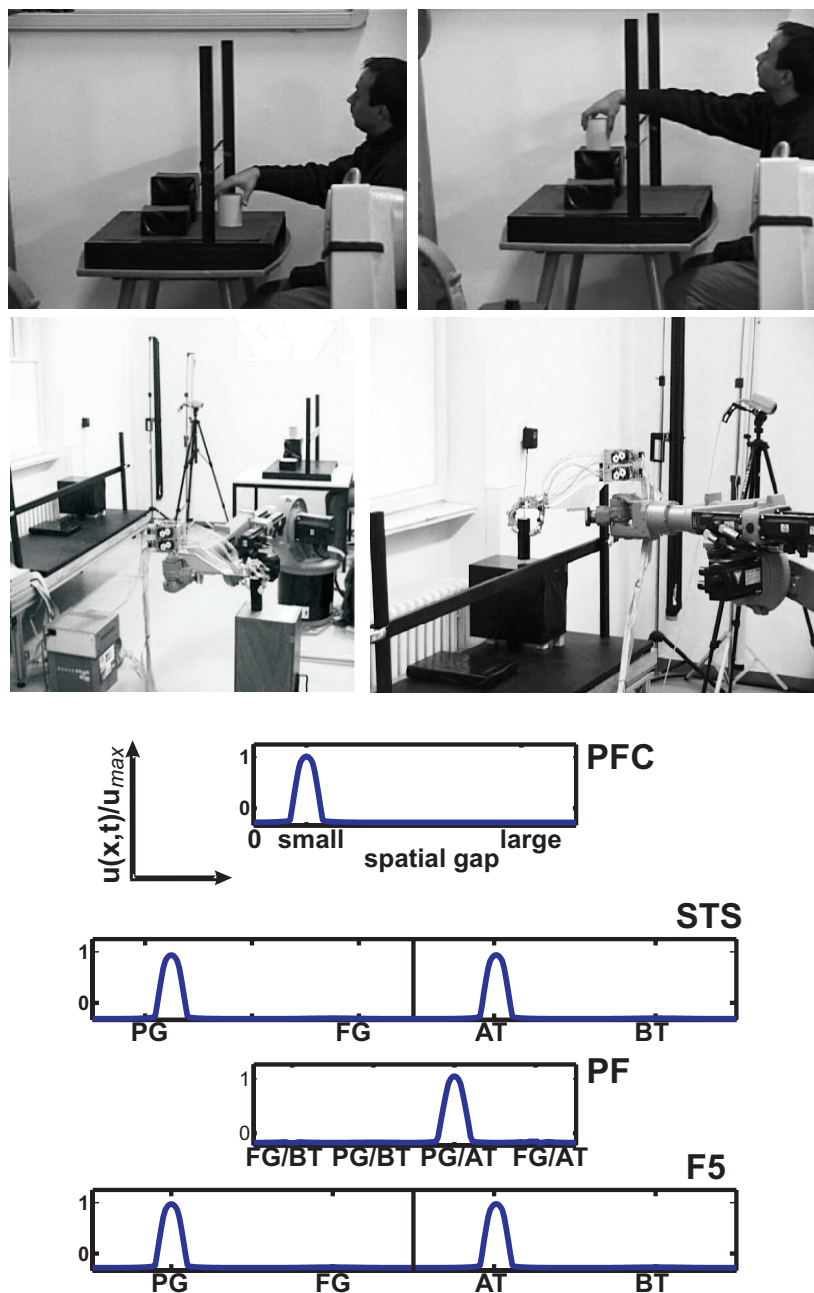


**Figure 2.17:** Copying the means: the teacher shows a complete grasping-placing sequence, here precision grip (PG) followed by a transport above the bridge (AT). The robot reproduces the observed placing at the lower target using the same means. The peaks of activation in layer F5 represent the means (motor primitives) selected by the robot to reproduce the same goal. The figure is adopted from<sup>79</sup>.

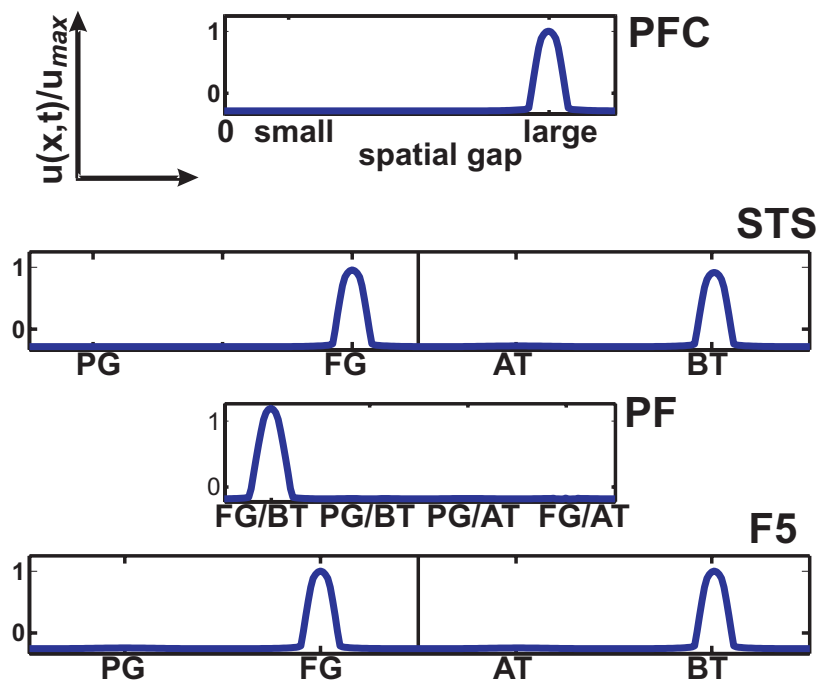


**Figure 2.18:** Copying the means: the teacher uses full grip (FG) in combination with transport below the bridge (BT).

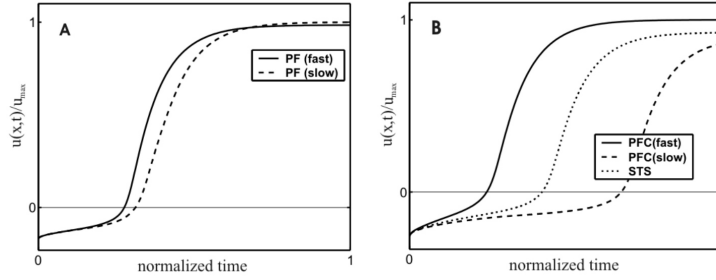


**Figure 2.19:** The time course of the maximum activated neuron in PF (A) and PFC (B) is shown as a function of the relative strength of the task input. The imitator’s means differ from the demonstrated action sequence in both grip type and trajectory type. A slowing down of the processing in PFC due to a weaker task input leads in PF to selection of the demonstrated sequence of means (dashed line). For the faster processing with stronger task input (solid lines), the PF neuron represents the preferred response strategy associated with the perceived goal. To allow for direct comparison, the time course of the representations in STS is plotted in (B). In both figures, time  $t = 0$  represents the onset of the visual stimulation in PFC. The figure is adopted from<sup>76</sup>.

Now imagine that the embodiment of the imitator allows, in principle, to adopt the demonstrator’s strategy to achieve the end-state. This may be the case when the obstacle is sufficiently low. We therefore assume that during training and practice also synaptic links between the particular goal representation and the observed strategy have been learned. The connections are, however, weaker compared to the links to the preferred action sequence. If the imitator is explicitly asked to pay attention to how the demonstrator achieves the goal, the observed means should dominate the decision processes in the mirror circuit. The intentional change in motor behavior can be achieved by weakening the task input to the goal layer. As shown in Fig. 2.19, a weaker “expectation” about potential targets results in a slower specification of the goal. This in turn delays the positive input to the associated sequence of means.

The proposed purely temporal mechanism for adapting the means is not restricted to the first part of the sequence. It works equally well when both the grasping and the transporting behavior have to be adapted. In Fig. 2.19.A we compare the temporal evolution of the maximum excited PF-neuron for an observed placing at the higher target. With weak preshaping of the goal representations, this neuron represents the demonstrator’s sequence FG/BT (dashed line) whereas with strong prior expectation the maximum excited neuron encodes the preferred sequence PG/AT (solid line). In both cases, the evolving pattern in the goal layer represents the perceived goal (Fig. 2.19.B). For the adaptation case, however, a conflict is introduced since the demonstrated sequence FG/BT represents

the observer’s preferred strategy associated with the other placing target. The resulting competition between neuronal populations is predicted to further delay the processing in PFC compared to the example shown in Fig. 2.19.A.

### 2.4.2 Discerning Motor Intention

The second set of experiments has been designed to reflect a challenge for all robotics systems cooperating in cluttered environments with other agents. Due to occluding surfaces, for instance, only partial visual information about the action displayed by the partner may be available and the observing robot has to infer the action goal. The control architecture implements the idea that a goal-directed motor simulation together with the integration of prior task knowledge underlies the capacity to discern motor intention. Consistent with this idea, it has been reported that mirror neurons may fire under appropriate conditions (e.g., with additional contextual cues) even if the goal of the motor act is hidden from view<sup>253</sup>. Umiltà and colleagues<sup>318</sup> have shown that a population of mirror neurons in F5 may encode a goal-directed action also when the crucial part defining that action is hidden from view. The information sufficient to trigger grasping neurons consisted of a hand disappearing behind an occluding surface combined with the knowledge that there is a graspable object behind the occluder.

In the example shown in Fig. 2.20, only the demonstrator’s grasping of the object with a full grip was observable. Since the robot is familiar with the task, links between goal representations and goal-directed sequences were established in previous trials. In addition, the constant task input results in a pre-activation below threshold,  $u_{TH}$ , of all task-relevant representations. As a result of the robot’s “expectation”, the evolving activation in STS encoding the observed FG-grip is sufficient to trigger first the sequence FG-BT and subsequently the representation of the associated lower goal (Panel B in Fig. 2.20). As depicted in Panel C, the robot shows its action understanding by combining a full grip and a trajectory below the bridge to reproduce the inferred action.

### 2.4.3 Goal Directed Imitation

The third set of experiments illustrates that the learned link from the mirror circuit to the goal representation is crucial. The bar of the bridge is removed for the human but not for the robot (Panel A in Fig. 2.21). Because of this change in the environmental constraints, the demonstrator now uses a full grip to place the object at the higher target. For the robot, a direct matching on the level of motor primitives would result in a collision with the bridge. As shown in the snapshot of the field model in Panel B of Fig. 2.21, the decisions in layer F5 represent the motor primitives PG and AT previously associated with the higher goal (compare Fig. 2.17). This choice is the result of the primacy of the goals over

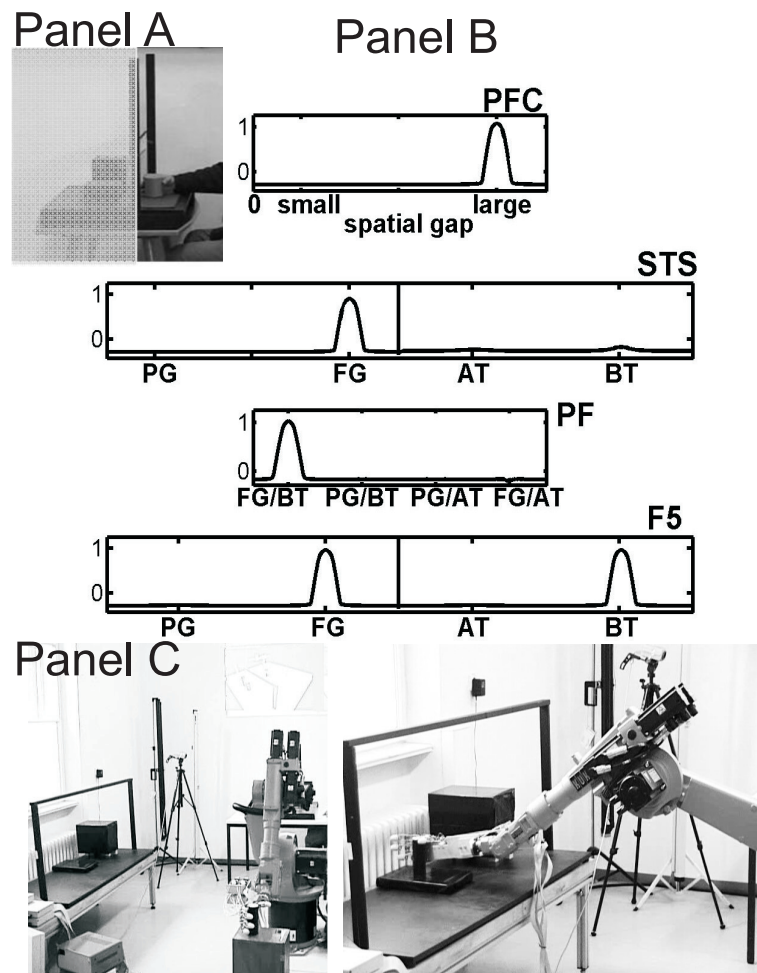


**Figure 2.20:** Inference task. **Panel A:** Only the grasping behavior is observable. **Panel B:** The stable state in layer PFC of the field model represents the inferred (lower) goal. **Panel C:** To reproduce the inferred action the robot combines a full grip (FG) followed by a trajectory below (BT) the bridge as represented in the motor layer F5 in Panel B. The figure is adopted from<sup>79</sup>.



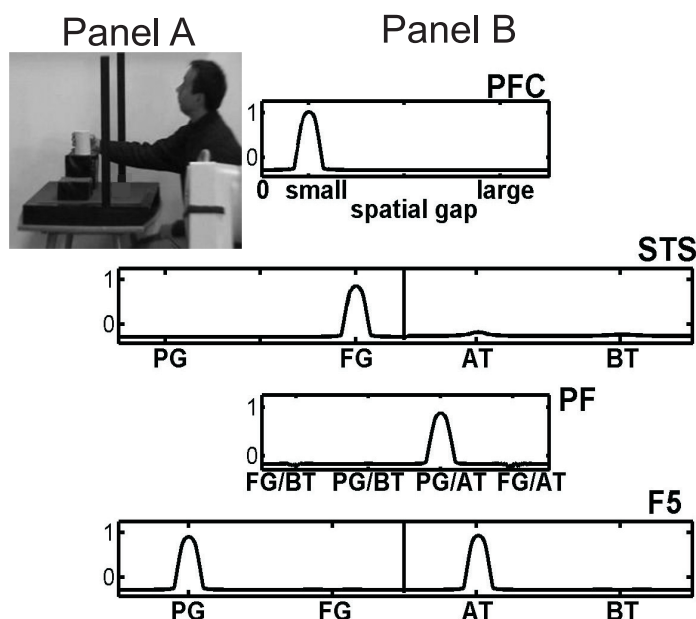


**Figure 2.21:** Goal directed imitation. **Panel A:** Conflict in the grasping behavior, i.e. the teacher uses a full grip for placing the object at the higher goal. **Panel B:** As shown in layer F5 of the field model, the robot decides to use a precision grip to reproduce the observed action effect. The figure is adopted from<sup>79</sup>.

the means implemented in the control architecture. The goal representation is triggered by direct input from the vision system. Through the learned links to layer PF, it biases the decision processes in the mirror circuit, thus overriding the direct mappings from the visual motion description in STS. Technically, we exploit here differences in time course with the goal representation being processed faster in a known task setting compared to the representations in STS (for a detailed discussion of the biological context see<sup>76</sup>).

Another example of the overt behavior of the imitator is shown in Fig. 2.22. Here, the column on the left illustrates the imitator's preferred strategy. In case of the higher target with the small spatial gap the preferred learned strategy is to use a precision grip (PG) with the above-bridge trajectory (AT), the decision based on PG/AT area activation in layer PF. The column sequence on the right illustrates the case when the imitator made a decision to copy also the grip type (FG) displayed by the demonstrator. While observing FG, STS sends subthreshold input signals to the FG areas in PF. The decision choice between PG/AT (learned), FG/AT or FG/BT is triggered only after the lower path planning module makes a test planning trial for a trajectory with FG preference and sends back the facilitating feedback input signal up to F5 layer, which in turn facilitates the switching to the FG/AT decision in PF. In the demonstrated case, only the FG/AT

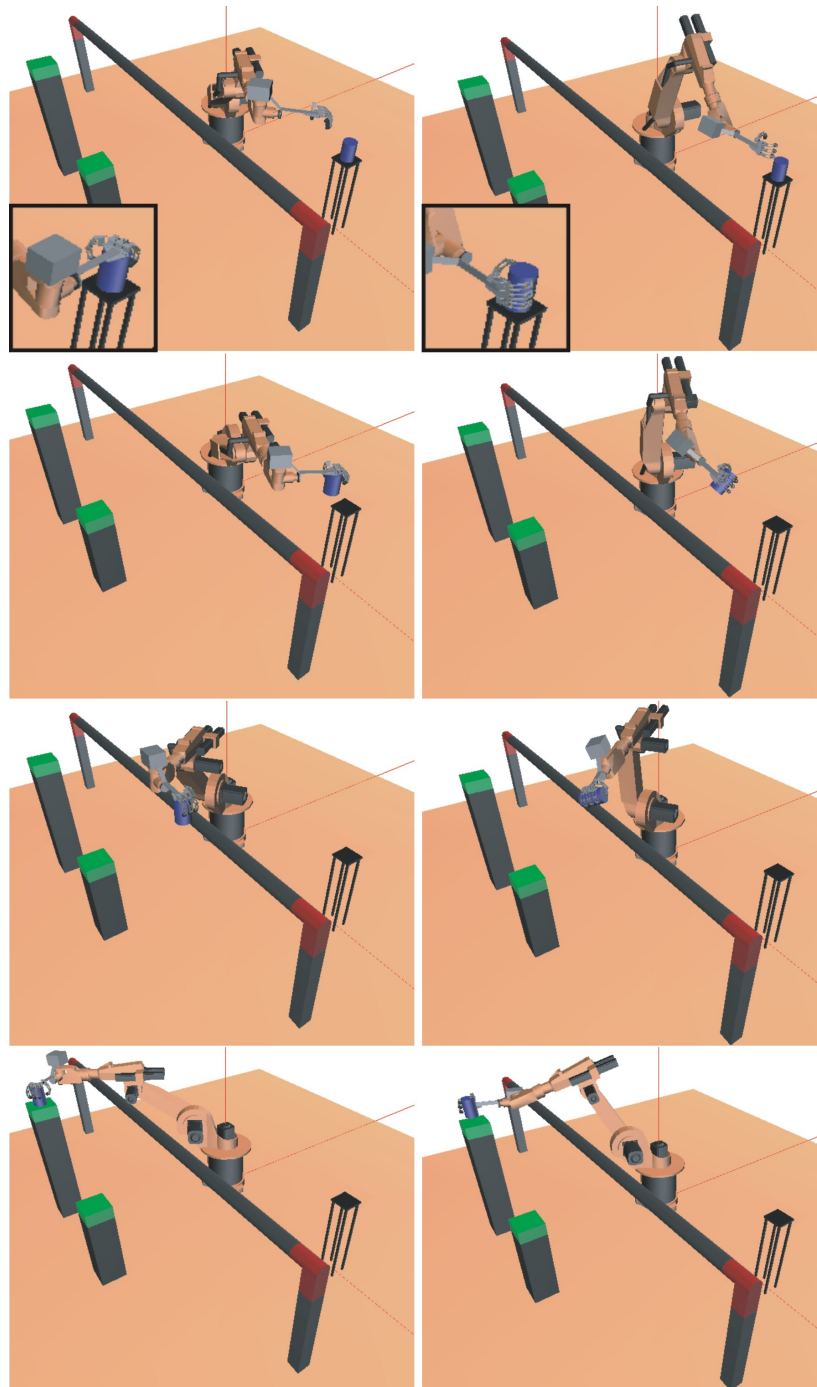


**Figure 2.22:** The overt behavior of the imitator is shown using a robot simulator. Each column represents two snapshots of postures generated by the path planning system. The column on the left illustrates the imitator's preferred strategy, the column on the right the case when the imitator made a decision to copy also the grip type displayed by the demonstrator.

trajectory is possible, thus the AT representation is triggered in F5. The video of the sequence presented in the left column of Fig. 2.22 can be found [[here](#)<sup>2</sup>]. The video of the right sequence Fig. 2.22 is [[here](#)<sup>3</sup>].

#### 2.4.4 Learning Color Cues

Next, we introduce an additional Neural Field (NF) representing the color cues, e.g. of the object to grasp. This new NF is only allowed to learn bi-directional connections with the PFC neural field, which represents the scene geometric features. After learning of one-to-one mapping between color cue and a scene parameter value (as presented on Fig. 2.23), the color of the object may trigger the corresponding representation in PF and facilitate inference of the motor means. Reversely, the goal assignment, which triggers the corresponding scene geometric features in PFC, will also trigger the color decision for the object to grasp as illustrated in Fig. 2.24.

#### 2.4.5 The Biological Relevance of the Results

I have presented a control architecture for imitation and learning which is inspired by insights about the processing principles in humans and other primates. The approach emphasizes the role of factors in imitation which are considered cognitive such as goal inference or decision making. The experiments with the robot system illustrate that an organization of imitative behavior toward reproducing the goal of an observed action complements purely motor approaches which focus on the kinematic trajectory<sup>33,276</sup>. The primacy of the goal over the action means allows coping with differences in embodiment and task constraints known as the correspondence problem in robot imitation<sup>222</sup>. The emphasis on “end state granularity”<sup>222</sup> as a measure for successful behavior does not exclude, however, that also the transfer of knowledge on the level of action means may be essential (e.g. compare Fig. 2.18). Importantly, learning to understand an observed behavior as a goal-directed action enables the robot to reuse the stored information in new contexts and to acquire more abstract knowledge associated with that action. For instance, association between specific object properties (e.g., color) and where to place an object of a particular category may be learned within the proposed control architecture (see Fig. 2.2).

The idea that the movement production system is essentially involved in action understanding has been proposed in the context of robotics research before (for a review see<sup>276</sup>). For instance, Demiris and Hayes<sup>70</sup> used internal forward models to predict the sensory consequences of observed actions in an imitation task. However, the questions how

<sup>2</sup><https://goo.gl/uZTsX4> (tiny.cc/de7l5y)

<sup>3</sup><https://goo.gl/BndCmC> (tiny.cc/ah7l5y)

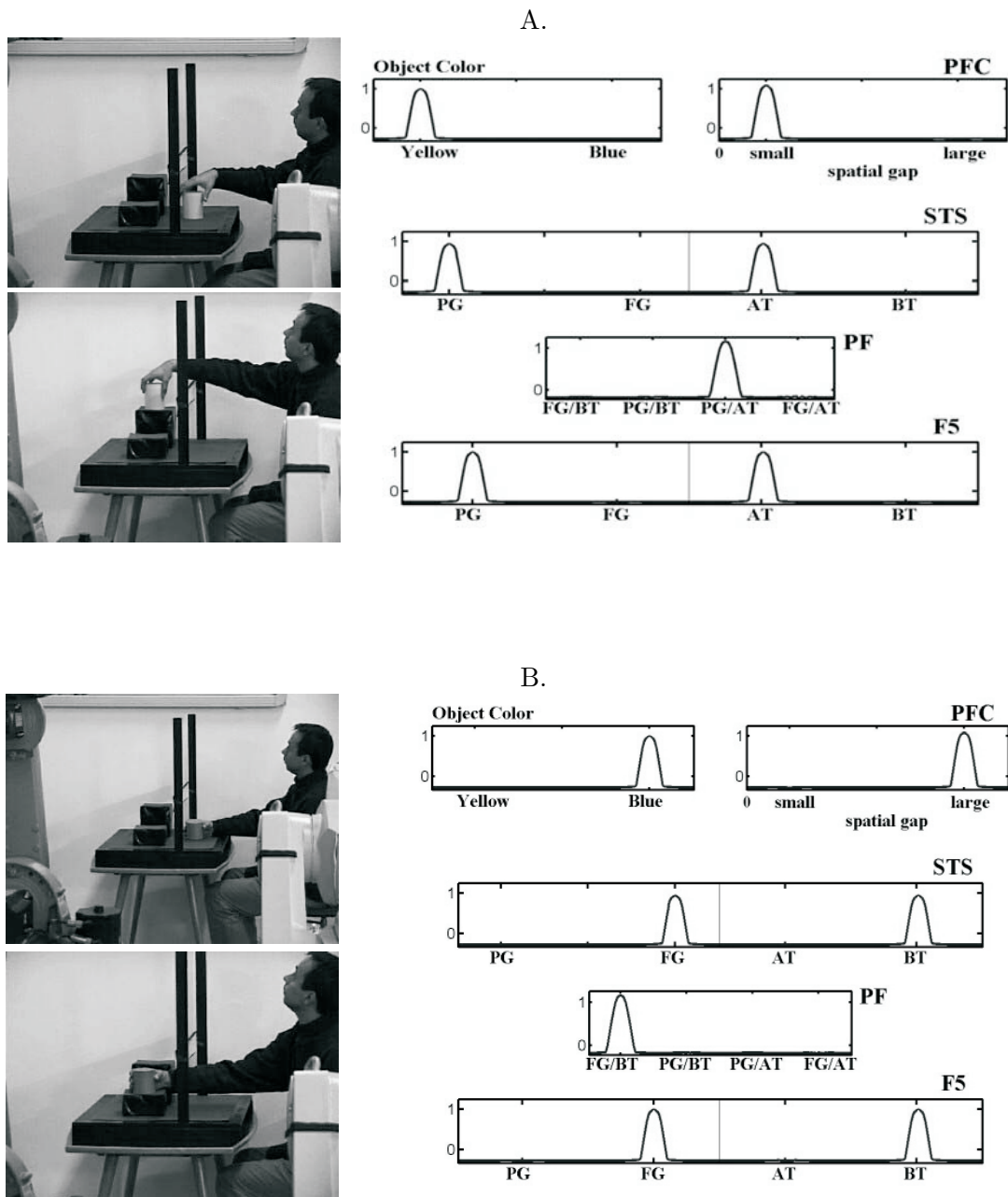


**Figure 2.23:** Learning the color cues. Here, an object color neural field is introduced which is allowed to learn the connections to the PFC neural field. **Panel A:** The light colored object is associated with the 'small spatial gap' in PFC (neural field representing scene geometry). **Panel B:** The dark colored object is associated with the 'large spatial gap' in PFC, which is connected to the FG/BT representation in PF.

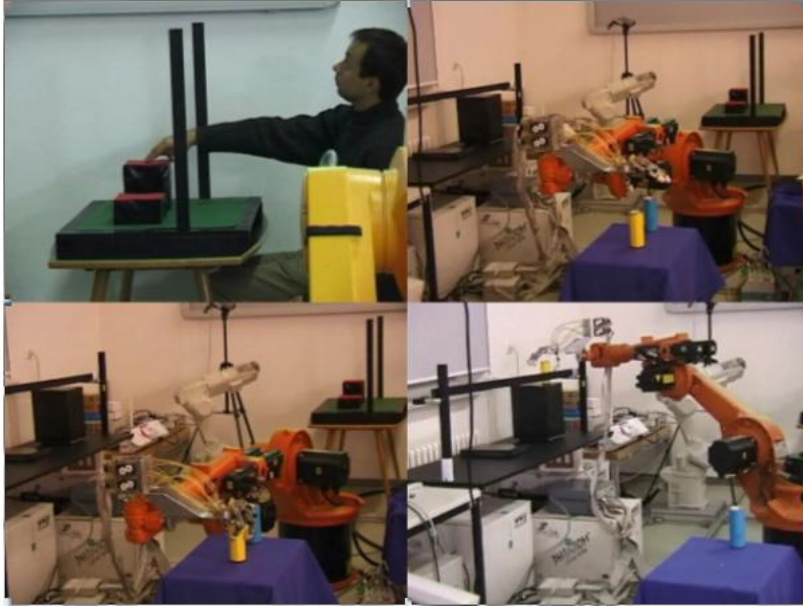


**Figure 2.24:** Goal-triggered inference. After learning of color-goal associations as shown at 2.23, the robot may also infer the object color from the goal assignment.

to cope with differences in embodiment, task constraints or motor skills have not been systematically addressed. In principle, the control architecture proposed here allows for learning to understand the purpose of a hand movement not strictly in the repertoire of the imitator. The only condition is that the observed action effect may be achieved using proper action means<sup>76</sup>.

## 2.5 Extension of the Learning Rule

Here I propose the single uniform extended Hebbian learning rule which accounts for both the merging-and-separation of correlated or anti-correlated events representations, and for the chaining of temporal correlated events for the learning of sequential representations. In case of merging-and-separation, if we present temporally correlated stimuli **A** and **B** having inputs to a single neural field (NF), the result is a merged representation for **A** and **B**. But if we present the same **A** and **B** anticorrelated (meaning that now **A** and **B** never show up simultaneously, but with randomly delayed time gaps, say, **A** after **B** as frequent as **B** after **A**), then the result of learning is a separated representation pattern for **A** and **B**. In case of the sequential chaining, if we present stimuli **A** and **B** projected onto two separated NFs (say, NF-**A** and NF-**B**) with a constant time delay between first **A**, then **B**, then the result is the growth of the forward synaptic connections from NF-**A** onto NF-**B**.

The first non-canonical heterosynaptic correlation-based rule to model simultaneous category formation and sequencing was proposed in<sup>68</sup>. The authors devised the so-called synaptic triad mechanism. In the proposed neural network architecture they differentiate between internal links inside clusters (intra-cluster synapses), and external, between-cluster links (inter-cluster bundles). Clusters represent a set of competing stimuli (vowels in bird songs), while the links between clusters reflect the sequencing of vowels in a song. The task was to enable the resulting network to learn a set of songs (which may contain repetitive vowels or repetitive chunks of vowels). The songs are represented as paths in the directed graph of the cluster network. The network then can recognize (parse) the songs heard with variations and is capable of producing of free-running or cued (externally triggered) songs. Our task is to endow a robot with high-level sequence learning and production; for the robot to stay close to the sequences demonstrated by a human, but, at the same time, to be flexible in re-planning accounting for online information.

In our case, the analogues of the clusters in<sup>68</sup> are the Neural Fields (NFs). Our main task is to propose a shunted learning rule that can provide temporal linking between action representations, even if those actions are separated by 200-400 ms intervals, far beyond time intervals of active LTP/LTD plasticity, which are about 20-40 ms. The second task is to use the same learning rule for the clustering and the separation of action representations inside each NF, based on competition between the action representations, and based on conflicting or complying external conditions for those motor acts. The overall task is similar to<sup>68</sup>, if we regard their clusters as our NFs, and their inter-cluster bundle links as our connections between separate NFs. Below is a schematic explanation of how the new shunted Hebbian learning rule works. It is a postsynaptic-activity-dependent Hebbian form of plasticity, first proposed in<sup>80</sup>.

For the simplified computational model of an NF with transient peaked activations, we introduced the Neural Fields as 1D lattice arrays of neurons, where at each lattice point we have one excitatory and one inhibitory neuron. Thus, each dynamic NF represents a population of  $2N$  neurons which splits into an excitatory and an inhibitory subpopulation, each of dimension  $N$ . The activation of an excitatory and an inhibitory neuron  $i$  at time  $t$ ,  $u_i(t)$  and  $v_i(t)$ , is governed by the following coupled system of differential equations:

$$\tau_u \frac{d}{dt} u_i(t) = -u_i(t) + h + S_i(t) + g(u_i(t)) \left[ \sum_{j=1}^N w_{ij}^u f(u_j(t)) - v_i(t) \right] \quad (2.6)$$

$$\tau_v \frac{d}{dt} v_i(t) = -v_i(t) + g(v_i(t)) \left[ \sum_{j=1}^N w_{ij}^v f(v_j(t)) \right] \quad (2.7)$$

where the constants  $\tau_u$ ,  $\tau_v$  and  $h < 0$  define the time scales and the resting level of the

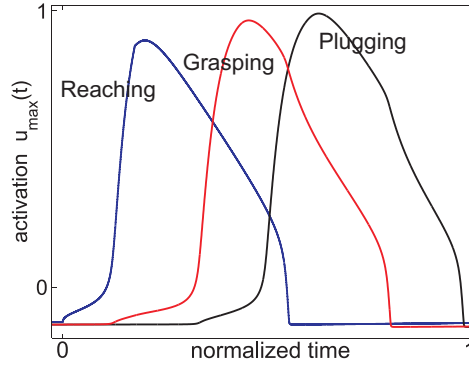


**Figure 2.25:** The time course of the transient neural population responses of the three NFs forming a linked chain. The chain is maintained through the inter-NF synaptic connection learning. The figure is adopted from<sup>80</sup>.

dynamics, respectively. The firing rate  $f(\cdot)$  and the shunting term  $g(\cdot)$  for the recurrent excitation are taken as non-linear functions of sigmoid shape. The interaction strength between any two neurons within the two subpopulations is defined by the fixed synaptic weight functions,  $w_{ij}^u$ , and  $w_{ij}^v$ , which decrease as a function of the distance between the neurons. We have chosen Gaussian profiles with the specific choice  $\sigma_u < \sigma_v$  and  $A_u > A_v$  for the standard deviations and the amplitudes, respectively. This choice guarantees that the inhibition dominates over larger distances. The term  $S_i(t)$  represents the summed input at time  $t$  to the excitatory neuron  $i$ .

Within a certain range of field parameters, in response to an input the excitatory population develops a transient activity pattern with a shape shown in Fig. 2.25. This figure demonstrates temporal dynamics of the transient peak maximal activation levels for three sequentially connected NFs (for the labels of the three NFs see<sup>80</sup>).

The *shunted Hebbian learning* rule<sup>80</sup> for increasing the synaptic efficacy,  $s_{ij}$ , between a presynaptic neuron  $j$  and postsynaptic neuron  $i$  is:

$$\tau_s \frac{d}{dt} s_{ij}(t) = h(u_i(t)) [\alpha f(u_j(t)) f(u_i(t)) - s_{ij}(t)] - \beta s_{ij}(t) \quad (2.8)$$

with a time scale  $\tau_s \gg \tau_u$  much larger compared to the time scale of the field dynamics. All weights passively decay with a slow rate defined by  $\beta > 0$ . The first term  $\alpha f(u_i) f(u_j)$  on the right side of Eq. 2.8 is the usual Hebbian modification to the synaptic weight with scaling parameter  $\alpha$  balanced by a memory decay. Both are shunted by a sigmoidal function  $h(u_i)$  with threshold  $u_h > u_f$ . For a sufficiently activated postsynaptic neuron  $u_i$ , the decay or growth of the weight to a presynaptic neuron  $u_j$  appears to be proportional to the factor  $h(u_i)$ . The accelerated weight decay in case of a silent  $u_j$  is the responsible

mechanism for the development of task specific subpopulations.

The shunting term  $h(u_i)$  is the sigmoid function with a high threshold in Eq. 2.8, its argument is the activity level  $u_i$  of postsynaptic neuron  $i$ . The activation (when it is close to 1) of the shunting term provides ‘*active learning*’ and ‘*active forgetting*’, called so due to the large constant  $\alpha$  ( $\alpha > \beta > 0$ , while  $-\beta s_{ij}$  is the slow forgetting term). The paper<sup>80</sup> describes how this learning rule provides the separation and the merging of motor action representations in a single NF. If two projected representations are close in the spatial coordinates of a single NF, then they are competing. In this case, only one activation peak survives, if two neighboring inputs are presented simultaneously. But if the inputs are separated more, the resulting peak activations become insensitive to each other, so they can be regarded as belonging to two separate NFs. If we have two different inputs projected to one NF, say, **A** and **B**, which are projected to the same spatial local region, and if they are stimulated simultaneously, then they give rise to a single activation peak. In the presence of a low-amplitude noisy input, when **A** or **B** is presented, the activation peak could appear slightly skewed or shifted in every trial.

Further, if the inputs **A** and **B** are always synchronous, the links from **A** or **B** to the NF are strengthened at every presentation for those NF neurons which are activated by **A** and **B** together. This merges synchronous input representations into a single one. When presenting **A** or **B** alone, an activation peak is produced at the same spatial position of the NF after learning. But, what if the two inputs presented are not correlated in time, how might the NF neurons remember that another input was activating them also, but a while ago? Assume, that now the neuron is activated by **A**, but **B** is not active at this time, while the link from **B** to this neuron is still strong. The postsynaptic shunting term  $h(u_i)$  now switches on ‘*active learning*’ for the connections from **A** and ‘*active forgetting*’ for the links from **B**, where both processes are acting on a faster time scale compared to passive forgetting. This means, that neurons activated asynchronously by **A** and **B** lose their connections from **B** and **A**, but those activated solely by **A** or **B** are preserving the connections from **A** or **B** separately. This leads to a spatial separation of **A** and **B** representations in the NF.

The process of the separation of projected representations is illustrated in Fig. 2.26, where panel A illustrates an early stage of learning and panel B illustrates a late stage. Blue and red distributions of the incoming synaptic links across the NF arise from two different input neurons, activated asynchronously (see explanation in figure caption).

There exists a temporal linking learning rule provided by the same mechanism. Imagine that **A** and **B** are represented by two separate NFs with transitive peak activations (NF with inhibitory dynamics Eq. 2.7). Transitivity means that the rise of activation to the peak value takes about 40-60 ms, then the activity peak does not stay fixed, but decays



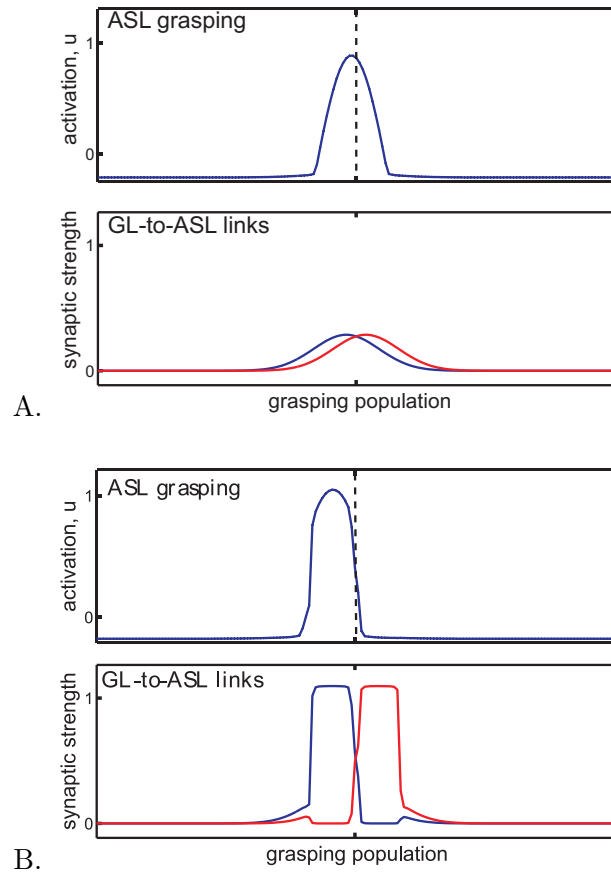


**Figure 2.26:** The two snapshots illustrate the developing NF connections driven by shunted plasticity. Panel A represents the state before and panel B the state after the learning period. In both top panels (of A and B), the maximal transient activity of the grasping NF is shown, with the input of one of two input neurons. In both bottom panels (of A and B) the weight profiles from the two input neurons (blue and red curves) to the grasping NF are plotted. Note that the influence of the initially weak input from the input neuron manifests in a slight shift of the population response to the left relative to the central line, the response with input from another input neuron appears slightly shifted to the right (not shown). The interplay between the learning and the field dynamics continuously increases this shift during practice, leading to a nearly complete separation of the weight profiles and the population responses, as shown in panel B.

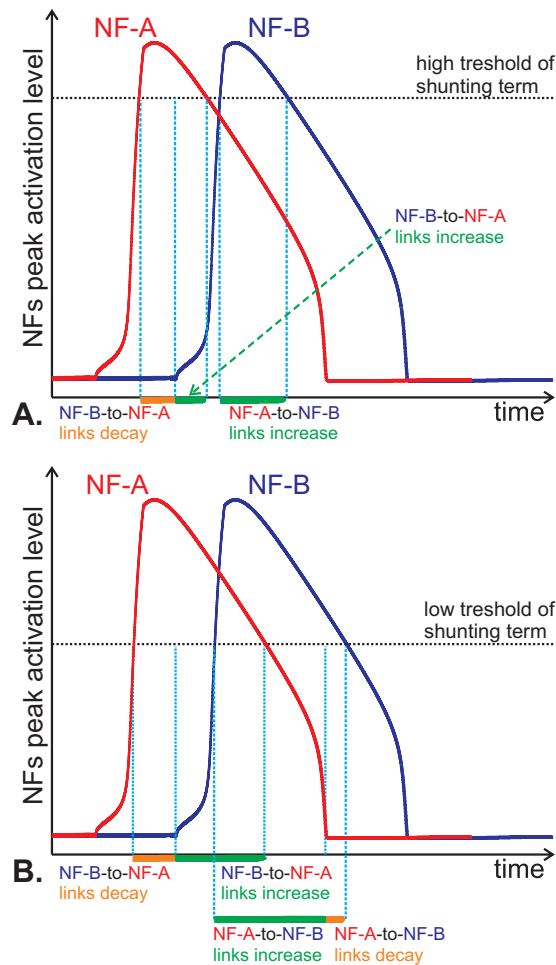


**Figure 2.27:** A schematic overview of time-asymmetric learning, affected by the value of the threshold for shunted Hebbian learning. Lowering of the shunting term threshold affects the learning in a similar way as reducing the delay between transient excitations.

actively by self-inhibition within a time interval of 200-300 ms. Then, if NF **A** is activated before NF **B**, the postsynaptic activity-dependent shunting term is enforcing the active learning of the link from **A** to **B**. And, with the same event order, if time gap is too close, the 'active forgetting' of the link from **B** to **A** is also enforced.

The role of the threshold value in this time-asymmetric learning is depicted in Fig. 2.27. The resulting learned link strengths are proportional to the average time separation between activations of **A** and **B** (**B** activity peak always follows the one of **A**). For sufficiently high threshold values, the links from NF-**A** to NF-**B** increase and the links from NF-**B** to NF-**A** decrease during several presentations of **B** following **A** (see upper panel: Fig. 2.27.A). This means, that in generative replay of the learned sequence, when one NF excites

the next one, the time interval between NF **A** activation triggering NF **B** will be roughly proportional to the average time interval observed during learning. This effect is achieved since when the time delay between two activations is too small, the learning dynamics starts to resemble one with a lower threshold (see Fig. 2.27.B), and learning and forgetting start to balance each other.



## Chapter 3

# Kinematic Motion Synthesis for Computer Graphics and Robotics

### 3.1 Introduction

The goal of the research work presented in this chapter is the development of a system for the online kinematic simulation of highly realistic human movements in real-time by combining motion capture with dynamical systems. The proposed real-time capable generative architecture is used in computer animation as well as in humanoid robotics.

The real-time synthesis of natural looking human movements is a challenging task in computer graphics and robotics. While dynamical systems provide the possibility to parameterize behavior in a flexible and adaptive way, the reconstruction of details of human movements with such systems is a challenge due to the large number of degrees of freedom. The chapter starts with concise literature review 3.2, and more references to related works are presented in main sections. In the next Section 3.3 an approach is presented for the synthesis of realistic human full-body movements in real-time that is based on the learning of motion primitives, or synergies, from motion capture data applying a novel blind source separation algorithm. The learned generative model can synthesize periodic and non-periodic movements, achieving high degrees of realism with a very small number of synergies. By application of kernel methods such components are mapped onto the phase spaces of low-dimensional dynamical systems, which can be iterated in real-time, and which are integrated in a stable overall system architecture<sup>103,210,214,236</sup>.

Standard dimension reduction methods, such as PCA (*Principal Component Analysis*,<sup>142</sup>) or ICA (*Independent Component Analysis*,<sup>57</sup>), have been commonly applied in computer graphics to reduce the dimensionality of motion capture data. It has been shown

that the approximation of complex body movements requires typically 8-12 principal components (e.g.<sup>268</sup>). It was shown for different classes of human movements that the number of source terms for approximation of human movement data can be significantly reduced by application of mixture models with time delays (e.g. to 3-4 terms for periodic and some non-periodic movements)<sup>210,235,236</sup>. These compact trajectory models have the advantage that they can be associated with relatively simple dynamical systems that synthesize the trajectories in real-time. To embed the learned synergies into a real-time animation system, I define “canonical” dynamical systems (dynamic primitives) that play a similar role as *Central Pattern Generators* in biological systems. The idea of using dynamical systems for the definition of movement primitives is quite common in robotics (e.g.<sup>132,276</sup>). Below, I show how this model can be integrated with other elements of computer animation systems, such as style morphing, synchronization with external rhythms or navigation.

In the following sections 3.4 ff. a learning-based technique is presented that models movement coordination in humans, illustrated by the example of the coordination of walking and reaching. The planning of human body movements is highly predictive. Within a sequence of actions, the anticipation of a final task goal modulates the individual actions within the overall pattern of motion. An example is a sequence of steps, which is coordinated with the grasping of an object at the end of the step sequence. In contrast to this coordination of natural human movements, real-time animation systems in computer graphics often model complex activities by a sequential concatenation of individual pre-stored movements, where only the movement before accomplishing the goal is adapted. Our control architecture generates adaptive predictive full-body movements for reaching while walking with human-like appearance. It was demonstrated that the generated behavior is robust to external perturbations, even in the presence of strong perturbations that require the insertion of additional steps in order to accomplish the desired task, cf.<sup>209</sup>.

In the last Section 3.8 a newly devised robot control architecture is presented that combines the online planning of complex coordinated full-body movements, based on the flexible combination of learned *Dynamic Movement Primitives* (DMPs), with a *Walking Pattern Generator* (WPG), based on *Model Predictive Control* (MPC, e.g.<sup>220,221</sup>), which generates dynamically feasible locomotion of the humanoid robot HRP-2. This section presents the work done together with LAAS/CNRS in Toulouse<sup>214,215</sup>. The synthesis of predictive behaviors planned for multiple steps ahead for humanoid robots is a challenge because standard approaches, such as optimal control, result in unrealistically large movements times. The proposed approach<sup>215</sup> addresses this problem of the flexible synthesis of multi-step planned full body trajectories by combining the kinematic trajectories planning with the Walking Pattern Generator. A *Dynamic Filter*<sup>343</sup> is another important block

of the new architecture. Its function is the flexible merging of kinematically planned upper body movements with the dynamically planned lower body motion. The Dynamic Filter (DF) corrects the *Zero Moment Point* (ZMP,<sup>330</sup>) trajectories in order to guarantee the dynamic feasibility of the executed behavior taking into account the upper-body movements, at the same time ensuring an accurate approximation of the planned motion trajectories (the last are synthesized by WPG exploiting the simplified MPC model), cf.<sup>220,300</sup>. Additional experiments demonstrated that a naïve approach, which generates adaptive motion using machine learning methods by interpolation between feasible training motion examples fails to guarantee the stability and dynamic feasibility of the generated behaviors<sup>215</sup>.

## 3.2 Related Work

### 3.2.1 Kinematic Primitives for the Adaptive Synthesis of Multi-action Sequences

The generation of realistic-looking reactive human movements is an important problem in computer animation. Physics-based animation is an alternative approach for the online generation of motion (e.g.<sup>85,284</sup>). Complex action sequences are segmented into individual actions, which are characterized by solutions of optimization problems, derived from mechanics and additional constraints (contact, friction, or specified via-points)<sup>1,181,208,347</sup>. While these approaches generate highly adaptive behavior for individual actions, the problem to generate natural-looking transitions between the individual actions is non-trivial. As consequence, artifacts (e.g. hesitation, jerky movement) can emerge at transition points<sup>342</sup>.

Another alternative to generate long movement sequences is by concatenation of motion captured segments from large databases<sup>255,256,340</sup> (as recorded from real human performance using motion capturing technics, *MoCap*). The concatenation of the captured trajectories typically requires tedious post-processing in order to adapt recorded movements to additional constraints<sup>105</sup> and it is difficult to transfer this approach to real-time applications. Most of these methods are based on search algorithms with considerable computational costs and are thus not suitable for the online synthesis of realistic human motion. Recent approaches have tried to simplify this procedure by automatic selection and concatenation of recorded motion segments, ensuring that the generated motion sequences fulfill constraints defined by the animator<sup>12,107</sup>.

Approaches more close to ours are based on learned low-dimensional parameterizations of whole body motion, which are embedded in mathematical frameworks for the online generation of motion (e.g.<sup>126,178,268,331,332</sup>). Several methods have been proposed that

segment action streams into individual actions, where models for the individual actions are adapted online in order to fulfill additional constraints, such obstacle avoidance or the correct positioning of end-effectors<sup>159,238</sup>. The dependencies between constraints in such action sequences have been recently exploited to generate more realistic animations. In<sup>87</sup> captured motion examples are blended according to a prioritized "stack of controllers". In<sup>286</sup> the instantaneous blending weights of controllers are pre-specified differently for different body parts involved in the current action and the priority of the different controllers is governed by their sequential order. In<sup>127</sup> the synthesis of locomotion plus arm pointing at the last step is carried out by blending of captured actions determining the weights by "inverse blending optimization". In this study arm pointing was blended with the arm swinging motion of the last step. The choice of the the arm pointing primitives depended on the gait phase, according to an empirical rule introduced by authors.

Skilled human motor behavior can be highly predictive in complex task performance. Within complex activities, action goals and the associated constraints influence actions that appear long before the constraint within the behavioral stream, and thus allow the generation of smooth and optimized behaviors over complex action sequences. This was investigated, for example, in a study on the coordination of walking and reaching. Human subjects had to walk towards a drawer and to grasp an object, which was located at different positions in the drawer. Humans optimized their behavior already significantly before object contact, consistent with the hypothesis of maximum end-state comfort during the reaching action<sup>165,257,335</sup>, and steps prior to the reach were modulated in order to accomplish the goal. The issue of predictability and the importance of model-based identification were also emphasized in the early days of classical control theory, see<sup>86</sup>.

Whole body movements of humans and animals are organized in terms of muscle synergies or movement primitives<sup>28,91</sup>. Such primitives characterize the coordinated involvement of subsets of the available degrees of freedom in different actions. An example is the coordination of periodic and non-periodic components of the full-body movements during reaching while walking, where behavioral studies reveal a mutual coupling between these components<sup>51,56,190</sup>. The realism and human-likeness of synthesized movements in robotics and computer graphics can be improved by taking such biological constraints into account, cf. <sup>92</sup>.

#### 3.2.2 Related Approaches in Humanoid Robotics

There is a great interest in robotics to exploit the biological concept of movement primitives. E.g. <sup>303</sup> extracted primitives from human reaching movements using Principle Component Analysis (PCA), successfully implementing reaching behavior on an HRP-2 humanoid robot.



Movement primitives, including the use of force feedback, have also been proposed by<sup>97,98</sup>. A related concept is the DMP-network that generates planned trajectories by appropriately designed nonlinear dynamical systems<sup>132,276</sup>. Such systems based on dynamic movement primitives have been proposed for the generation of complex movements in real-time<sup>5,131</sup>. But all these online DMP-based methods of modeling the kinematic trajectories do not guarantee the dynamic feasibility of the resulting motion, which is a critical issue.

For the synthesis of dynamically feasible walking in combination with grasping movements a number of different approaches were proposed. For the DARPA robotic challenge valve manipulation task,<sup>6</sup> proposed a hybrid controller with a goal-driven fast foot step planner combined with visual servoing for the reaching and grasping of the valve.<sup>162</sup> proposed a control architecture for the humanoid robot **Atlas** that automatically finds foot steps around and over obstacles, in order to reach for a goal object and to realize more complex actions. Other solutions for the combination of walking and vision-controlled reaching of a static and mobile targets during walking have been proposed in<sup>301</sup> and<sup>34</sup>.

Some researchers have used randomized motion planning algorithms for whole-body walking combined with manipulation tasks in constrained environments<sup>62</sup>. For example,<sup>144</sup> proposed a method that is based on a virtual kinematic tree for the planning of foot placements, which was successfully implemented on the HRP-2 robot. A framework that decomposes reach-to-grasp human movements into sequences of kinematic tasks has been developed in<sup>299</sup>. Further work applied imitation learning<sup>207</sup>, where walking and grasping were modeled as a sequence of separate actions. A task priority approach based on a generalized inverse kinematics was used in<sup>346</sup> in order to organize several sub-tasks, including stepping and hand motion. The related approaches to optimize multi-action behaviors in robotics were proposed in a series of papers<sup>100–102</sup>, where authors computed optimized stance locations with respect to the position of a reaching target, using a dynamical systems approach for the generation of reaching behavior.

The control of human-like multi-joint systems taking into account contact constraints and guaranteeing dynamic balance is a challenging problem. Current solutions range from near real-time whole body Model Predictive Control (MPC) with regularized modeling of contacts in order to decrease the computational cost<sup>156,305</sup> to approaches based on optimal control with precise modeling of contact phases, requiring typically hours of off-line computation time<sup>158</sup>. Another solution, based on prioritized *IK*, that integrates DMPs with MPC for individual actions has been proposed by<sup>329</sup>.

The Walking Pattern Generator (WPG) used in the robotic control architecture presented in this chapter is based on Model Predictive Control. The first WPG of this class was proposed by<sup>143</sup>. This method computes the reference nominal *Zero Moment Point* trajectory (ZMP,<sup>330</sup>) from the desired placements of feet during the gait cycle. A simplified linear inverted pendulum dynamics (Cart-Table Model) was used to link the *Center of*

*Mass* (CoM) and the ZMP. Preview control was exploited to compute the CoM trajectory from the desired ZMP. Due to the model simplifications, the real ZMP trajectory deviates from the desired one. This deviation is the result of neglecting the inertial and Coriolis forces generated by the leg swing and by fast movements of the upper-body. In order to alleviate this problem, the authors ran the full body inverse dynamics in order to compute a better approximation of the real ZMP. This new ZMP trajectory can be computed for the preview horizon in real-time. The resulting ZMP error was transformed into a resulting CoM error via the Preview Control, following the approach proposed by<sup>143</sup>. This result can then be exploited to correct the CoM trajectory. The described two steps of preview control combined with an evaluation of the inverse dynamics can be repeated iteratively, successively reducing the ZMP error. This approach for the dynamic correction can be interpreted as a kind of Newton-Raphson iteration<sup>300</sup>, and is referred to as a Dynamic Filter in Section 3.8. Another improvement of MPC-based WPG is the integration of the computation of the optimal ZMP trajectory within the constrained quadratic optimization framework that computes the optimal CoM trajectory, see<sup>336</sup>. This approach requires only the specification of the preplanned foot positions as input, returning the optimal trajectories for the ZMP and the CoM. The default modern approach for nonlinear MPC relies in addition on another improvement of the same framework made by<sup>121</sup>, which is the further extension of the approach by<sup>336</sup>. This reformulation of the optimization framework allows to exploit positional and angular velocities of the CoM as reference trajectories (for a time horizon of the next two steps), returning the foot placements and the optimal ZMP trajectories as result of the nonlinear predictive control problem. This framework, which is described in detail in [Naveau et al.<sup>220</sup> and<sup>221</sup>], was exploited in our system, as presented below in Section 3.8.

### 3.3 Kinematic Motion Synthesis Architecture

This section starts with a description of the motion capture data sets in 3.3.1, followed by descriptions of the motion trajectory representations and the motion retargeting techniques in 3.3.2. Next, the core steps of the developed method are presented: 1) a novel unsupervised learning method for the approximation of trajectory sets based on *anechoic mixing models* with very few source components in 3.3.3; 2) the *machine learning* methods for the learning of online capable control of generated motions in 3.4.2; 3) a method for establishing mappings between the learned synergies and simple dynamical systems, called *dynamic primitives*, that can be combined into more complex systems with well-defined dynamical properties in 3.3.4. The section also presents the full architecture for the kinematic synthesis of motion trajectories. Its performance is illustrated by a number of examples and multi-agent interactive scenarios 3.6.

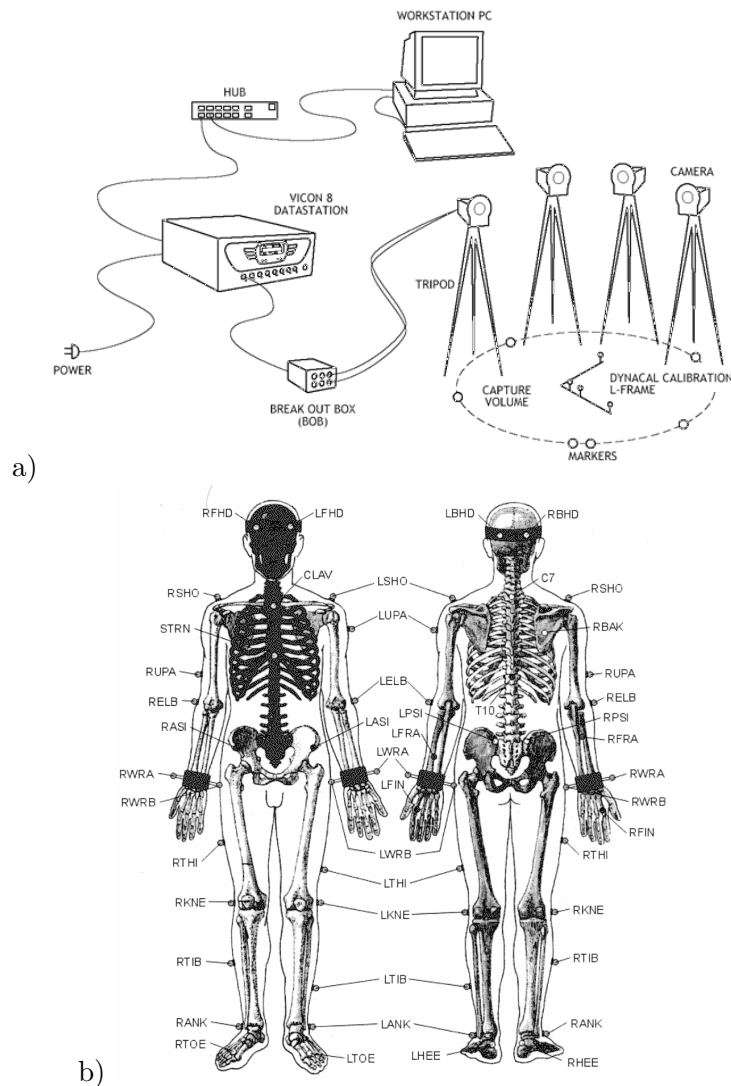


**Figure 3.1:** a) The Vicon system. b) PluginGait marker set.

### 3.3.1 Data Sets

The motion primitives were learned from motion capture data that was recorded in the Tübingen University Clinic using a Vicon/Nexus Motion Capture System with 8-12 cameras (Fig. 3.1.a), using 41 reflecting markers of the PluginGait marker set (Fig. 3.1.b) and a sampling frequency of 120 Hz. The first dataset comprises **different types of gaits**, periodic gaits, straight walking with neutral and different emotional styles (e.g. happy and sad, illustrated on Fig. 3.2), and walking with a stooped posture. In addition, walking along a circular path (forward and backward) with rotations of  $90^\circ$  per full gait cycle, and

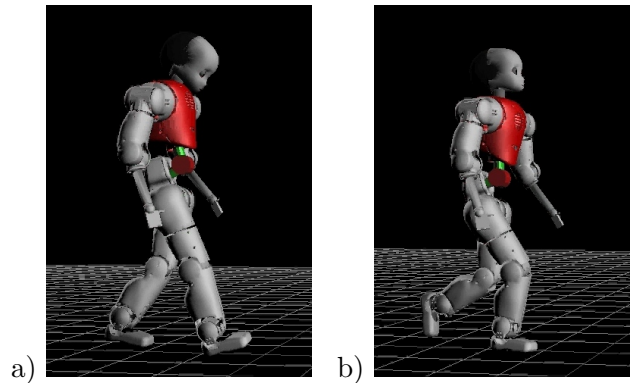


**Figure 3.2:** 'Sad' a) and 'Happy' b) walking styles recorded from human subject and retargeted to CoMan humanoid model.

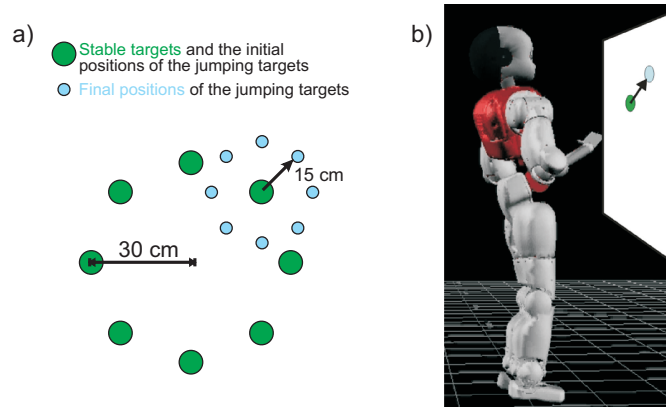


**Figure 3.3:** a) The arm reaching targets placement on vertical frontal plane. b) The CoMan humanoid reaching the jumping target in simulation.

turning on spots (120 degrees) left or right per double step were recorded. Movements were retargeted to a skeleton model with 17 joints using an axis-angle representation (normalized quaternion representation) for the parametrization of the 3D rotations between adjacent segments. In addition, the recorded gaits were combined with non-periodic arm movements, such as swinging the right or left arm up, or holding the arm in a fixed posture during the whole gait cycle (for the so called “bridge dance” scenario). For these recorded movements the arm moved independently of the legs, thus the arm lifting actions were recorded at different phases of the gait cycle. This dataset was used in the project dedicated to computer animation DFG Forschergruppe “Perceptual Graphics” and EC FP6-43403 project “COBOL”.

The second dataset was recorded for the controlled experiments on human arm reaching. It was collected in the Computational Sensomotorics Lab, University Clinic Tübingen using a Vicon MoCap system (using the PluginGait marker set) integrated with an VR setup.

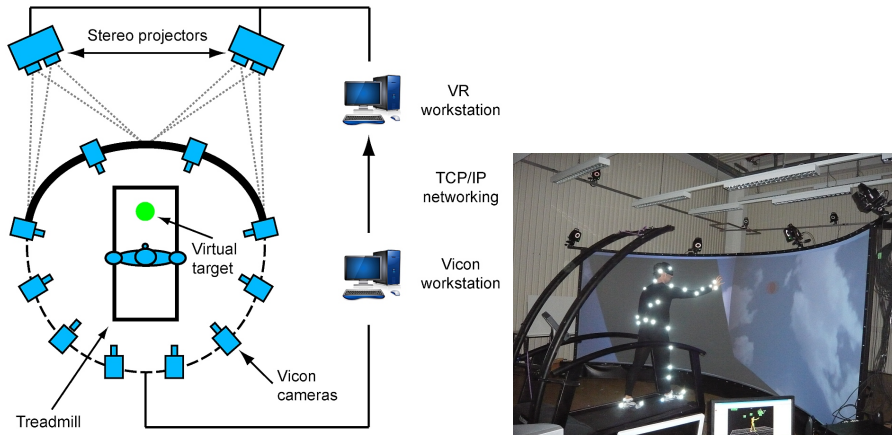


**Figure 3.4:** The setup combining MoCap on a treadmill with VR projected on a stereo screen. The arm reaching targets are presented at specific phases of the walking. (Figure adopted from<sup>56</sup>).

The VR setup is capable of displaying targets positioned relative to the human body and it is capable of online control of displayed objects aligned in time with the subject’s motion. For **the training dataset** the reaching targets were displayed in VR on two vertical planes at two distances from the chest and at 25 positions inside each plane. The training dataset is named as such, since it was used for training of robot algorithms, which were implemented on a Coman robot physical simulator. The subject was asked to perform right arm reaching and grasping of virtual objects with 4 different hand orientations at the final posture. The final hand posture orientations are specified by an orthonormal hand frame anchored at wrist joint, where the 1st frame vector is aligned with the middle finger direction, the 2nd is the open hand normal vector and the 3rd one is aligned in a direction of the thumb. For all trials we asked our subjects to approach the final open hand posture keeping the 1st frame vector possibly close to the horizontal plane and in the direction orthogonal to the frontal plane. For the 4 different subsets of trials we asked our subjects to keep the hand as close as possible to one of the 4 following orientations of the 3rd frame vector: a) horizontal (3rd vector in horizontal plane, hand is facing downwards), b) skew-closed (3rd vector is at  $45^\circ$  in respect to horizontal plane), c) vertical ( $90^\circ$  - 3rd vector is vertical), d) skew-open (3rd vector is rotated  $135^\circ$  from the ‘horizontal’ position a). After cleaning and reconstruction, the resulting dataset consisted of 176 trajectories for all 4 final hand orientations for one subject.

For **the evaluation dataset** the movements of 5 human subjects were captured, who performed reaching to stable targets at 8 different positions in a single vertical plane at a distance of  $55\text{cm}$  from the chest (placed symmetrically at 8 directions  $n\pi/4, n = [0 \dots 7]$ , and a distance of  $30\text{cm}$  from the central point opposite to the chest center). Each target was randomly repeated 8 times, giving 64 reaches in total. Additionally subjects performed

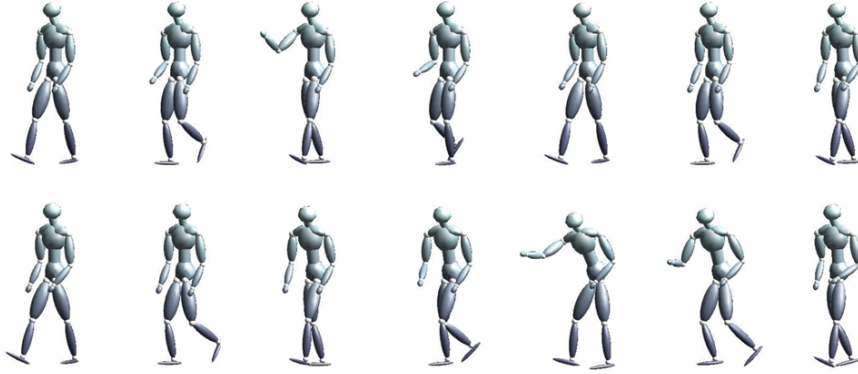


**Figure 3.5:** Two rows of snapshots of two reaching while walking trajectories. Two arm reaches towards two different goals start at different phases of the gait cycle.

64 reaches to moving targets. For these we presented the target initially at one of 8 initial positions (same as for the stationary targets), but during the arm reaching the target jumped in the vertical frontal plane with one of 8 possible displacements (8 directions:  $n\pi/4, n = [0 \dots 7]$ , fixed distance of  $15cm$ ), see the scheme on the Fig. 3.3. The jumps occurred at the moment when the hand (the base of index finger) crossed a distance of  $30cm$  from the target's vertical plane. The set of 128 reaching trajectories (64+64) was captured 4 times for each subject, each time for one of 4 preferred final hand postures orientations, providing 512 trajectories for each subject. These arm reaching datasets were captured with the subjects standing still without stepping.

Additionally, a set of **reaching while walking trajectories** was recorded for the subjects walking normally straight on the treadmill in front of the VR projection screen. See Fig. 3.4. In this setup we also tracked the stepping events, the touchdown of the left heel. The targets were presented at different times relative to the stepping events, to cover all possible gait phases. The reaching targets were presented for short time intervals (typically 0.4-0.6 sec) to force the subjects towards reaching without adaptation of the normal gait pattern. The targets were presented by VR in the right-arm reachable space in front of the subject. It allowed to collect a large dataset of the adaptive reaching motions at all the phases of the gait cycle. The reconstructions of two reaching while walking trajectories are presented on Fig. 3.5. These datasets for arm reaching while standing or walking were used in the robotics EC FP7-ICT-248311 project “AMARSi” (WP7) and in FP7-ICT-249858 project “TANGO”.

The **drawer walking-reaching task dataset** is the motion capture data from a single human subject that executed a drawer opening task, walking towards a drawer and then reaching for an object in the drawer. The dataset consists of the trajectories of ten trials of

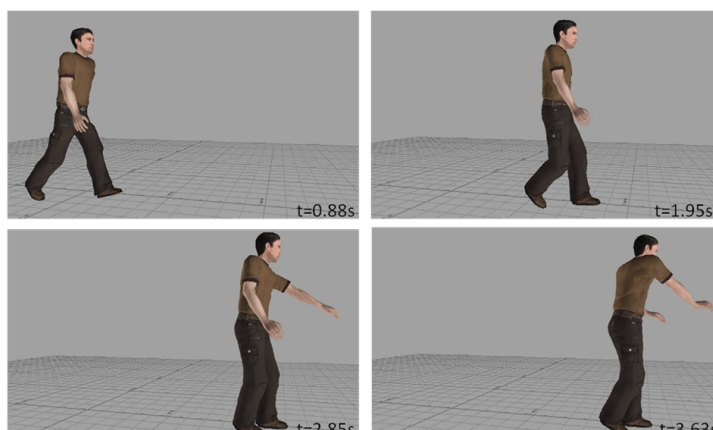


**Figure 3.6:** Illustration of human behavior in the drawer walking-reaching task. The panels illustrate intermediate postures (normal walking step, step with initiation of reaching, standing while opening the drawer, and object reaching).

single participant, recorded at the University of Bielefeld with an optical motion capture system (Vicon Motion Systems, Oxford, UK) consisting of 12 MX-F20 CCD cameras at a frame rate of 200 Hz with a spatial accuracy of about 0.25 mm. The PluginGait marker set was used with 41 markers. The initial distance of the subject standing in front of the drawer was about 3 meters and the position of the object to grasp inside the drawer was varied. The setup is described in detail in<sup>165</sup>. The indicator screen on the top of the drawer gave a hint about one of 4 positions of the graspable object (a dowel) inside the drawer. The dowel could be located in the front left or right, or back left or right inside the drawer. To grasp the dowel in the front of the drawer, the drawer had to be opened at least 14 cm to permit clearance of the hand, whereas a minimum of 28 cm was needed to allow clearance for grasping the dowel at the back position. The typical recorded motion consisted of a reduced gait cycle - a transitional step from standing to walking; and the rest of walking, drawer opening, object grasping and lifting sequence. These last parts of sequences used for modelling while segmented into three subsequent movements, (which we call 'actions'): 1) a normal walking step; 2) a shortened step which ends with the left hand is reaching the drawer. This step showed a high degree of adaptability, and was typically adjusted in order to create an optimum distance from the drawer (maximum comfort) for the reaching movement during the last action; 3) the drawer opening (pulling) with the left hand and the right hand reaching for the object. (<sup>209</sup>, Fig. 3.6, see also video [[movie](#)<sup>1</sup>].)

The analysis of the distances between the pelvis and the drawer or the object in these action sequences reveals the predictive nature of human movement planning, as shown in Fig. 3.7 where the distances are ordered according to the initial distance to the drawer.

<sup>1</sup><https://goo.gl/5HKiG7> (tiny.cc/st8l5y)

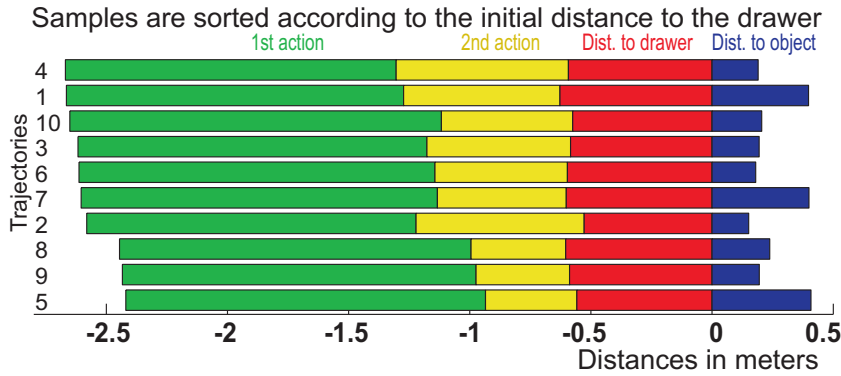


**Figure 3.7:** Predictive planning in human trajectories. Distances from the pelvis to the front panel of the drawer (green, yellow, red), and the distance between the front panel and the object (blue) for different trials. Mainly the second action is adjusted as function of the initial distance from the goal. The figure is adopted from<sup>209</sup>.

The length of the first two steps (of normal gait cycle, depicted as green bar) is relatively constant across trials. The distance from the drawer during standing while grasping (indicated as red bar) is almost constant, but positively correlated with the depth of object placement inside the drawer, the blue bar. The major distance adjustment is made in the second adaptive step of the final reduced gait cycle (yellow bar). The length of the first step is not significantly correlated with the initial distance to the drawer at the start of normal gait cycle, the start of the green bar (linear regression:  $R^2 = 0.08, p = 0.429$ ), while the correlations with the distance to the drawer after first step, and the length of the second step are highly significant ( $R^2 = 0.95, p = 1.4 \cdot 10^{-6}$ ). This dataset was used for the learning of new walking-and-grasping sequences in robot control architectures in EU projects: EC FP7 grant agreements FP7-ICT-248311 “AMARSi” and FP7-ICT-611909 “Koroibot”.

### 3.3.2 Kinematic Angle Trajectories Representations and Retargeting

The Vicon/Nexus MoCap system (Vicon Motion Systems, part of Oxford Metrics, Oxford, UK) exports marker positions in a global coordinate frame as CSV or C3D files (<https://www.c3d.org/>). The goal of the re-targeting procedure is the optimal reconstruction of the motion of the skeleton of human avatars or of robots, that have geometries and joint angles constraints different from the one of the recorded human subject.



### Unconstrained human avatars

The work presented in Section 3.6 used unconstrained human avatars built in Matlab<sup>®</sup> (The MathWorks, Inc.) using simple ellipsoid-like shapes for the limb segments. The first step in motion re-targeting is the estimation of the positions of the joint rotation centers from the recorded marker positions. A nominal trajectory is a section of a recording where all the markers are present (without gaps). The markers are grouped in subsets - each subset belongs to a single rigid-body (one marker may belong to more than one subset). Here also a tree structure of linkage of the rigid bodies is considered, where we assume no kinematic looped-chains to exist in the human skeleton. The minimum sum of squared errors estimation procedure is used to reconstruct a single rotation center (*Center of Rotation*, CoR) for each pair of linked rigid bodies. This procedure is adopted from<sup>53</sup>. Here, for the nominal trajectory, we obtain also information about the average markers positions in the coordinate frames of the corresponding rigid bodies, anchored at their CoRs. The estimated joint center (CoRs) trajectories (translational and rotational, for the associated stable local coordinate frames) are used at the next step for de-noising and gap filling of the markers trajectories for the other snapshots of motions recorded in the same session, (i.e. with the same markers placement as in the nominal trajectory). This optimal reconstruction and de-noising is done in Matlab<sup>®</sup> for the imported C3D Vicon files. For example, the reconstructed CoRs were used as point-light stimuli in the work done together with Weizmann Institute of Science, Rehovot,<sup>66</sup>.

A *nominal* human avatar was built in Matlab<sup>®</sup> using the average links lengths of recorded human subjects. This nominal (reference) avatar has a nominal PluginGait marker set placement, which defines the local coordinate systems for each limb segment ('rigid body'). The joint centers are defined based on a prior knowledge of human limb junction positions with respect to the marker set used. For every session with new markers placement, a new avatar is created, where the limb junction positions are re-identified from the marker positions. The re-targeting of each posture in default recording was done by following the linkage tree structure from its root,<sup>226</sup>. The matching of the limb segments lengths is done by scaling and the rotational matching is done by solving the orthogonal Procrustes problem (to find the optimal rotational correspondence between the markers of the same rigid body in the default and in the nominal session). The numerical solution of the orthogonal Procrustes problem uses SVD decomposition, cf.<sup>74</sup>. The zero posture in the nominal session, corresponding to the zero rotations of limb segments, was the T-posture, where a human participant stretches the arms sideways at shoulder height. The output of this scaling-and-rotation procedure is the default rotation for every time step of the nominal skeleton from its T-pose for the best matching of the markers positions in the

new recorded clip. The best results are achieved when we first match the two T-poses of the nominal and default marker sets and save the mismatch rotations as constant biases, to be used later as correction offset values for all other poses. The result was saved using Denavit-Hartenberg parametrization (DH-format, cf. <sup>287</sup>) of rotations and translations for every limb segment frame for the nominal skeleton.

The *axis angles* representation of the joint rotations is introduced for learning new motions. Any 3D rotation of a rigid body can be represented by a unit vector  $\mathbf{w}$  in the direction of the rotation axis ( $\|\mathbf{w}\| = 1$ ) and an angle of revolution  $\theta$  about that vector. The rotation formula by O. Rodrigues (<sup>254</sup>) for the matrix  $\hat{w}$  and rotational orthogonal matrix  $\mathbf{Q}$  is:

$$\hat{w} := \begin{bmatrix} 0 & -w_3 & w_2 \\ w_3 & 0 & -w_1 \\ -w_2 & w_1 & 0 \end{bmatrix} \quad (3.1)$$

$$\mathbf{Q} = \mathbf{I} + \sin(\theta)\hat{w} + (1 - \cos(\theta))\hat{w}^2 \quad (3.2)$$

The three parameters of the axis angle parametrization are then defined as the entries of the vector  $\theta\mathbf{w}$  with length  $\theta$  and direction  $\mathbf{w}$ . The mapping from the  $\mathfrak{so}(3)$  representation  $\theta\mathbf{w}$  to the orthogonal rotation  $\mathbf{Q} \in SO(3)$  is called the exponential map:  $\mathbf{exp} : \mathfrak{so}(3) \rightarrow SO(3)$ . And the transform is the matrix exponential as  $\mathbf{Q} = \exp(\theta\hat{w})$ . Considering  $\det(\hat{w} - \lambda\mathbf{I}) = -(\lambda^3 + \lambda)$ , which gives us due to Cayley-Hamilton theorem (<sup>29,99</sup>):  $\hat{w}^3 = -\hat{w}$ . Using this identity for  $\hat{w}$ , one can separate terms in the Taylor expansion of the matrix exponent and obtain Rodrigues' formula (3.2) for  $\mathbf{Q}$ . Reversibly, using matrix logarithm of orthogonal rotation matrix  $\mathbf{Q}$  we may obtain the skew symmetric matrix  $\theta\hat{w}$  that provides  $\theta$  and a normalized vector  $\mathbf{w}$ . The simplified inverted formulas are  $\theta = \arccos\left(\frac{\text{Trace}(\mathbf{Q})-1}{2}\right)$  and  $\mathbf{w} = \frac{1}{2\sin(\theta)} [\mathbf{Q}_{3,2} - \mathbf{Q}_{2,3}, \quad \mathbf{Q}_{1,3} - \mathbf{Q}_{3,1}, \quad \mathbf{Q}_{2,1} - \mathbf{Q}_{1,2}]$  can be obtained from Rodrigues' formula (3.2). The unit quaternion  $\mathbf{q}$  corresponding to the axis angle in our notation is:  $\mathbf{q} = (\cos(\frac{\theta}{2}), \mathbf{w} \sin(\frac{\theta}{2}))$ .

All the joint frames rotations recorded in the DH-format are saved as axis angles as 3D vectors  $\theta\mathbf{w}$ . This representation allows good linearized morphing and interpolation of rotations. The norm of this representation is affected by the  $2\pi$  rotational angle ambiguity. In all the manipulations with axis angles, we keep track of rotations, relating them to the reference T-pose as zero point, and removing  $2\pi$  offsets when necessary.

In computer graphics applications the unconstrained human avatars from the Complete Characters Library created by Rocketbox Studios GmbH were used. The motion clips are retargeted to these characters using MotionBuilder (Autodesk). The resulting

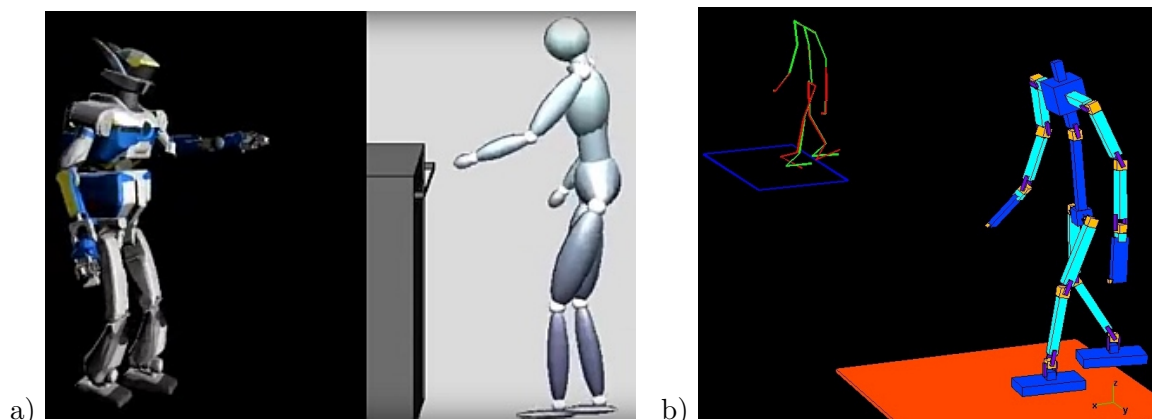


**Figure 3.8:** a) Retargeting of the movements from a human to the unconstrained skeleton of the HRP-2 robot. A snapshot from a long sequence of Fig. 3.6. b) Retargeting of the movements to the constrained kinematic model of the HRP-2 robot in Matlab. The small inset compares the unconstrained (red) and constrained (green) postures of robot skeleton at a moment during the normal gait cycle.

scenes are exported in COLLADA format (open standard XML schema developed by Sony Computer Entertainment and the Khronos Group). The resulting joint angle rotations in DH-format are exported using custom scripts made for MotionBuilder. Additional custom scripts are created resolving the correspondence problems of frame orientations between the COLLADA format and our export format. The resolved DH-representations are converted to axis angles. The learning and generation of new trajectories is done in the axis angles representation. The online animations of these characters are made using the Horde3D graphics engine (<sup>278</sup>, <http://www.horde3d.org/>), which is controlled from the Psychophysics Toolbox (<sup>155</sup>, <http://psychtoolbox.org/>) in Matlab<sup>®</sup>.

### Constrained kinematic skeletons of humanoid robots

For the robotics applications (see Section 3.8) the learning of the kinematic motion generative models is done in the space of angles of the robot actuators. These actuators have angular limits and the retargeted motion must respect these limits. As first step the motion is retargeted to an unconstrained robot skeleton model in MotionBuilder (Autodesk). This retargeting is done by rescaling, translation and rotation while respecting the non-sliding constraints using the built-in IK tools of MotionBuilder. The kinematic skeletons of the robots and their joint angle limits are provided by Istituto Italiano di Tecnologia (IIT) for CoMan and iCub humanoid robots and by Kawada Industries, Inc. and AIST for the HRP-2 humanoid robot. The robot joint rotation matrices are exported from MotionBuilder in DH-format by custom scripts or in BVH file format (Biovision).

The output is a motion clip, unconstrained with respect to the actuators angles limits. An illustration of this preprocessing is given in [movie<sup>2</sup>], which shows the angular trajectories, animating a human avatar, and the corresponding retargeted trajectories for a HRP-2 kinematic model in MotionBuilder. A snapshot from the movie is presented in Fig. 3.8. See also the snapshots of the walking CoMan above at Fig. 3.2.

As the next step, the complete trajectories of the unconstrained robot skeleton are reconstructed in Matlab<sup>®</sup> (The MathWorks, Inc.). In Matlab<sup>®</sup> I use the custom IK tool for the matching of the target skeleton (which is controlled by the actuators angles) against the posture of the imported unconstrained motion. During the matching the actuators limit values are avoided by IK corrections in the actuators' angle space. These iterative corrections are proportional to the gradient of a barrier function, projected to the null space of Jacobian of the end effector. The Jacobian of the end effector for a particular posture is the linear part of the mapping from actuator angles velocities onto the space of linear translational and rotational velocities of the end-effector. In this procedure I am trying to keep position and rotation of a particular end effector unchanged, while moving the actuator angles possibly away from their limits. If no limits are violated, then configuration matching is exact. Here, the temporal smoothness cost is introduced when computing barrier functions. The temporal smoothness is enforced by minimizing sums of squared displacements of the postures relative to their time-neighbors. The total smoothness cost  $E$  of trajectory can be defined as  $E = \sum_{t=2}^{T-1} \|2\mathbf{q}_t - \mathbf{q}_{t-1} - \mathbf{q}_{t+1}\|^2$ , where  $\mathbf{q}_t$  is the vector of actuator angles at time  $t$  (the two postures  $\mathbf{q}_1$  and  $\mathbf{q}_T$  are fixed). The gradient of the smoothness cost in respect to the intermediate postures  $dE/d\mathbf{q}_t$ ;  $t = [2 : T - 1]$  is also projected to the null space of the Jacobian of the end effector. The resulting robot actuator angle trajectories and the resulting hand and feet postures after this retargeting constitute the dataset for the training of learning algorithms and evaluation.

For the robotics application, the trajectories of the drawer walking and reaching task were resampled, resulting in a normalized duration of 1.6 sec for each action (3 actions are segmented as presented in Fig. 3.7). The data was split into two subsets, separating the stored pelvis trajectories (time course of pelvis position and pelvis direction in the horizontal plane), and the upper body trajectories (HRP-2 actuators angles). The pelvis position trajectories were rescaled, ensuring the maximally admissible propagation velocity for the HRP-2 (0.5 m/sec). The pelvis yaw-angle trajectories were rescaled by a constant factor, and a fraction of the yaw angle trajectory was added back to the trunk yaw-angle for compensation. As input to the Walking Pattern Generator (WPG) we used the time course of pelvis velocities in the horizontal plane, and of the pelvis yaw angular velocity. The upper body arm reaching motions were retargeted separately as described above in

---

<sup>2</sup><https://goo.gl/ucbVA2> ([tiny.cc/gv8l5y](http://tiny.cc/gv8l5y))

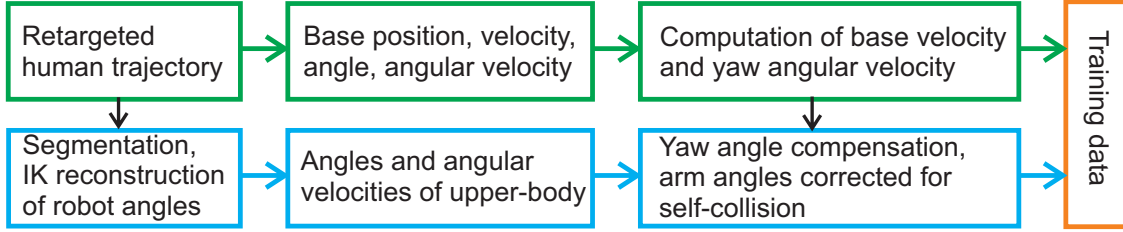


**Figure 3.9:** Offline pre-processing of motion capture data from humans for the HRP-2 walking and reaching task.

order to satisfy actuators angles limiting constraints. An overview of the pre-processing steps is given in Fig. 3.9. In order to augment the training data set for the learning of the mappings between the task parameters and the model parameters, we generated additional artificial kinematic data by scaling of the pelvis forward propagation velocities for all gait cycles uniformly (by the factors 0.8, 0.92, and 1.2), while keeping the upper body trajectories fixed. In this way, a total of 30 training examples were generated from the original 10 motion capture trials<sup>215</sup>.

### 3.3.3 Learning of Kinematic Movement Primitives

In this section the new approach for the online synthesis of complex human movements is presented, that is inspired by concepts from biological motor control. A classical idea in this field is that complex motor behavior might be structured in terms of lower-dimensional primitives, or *synergies*. In motor control unsupervised learning methods have been applied successfully to extract low-dimensional spatio-temporal components from trajectories and EMG signals<sup>63,65,135,271</sup>. Standard dimension reduction methods, such as PCA, that are based on instantaneous mixture models have been commonly applied in computer graphics, where the approximation of complex body movements requires typically 8-12 principal components (e.g.<sup>268</sup>). Applying the novel statistical method I learn compact models for human motion trajectories, exploiting time-shift invariant synergies. In a series of papers we have shown for different classes of human movements that the number of source terms for the accurate approximation of human movement data can be reduced by mixture models with time delays (e.g. to less than 3 terms for periodic and some non-periodic movements)<sup>103,210,235</sup>.

The original joint angle trajectories  $\hat{\xi}_n(t)$ ,  $n = [1 : N]$ , after subtraction of the mean values  $m_n = \int \hat{\xi}_n(t) dt$ , were approximated by a weighted mixture of source signals. A compact model for the joint angle trajectories  $\xi_n(t) = \hat{\xi}_n(t) - m_n$  can be obtained by fitting

an *anechoic mixture model* that is given by:

$$\xi_n(t) = \sum_k w_{nk} s_k(t - \tau_{nk}) + \eta_n(t) \quad (3.3)$$

with  $\eta_n(t)$  assumed to be non-delayed uncorrelated white noise. The functions  $s_k$ ,  $k = [1 : K]$  denote hidden source signals, and the parameters  $w_{nk}$  are the mixing weights. In contrast to blind source separation techniques, like PCA or ICA (<sup>57</sup>), this mixing model allows for time shifts  $\tau_{nk}$  of the sources in the linear superposition. Time shifts (*delays*), source signals and mixing weights are determined by an algorithm based on a time-frequency integral transform. The task of this anechoic demixing algorithm is to estimate simultaneously the shapes of hidden source signals  $s_k(t)$ , their weights  $w_{nk}$  and delays  $\tau_{nk}$ , given the dataset  $\xi_n(t)$ . This problem is computationally difficult. Each source signal can be regarded as linear mixture of harmonics with fixed local weights and delays, where both are locally defined for a particular source signal. The *harmonic* is the Fourier component, the sinusoidal wave form of a fixed frequency. It can be represented as weighted and shifted sine, or as linear combination of sine and cosine of the same frequency. In case of discrete time signals, the harmonics can be defined similarly, as built from the eigenspaces of the time-shift operator, cf. <sup>189</sup>. Thus the weights of harmonics are not independent in anechoic mixtures: their local weights fixed for each source are multiplied with global weights of the sources in mixtures. The local delays of harmonics, while being fixed for each source, are added to the global delays of the sources in mixtures.

### **Anechoic demixing using Wigner-Ville distribution marginals**

The first version of the algorithm used for the *over-determined problem* of anechoic demixing was based on the Wigner-Ville spectrum (<sup>192,193</sup>) that is defined by the partial Fourier transform of the symmetric autocorrelation function of the signal  $\xi$  (the upper bar denotes complex conjugate, and  $i^2 = -1$ ), where the result is presented in form of a spectrogram, with new time  $t$  and frequency  $\omega$ :

$$\mathcal{W}_\xi(t, \omega) := \int E \left\{ \xi\left(t + \frac{\nu}{2}\right) \overline{\xi\left(t - \frac{\nu}{2}\right)} \right\} e^{-2\pi i \omega \nu} d\nu \quad (3.4)$$

Applying this integral transform to equation (3.3) results in:

$$\begin{aligned} \mathcal{W}_{\xi_n}(t, \omega) &= \int E \left\{ \sum_l \sum_k w_{nl} \overline{w_{nk}} s_l(t + \frac{\nu}{2} - \tau_{nl}) \overline{s_k}(t - \frac{\nu}{2} - \tau_{nk}) \right\} e^{-2\pi i \omega \nu} d\nu \approx \\ &\approx \sum_k |w_{nk}|^2 \mathcal{W}_{s_k}(t - \tau_{nk}, \omega) \end{aligned} \quad (3.5)$$

where the last approximation is performed under the assumption that the sources are statistically independent (assuming the statistical independence of the local weights of harmonics across sources).

As two dimensional representation of one dimensional signals, this equation is redundant and can be solved by computing a set of projections onto lower dimensional spaces that specify the same information as the original problem. With additional approximation assumptions, from computing the zero and the first moments of Wigner-Ville distributions of  $\mathcal{W}_{\xi_n}(t, \omega)$ , the following two equations are obtained<sup>227-229</sup>, providing the separation of the amplitudes  $|w_{nk}|$  of source signal weights ( $\mathcal{F}$  denotes Fourier transform):

$$|\mathcal{F}_{\xi_n}|^2(\omega) = \sum_k |w_{nk}|^2 |\mathcal{F}_{s_k}|^2(\omega) \quad (3.6)$$

$$\begin{aligned} |\mathcal{F}_{\xi_n}|^2(\omega) \cdot \frac{\partial}{\partial \omega} \arg \{ \mathcal{F}_{\xi_n} \}(\omega) &= \\ \sum_k |w_{nk}|^2 |\mathcal{F}_{s_k}|^2(\omega) \cdot \left[ \frac{\partial}{\partial \omega} \arg \{ \mathcal{F}_{s_k} \}(\omega) + \tau_{nk} \right] \end{aligned} \quad (3.7)$$

As the first step, using *Non-negative Matrix Factorization* (NMF,<sup>174,175</sup>), applying non-negative PCA or ICA, the amplitudes of weights  $|w_{nk}|^2$  and the amplitudes of the source harmonics  $|\mathcal{F}_{s_k}|^2(\omega)$  can be extracted using (3.6). Then, after initializing the delays  $\tau_{nk}$ , one can compute  $\arg \{ \mathcal{F}_{s_k} \}(\omega)$  from equation (3.7). The new sources  $s_k$  are defined by their harmonic amplitudes  $|\mathcal{F}_{s_k}|^2(\omega)$  and harmonic phases  $\arg \{ \mathcal{F}_{s_k} \}(\omega)$ . Given the sources one may find their optimal delays in mixtures numerically by cross-correlation based methods, e.g. Gerchberg-Saxton phase retrieval algorithm<sup>302,313</sup>. With the new delay estimates one iteratively solves again equations (3.6-3.7) obtaining the new estimates of sources. The latest version of the algorithm<sup>229</sup> exploited the framework of Fractional Fourier Transform and Linear Canonical Transform (<sup>230,231,267</sup>), and was extended to non-negativity constraints.

The version of the algorithm presented above does not put any constraints on the source signal shapes, but enforces the statistical independence of the signals, which is minimal cross-correlation between the signals for all time-shifts. However, the algorithm also allows to put positivity constraints on the weights together with any user-specified constraints

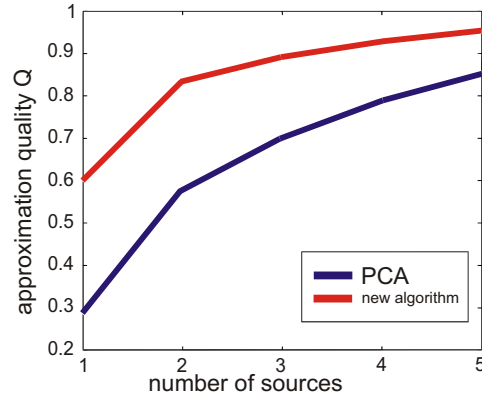


**Figure 3.10:** Comparison of different blind source separation algorithms for our captured data set including periodic and non-periodic movements. The approximation quality measure  $Q$  is shown as a function of the number of sources for traditional blind source separation algorithm (PCA) and the new algorithm of anechoic demixing based on Wigner-Ville marginals. The figure is adopted from<sup>210</sup>.

on signals delays. The anechoic demixing algorithm was used in series of papers on computer animation of different walking gait styles, e.g. in<sup>103,210,235,236</sup>. Different versions of approximate anechoic demixing algorithms were proposed in the last years, which allow positivity constraints for source signals. The first versions of an EM-like (Expectation-Maximization) procedure for non-negative anechoic demixing was proposed in<sup>65</sup> and<sup>64</sup> and it was continued by<sup>69</sup>. The anechoic NMF was proposed by<sup>206</sup>. The recently developed unified framework allow the estimation of anechoic mixtures with positivity constraints for the sources and for their global mixing weights: see<sup>56</sup> and<sup>55</sup>.

Detailed comparisons for periodic and non-periodic trajectory data show that this model provides a more compact approximation of human movement trajectories, requiring fewer source terms than models based on instantaneous mixtures. This is illustrated in Fig. 3.10 for the data set of different walks. The figure shows the approximation quality as function of the number of sources  $s_k$ . Instead of explained variance we used quality measure that is more sensitive to differences in the regime of small approximation errors. It was given by the expression  $Q = 1 - \frac{\|X - \hat{X}\|_F}{\|X\|_F}$ , where  $X_{n,t} = \xi_n(t)$  signifies the original data matrix and  $\hat{X}$  its approximation by the source model, and where the norm is the Frobenius norm. The approximation quality of the recorded trajectory set including periodic and non-periodic movements, with only four source signals was  $Q = 0.92$ , sufficient for an accurate approximation of the walking trajectories. Their shapes are depicted on Fig. 3.11. There, source signal number 4, which has discontinuity at the borders of the motion period is called the *non-periodic source* signal. Its delay is always fixed and equal zero for all



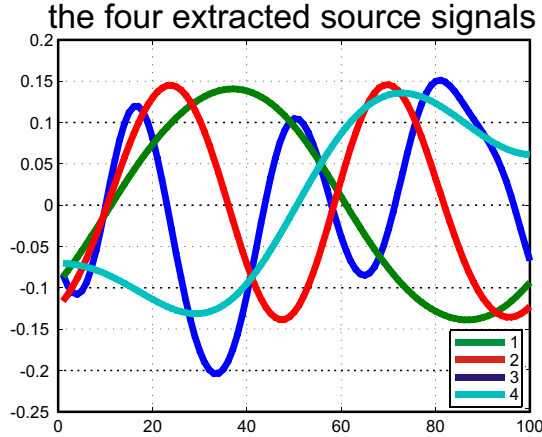


**Figure 3.11:** Four source-signals extracted from the data set containing gaits combined with non-periodic arm movements, which are sufficient for an almost perfect approximation of the original trajectories. Source 4 corresponds to the synergy that is associated with the non-periodic movements in the data set. The figure is adopted from<sup>210</sup>.

trajectories, but its weight may change across trajectories. PCA and ICA require more than 7 sources to achieve the same level of accuracy. Varying the mixing weights and delays for the different motion styles, a continuous spectrum of intermediate motion styles can be generated by interpolation (blending) of these parameters,<sup>235,236</sup>.

### **Anechoic demixing with constrained delays using Shift Invariant Subspace Analysis**

In other applications the statistical independence of the source weights might be less important, but clustering of the sources delays might be more important. For example, for smooth morphing between motion clips one may use the source signals with delays fixed across motion styles for any particular DoF, but different for the same source across joint angles. For this purpose I adapted the *Shift Invariant Subspace Analysis* (SISA) algorithm, which was presented as part of Shifted ICA (SICA) by<sup>205</sup>. The version presented below does not put any constraints on source shapes and currently does not implement positive constraints for the weights. A similar computational framework allowing positivity constraints on source signal is the FADA algorithm<sup>55</sup>.

Following<sup>205</sup> I represent the discrete time sampled trajectories  $\xi_n(t)$ ,  $n = [1 : N]$ ,  $t = [1 : T]$  (with their mean values extracted) as data matrix  $X_{n,t} = \xi_n(t)$ . Then the anechoic model

3.3 is approximating the data as:

$$X_{n,t} = \sum_k W_{n,k} S_{k,t-\tau_{n,k}} + \eta_{n,t} \quad (3.8)$$

here  $W_{n,k}$  is the weight of source signal number  $k$  (which is the matrix row  $S_{k,:}$ ) in data trajectory number  $n$ , the corresponding discrete time delay is denoted as  $\tau_{n,k}$ .  $\eta_{n,t} = \eta_n(t)$  is assumed to be non-delayed uncorrelated white noise as above. Denoting the row-wise discrete Fourier transform as tilde on top of a variable, we have 3.8 in frequency domain as:

$$\tilde{X}_{n,f} = \sum_k W_{n,k} \tilde{S}_{k,f} e^{-i2\pi \frac{f-1}{T} \tau_{n,k}} + \tilde{\eta}_{n,f} \quad (3.9)$$

where  $f = [2 : T]$  is now indexing discrete Fourier transform harmonics. Using the notation  $\tilde{W}_{n,k}^{(f)} = W_{n,k} \bullet e^{-i2\pi \frac{f-1}{T} \tau_{n,k}}$  for the weight matrix dependent on  $f$  (and  $\tau$ 's), we re-write equation (3.9) as a set of  $f$  optimal estimation problems to be solved simultaneously:

$$\tilde{X}_f = \tilde{W}^{(f)} \tilde{S}_f + \tilde{\eta}_f \quad (3.10)$$

The anechoic demixing problem can be solved approximately obtaining  $S_{k,t}$ ,  $W_{n,k}$  and  $\tau_{n,k}$  by the following (SISA) algorithm<sup>205,344,345</sup>:

**SISA** algorithm

**Initialize** source signals  $S_{k,:}$  by orthonormal set of sinusoidal harmonics:

$$S_{k,t} = \alpha_k \text{Re}(e^{2\pi ikt/T}) + \beta_k \text{Im}(e^{2\pi ikt/T}).$$

**Compute** the optimal weights  $\alpha_{n,k}$ ,  $\beta_{n,k}$  in each trajectory  $n$  by linear regression, the weights  $W_{n,k} = \sqrt{(\alpha_{n,k})^2 + (\beta_{n,k})^2}$ , the delays  $\tau_{n,k} = \arctan(\beta_{n,k}/\alpha_{n,k})$ .

**External cycle** (iteration including re-estimation of delays)

**Internal cycle** (iterative solving for joint-diagonalization task)

**S-update** (optimal sources shapes estimation):

with the default  $W$  and  $\tau$  estimate amplitudes and phases of harmonics, by linear regression ( $\dagger$  is pseudoinverse):

$$\tilde{S}_f = (\tilde{W}^{(f)})^\dagger \tilde{X}_f$$

**W-update** (optimal weights  $W$  estimation):

with the default  $S$  and  $\tau$  find  $W$  by linear regression:

$$W_{n,:} = \tilde{X}_{n,:} (\tilde{S}^{(n)})^\dagger$$

here  $\tilde{S}_{k,f}^{(n)} = \tilde{S}_{k,f} e^{-2\pi i \frac{f-1}{T} \tau_{n,k}}$ , thus  $\tilde{S}_{k,:}^{(n)}$  is the F.t. of the delayed version of source signal  $S_{k,:}$  with its delay in trajectory  $n$

**End of Internal cycle**

**$\tau$ -update** (delay re-estimation)

**Delay clustering** (optional)

**W-update** (with new delays  $\tau$ )

**End of External cycle**

At the exit, do few more iterations of **Internal cycle**, of the paired **S-update** and **W-update**.

The iterative solving of weights and delays (alternation between **S-update** and **W-update**) in the Internal cycle can be regarded as a simultaneous matrix diagonalization problem (e.g. <sup>309</sup>) solved by intermittent linear estimations<sup>344</sup>. The delays re-estimation  **$\tau$ -update** in External cycle can be also done with the Gerchberg-Saxton phase retrieval algorithm<sup>302</sup>. In case of only two sources, the delays estimation can be done algebraically, cf. <sup>344,345</sup>, and the currently used  **$\tau$ -update** for 3 or more sources is described below. In practical applications, the estimation of optimal source shapes, weights and delays for up to 6-7 sources converges with 5-6 iterations of the External cycle, and 2-4 iterations of each Internal cycle.

The  **$\tau$ -update** finds the optimal delays of all of  $K$  sources for the best linear mixture in data sample  $n$ , given the source signals shapes. The simplest algorithm for this delay re-estimation (for  $K > 2$ ), is as follows:

**$\tau$ -update algorithm****External cycle****Internal cycle**

- For the default delays of all sources, leave one randomly selected source out and re-estimate the optimal weights for  $K - 1$  shifted sources left;
- Extract these  $K - 1$  sources with their optimal weights from trajectories;
- Find the maximum cross-correlation between the residual trajectories and the left-out source - it gives a new delay of this left out source

**End of Internal cycle**Do the local optimization of the delays using gradient descent (<sup>205</sup>)**End of External cycle**

The algorithm presented above can be appropriately modified for the estimation of source signals and weights, but enforcing their delays to be equal across subsets of trajectories. For that purpose, each  **$\tau$ -update** must be followed by delay clustering (before the final **W-update** in the External cycle of SISA algorithm). Delay clustering must also account for delay disambiguation. The resulting source shapes are close to some harmonics, or they have a dominant frequency, where most energy is concentrated. If the dominant is the first harmonic, then all the delays which differ approximately by  $n\pi, n \in \mathbf{Z}$  are substituted by the same circular average, the cluster mean value. If dominant harmonic is number  $f$ , then the equivalence class is  $nf\pi, n \in \mathbf{Z}$ . The clustering is done as follows. For a source signal with dominant harmonic  $f$  plot all the delays  $\tau$  of this source (as varied across the subsets of trajectories) on the unit circle of complex plane as  $e^{2\pi if\tau/T}$ . For balancing, double the number of points adding their inverted images  $-e^{2\pi if\tau/T}$ . Do 1d-PCA in the plane, now regarded as 2d real plane. The largest PCA component direction angle is the cluster mean angle, which gives the new  $\tau$ . Set the new delay values for the source signal for the subsets of considered trajectories to the value of the new  $\tau$ . This algorithm with the delay clustering results in minimizing the sum of squared errors of the anechoic mixture approximation, enforcing the source delays to be equal across the specified subsets of trajectories. For example, one can enforce all the delays of a particular source signal to be equal across the trials of motion, but still different across the DoFs, or joint angles. Without the delay constraint this version of SISA guarantees a smaller approximation error than the version based on Wigner-Ville marginals, since the independence of source signals. But the solution given by SISA is not unique, there exists a space different solutions with the same approximation error. With the delay constraints introduced the solution space dimension is decreasing, but the approximation error is increasing: see comparisons in the next subsection.

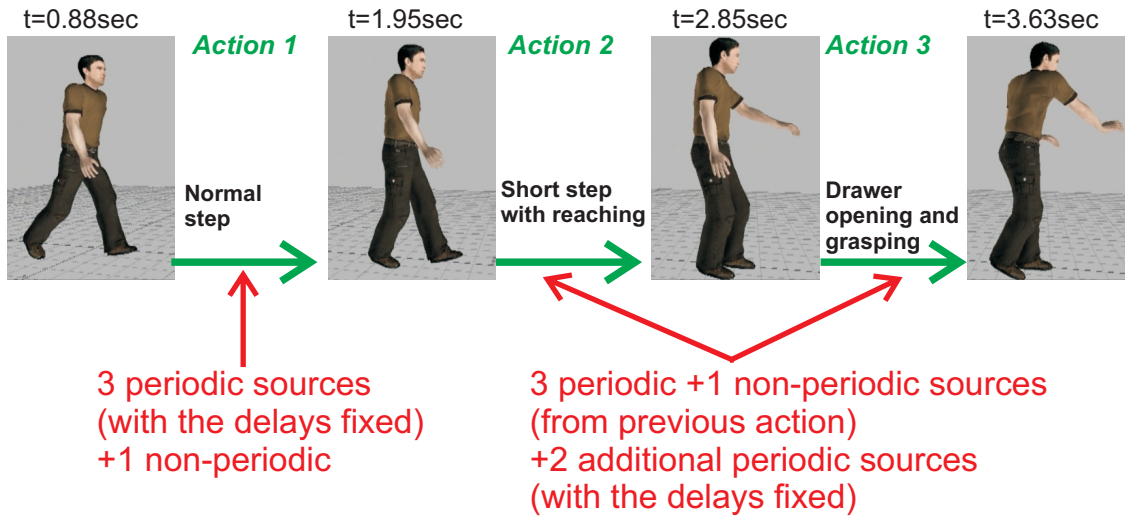


**Figure 3.12:** Drawer walking-reaching-opening scenario. Three elementary actions extracted for learning and their control dependencies: 1) normal step; 2) step with initiation of reaching; and 3) standing with opening of the drawer and reaching for the object. The sequence demonstrates the step-wise regression approach in modelling of the subsequent actions with different subsets of source signals.

### Stepwise estimation of spatially localized anechoic primitives

The coordination of arm reaching during walking on a treadmill (see dataset description in 3.3.1), as analyzed by<sup>56</sup>, requires simultaneous control of arm reaching towards a goal and timing relative to the gait cycle. In order to model such motion we represent the whole body trajectory as a mixture of spatially overlapping synergies. The periodic primitives (time-shift invariant synergies) control the gait-related part of the motion of the whole body, while the non-periodic bump-like primitive is controlling the reaching-related movement of the upper body. Here I use a *stepwise regression approach*: first, approximate the normal gait cycle by periodic sources, then, approximate the residual of joint angles of the upper body (trunk, neck and arms) by a non-periodic primitive. In this model the delays of the periodic primitives are assumed to be fixed for each joint angle across different gaits and the weights of these periodic source signals are learned as functions of the step size. The weights of the non-periodic primitives are dependent on target position with respect to the trunk (in the chest coordinate frame), and they are dependent on the phase of the gait cycle, when the arm reaching starts. The timing of switching-on of the non-periodic primitive is the moment of target presentation. A similar stepwise regression approach is used in the modelling of the bridge dance, which will be described later (3.6), where the non-periodic primitive controls the arm lifting for the arm bridge formation, but the delays of periodic primitives were not fixed across dancing steps in this case.

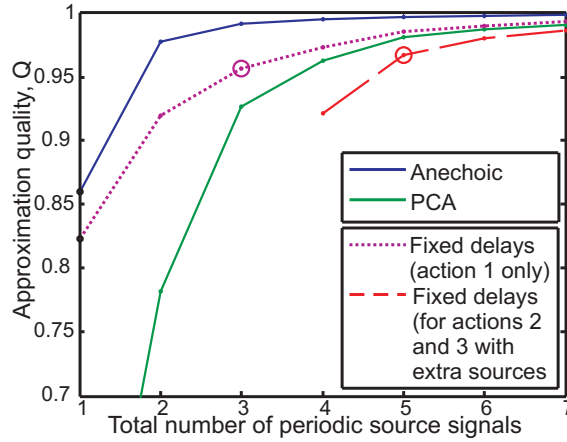


**Figure 3.13:** Comparison of approximation quality for different methods for blind source separation as function of the number of sources, using a step-wise regression approach (residuals after subtraction of the contribution of the non-periodic source signal). *Solid lines:* Approximation quality for trajectories of all three actions as a function of the number of (periodic) source functions for anechoic demixing (*blue*) and principle component analysis (PCA) (*green*). The *purple* dotted line shows the approximation quality for the first action, fixing the delays across trials. The *red* dashed line shows approximation quality when 2 additional sources (with fixed delays) were included in order to model the remaining residuals. Circles mark the chosen numbers of sources in our implementation. The figure is adopted from<sup>209</sup>.

I use the stepwise regression approach also in modelling of multi-action sequences, in the drawer walking-reaching-grasping task (see description in 3.3.1, 3.6). I introduce different types of source signals for the three different sequential actions. The non-periodic source signal is defined by  $s_0(t) = \cos(\pi t/T)$ ,  $t = [1 : T]$  (where  $T$  is the period of the gait cycle). In rare cases, though the periodic source signals are continuous functions, they still might have discontinuous first derivatives. In these cases one needs to filter the source signals by smoothing (e.g. with a Savitzky-Golay filter<sup>272</sup>), then to re-estimate the optimal weights. This is the approach I follow in the drawer walking-reaching task model. But if the goal is to model the discontinuity of the first derivative at the ends of the trajectories, then one needs to employ more non-periodic source signals, e.g.:  $s_0^{nonper} = \cos(\pi t/T)$ ,  $s_1^{nonper} = \cos(\pi t/(2T))$ ,  $s_2^{nonper} = \sin(\pi t/(2T))$ ,  $t = [1 : T]$ .

The three actions of the training sequences are modeled as follows (see<sup>209</sup> and Fig. 3.12):  
**1st action:** The weights of the non-periodic sources were determined in order to account for the non-periodic part of the training trajectory. Then, this component was subtracted from the trajectory data. The periodic source signals were determined by anechoic demixing, constraining all delays belonging to the same source signal to be equal for a particular joint angle. This constraint simplifies the blending between different motion styles, since the delays of the sources are identical over styles, so that they do not have to be blended. Compared to the unconstrained anechoic model, this constraint requires the introduction

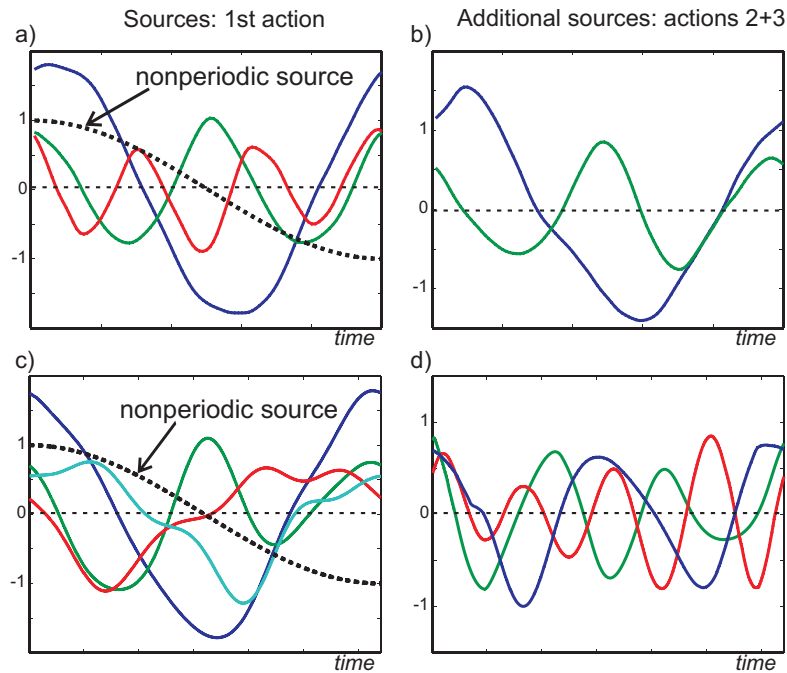


**Figure 3.14:** The source signals extracted by the anechoic de-mixing algorithm for the drawer walking-reaching scenario. In the left column - periodic source signals extracted from the first action and the non-periodic source signal (dashed line). **a)**: 3 periodic sources; **c)**: 4 periodic sources. In the right column - the additional periodic source signals used for modeling of the second and the third actions. **b)**: 2 additional sources for the case **a)** - 4+2 total sources; **d)**: 3 additional sources for the case **c)** - 5+3 total sources.

of more sources for the same approximation quality (see Fig. 3.13). The first gait cycle is modeled with sufficient accuracy using three periodic sources in addition to the non-periodic one.

**2nd action:** In order to model the second adaptive step with the left arm reaching towards the drawer, five periodic sources are required. The first three periodic sources are identical to the ones used for the approximation of the first action, and also their corresponding delays are the same. Their weights were re-estimated, optimized in order to minimize the remaining approximation error in the 2nd action. The contributions of these three periodic sources (and of the non-periodic sources), were subtracted from the training data, and two additional periodic sources were learned from the residuals (with constant delays across trials).

**3rd action:** In order to approximate this action, we used the same non-periodic and five periodic source signals, with the same time delays, that were identified for the modeling of the second action, while the weights of all these sources were re-estimated.

The estimated source functions are shown in Fig. 3.14. The dotted curve illustrates the non-periodic source. The source functions illustrated in panel **a)** (and panel **c)**) are

The distribution of the amplitudes of sources weights

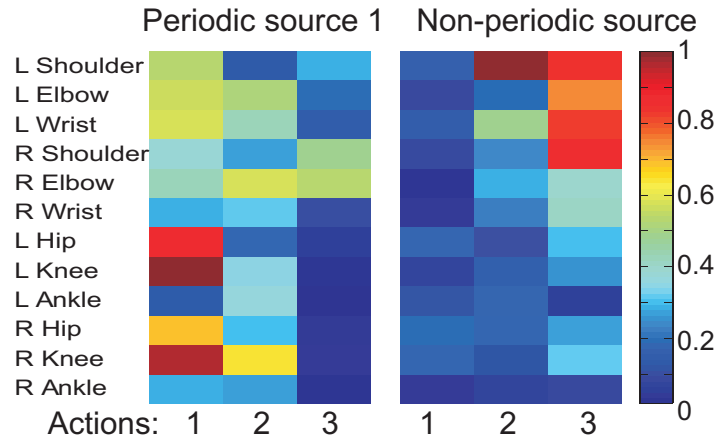


**Figure 3.15:** Absolute values of the weights for an example trajectory of the data set. The mixing weights are shown from the different actions within the sequence for the periodic source function with minimum frequency and for the non-periodic source. The color code is the same for both panels. The figure is adopted from<sup>209</sup>.

used for the approximation of all three actions, and the two in panel **b)** (and panel **d)**) are additional - only for actions two and three.

Fig. 3.13 shows the approximation quality as a function of the number of source functions for the first and the second action, comparing anechoic demixing without delay constraints<sup>229</sup>, the default SISA algorithm with constant delays over the different conditions, and a reconstruction using PCA. The measure for approximation quality was defined again as  $Q = 1 - (\|X - \hat{X}\|_F^2) / \|X\|_F^2$ , where  $X$  is the matrix with the samples of the original signal, and  $\hat{X}$  is the reconstructed signal,  $\|\cdot\|_F^2$  is the squared Frobenius norm. Especially the model without constraints for the delays achieves significantly better approximation quality than PCA. The reconstruction error for the first action (purple circle on Fig. 3.13) is 95.6%, while the one with the two additional sources, used for actions 2 and 3, is 96.7% for the whole dataset (red circle).

The absolute values of the amplitudes of the weights for a single trajectory are depicted in Fig. 3.15, separately for the two source signals that carried the maximum amount of variance. This are the non-periodic source signal and the periodic source signal with the lowest frequency. The figure shows that the primitives clearly contribute to the different degrees of freedom of the human body. The non-periodic source primarily contributes to the joint angles of the arm, while the periodic source function strongly influences the hip and the leg joints. This reflects the organization of human full body movements in terms of movement primitives. The figure also shows that the contribution of the sources changes between the steps. In the first action the contribution of the first periodic source



is dominant, while in the second and last actions the non-periodic source function has a dominant contribution reflecting the non-periodic reaching movement.

### 3.3.4 The DMP Architectures for the Online Synthesis of Kinematic Motion Trajectories

Real-time animation necessitates flexible systems that can react in an online fashion, adapting to external constraints. Such online systems are suitable for the self-organization of complex behaviors by the dynamic interaction between multiple autonomous characters in the scene. The learned generative model can synthesize periodic and non-periodic movements, achieving high degrees of realism with a small number of synergies. By introduction of dynamic couplings between the primitives the temporal coordination between the different source components can be ensured. In an abstract sense, the resulting system is similar to a set of coupled '*Central Pattern Generators*' (CPGs) in a biological system.

For the online generation of the source signals we construct a nonlinear mapping between the solutions of the dynamical systems and the source signals. This gives flexibility for the choice of the dynamical system, which can be optimized in order to simplify the design of a stable overall system dynamics. As basic building blocks for the dynamics we use nonlinear oscillators for the synthesis of periodic behaviors, and a fixpoint attractors for the synthesis of non-periodic movements. We decided to use nonlinear dynamical systems whose structural properties do not change in the presence of weak couplings. In this way we can design the qualitative properties of the different dynamic primitives – to some degree – independently from their interaction with other system components. The idea to map desired behaviors onto solutions of nonlinear dynamical systems is common in behavioral research, robotics<sup>40,132,276</sup> and computer animation<sup>92</sup>.

#### The limit cycle attractor of the Van der Pol oscillator as DMP

As basic dynamics for the generation of the periodic signals we used a limit cycle oscillator: The Van der Pol oscillator, for adequate choice of the parameters, has an asymptotically stable limit cycle<sup>323,333</sup>. It was used in several of our own publications<sup>103,210,235,236</sup>. Its dynamics is given by the differential equation:

$$\ddot{x}(t) + \nu \left( x(t)^2 - \rho \right) \dot{x}(t) + \omega_0^2 x(t) = 0 \quad (3.11)$$

The parameter  $\omega_0$  determines the eigenfrequency of the oscillator, and the parameter  $\rho$  the amplitude of the stable limit cycle. The force that pushes the state back towards the limit cycle is determined by the parameter  $\nu > 0$ . For appropriate choice of the oscillator

parameters, in absence of external input signals, the form of the stable limit cycle can be made almost perfectly circular in the  $x-\dot{x}$  plane (*phase plane*), assuming appropriate scaling of the two axes. This property is critical for the online implementation of the phase delays.

One source is non-periodic and has a ramp-like characteristics (Fig. 3.11). This source is crucial for the approximation of non-periodic point-to-point arm movements. I model this behavior by a fixed point attractor. Considering that natural arm movements are characterized by a bell-shaped velocity profile<sup>202,295</sup>, we chose a nonlinear dynamics that generates solutions with this property. In addition this dynamics can generate identical movements in opposite directions by the change of a single parameter. This dynamics is given by the differential equation:

$$\dot{x}(t) = ux(t)(1 - x(t)) \quad (3.12)$$

We restrict the values for  $x$  to the interval  $I = [0, 1]$ . For  $u < 0$  this dynamics has a stable fixpoint at 0, and for  $u > 0$  a stable fixpoint at 1 that is approached asymptotically from inside the interval  $I$ . The value of  $|u|$  determines how fast this fixpoint is approached. The solution of this differential equation can be computed analytically and is given by  $x(t) = (1 + \tanh(\frac{u}{2}(t - t_0))) / 2$ , showing that its derivative  $\dot{x}(t) = \frac{u}{4} (1 - \tanh^2(\frac{u}{2}(t - t_0)))$  is bell-shaped. By clipping we ensure that in presence of noise  $x$  does not leave the permissible interval. For the online simulations of Van der Pol oscillators we use 5-step Adams-Bashforth method (e.g.<sup>44,115</sup>).

The dynamical primitives that generate the signals for different synergies must be synchronized for the generation of coordinated behavior. *Synchronization* can be accomplished by introducing couplings between the dynamic primitives. The oscillatory primitives are modeled by Van der Pol oscillators. Applying concepts from *Contraction Theory*<sup>333</sup> (see also Chapter 4), it can be shown that complex networks of such oscillators can be guaranteed to have a single stable solution if the oscillators are coupled by *velocity couplings*. For 3 Van der Pol oscillators coupled symmetrically and bi-directionally this type of coupling is defined by the equations (the value of parameter  $k > 0$  is specifying the uniform coupling force):

$$\begin{aligned} \ddot{x}_1 + \nu (x_1^2 - \rho) \dot{x}_1 + \omega_0^2 x_1 &= \alpha (\dot{x}_2 - \dot{x}_1) + k (\dot{x}_3 - \dot{x}_1) \\ \ddot{x}_2 + \nu (x_2^2 - \rho) \dot{x}_2 + \omega_0^2 x_2 &= \alpha (\dot{x}_1 - \dot{x}_2) + k (\dot{x}_3 - \dot{x}_2) \\ \ddot{x}_3 + \nu (x_3^2 - \rho) \dot{x}_3 + \omega_0^2 x_3 &= \alpha (\dot{x}_1 - \dot{x}_3) + k (\dot{x}_2 - \dot{x}_3) \end{aligned} \quad (3.13)$$

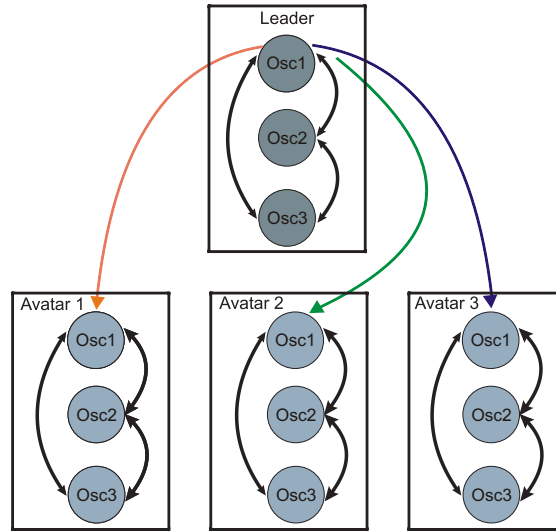


**Figure 3.16:** Exemplary coupling of multiple avatars, each of them comprising three coupled oscillators (Osc1..3), permits the simulation of the behavior of coordinated crowds. The figure is adopted from<sup>210</sup>.

For values of  $\alpha$  below a specific bound, which depends on the coupling graph, the overall system dynamics has only a single stable solution. It is characterized by synchronization of all oscillators. The same type of couplings can be introduced between oscillators that represent dynamic primitives of different characters in the scene. This allows the modeling of synchronized behavior of multiple avatars (e.g. soldiers in lock-step). To implement such couplings we only connected the oscillators assigned to the source with the lowest frequencies (Osc1 in Fig. 3.16). By introducing directional couplings it is also possible to make multiple characters following one, who acts as a leader<sup>333</sup>.

To synchronize the non-periodic primitives with external events the sign of the parameter  $u$  in equation (3.12) was switched dependent on an external signal, which triggers the raising of the arm. In this way, the previously stable fixed point of this dynamics becomes unstable, while its unstable fixpoint becomes stable. In addition, we added a short pulse input to this equation that displaces the state away from the unstable fixpoint. This ensures a transition to the novel stable point with a well-defined timing.

### The mapping of DMPs onto the source signals

To map the attractor solutions of the differential equations defining the dynamic primitives onto the source signals we construct a nonlinear mapping. This mapping is defined by

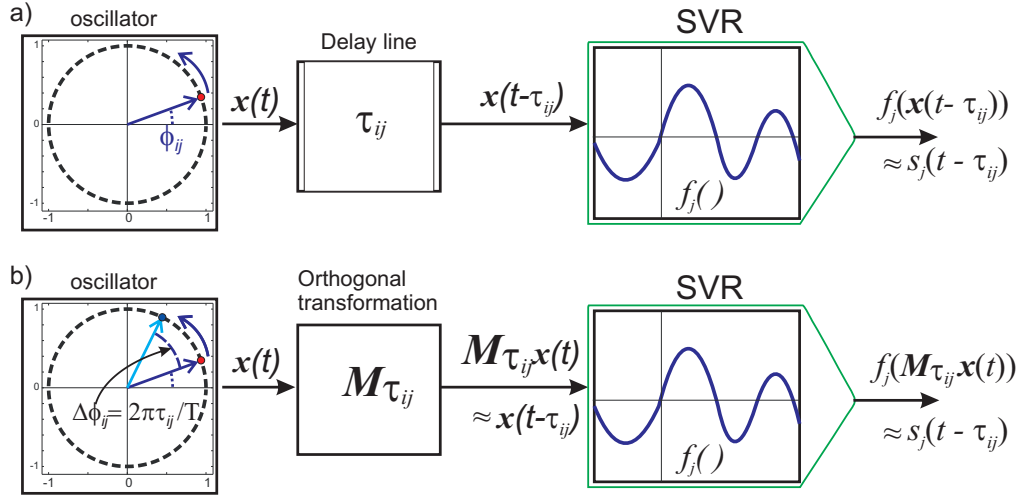


**Figure 3.17:** Online implementation of delays. a) Direct implementation introduces explicit delay lines, resulting in a complex system dynamics that is difficult to control. b) Approximation by a rotation in the phase space, defined by the instantaneous orthogonal transformation  $\mathbf{M}_{\tau_{ij}}$  in the phase plane of the oscillator avoids a dynamics with delays. The figure is adopted from<sup>103</sup>.

a concatenation of a rotation in phase space, modeling the influence of the time delays  $\tau_{ij}$ , and a nonlinear function, which is learned from the training data by *Support Vector Regression (SVR)*,<sup>52,325</sup>.

Treating the oscillatory primitives first, the purpose of the mapping is to associate the points  $\mathbf{x} = [x, \dot{x}]^T$  along the attractor in the phase plane of the oscillators with the corresponding values of the source function  $s_j$ . We try to avoid the introduction of explicit time delays in the implementation since this would lead to complex system dynamics. As illustrated in Fig. 3.17 we try to approximate the terms  $s_j(t - \tau_{ij})$  in (3.3) in the form:

$$s_j(t - \tau_{ij}(t)) \approx f_j(\mathbf{M}_{\tau_{ij}}\mathbf{x}(t)) \quad (3.14)$$

where  $\mathbf{M}_{\tau_{ij}}$  is a scaling transform and an orthogonal transformation combined:

$$\mathbf{M}_{\tau_{ij}} = \begin{bmatrix} \cos(\phi_{ij}) & -\sin(\phi_{ij}) \\ \sin(\phi_{ij}) & \cos(\phi_{ij}) \end{bmatrix} \mathbf{\Theta} \quad (3.15)$$

This transformation is a concatenation of a scaling and rotation in the two dimensional phase space. The matrix  $\mathbf{\Theta}$  is diagonal and scales the axes of the phase plane in a way that makes the attractor solution of the Van der Pol oscillator approximately circular. The rotation angles are given by  $\phi_{ij} = -2\pi\frac{\tau_{ij}}{T}$ , where  $T$  is the duration of one period of the stable oscillatory solution. The nonlinear function  $f_j(\mathbf{x})$  maps the phase plane onto a scalar. It is learned from training data pairs that were obtained by temporally equidistant

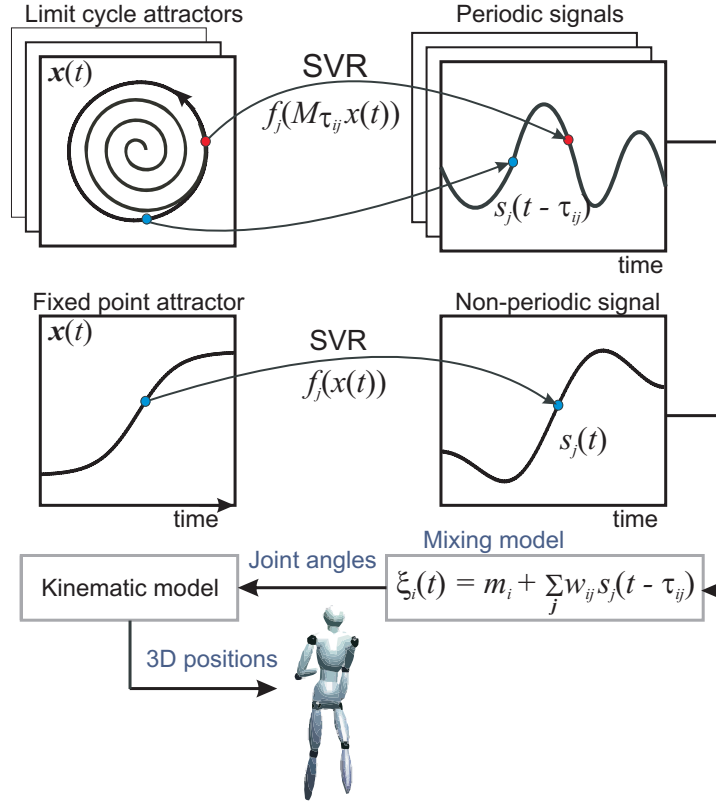


**Figure 3.18:** Illustration of the dynamic architecture for real-time animation. Periodic and non-periodic movements are generated by dynamic primitives. The solutions of these dynamical systems are mapped onto the source signals by a nonlinear mapping that models the time delays and a nonlinear transformation that is learned by SVR. Joint angle trajectories can be synthesized by combining the signals linearly according to the learned mixture model (3.3). A kinematic model converts the joint angles into 3-D positions for animation.

sampling of the signals  $\mathbf{x}(t)$  and  $s_j(t - \tau_{ij}(t))$ , where we used the solutions of the uncoupled dynamic primitives (the stable limit cycles of oscillators). The functions were learned by Support Vector Regression<sup>52</sup> using a Gaussian kernel.

For the non-periodic source, the solution of the point-attractor equation (3.12) was mapped in a similar way onto the values of the non-periodic source signal. In principle, the effect of the time delay can be modeled by an application of a conformal mapping to the solution of this equation. The overall system dynamics for the animation of different walking and dancing styles was defined by three oscillators and the point attractor dynamics (3.12). The state variables of the dynamic primitives were mapped onto the source signals by the described nonlinear observers. The synthesized source signals were then linearly combined according to (3.3), where the complete reconstruction of the joint angle trajectories requires the addition of the average joint angles  $m_i$ . An overview of the whole

algorithm is given in Fig. 3.18.

### The limit cycle attractor of Andronov-Hopf oscillator as DMP

In the following work in computer graphics<sup>209,211–213,237</sup> and robotics<sup>5,148,214,215</sup> we used the classical Andronov-Hopf oscillator as DMP (canonical dynamics). The **Andronov-Hopf oscillator** is a nonlinear oscillator whose choice of parameters is characterized by a limit cycle that corresponds to a circular trajectory in phase space. This oscillator is characterized by the decoupled phases and radial dynamics, where phase dynamics is indifferent to external perturbations and the radial dynamics is stable. This property facilitates the application of *Contraction Theory* for the stabilization of inter-coupled dynamics of networks of such oscillators (see details in Chapter 4).

For appropriate re-parametrization (rescaling of time and state-space axes) the dynamics of this oscillator is described by the differential equations<sup>11</sup>:

$$\begin{cases} \dot{x}_1(t) = (1 - (x_1^2(t) + x_2^2(t))) x_1(t) - \omega x_2(t) \\ \dot{x}_2(t) = (1 - (x_1^2(t) + x_2^2(t))) x_2(t) + \omega x_1(t) \end{cases} \quad (3.16)$$

Here  $\omega$  is the eigenfrequency of the oscillator's phase. Introducing polar coordinates  $r(t) = \sqrt{x_1^2(t) + x_2^2(t)}$  and  $\phi(t) = \arctan(x_2(t)/x_1(t))$ , this system can be rewritten:

$$\begin{cases} \dot{r}(t) = r(t) (1 - r^2(t)) \\ \dot{\phi}(t) = \omega \end{cases}$$

The radial dynamics is asymptotically stable (cf. Chapter 4), and the limit cycle attractor is a circle with radius equal to 1.

The DMP dynamics be written compactly in vector form (with  $\mathbf{x} = [x_1, x_2]^T$ ):

$$\dot{\mathbf{x}}(t) = \mathbf{f}(\mathbf{x}(t)) \quad (3.17)$$

If the oscillator is coupled unidirectionally (and by linear coupling of phase variables) with another oscillator providing an input signal  $\mathbf{x}_{ext}(t)$ , then the dynamics of the influenced oscillator is represented as:

$$\dot{\mathbf{x}}(t) = \mathbf{f}(\mathbf{x}(t)) + \alpha(\mathbf{x}_{ext}(t) - \mathbf{x}(t)) \quad (3.18)$$

where  $\alpha$  is the linear coupling strength.

For the online simulation of the Andronov-Hopf oscillators I use 5-step Adams-Bashforth or 4th-order Runge-Kutta methods (cf.<sup>44</sup>). The phase space variable  $\mathbf{x}$  is mapped onto the source functions  $s_j$  by nonlinear mapping functions  $f_j(\mathbf{x})$ , which were learned by

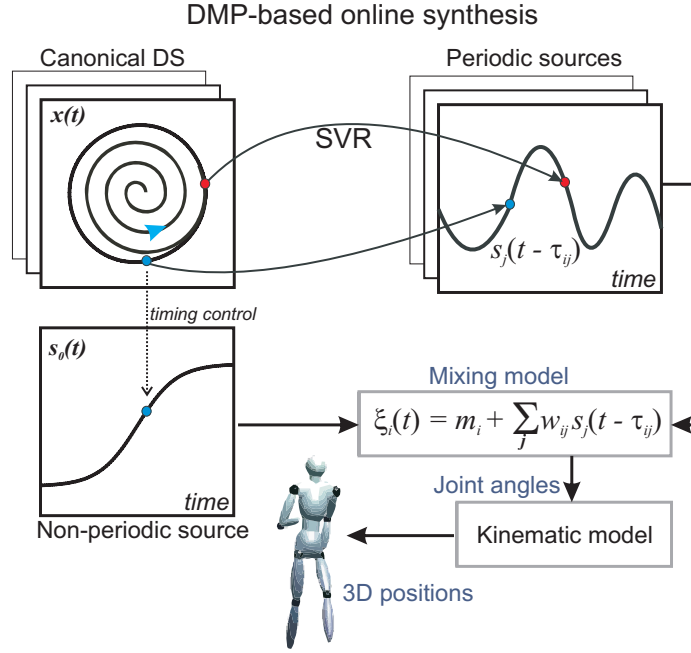


**Figure 3.19:** Architecture for the online synthesis of body movements using dynamic primitives. The DMPs architecture is modified using time-locking of the non-periodic primitive, as triggered by the leading DMP.

Support Vector Regression (using a Radial Basis Function kernel and the LIBSVM Matlab<sup>®</sup> library<sup>52</sup>). The learned source functions  $s_j(t)$  and corresponding states  $\mathbf{x}(t)$  from the attractor solution of the limit cycle oscillator were used as training data.

Exploiting the fact that the attractor solution of the Andronov-Hopf oscillator lies on a circle in state space, the delays can be replaced by appropriate rotations of the variables of the phase space  $\mathbf{x}$ , see Fig. 3.17. The scaling matrix  $\Theta$  (3.15) is just an identity matrix in this case. In this way, we obtained a dynamics without explicit time delays, avoiding difficulties with the design of appropriate controllers.

In DMPs architecture we used one leading oscillator, and the other oscillators were coupled to this leading oscillator in the described form (star topology of the coupling graph, where couplings are unilateral from the center to the leaves of the star). The stability properties of this form of coupling were studied in detail in<sup>237</sup>, and in the next Chapter 4, where I show that this dynamics has a single exponentially stable solution.

The state of the leading oscillator was also used for the control of the non-periodic source function. In order to generate such a function online, the phase of the leading Andronov-Hopf oscillator was derived from the state variables according to the relationship  $\phi(t) = \text{mod}_{2\pi}(\arctan(x_2(t)/x_1(t)))$ , (ensuring  $0 \leq \phi < 2\pi$ ). The non-periodic source signal was not learned, but defined as  $s_0(t) = \cos(\phi(t)/2)$ , and its corresponding delay was set to zero for all trajectories samples. The modification of the system architecture is

presented on Fig. 3.19.

### 3.4 Motion Style Morphing by Anechoic Mixture Parameter Blending

The proposed model for the real-time generation of trajectories permits style morphing by linear interpolation of the average angles  $m_i$ , the mixing weights  $w_{ij}$  and the delays  $\tau_{ij}$ . The interpolation of the mean angles and of the weight matrices is straight forward. However, the interpolation of the delays requires an additional approximation to avoid artifacts that are caused by ambiguities in the estimation of the delays. The technique of the delays interpolation presented below was used in the Bridge and Welsh dance synthesis scenarios<sup>103,210</sup> presented in Section 3.6.

For periodic source signals ambiguities in the estimation of weights and delays can arise that have to be removed prior to interpolation. Periodic source signals fulfill  $s_j(t + rT) = s_j(t)$  with integer  $r$ . In addition, source signals can be approximately periodic, fulfilling  $s_j(t + qT/n) \simeq s_j(t)$  with integer  $q$  and  $n$ . Such ambiguities are specifically a problem for the source signals that model the higher frequency components, where  $T/n$  is an integer fraction of the gait cycle time  $T$ . This (approximate) periodicity can cause ambiguities in the estimated delays, which might differ by multiples of  $T/n$ . If such delays are linearly interpolated they introduce phase differences between the sources that do not interpolate correctly between similar motion styles. To remove such ambiguities, the delays in the estimation step of the anechoic de-mixing algorithm are replaced by the modified source delays  $\tilde{\tau}_{ij} = \tau_{ij} - qT/n$ , where  $q$  was chosen to minimize the values of the delay differences. This is done by finding the local extrema (closest to zero) of the cross correlation function between the original and time shifted versions of the source signals. This made it possible to restrict and interpolate the delays within the intervals  $[-T/2n, T/2n]$ , removing the ambiguity.

With the corrected time delays  $\tilde{\tau}_{ij}$  and weights the interpolation between two movement styles (a) and (b), e.g. neutral and emotional walking, can be characterized by the equations

$$m_i(t) = \alpha(t) m_i^a + (1 - \alpha(t)) m_i^b \quad (3.19)$$

$$w_{ij}(t) = \alpha(t) w_{ij}^a + (1 - \alpha(t)) w_{ij}^b \quad (3.20)$$

$$\tilde{\tau}_{ij}(t) = \alpha(t) \tilde{\tau}_{ij}^a + (1 - \alpha(t)) \tilde{\tau}_{ij}^b \quad (3.21)$$

The time-dependent morphing parameter  $\alpha(t)$  specifies the movement style at time  $t$ . Additionally, the gait speed can be adjusted by interpolating the eigenfrequencies of the



oscillators:

$$\omega_0(t) = \alpha(t)\omega_0^a + (1 - \alpha(t))\omega_0^b \quad (3.22)$$

### 3.4.1 Event-based Transitions between Actions in Multi-action Sequences

For the online blending between different actions in multi-action sequences (like the drawer walking-reaching scenario,<sup>209</sup>), we constrained the delays of the source signals during the extraction of the anechoic mixtures obtaining the same delay value for a particular source and particular angle across all actions. So, in event-based morphing we only blend online the mixing weights  $w_{ij}$  and angle mean values  $m_i$ .

For the weights associated with the periodic sources, the corresponding weight matrices were linearly blended according to the relationship  $W(t) = (1 - \alpha(t))W_{\text{prev}} + \alpha(t)W_{\text{post}}$ , where  $W_{\text{prev}}$  is the weight matrix ( $w_{ij}$ ) in the step prior to the transition and  $W_{\text{post}}$  the one after the transition. The mean values for each of the angle trajectories were morphed accordingly:  $m(t) = (1 - \alpha(t))m_{\text{prev}} + \alpha(t)m_{\text{post}}$ , where  $m_{\text{prev}}$  is the mean value in the step prior to the transition and  $m_{\text{post}}$  is the one after the transition. The time-dependent blending weight  $\alpha(t)$  was constructed from the phase variable  $\phi(t)$  of the leading oscillator. Identifying the transition point, where the weights switch between the subsequent actions with phase  $\phi = 0$ , the blending weight was given by the equation (here, regarding only two adjunct actions, we use convention:  $\phi \in [-2\pi; 0[$  for a previous action, and  $\phi \in [0; 2\pi[$  for a next one):

$$\alpha(t) = \begin{cases} 0 & \phi < -\beta\pi, \\ (1 + \sin(\frac{\phi(t)}{2\beta}))/2 & \phi \in [-\beta\pi; \beta\pi], \\ 1 & \phi > \beta\pi \end{cases} \quad (3.23)$$

The parameter  $\beta = 1/5$  determines the width of the interpolation interval and was chosen to guarantee natural-looking transitions<sup>209</sup>.

The weights of the non-periodic source had to be treated separately since they can have different signs before and after the transition. Since the timing of this source is completely determined by the phase  $\phi(t)$  of the leading oscillator, we constrained the blending by allowing sign changes for these weights only at the point where this phase crosses zero ( $\phi(t) = 0$ ). The ramp-like non-periodic source is normalized in a way so that  $s_0(0) = 1$  and  $s_0(T) = -1$  ( $T$  being the duration of an oscillation of the leading oscillator in the attractor state). The following morphing rule  $W(t) = \text{sign}(\phi(t))[(\alpha(t) - 1)W_{\text{prev}} + \alpha(t)W_{\text{post}}]$  ensures a smooth transition making the weights for this source converge at the boundaries between the actions to the intermediate value  $W_{\text{trans}} = (m_{\text{prev}} + m_{\text{post}})/2 + (W_{\text{post}} - W_{\text{prev}})/2$ .

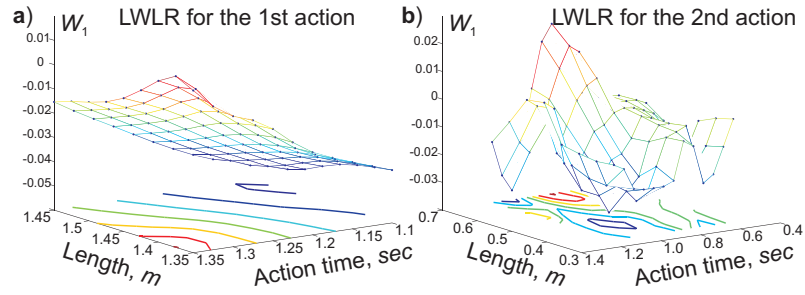


**Figure 3.20:** Learned nonlinear mappings between action length and duration and the mixing weight of the 1st source for hip flexion angle: a) 1st action, b) 2nd action. The figure is adopted from<sup>209</sup>.

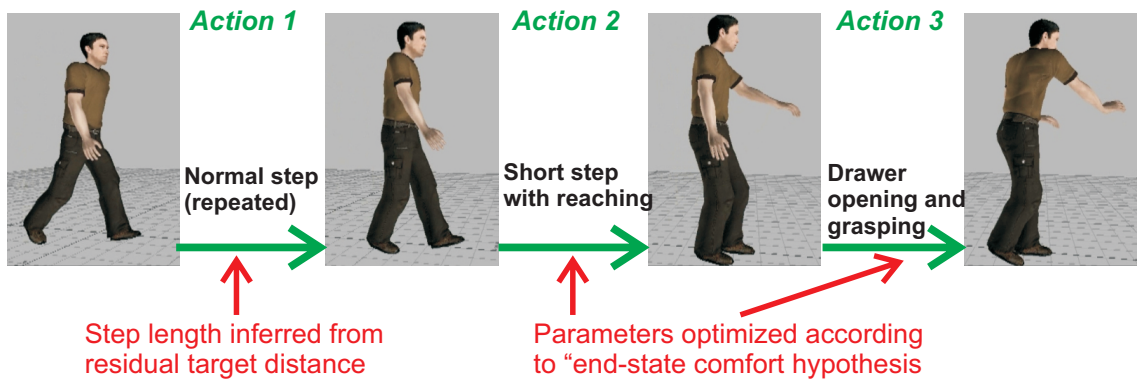


**Figure 3.21:** Drawer walking-reaching-opening scenario. Three elementary actions extracted for learning and their control dependencies: 1) normal step; 2) step with initiation of reaching; and 3) standing with opening of the drawer and reaching for the object.

### 3.4.2 Learning of Behavior Specific Mappings between Action Parameters and Mixing Weights

In order to make the generated behavior adaptive for conditions that were not in the training data and for dynamic changes of the environment, I devised an online control algorithm for the blending of the weights  $W$  and angle mean values  $m$ , separately for each action. For this purpose, I learn nonlinear functions that map the step lengths and the duration of the steps onto the mixing weights. For the learning of this highly nonlinear mapping, Locally Weighted Linear Regression (LWLR,<sup>16</sup>) is used. Fig. 3.20 shows an example for the weights of the first periodic source.

The required step lengths are computed online from the total distance to the drawer. The schematic view is presented in 3.21. The length of the step of the second action was optimized in order to generate an optimum (maximally comfortable) distance for the third action, which was estimated from the human data to be about  $0.6m$ . The total distance

between the start position and the drawer  $D$  was then redistributed between the first two actions using a linear weighting scheme, specifying the relative contributions by the weight parameter  $\gamma$ . The remaining distance  $D - 0.6\text{m}$  was then distributed according to the relationships  $D_1 = (D - 0.6\text{m})\gamma$  and  $D_2 = (D - 0.6\text{m})(1 - \gamma)$ , where we fitted  $\gamma = 0.385$  based on the human data. This approach is motivated by the hypothesis that in humans predictive planning optimizes *end-state comfort*, i.e. the distance of the final reaching action<sup>165</sup>.

This algorithm is extended by a method that introduces additional normal steps (corresponding to action 1), in cases where the goal distance exceeds the distance that can be modeled without artifacts by a three-action sequence. If the distance between the goal and the agent was too short for the introduction of long steps, instead a variable number of short steps as in action 2 were introduced.

### 3.4.3 Semi-supervised Learning for *Style* vs *Content* Separation

#### The Structural Learning problem in motion synthesis

*Structural Learning*, the learning and inference of the hidden parameterized *style* manifold of human motion structure is a hot topic in recent research<sup>35,36</sup>. Researchers are interested in human strategies for the synthesis of articulated motion<sup>36</sup> as well as in motion synthesis algorithms for the purpose of robotics<sup>188</sup> and computer animation<sup>17</sup>.

There is the well-known problem of redundancy of degrees of freedom (DoFs) for human limbs<sup>28</sup>. E.g. for an arm (actuator) with 7 DoFs, a one-dimensional manifold (or variety) of actuator's postures corresponds to a single final position of the end-effector, the hand with its 6 DoFs of position and orientation in space. This is redundancy in an *inverse statics* (IS) task: for a given hand position and orientation we want to infer the "most appropriate" arm-configuration, one from many. Even in case of a planar arm with 2 links and 2 DoFs and with a point-like end-effector, for any reachable target point - the 2 feasible arm configurations provide the target touching. A similar redundancy is present in the *inverse kinematics* (IK) task, which is to find the mapping from the desired instantaneous 6-DoF velocity of the hand onto the instantaneous velocities of 7 joint angles of the arm. These redundancies allow humans to exploit the flexibility in the arm reaching task, providing the freedom for concurrent tasks during the execution of the main one. Those auxiliary lower priority tasks can be: obstacle avoidance at final or intermediate postures, reduction of work against gravitational forces, optimization of torque loads across limbs<sup>319</sup>, utilization of reactive and Coriolis forces in fast motion, intrinsic noise reduction<sup>117,314</sup>, minimization of torque control<sup>269</sup>, and other tasks of enhancing the robustness of motion

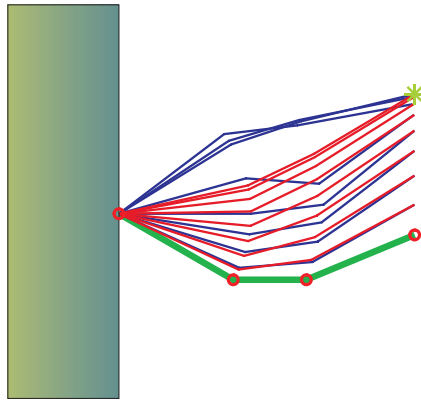


**Figure 3.22:** The snapshots of two reaching trajectories (red and blue) of a 3-DoFs planar arm starting with the same configuration (green, joint centers are red circlets) and reaching the same goal (light green star). The trajectories are produced by the prioritized inverse kinematics, preferring arm joint configurations with "elbow down" or "elbow-up".

with respect to the expected online disturbances. The computational framework for the inverse kinematics in robotics, which takes into account multiple parallel tasks, was first proposed by<sup>187</sup> (cf.<sup>154</sup>) and then developed in full mathematical detail by<sup>288</sup>. Later, this approach was named *Stack-of-Tasks*<sup>82</sup> and extended to constrained *inverse dynamics* (ID) tasks as well<sup>188</sup>.

The unconstrained local inverse kinematics and inverse dynamics tasks are linear. In general motion synthesis using learning-based approaches we consider more general nonlinear mappings between task space (e.g. hand state-space) and effector state space (e.g. arm joint angles). As an example, in Fig. 3.22 there are snapshots of two alternative reaching trajectories of a 3-DoFs planar arm presented. Both trajectories start with the same initial arm configuration, both have the same trajectories of the end-effector in working space - a vertical straight line. But these two trajectories are produced with different arm joint angles prioritization by means of *prioritized inverse kinematics*, in the framework proposed in<sup>17</sup>. The red one uses the preferred negative shoulder angle, keeping the shoulder below the horizontal line (and preferred positive elbow angle "elbow down" style), whereas the blue trajectory was made with "elbow-up" style preference (with the preferred positive shoulder angle and negative elbow angle). In this *prioritized IK* framework<sup>17</sup>, the style preference is the second priority task, which does not interfere with the main task - moving the end-effector along the prescribed vertical trajectory.

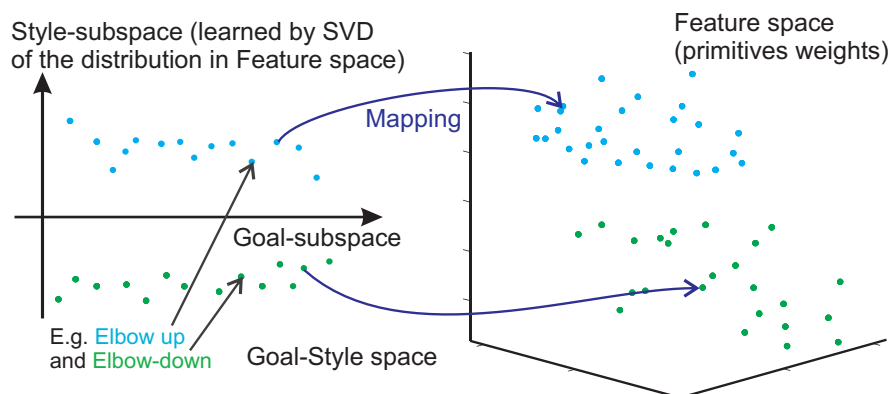


**Figure 3.23:** Sketch of an example distribution of arm reaching trajectories represented as dots in *extended goal-style space* (on the left panel). The same trajectories represented in the space of primitives weights (*feature space* on the right).

### The task of semi-supervised learning of goal-style representations for arm reaching movements.

For motion synthesis, we might approximate the set of different planar arm reaching trajectories by a linear mixture of primitives, e.g. by PCA components. For the example of the planar arm motions depicted above, in the space of the weights of the PCA components of the arm joint angles one may distinguish two submanifolds corresponding to each reaching goal, or even to each end-effector reaching trajectory. The directions in this space corresponding to the preference of the style of reaching motion can be parameterized by *style* variable(s). If such style submanifold attached to every goal value is an affine subspace in feature space, identical at every goal point, we may take any fixed linear subspace of the feature space and use it for style parametrization. For example, we may take one or two largest PCA components of the point distribution in feature space and claim those 1d or 2d subspaces as representing a 1d or 2d motion-style parameter.

Let us consider goal-space (which is the *task space*, the space of parameters of arm reaching targets, (e.g. 3d-positions and 3d-orientations), which is extended by style parameter(s) - see the left panel of Fig. 3.23. This extended representation makes it possible to learn a regression mapping from the extended goal-style space onto the *feature space*, the space of primitives weights. In order to synthesize a new motion towards new target, first we need to infer the feasible values of the style parameter(s) given the goal value. Then, as second step we might use the learned mapping between the goal-style and feature spaces to infer the appropriate weights of the motion primitives. For example, if we continuously morph the motion online, in pursuit of a moving target, we recompute at each time-step the new primitives weights for a new goal position, but simultaneously, we try to stay

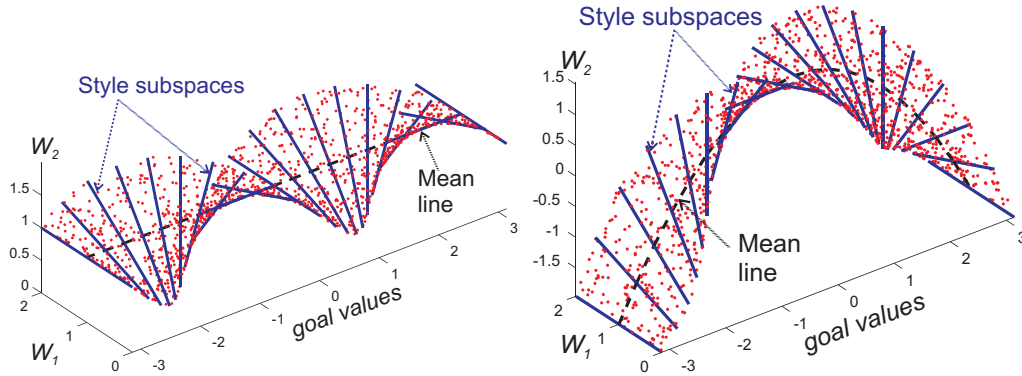


**Figure 3.24:** Synthetic examples of the testing distributions in *extended goal-style space* - the product of goal space and feature space  $W_1W_2$ . The affine style subspaces are one-dimensional - blue thick lines. Left panel - the mean value of style parameter is constant, but the style subspace is smoothly varying along with the goal values. Right panel - the mean value of style parameter is also variable.

close to the style parameter value chosen at the last time-step. Thus, the style preference at the last time-step must be used to generate a prior for optimal inference of the style parameter at the next time-step. If at the first stage of the 2-stage inference we obtain the style parameter as an average of its posterior distribution inferred without any prior, we may get the averaged value of the style parameter from the area in-between "elbow-up" and "elbow-down" subsets (Fig. 3.23). In the second stage, it may result in very inexact inference of primitives weights in the feature space and finally in a large task-space error. Thus, prioritization in style inference is necessary.

### The default approach for semi-supervised learning combined with non-linear regression.

In feature space the affine style manifold corresponding to every goal point may be not just a translated linear subspace, but the mean point of the style parameter distribution, and the style manifold principal directions may vary (may be smoothly) along the variation of the goal value. In Fig. 3.24 we present two synthetic trial distributions where the style subspace is a 1d affine space in the 2d *feature space*  $W_1W_2$ , but it is smoothly varying along with the goal values. We may choose the style-goal distribution model, where the affine style varies its orientation or it may also vary the mean value of its localized distribution.

We present a simple machine learning approach to learn complex distributions in extended goal-style space. The aim of our machine learning approach is to assure not

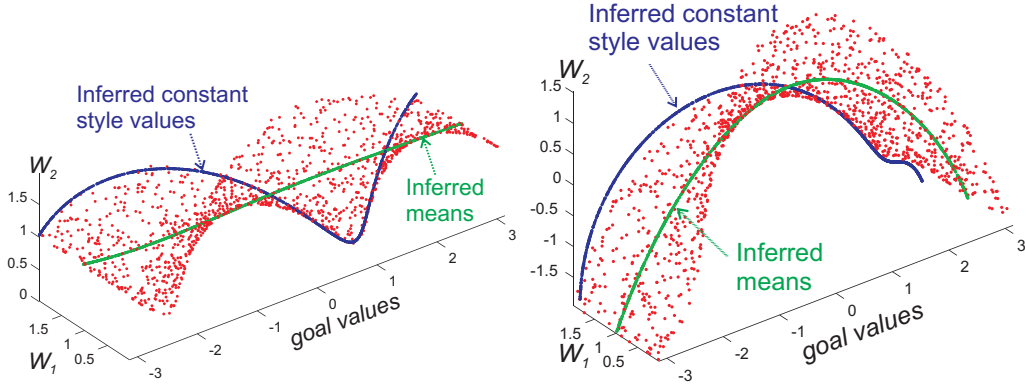


**Figure 3.25:** Results of the learned regression models for the two artificial testing distributions presented in the previous figure. The inferred means of local style distributions are shown as green lines. The positions of points corresponding to a fixed style value (constant across goals) are depicted as blue lines.

only the smoothness of the mean values of modelled style distributions across goals, but also the smoothness of the affine transform in transitions from one goal base point to another. We exploit the *semi-supervised learning approach* - the values of goal parameters are known, but the style parameter manifolds must be learned in an *unsupervised* fashion. The style-goal (*style-content*) separation in semi-supervised machine learning was first introduced for bilinear and multi-linear models<sup>306</sup>. We are extending this approach to nonlinear dependencies of the affine style manifold on the goal parameters.

As nonlinear regression learning technique we use the Locally Weighted Linear Regression (LWLR) approach<sup>16</sup>. It is a kernel-based approach, which combines the local inference of linear models with the optimal averaging of the predictions provided by these local models. Another machine learning technique which can be used here is nonlinear regression with a Gaussian Process prior<sup>248</sup>, e.g. with the stationary (homogeneous) or non-stationary covariance function. For the sake of clarity, below we present an example using the Radial Basis Function (RBF) kernel method as the non-linear regression.

For the testing examples we use a uniform distribution of  $N$  points equally spread in the rectangle of interval ranges of goal  $g_i$ ,  $i \in [1 \dots N]$  and style values. Next, we warp the supporting rectangle to embed it in 3d full space as shown in Fig. 3.24 (right panel). The resulting 2d *feature space* ( $W_1W_2$ ) values for all  $N$  points are collected in data matrix  $\mathbf{X}$ , which has  $N$  rows and 2 columns. For the local style mean-values estimation we use  $K$  Radial Basis Functions with their centers  $c_k$  ( $k \in [1 \dots K]$ ) equally distributed along the range of the goals. We take Gaussian functions with fixed width  $\sigma$  as basis

functions. The value of each basis function  $k$  evaluated at goal position  $g_i$ ,  $i \in [1 \dots N]$  is:  $\Psi_{ik} = \exp\left(\frac{-(g_i - c_k)^2}{2\sigma^2}\right)$ . All the values are collected in matrix  $\Psi$  (of  $N$  rows and  $K$  columns). Then, the mean values  $\mathbf{M}$  evaluated at every goal position  $g_i$  are obtained by:

$$\mathbf{M} = \Psi(\Psi^T \Psi)^\dagger \Psi^T \mathbf{X}$$

Here, the  $\dagger$  symbol denotes pseudoinverse of the kernel  $(\Psi^T \Psi)$ . The size of matrix  $\mathbf{M}$  is  $N$ -by-2 for our test examples. The last formula for  $\mathbf{M}$  provides the local regularization across goal positions together with the averaging across style dimension(s). The resulting inferred locations of the mean values  $\mathbf{M}$  are depicted as green lines in Fig. 3.25.

In order to infer the new mean-point  $\tilde{m}$  at new goal input  $\tilde{g}$ , compute vector  $\psi_k = \exp\left(\frac{-(\tilde{g} - c_k)^2}{2\sigma^2}\right)$ , then  $\tilde{m} = \bar{\psi}(\Psi^T \Psi)^\dagger \Psi^T \mathbf{X}$ .

As next step we perform iterative estimation of the directions of the style fibers at every goal position. The procedure is similar to *EM*-like semi-supervised learning for bilinear models, but using the RBF network. We denote the 2-dimensional style fiber direction vector in feature space as  $\mathbf{v}$ . Each of these 1-dimensional style affine subspaces in feature space must have its origin at the estimated mean point  $\mathbf{M}_{i,:}$ . The matrix  $\mathbf{V}$  is the concatenation of all these style-spanning row vectors, this matrix has size  $N$ -by-2. Introduce a data matrix of residuals  $\mathbf{R} = \mathbf{X} - \mathbf{M}$ , where the estimated mean values are extracted. We also introduce the vector of local style values to infer for each point  $i \in [1 \dots N]$ :  $\mathbf{s}$ . Then, the iterative algorithm runs as follows:

1) Initialize the style values as  $\mathbf{s} = (\text{diag}(\mathbf{R}\mathbf{R}^T))^{1/2}$ ;

2) for a number of iterations, do:

    a non-linear regression step using RBF:

$$\mathbf{V} = \Psi(\Psi^T \Psi)^\dagger \Psi^T (\mathbf{R} \circ [\mathbf{s}\mathbf{1}^T]),$$

    for  $i \in [1 \dots N]$ :

$$\mathbf{s}_i = \mathbf{V}_{i,:} \mathbf{R}_{i,:}^T / \text{norm}(\mathbf{V}_{i,:});$$

    end of  $i$ -cycle;

    with the renewed values of  $\mathbf{s}$  go back to non-linear regression step.

The norm of 2-dimensional row vector  $\mathbf{V}_{i,:}$  is:  $\text{norm}(\mathbf{V}_{i,:}) = \sqrt{(\mathbf{V}_{i,1})^2 + (\mathbf{V}_{i,2})^2}$ . The operation of taking the diagonal of a matrix and converting it to column vector is denoted as  $\text{diag}(\cdot)$ .

In order to infer the new style direction vector  $\tilde{\mathbf{v}}$  at new goal input  $\tilde{g}$ , use previously computed vector  $\bar{\psi}$ , then  $\tilde{\mathbf{v}} = \bar{\psi}(\Psi^T \Psi)^\dagger \Psi^T \mathbf{R}$ .

This algorithm can be regarded as bilinear estimation in a semi-supervised style-content learning framework<sup>306</sup>, where linear estimation is substituted by nonlinear RBF regression.



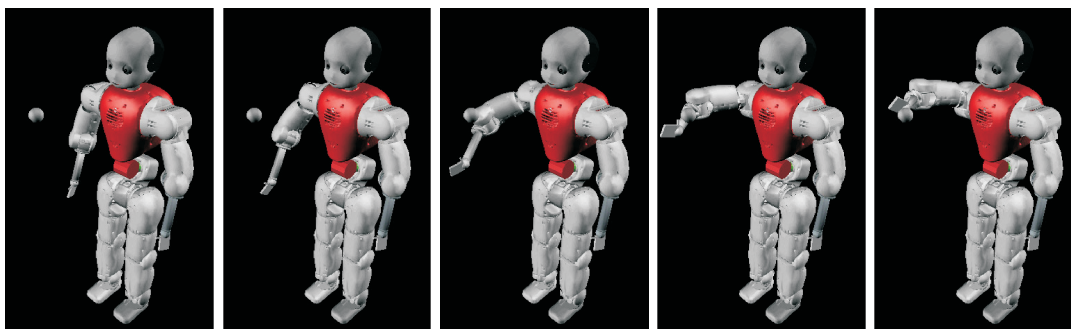


**Figure 3.26:** Sequential snapshots of arm reaching movement towards a stable target by CoMan.

The results of estimation of style directions and style values for our testing examples are depicted in Fig. 3.25, where the thick blue line is corresponding to the style parameter values equal to the maximal value.

### Evaluation of semi-supervisory learned mappings

In order to test the style-preserving regression I used the reaching dataset for learning. It is the second dataset of right arm reaching movements described in Section 3.3.1. The content input is the reaching goal position and hand orientation angle at the moment of reaching. The content input together with the inferred most probable style are mapped to the parameters of motion (weights of source signals) by means of learned LWLR. In case of the moving targets I track and low-pass filter the target positions online during reaching, and map their filtered positions to the weights of the generated source signals, thus modifying the motion during flight. The illustration of the single reaching movements with specified skew-closed hand orientation (3rd hand-frame vector is at  $45^\circ$  with respect to the horizontal plane) is demonstrated in Fig. 3.26. The additional video [movie<sup>3</sup>] demonstrates 4 different reaching movements: for 2 different final hand postures while reaching a stable and a jumping target.

The comparison of arm reaching movements generated with and without style-inference technique are presented in Fig. 3.27 and the related videos are [movie<sup>4</sup>] for panel **a**) and [movie<sup>5</sup>] for panel **b**). The inference of motion parameters given the goal positions is done with and without the style-preserving technique. In the last case, the resulting motion is characterized by a larger reaching error.

<sup>3</sup><https://goo.gl/fBn2mK> (tiny.cc/yw8l5y)

<sup>4</sup><https://goo.gl/jUAri9> (tiny.cc/ny8l5y)

<sup>5</sup><https://goo.gl/5ZzzjL> (tiny.cc/5z8l5y)

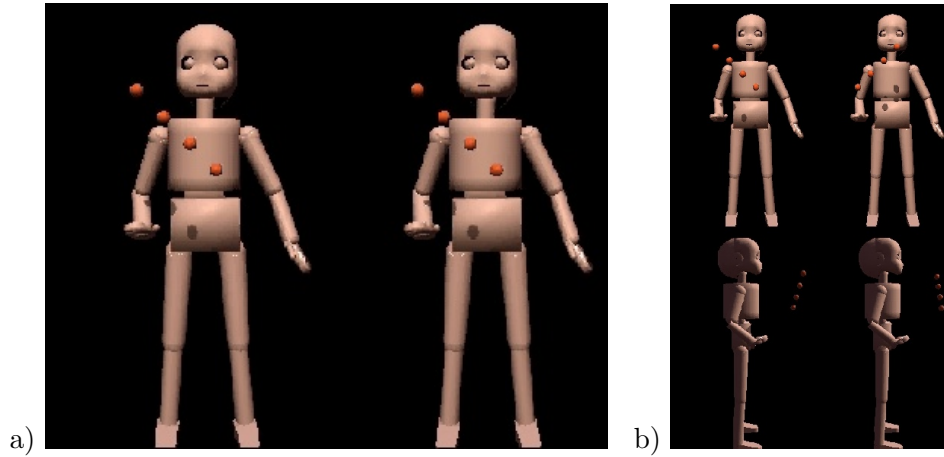


**Figure 3.27:** The figure demonstrates the distributions of the interpolated positions of the reaching goals (orange balls). The simplified avatar of iCub is animated by the Horde3D graphics engine<sup>278</sup>. Panel **a** Left avatar: produced by style-preserving morphing (target error: 1-2 cm). Right avatar: general LWLR with respect to the goals, not style-preserving (target error: 7-8 cm). Panel **b** shows front and side views of reaching, left column - style-preserving; right column - not style-preserving. See [video](#) linked in text.

The style-preserving regression was used in modelling the arm reaching while walking on treadmill (the dataset is described in Section 3.3.1). Here, the source signals are subdivided into two synergies: 1st subset of 3 periodic anechoic sources controlling the whole body along the normal walking gate cycle (the source delays are fixed across walking grasping trials, but are different for different joint angles and the source weights vary for every trial); and the 2nd subset of 3 periodic sources plus a bump-like source (the delays and the weights vary across joints and across trials). The second subset of source signals contributes most to the upper body degrees of freedom at the time interval when the arm reach is performed. The delays of the bump-like source are aligned in time with the target reaching movement. The goal-style separation framework is tested for the synthesis of adaptive walking and grasping of stationary and moving targets. For the latter, weights and delays are adaptively changed along with time, accounting for the predicted target trajectory and grasping moment. The regression inputs are the time of goal reaching with respect to gait phase and the default position of the target in the chest coordinate frame (with respect to the upper body). The default target position was the predicted position computed using the simplified version of the *sliding control* framework<sup>15,293</sup> and low-pass filtered.

Fig. 3.28 displays snapshots of the synthesized motions on a kinematic model of the human body. In the figure, 4 different stable target positions are reached all at the same phase of the gait cycle. In Fig. 3.29 2 different target positions are reached at 2 different phases of the gait cycle. The figure presents two successive moments at 0.8 sec and at

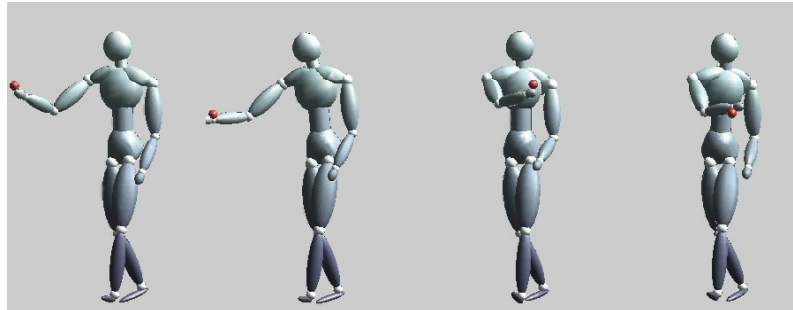


**Figure 3.28:** The synthesized arm reaching during walking. 4 different stable target positions are reached all at the same phase of the gait cycle.

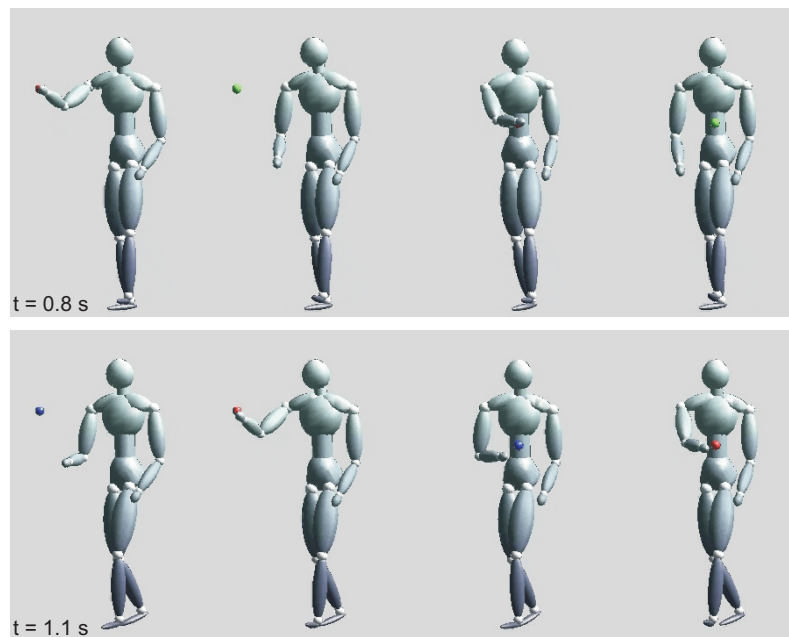


**Figure 3.29:** The synthesized arm reaching during walking. 2 different target positions are reached all at 2 different phases of the gait cycle. Before reaching the target balls are green, for a short period after reaching the target balls are red, and they turn blue after that period. See video linked in text.

1.1 sec (0.0 sec is the start of the gait cycle). The corresponding video can be found at [movie<sup>6</sup>]. The synthesized online-reactive arm reaching during walking for the moving targets is demonstrated in the videos [movie<sup>7</sup>] and [movie<sup>8</sup>].

## 3.5 Navigation

For the modelling of ground walking in computer graphics applications I use the simplified algorithms of computing the propagation and rotation velocities of the avatars from the resulting synthesized joint angle trajectories. These trajectories also contain three axis angles of the root node of the kinematic chain of our avatar model, which is the pelvis frame. In reconstruction of pelvis frame orientation we align its heading direction with the first global horizontal coordinate axis, which nullifies the pelvis pan angle, (but does not affect its pitch and roll). The instantaneous pan angle velocity of the pelvis is computed later from the instantaneous rotational velocity of the support foot relative to the pelvis coordinate frame (projected onto the global vertical coordinate axis). This computation is to be done similar to the inference of the pelvis propagation velocity after deciding which is the supporting foot. So, at every time instance, after the reconstruction of the full body posture of the avatar in the global coordinate frame, the algorithm is identifying which one is the support leg. The simplest approach is to identify which toe base or hill (left or right) is at the lowest position in global coordinate frame. The lowest one defines the supporting foot, but there are also more sophisticated algorithms proposed by<sup>105,160</sup>. The posture reconstruction errors may heavily affect the decision on the lowest feet elements. Within a certain error-defined threshold of the height differences of lowest feet elements it is not possible to identify the supporting foot. The relative vertical positions of the ankles also do not provide enough information, since in many dances and walks the phase when the supporting foot is rising on its toes is very prominent. In such moments the vertical positions of the support leg ankle joint and hill are higher than those of the swinging leg. For normal walking forward, the horizontal velocity of the ankle joint is directed forward in respect to the pelvis heading direction for the swinging leg, and this velocity is directed backward for the support leg. This information helps to identify the supporting foot for some simple scenarios. For this purpose, we compute the horizontal velocities of the ankle joints and feet elements (hills and toe bases) in the coordinate frame of the pelvis. The decision of the supporting foot is then based on the relative height of the lowest feet element and based on the horizontal velocity of both ankle joints with respect to the pelvis

---

<sup>6</sup><https://goo.gl/K2H3eS> (tiny.cc/h18l5y)

<sup>7</sup><https://goo.gl/sLfw92> (tiny.cc/818l5y)

<sup>8</sup><https://goo.gl/F8aTAV> (tiny.cc/k28l5y)

heading direction in the global coordinate frame. When the supporting foot is identified, the rotational velocity (pan angle velocity with respect to the vertical axis of the global coordinates) and the horizontal propagation velocity of its lowest element with respect to the pelvis frame are taken as new pan angle rotational velocity and propagation velocity for the pelvis, (assuming that this supporting foot element is stable on the ground). For more complicated scenarios of dances with sharp turns, employing stepping forward and backward (and when the ankle joint relative motion is not informative any more), we also employed a method of pre-computing the two possible pelvis propagation and pan angle rotation velocities, supposing each of two feet being possibly supporting, and then using the information about instantaneous pelvis accelerations to decide, when the supporting foot switching is acceptable and results in the least jerk and acceleration of the pelvis.

Using the morphing of the model parameters online (eq. 3.21) one may produce different walking gait styles, including gradual changes of the walking direction of the avatars to the left or right. We use this online control of the walking direction for the control of navigation for the purposes of goal directed walking, avoiding stable and moving obstacles. For this purpose our trajectory generation algorithm is combined with a simplified version of an online-reactive navigation model, (similar to those, that have been applied successfully in robotics before<sup>277,334</sup>). We extended this model by inclusion of *predicted collisions* in the navigation dynamics<sup>235</sup>, and a similar approach was employed also by<sup>234</sup>. The navigation dynamics was given by a differential equation for the heading direction  $\varphi_i$  of the characters. The turning rate of the avatars was controlled by morphing between straight and curved walking steps. The morphing weights were dependent on the temporal change of heading direction  $\dot{\varphi}_i$ . The navigation dynamics specifies this change by a differential equation that integrates three different components (where  $\mathbf{p}_i$  denotes the position of character  $i$ ):

$$\begin{aligned} \frac{d\varphi_i}{dt} = & \underbrace{h^{\text{goal}}(\varphi_i, \mathbf{p}_i, \mathbf{p}_i^{\text{goal}})}_{\text{goal-finding}} + \underbrace{\sum_j h^{\text{avoid}}(\varphi_i, \mathbf{p}_i, \mathbf{p}_j)}_{\text{instantaneous obstacle avoidance}} \\ & + \underbrace{\sum_j h^{\text{pcoll}}(\varphi_i, \varphi_j, \mathbf{p}_i, \mathbf{p}_j)}_{\text{predictive obstacle avoidance}} \end{aligned} \quad (3.24)$$

The first term determines a goal-finding term, where  $\varphi_i^{\text{goal}}$  defines the goal direction angle relative to character  $i$ :

$$h^{\text{goal}}(\varphi_i, \mathbf{p}_i, \mathbf{p}_i^{\text{goal}}) = \sin(\varphi_i^{\text{goal}} - \varphi_i) \quad (3.25)$$

This term introduces a force that steers the avatars towards the goal (cf. Fig. 3.30a).

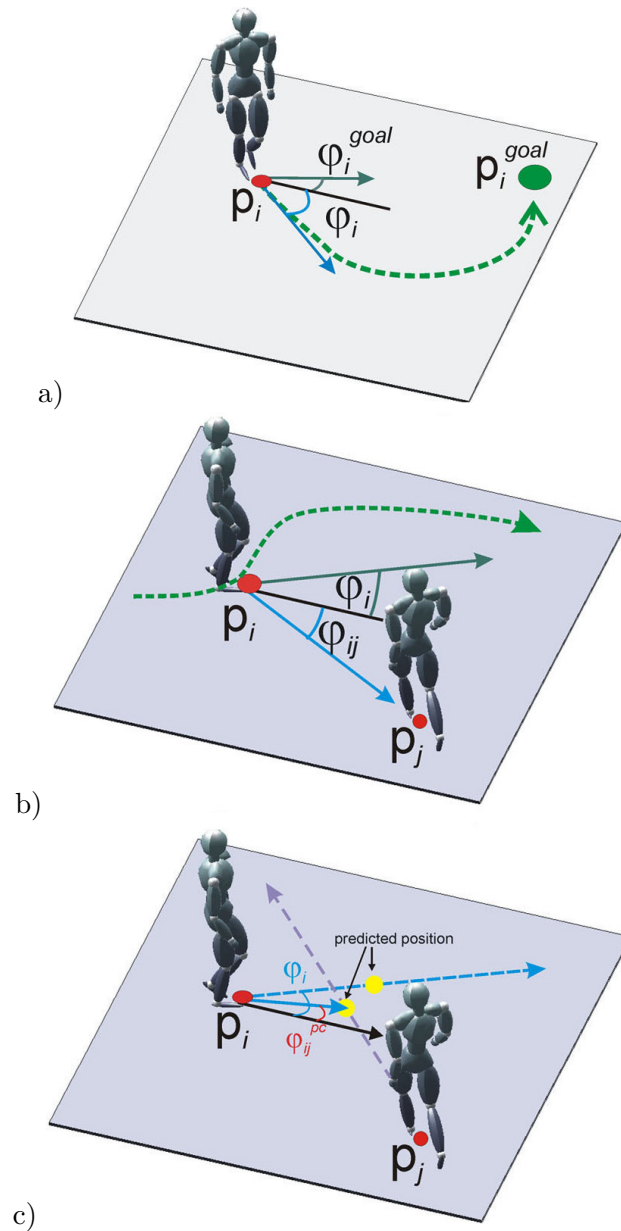


**Figure 3.30:** Navigation dynamics depending on: a) Goal-finding term, b) instantaneous obstacle-avoidance term, and c) predictive obstacle-avoidance term. The figure is adopted from<sup>103</sup>.

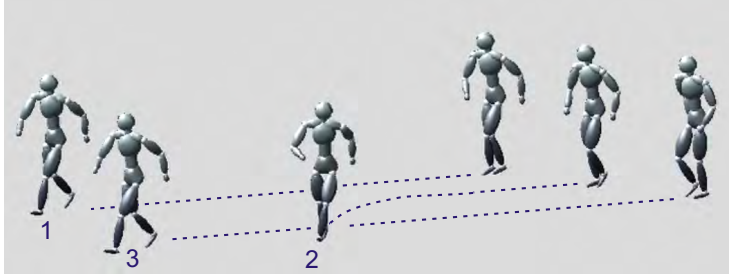


**Figure 3.31:** An exemplary video showing the comparison of a synchronization behavior generated by my method with a standard approach such as PCA. The figure is adopted from<sup>103</sup>. See text for more details.

The second term implements obstacle avoidance, where obstacles can also be defined by moving objects like other avatars (Fig. 3.30b). This term is given by the expression:

$$h^{\text{avoid}}(\varphi_i, \mathbf{p}_i, \mathbf{p}_j) = \sin(\varphi_i - \varphi_{ij}) \cdot \exp\left(-\frac{(\varphi_{ij} - \varphi_i)^2}{2\sigma_\varphi^2}\right) \cdot \exp\left(-\frac{d_{ij}^2}{2\sigma_d^2}\right) \quad (3.26)$$

More realistic collision avoidance is accomplished by inclusion of a third term in the navigation dynamics that is dependent on the predicted future positions of the avatars (Fig. 3.30c). This helps to prevent collisions by steering the characters away from each other already at an early stage, when a collision is likely to occur in the future. The prediction assumes straight trajectories of the avatars and computes the closest point between their predicted trajectories. This third term has the form:

$$h^{\text{pcoll}}(\varphi_i, \varphi_j, \mathbf{p}_i, \mathbf{p}_j) = \sin(\varphi_i - \varphi_{ij}^{\text{pc}}) \cdot \exp\left(-\frac{(\varphi_{ij}^{\text{pc}} - \varphi_i)^2}{2\sigma_\varphi^2}\right) \cdot \exp\left(-\frac{(d_{ij}^{\text{pc}})^2}{2\sigma_d^2}\right) \quad (3.27)$$

Where  $\varphi_{ij}^{\text{pc}}$  signifies the direction of the predicted collision point (Fig. 3.30c). See<sup>103,235</sup> for more details.

## 3.6 Computer Graphics Applications

In the following scenario I compare the synchronized propagation of a group of avatars animated using my architecture generating anechoic source signals with the same architecture using more canonical dynamic systems generating PCA components (cf. Fig. 3.31

and demo [[movie](#)<sup>9</sup>]).

Avatar 3 acts as a 'leader'. It is driven by three coupled oscillators without additional external couplings. The other two avatars are coupled to this leader and start with equal initial phases that are different from the phase of the leader. The movement of one character (avatar 1) was generated applying our novel method, using an anechoic mixture model with three sources. The movement of the second character (avatar 2) was generated with a PCA model with 7 components in order to obtain the same approximation quality. This avatar was driven by 7 coupled Van der Pol oscillators, where we tried to optimize the coupling for maximum naturalness of the obtained animation. The detailed comparison shows that the avatar whose motion was generated by the novel architecture (oscillator dynamics with 6 degrees of freedom) shows a natural-looking transition from its initial state to the equilibrium state that is synchronized with the leader. The movement of the avatar whose movement was generated using PCA (oscillator dynamics with 14 degrees of freedom) shows artifacts. These artifacts are even increased if translational body motion is added by enforcing the kinematic foot-contact constraints on the ground, resulting in a turning motion of the avatar (see Fig. 3.31 and demo [[movie](#)<sup>10</sup>]). If the internal coupling strength within the avatars is increased the synchronization between multiple avatars slows down and an unnatural reduction of step size arises. If the number of components in the PCA model is increased to 12, similar problems remain also for stronger coupling forces (cf. demo [[movie](#)<sup>11</sup>]). The proposed novel trajectory model thus produces more natural transitions between different coordination states. Present work focuses on a more systematic quantitative comparison between different methods.

#### **Online style morphing and integration of periodic and non-periodic synergies**

The algorithm for online style morphing (Section 3.4) was tested by applying it to a complex sequence of locomotion patterns, which is a subset of steps from a folk dance. The movements were generated by interpolation between five prototypical gaits in our data set: straight walking neutral and happy, rotation steps of backward and forward walks, walking with stooped posture and turning on the spot. Even though these types of locomotion were quite different we were able to approximate them with only three different source terms. Applying the proposed technique for the interpolation between weights, posture vectors, and time delays we were able to create realistic transitions between these different patterns, resulting in a complex sequence of steps that could be part of a dancing scenario

---

<sup>9</sup><https://goo.gl/4eC9cY> (tiny.cc/p38l5y)

<sup>10</sup><https://goo.gl/aTkPnF> (tiny.cc/248l5y)

<sup>11</sup><https://goo.gl/j8RsDa> (tiny.cc/p68l5y)





**Figure 3.32:** Dancing figure from a folk dance. The sequence was generated online by blending and recombination of the learned synergies with dynamically changing morphing weights. An external trigger signal initiates the raising and lowering of the arms of the avatars. See text for further details.

(demo [[movie](#)<sup>12</sup>]).

We tested that our method correctly identifies the spatial localization of periodic and non-periodic motion components (synergies) in the training data. The mixing weights  $w_{ij}$  for the fourth non-periodic source are significantly different from zero only for the angles of the shoulder and elbow joint, reflecting the fact that in our data set the non-periodic movements were mainly executed with the arms. The separation of different spatially localized movement components makes it possible to modify the movement styles of different synergies separately. This is particularly true for periodic and non-periodic primitives, and novel movement patterns can be generated by combining such primitives in ways that were not present in the training data. A simple example can be downloaded as [[movie](#)<sup>13</sup>]. In this case, an arm movement is superposed with different relative timings on the periodic movements of the feet of the two avatars. The sequence is generated using the blending method described in Section 3.4 by recombining the learned synergies with dynamically changing morphing weights and an external trigger signal that initiates the raising and lowering of the arms of the avatars. The whole sequence can be coupled easily to an external rhythm that represents, for example, the beat of the music.

The same method can be applied for more complex scenarios, like dancing of two couples. As illustrated in Fig. 3.32 and demonstration [[movie](#)<sup>14</sup>], one of the two couples forms a bridge with the arms while locomoting forwards, while the second couple walks through this bridge one-by-one, in a crouched posture. Then the partners turn around and change roles. The whole scenario was simulated online, modulating the dynamics by a few binary control signals that define the action mode of each avatar (forming bridge, crouching, or turning). In this case, periodic and non-periodic movement primitives were

<sup>12</sup><https://goo.gl/xN98MG> (tiny.cc/s78l5y)

<sup>13</sup><https://goo.gl/v6Grzs> (tiny.cc/m88l5y)

<sup>14</sup><https://goo.gl/wkmWQ8> (tiny.cc/ba9l5y)

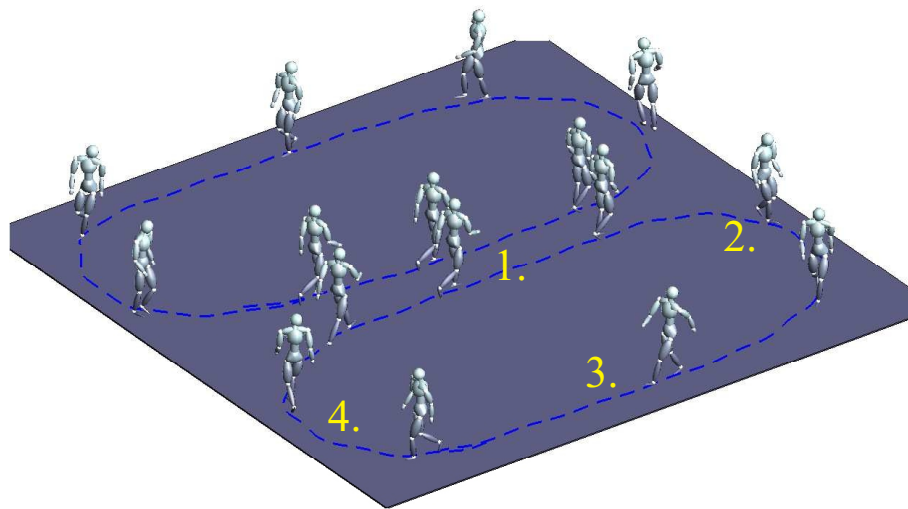


**Figure 3.33:** Simulation of a 'folk dance'. Behavior is self-organized by combining the different elements described in this chapter. Characters act fully autonomously and synchronize with the music in the central corridor. See text for details. The figure is adopted from<sup>210</sup>.

coupled in a way that permits an initiation of the the arm movement at any time during the step cycle (e.g. dependent on whether the partner has already completed his turning step).

### Self-organization of a rhythmic crowd dance

To further explore the capabilities of the proposed framework we tried to self-organize a folk dance scenario, where a larger group of avatars has to walk in synchrony with the music in a formation. After reaching the wall of the ball room the characters have to run back to their initial point and to re-synchronize with the music and the other dancers. A video showing this self-organized animation scenario can be downloaded as [movie<sup>15</sup>].

Fig. 3.33 illustrates the simulated scenario. It is characterized by four spatial sectors:

- 1) At the entrance of the corridor the characters wait for the corresponding partner and start to move in synchrony. This behavior is implemented by the introduction of couplings between the avatars of one couple and between subsequent couples within the corridor and a coupling to an external periodic signal derived from the music.

- 2) At the end of the corridor the two avatars of each couple separate, and the coupling between their oscillators is removed. This results in an asynchronous movement that is controlled by the navigation dynamics (Section 3.5). In addition, within this zone the

---

<sup>15</sup><https://goo.gl/qc5gzY> (tiny.cc/ua9l5y)

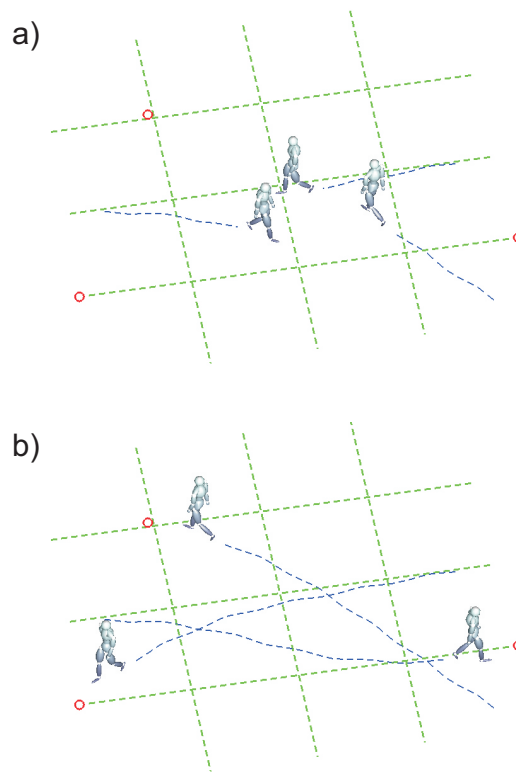


**Figure 3.34:** Avoidance behavior and change of emotional style. a) Avatars starting from different positions with a sad emotion are heading towards their goals (red circles). b) At the meeting point the emotional style changes to happy. In addition, the characters avoid each other. The figure is adopted from<sup>236</sup>.

emotional walking style of the characters changes from happy to neutral. The curved walking paths were generated by defining appropriate intermediate goal points.

3) Along the straight paths outside the corridor the avatars accelerate to catch up with their partner at the beginning of the corridor in time, simulated by a temporary increase of the eigenfrequency of the corresponding oscillators.

4) In the last zone the characters decelerate, modeled by a decrease of the eigenfrequency of the oscillators. A difficult problem is the re-synchronization with the correct foot at the entrance of the corridor. This is accomplished by slightly adjusting the oscillator frequencies to ensure re-synchronization with the appropriate leg.

### Examples of pedestrian navigation with obstacle avoidance

In order to test the obstacle avoidance navigation algorithms we tested the following scenarios. For the first one see Fig. 3.34. A group of avatars that meet in the center of the scene changes their affect upon contact with the others. This behaviour was implemented

by making the affect of each avatar dependent on the distance from the others. In addition, the avatars avoid each other, due to the navigation dynamics described in Section 3.5. In this simulation, navigation and changes of emotional styles were combined, based on only three prototypical gaits: neutral walking with rotation right or left and emotional straight walking. The **demos**<sup>16</sup> show examples of navigation with emotional changes from neutral to happy, neutral to sad, and sad to happy.

In order to produce the morphs between straight emotional gaits and neutral curved walking (Left and Right), we first created an intermediate balanced mixture by interpolating the mixing weights according to the relationship:

$$w_{ij} = \frac{3}{4}w_{ij}^{emotional} + \frac{1}{8}((1 + \beta_{LR})w_{ij}^{Left} + (1 - \beta_{LR})w_{ij}^{Right}) \quad (3.28)$$

Where parameter  $\beta_{LR}$ , with  $0 < \beta_{LR} < 1$ , was adjusted for different emotional styles in order to balance left-right declinations from the straight line. Corresponding with Section 3.4, morphing was done in a piecewise linear manner dependent on the sign of the change of the heading direction.

The second scenario based on a similar implementation is shown in Fig. 3.35. Here two groups of avatars cross each other, avoiding collision. When they meet each other their emotions switch to another affect. The simulation shows that the proposed framework integrates style morphing and autonomous navigation of characters. Examples are demonstrated in **demos**<sup>17</sup>, including transition between neutral and emotional gaits and different emotional gaits.

The second scenario [**demo**<sup>18</sup>] is illustrated in Fig. 3.36. A group of avatars that meets in the center of the scene changes their affect upon contact with the others. This behaviour was implemented by making the affect of each avatar dependent on the distance from the others. In addition, the avatars avoid each other and avoid stationary pillars, due to the navigation dynamics described in Section 3.5. In this simulation, navigation and changes of emotional styles were combined, based on only three prototypical gaits: neutral walking with rotation right or left, and emotional walking. In order to produce the emotional gait for blending with left and right neutral paces, we first created an intermediate balanced mixture by interpolating the mixing weights. Corresponding with Section 3.4, gait morphing was based on a piece-wise linear interpolation dependent on the sign of the change of the heading direction  $d\phi/dt$ .

---

<sup>16</sup><https://goo.gl/m5UqfB> (tiny.cc/6d9l5y)  
<https://goo.gl/3q8whT> (tiny.cc/0g9l5y)

<sup>17</sup><https://goo.gl/qJRw4R> (tiny.cc/4h9l5y)  
<https://goo.gl/QTbXrw> (tiny.cc/ik9l5y)

<sup>18</sup><https://goo.gl/6FcRRq> (tiny.cc/gl9l5y)

<https://goo.gl/e7QQnE> (tiny.cc/2f9l5y)

<https://goo.gl/xzThvS> (tiny.cc/2i9l5y)

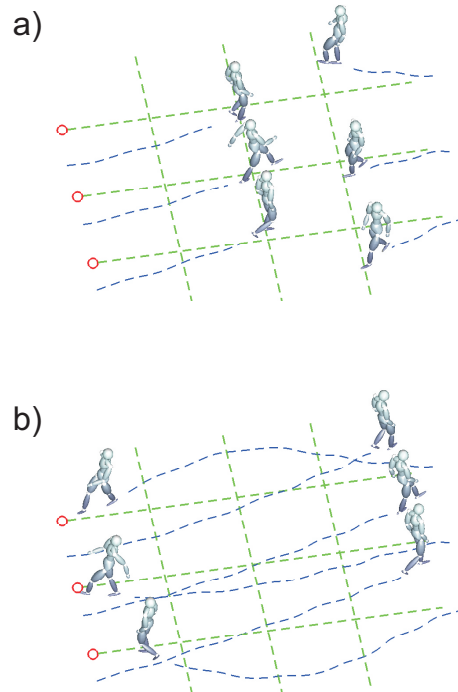


**Figure 3.35:** Avoidance behavior and change of emotional style. Three avatars, starting from the left side, change their emotion from happy to sad while proceeding to their goals. A second group of 3 avatars starting from the right side change their emotions from sad to happy while avoiding the opposing group. The figure is adopted from<sup>236</sup>.

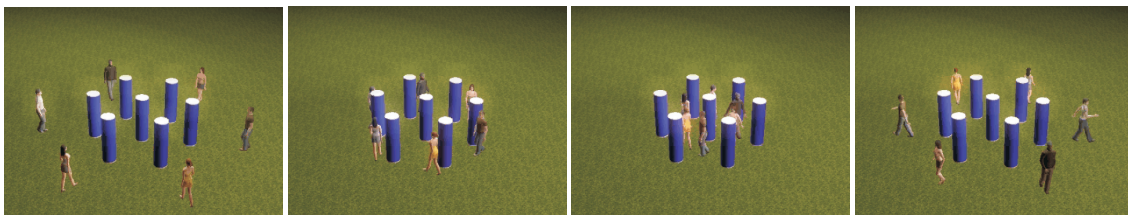


**Figure 3.36:** Reactive online control of locomotion. Agents avoid the obstacles (pillars) and other agents in the scene. Trajectories are generated by morphing between steps with different length, and curvatures of the walking path (left, straight, right), where blending weights are controlled by a navigation dynamics that controls the heading direction dependent on obstacle and goal positions.

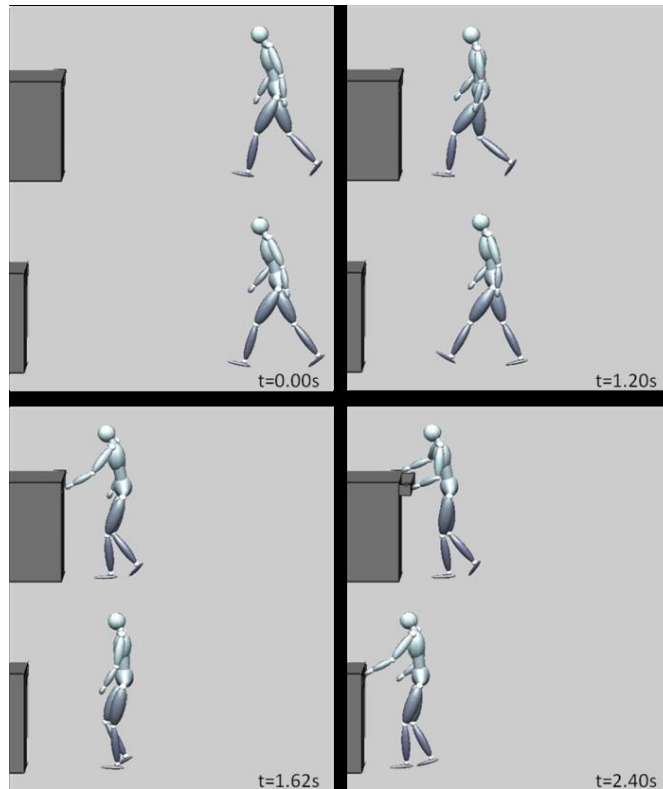


**Figure 3.37:** Two synthesized trajectories, illustrated in parallel for two conditions with different initial distance of the character from the drawer. Both animations look highly natural even though these goal distances were not present in the training data.

### 3.7 Modelling and Online-reactive Simulations of Walking-and-reaching Sequential Behaviors

In this section I present the online animations of multi-step human movements. The planning is predictive and optimizes the 'comfort' during the execution of the final action. The proposed system exploits the concept of movement primitives in order to implement a flexible and highly natural-looking coordination of periodic and non-periodic behaviors of the upper and lower limbs, and to realize smooth transitions between subsequent actions within the sequence. The learning was done on the walking-reaching task dataset (Section 3.3.1). *Stepwise estimation* of spatially localized anechoic primitives is described in the last subsection of Section 3.3.3 and the learning of behavior specific mappings between action parameters and mixing weights is described in detail in Section 3.4.2 above.

Two example sequences of concatenated actions generated by our algorithm, for dis-

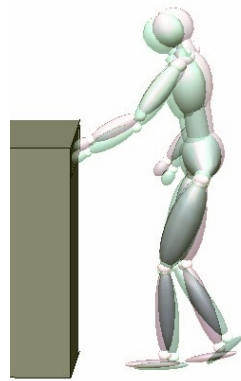


**Figure 3.38:** Postures at the transition between actions 2 and 3 for different lengths of the second action (red: 0.53 m , green: 0.39 m). Even though the distances to the drawer are the same in the last action the postures differ due to the predictive planning of the second action.

tances to the goal object that were not in the training set are shown in Fig. 3.37. An example video can be downloaded from [Demo<sup>19</sup>].

A more systematic evaluation shows that the system can, without introducing additional steps, create natural looking coordinated sequences for goal distances between 2.34 and 2.94 m [Demo<sup>20</sup>]. If the specified goal distance exceeded this interval our system introduced additional gait steps, making the system adaptive for goal distances beyond 3 meters. This is illustrated in [Demo<sup>21</sup>] that presents two examples of generated sequences for goal distances 3.84 and 4.62 m. With 3 actions the largest achievable range of goal distances without artifacts was about 60 cm, while adding another step increases this range to about 78 cm. Adding two or more normal gait steps our method is able to simulate natural-looking actions even for goal distances longer than 5 m. The next [Demo<sup>22</sup>] illustrates the sequence of three actions of first type followed by actions 2 and 3 for the goal distance 5.3 m.

Fig. 3.38 illustrates that, like in humans, the posture at the transition between the second and third actions depends on the previous step. In one case the step lengths for action 2 were 0.53m and 0.39m, while the distance in the last step was identical (0.6m). This illustrates that in fact the posture for the reach is modified in a predictive manner over multiple steps, where the predictive planning modifies the posture at the beginning of the last action even if the distance to the goal object for this action is identical. A planning scheme that is not predictive would predict here the same behaviors for the last ac-

<sup>19</sup><https://goo.gl/QhR9SE> (tiny.cc/fm9l5y)

<sup>20</sup><https://goo.gl/1jM5uG> (tiny.cc/in9l5y)

<sup>21</sup><https://goo.gl/o8xh83> (tiny.cc/2n9l5y)

<sup>22</sup><https://goo.gl/tvjTi2> (tiny.cc/bp9l5y)

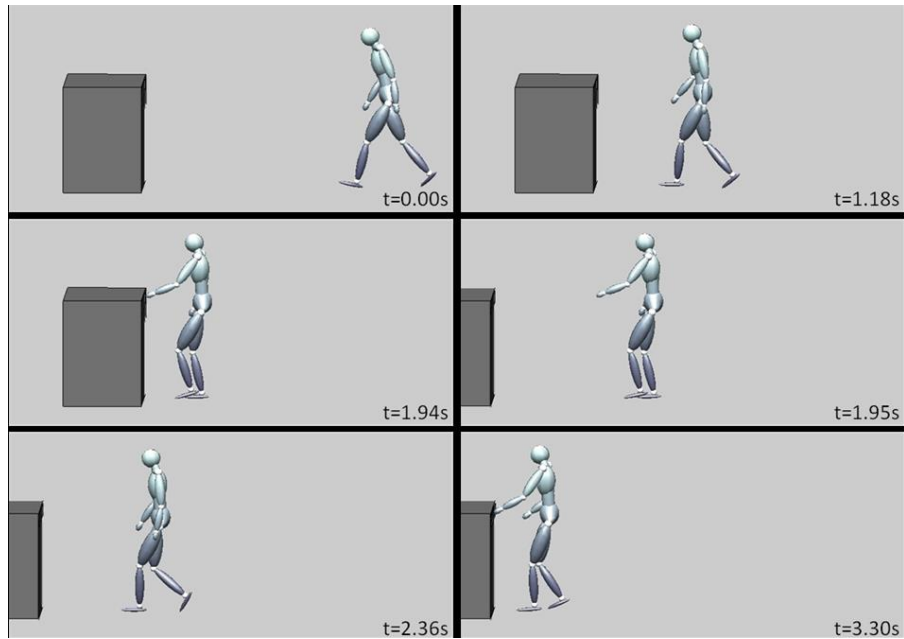


**Figure 3.39:** Online perturbation experiment. The goal (drawer) jumps away during the approach of the character. The online planning algorithm introduces automatically an action of type 2 (short step) to adjust for the large distance to the goal.

tion since the relevant control variable (distance from the object) is identical for both cases.

An even more extreme demonstration of this online adaptivity is shown in movie [Demo<sup>23</sup>]. Here the drawer jumps away during the approach by a large distance so that it can no longer be reached with the originally planned number of steps. (Fig. 3.39). The online planning algorithm adapts to this situation by introducing an additional step so that the behavior is successfully accomplished. Again the behavior has a very natural appearance even though this scenario was not part of the training data set.

### 3.8 Adaptive Synthesis of Feasible Full Body Movements for HRP-2

In previous sections I have presented a kinematic pattern synthesis architecture that provides flexible online planning of coordinated full-body movements, based on learned dynamic movement primitives. This section presents the results of the work done together with LAAS/CNRS, Toulouse, of the implementation of the architecture to control real robot behavior, where the kinematic pattern synthesis is combined with a control architecture that is based on a Walking Pattern Generator exploiting nonlinear Model Predictive

<sup>23</sup><https://goo.gl/EzTpsh> ([tiny.cc/tp9l5y](http://tiny.cc/tp9l5y))



Control. The proposed merged architecture is suitable for online generation of human-like coordinated full-body movements with long planning horizons. It generates dynamically feasible behavior of the robot, ensuring appropriate balance control during walking in presence of fast online replanning.

The central innovation of this work is the integration of the described online-planning algorithm with a control architecture for the HRP-2 humanoid robot, which is based on *Nonlinear Model Predictive Control* (NMPC). This does not only involve the combination of trajectories derived from human data, as described in Section 3.3.2, but it requires specifically the approximation of human data by dynamically feasible trajectories, exploiting the NMPC framework. These feasible trajectories form a novel training set, from which a new set of optimized dynamic primitives was derived.

All other approaches in humanoid robotics have only limited capability for allowing the realization of such human-like long-term predictive motion planning in combination with a guarantee of dynamic balance during walking in combination with other tasks for the robot upper body. Common alternative approaches, such as the optimization of such complex behavior by model-based optimal control approaches [158] are presently computationally too costly to allow the online generation, where even the optimization of short multi-step sequences can take easily hours of computation time with the presently available optimization methods. The functionality and flexibility of the proposed architecture is demonstrated by simulation using the OpenHRP physics simulator and also in trials on the real HRP-2 robot. In addition, the proposed system realizes predictive motor behavior that is compatible with the end-state comfort hypothesis [257,335].

### 3.8.1 Overview of Robot Control Architecture

The control architecture for the HRP-2 robot is shown in Fig. 3.40. It consists of three main building blocks. The online kinematic synthesis algorithm, which was laid out in Section 3.3.4, provides input to the control architecture (shaded box in Fig. 3.40) in terms of two sets of variables: the linear and angular velocity of the pelvis (variables  $\mathbf{v}^{\text{ref}}$  and  $\omega^{\text{ref}}$ ), and the joint angles of the upper body  $\mathbf{q}^{\text{upper body}}$ .

The first building block is a Walking Pattern Generator (WPG) that computes from the variables  $\mathbf{v}^{\text{ref}}$  and  $\omega^{\text{ref}}$ , for one gait cycle, foot placements  $\mathbf{x}_{\text{feet}}$  and trajectories of the Center of Mass (CoM)  $\mathbf{x}_{\text{CoM}}$  and of the Zero Moment Point (ZMP)  $\mathbf{x}_{\text{ZMP}}$  that ensure the dynamic stability of the gait<sup>330</sup>. This computation is based on model predictive control (MPC), and further details about the underlying computations can be found in the next subsection and in<sup>220,221</sup>.

The second block is a Dynamic Filter (DF) that corrects the preplanned foot, CoM, and ZMP trajectories, taking into account the planned whole-body motion, resulting in the

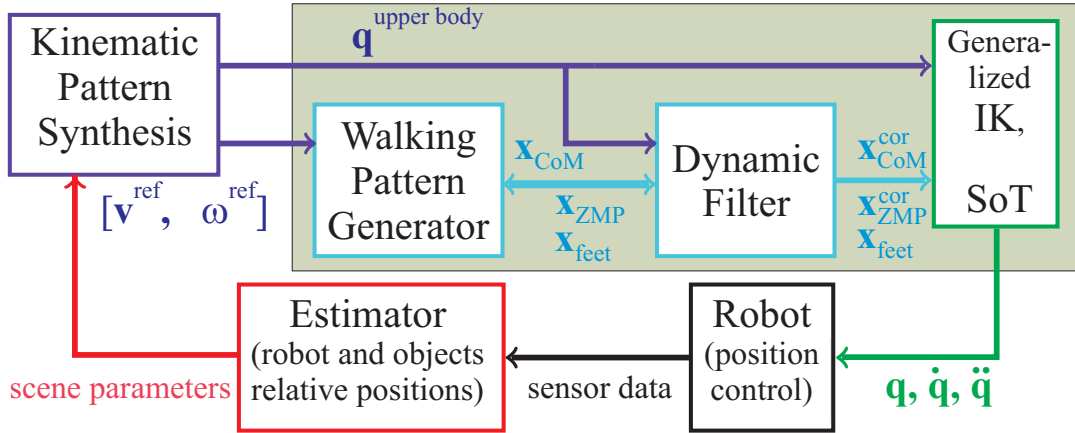


**Figure 3.40:** Control system for the humanoid robot HRP-2. The Walking Pattern Generator computes foot positions and CoM and ZMP trajectories, which are further adjusted by the Dynamic Filter, depending on the planned upper body motion. The resulting trajectories are consistent with the dynamic stability constraints of the robot. The approximation of the planned upper body movement and dynamic stability of walking are guaranteed by a Stack-of-Task approach, where optimal trajectories are computed by sequential quadratic programming. (See text and <sup>215</sup> for details.)

corrected trajectories  $\mathbf{x}_{\text{feet}}^{\text{cor}}$ ,  $\mathbf{x}_{\text{CoM}}^{\text{cor}}$  and  $\mathbf{x}_{\text{ZMP}}^{\text{cor}}$ . The DF operates in closed-loop together with the WPG, and further details about the underlying algorithms are described in <sup>220,221,300</sup>.

The third building block is the generalized Inverse Kinematics (IK) module that implements a 'Stack-of-Task' approach. This module combines the corrected CoM and ZMP trajectories, and the upper-body motion (specified by joint angles). This module outputs joint angle trajectories for the legs and the upper-body that respect the dynamic stability constraints of the robot, at the same time approximating, as far as possible, the planned behavior of the upper body. For this purpose the task of stabilizing the locomotion is given the highest priority, and the approximation of the planned trajectories is realized in the null-space of the control signals for this prioritized task. The resulting optimization problem is solved by a sequential quadratic programming approach (QP-solver).

The resulting optimal trajectories  $\mathbf{q}$  are dynamically feasible and can be realized by the low-level controller of the HRP-2 robot. During motion execution, the real-world environmental and task parameters and the current state of the robot are fed back to the kinematic planner, closing the control loop for an adaptive interaction between online planning and MPC in the real world.

### 3.8.2 WPG based on Optimal Predictive Control

The Walking Pattern Generator (WPG) is based on Model Predictive Control (MPC). The first WPG of this class was proposed by <sup>143</sup>. This method computed the reference nominal Zero Moment Point (ZMP) trajectory from the desired placements of feet during

the gait cycle. A simplified linear inverted pendulum dynamics ('Cart-Table Model') was used to link the Center of Mass (CoM) and the ZMP. Preview control was exploited for computing the CoM trajectory from the desired ZMP. Due to the model simplifications, the real ZMP trajectory deviates from the desired one. This deviation is the result of neglecting the inertial and Coriolis forces generated by the leg swing and by fast movements of the upper-body. In order to alleviate this problem, the authors ran the full body inverse dynamics in order to compute a better approximation of the real ZMP. This new ZMP can be computed for the preview horizon in real-time. The resulting ZMP error was transformed into a resulting CoM error via Preview Control, following the approach proposed by<sup>143</sup>. This result can then be exploited to correct the CoM trajectory. The described two steps of preview control combined with an evaluation of the inverse dynamics can be repeated iteratively, successively reducing the ZMP error. This approach for the dynamic correction can be interpreted as a kind of Newton-Raphson iteration<sup>300</sup>, and was referred to as Dynamic Filter in the previous Section 3.8.1.

Another improvement of MPC-based WPG is the integration of the computation of the optimal ZMP trajectory within the constrained quadratic optimization framework that computes the optimal CoM trajectory<sup>336</sup>. This approach requires only the specification of the preplanned foot positions as input, returning the optimal trajectories for the ZMP and the CoM. Our approach for nonlinear MPC relies in addition on another improvement of the same framework made by<sup>121</sup>, which is the further extension of the approach by<sup>336</sup>. This reformulation of the optimization framework allows to exploit positional and angular velocities of the CoM as reference trajectories (for a time horizon of the next two steps), returning the foot placements and the optimal ZMP trajectories as result of the nonlinear predictive control problem. This framework (which is described in detail in<sup>220,221</sup>) was exploited in our system.

### **3.8.3 Approximation of Dynamically Feasible Training Trajectories by Robot Movements**

In order to link the described approach for the online synthesis of movements with the NMPC approach described above, we transform a set of human-compatible movement trajectories that were generated by interpolation from the original human data into trajectories that result in dynamically feasible behavior of the robot. For this purpose, we approximated the human-like trajectories by the ones generated by physics-based simulations, exploiting the NMPC framework discussed in Section 3.8.1. This training of our learning-based approach using dynamically feasible training data is one of the key concepts of our approach. The details of retargeting and transformation in dynamically feasible

trajectories are following below.

In order to validate our new architecture, we first tested the system by the realization of open-loop control, simulating a physical model of the HRP-2 robot (using the OpenHRP simulator). In a first set of simulations the robot started from a parking position and made a transition to a normal step. At the end of this step the pelvis velocities (propagation and angular) were determined and used as initial conditions for the generation of a three-action sequence. At the end of the last action, a step back to the final parking position was generated by spline interpolation of the pelvis angular and positional coordinates between the final state of the last step of the action sequence and the final position, introducing two additional steps on the spot. We also generated examples of four-action sequences. For this purpose, the retargeted trajectories were extended by an additional normal walking gait cycle. In order to augment the training data set for the learning of the mappings between the task parameters and the model parameters, we generated additional artificial kinematic data by scaling of the pelvis forward propagation velocities for all gait cycles uniformly (by the factors 0.8, 0.92, and 1.2), while keeping the upper body trajectories fixed. In this way we generated a total of 30 training examples from the original 10 motion capture trials. Examples of the generated three- and four-action sequences are shown in **movie**<sup>24</sup>.

These trajectories were dynamically feasible for the robot, but still based on movement primitives learned from human data. In order to construct primitives for the control of the robot, 30 trajectories were simulated with the OpenHRP physics simulator of the robot as novel training data. The new optimized movement primitives were learned from this newly produced training data. For this purpose, the trajectories were approximated using 4 sources for the approximation of the first step, and 3 additional ones for the approximation of the residuals of the other steps, because this resulted in the best approximations with a small number of sources (Fig. 3.14).

A systematic validation of the approximation quality, dependent on the number of learned sources, is presented in Fig. 3.41. This figure shows histograms of the reproduction errors of the step sizes of the first two actions and the resulting arm reaching distance for the last action for different choices of the number of source functions. In all cases the spatial errors of the parameters, realized by the full control system, are small, always below 10 mm and often below 5 mm. This shows that in spite of the high complexity of the operations that are necessary to transform the original human motion into a motion sequence that is feasible for the robot, the final control system produces movements that approximate the planned step sizes and reaching distances quite accurately.

---

<sup>24</sup><https://goo.gl/7IZ0P1> (tiny.cc/pq9l5y)

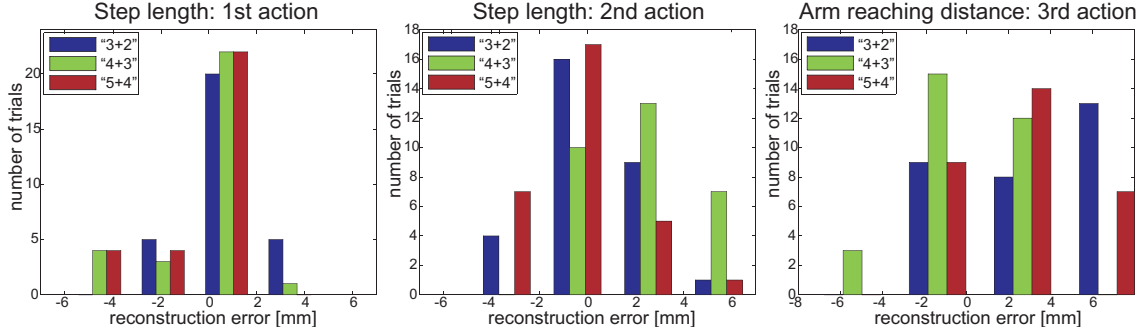


**Figure 3.41:** Reconstruction accuracy of the step-sizes and reaching goal distances for different numbers of sources. The figure shows the histograms of the spatial errors. The first number indicates the number of sources learned from the first step (action 1), and the second number the number of sources used to approximate the residuals of the other actions (2 and 3). The figure is adopted from<sup>215</sup>.

Some of these feasible re-synthesized trajectories were also tested using the real HRP-2 robot (cf. Fig. 3.42). A demonstration of the resulting behaviors for the three-action sequence is shown in **movie**<sup>25</sup>, and a four-action sequence is shown in **movie**<sup>26</sup>.

We also quantified the improvement of the behavior resulting from the inclusion of the Dynamic Filter in comparison with an architecture without this stage. Fig. 3.43 shows the  $x$ -coordinate trajectories of the Zero Moment Point (ZMP) for different model variants: 1) the idealized inverted pendulum model, which provides a reference trajectory for the underlying MPC approach (solid blue line  $\mathbf{x}_{\text{ZMP}}^{\text{reference}}$ ); 2) the architecture without the Dynamic Filter correction (green dashed-dotted line  $\mathbf{x}_{\text{ZMP}}^{\text{unfiltered}}$ ); 3) application of the Dynamic Filter only to the lower body degrees of freedom, assuming the upper body degrees-of-freedom to be frozen (magenta dashed-dotted line  $\mathbf{x}_{\text{ZMP}}^{\text{DF(legs only)}}$ ) and 4) when the Dynamic Filter takes in account the full body motion (orange dashed-dotted line  $\mathbf{x}_{\text{ZMP}}^{\text{DF(full body)}}$ ). The trajectory of a model without Dynamic Filter correction (green) deviates significantly from the planned reference trajectory (blue). The inclusion of the Dynamic Filter results in a much better approximation of the reference trajectory (orange color curve). This correcting effect of the Dynamic Filter is significantly reduced when it is only applied to the lower body degrees-of-freedom (magenta curve). This implies that only if the Dynamic Filter is applied to all degrees of freedom the robot motion is close to the planned dynamically feasible motion.

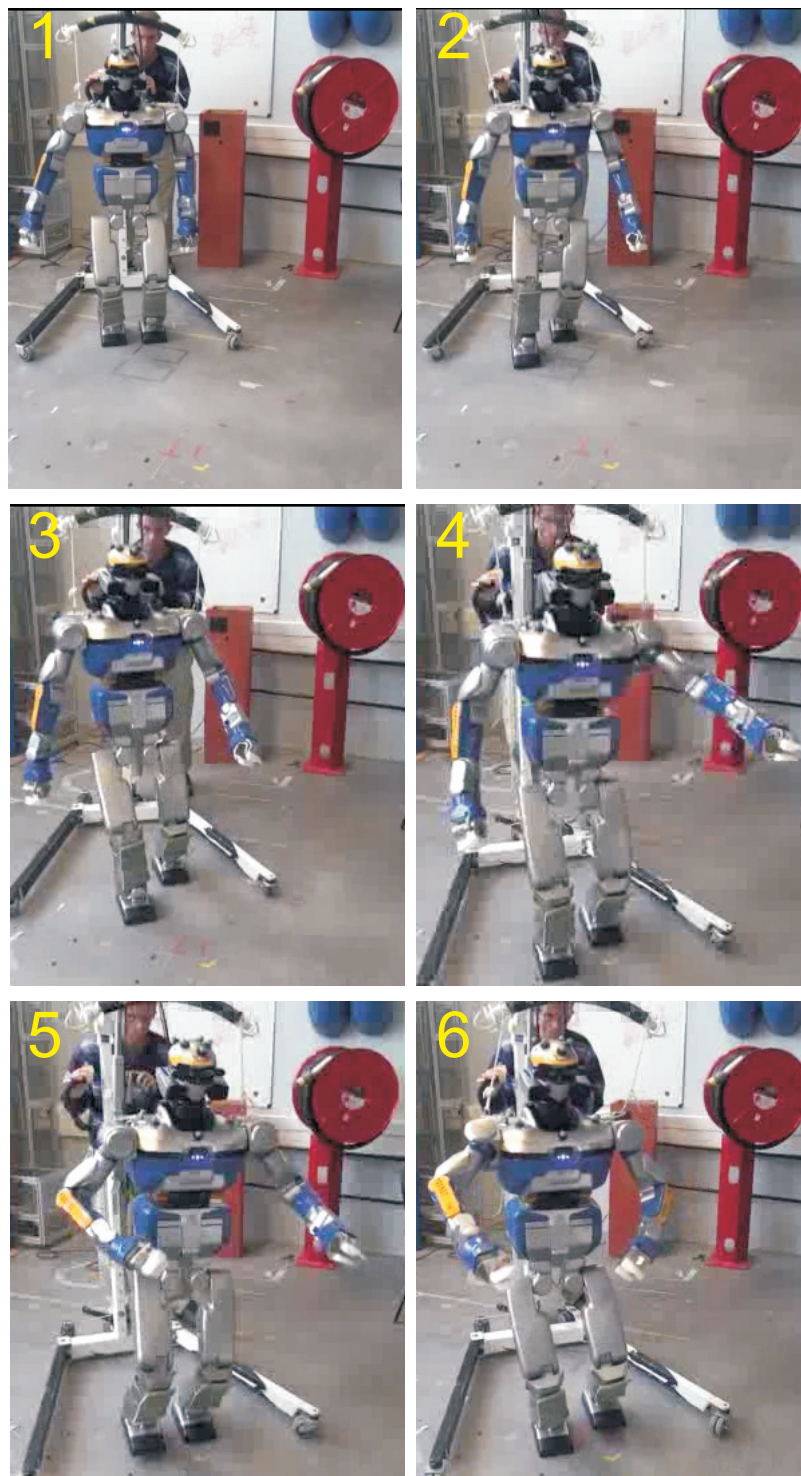


**Figure 3.42:** Real HRP-2 robot performing a 4-action walking-reaching sequence in the laboratory of LAAS/CNRS. The figure is adopted from<sup>215</sup>.

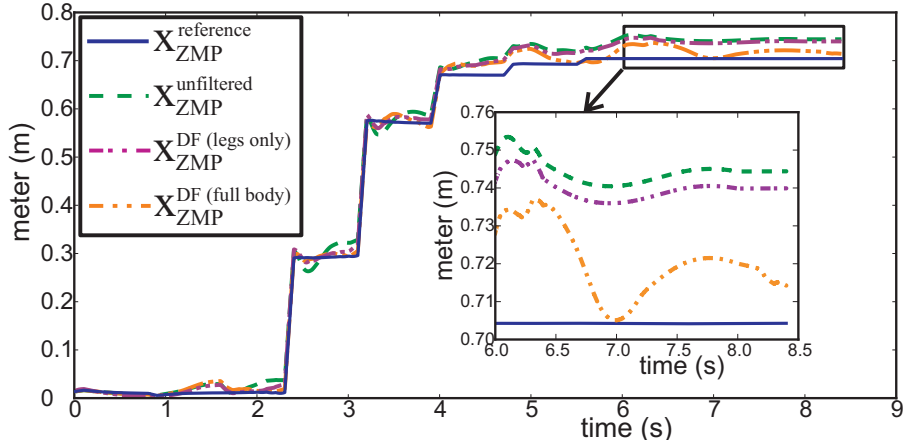


**Figure 3.43:** Trajectories of the Zero Moment Point (ZMP) (in walking direction,  $x$  coordinate) for different architectures. The blue curve  $\mathbf{x}_{\text{ZMP}}^{\text{reference}}$  indicates the reference ZMP trajectory computed from the linear inverted pendulum model. The green curve  $\mathbf{x}_{\text{ZMP}}^{\text{unfiltered}}$  shows the ZMP trajectory without filter correction. The trajectory with filter correction of all degrees-of-freedom is indicated in orange color  $\mathbf{x}_{\text{ZMP}}^{\text{DF (full body)}}$ , and the case where the Dynamic Filter was only applied to the lower-body degrees-of-freedom is indicated by the magenta trajectory  $\mathbf{x}_{\text{ZMP}}^{\text{DF (legs only)}}$ . The figure is adopted from<sup>215</sup>.

### 3.8.4 Further Experiments on the Open-HRP Simulator and the real HRP-2

#### Inference of adaptive behaviors for novel gait distances

In order to test the architecture, with an online generation of new behaviors (step lengths and reaching movements) dependent on the state of the robot, we synthesized the control signals for 30 different 4-action sequences, where a spectrum of step sizes was generated by linear morphing of the source weights. The first normal walking step length spanned 30 values in the range of 50.5 and 56.1cm, and the size of the second step was linearly sampled within the interval between 16.3 and 35.9cm. The reaching distance of the box in the last step varied in the interval of 66.3 to 75.5cm. The distance between the object and the front of the drawer was varied within the interval between 12.4 and 27.3 cm. The generated behaviors for the most extreme step sizes (smallest and largest) are shown in Fig. 3.44. **Movie**<sup>27</sup> shows these action sequences. For all tested intermediate step sizes that were not part of the initial training set a human-like coordinated behavior was generated.

We also tested the feasibility of walking-and-reaching sequences generated in the on-

<sup>25</sup><https://goo.gl/jjAVfT> (tiny.cc/mr9l5y)

<sup>26</sup><https://goo.gl/RqT6Q3> (tiny.cc/7r9l5y)

<sup>27</sup><https://goo.gl/IcwrXb> (tiny.cc/3s9l5y)



**Figure 3.44:** Synthesized behaviors simulated with the OpenHRP simulator for the two most extreme goal distances. The figure is adopted from<sup>215</sup>.



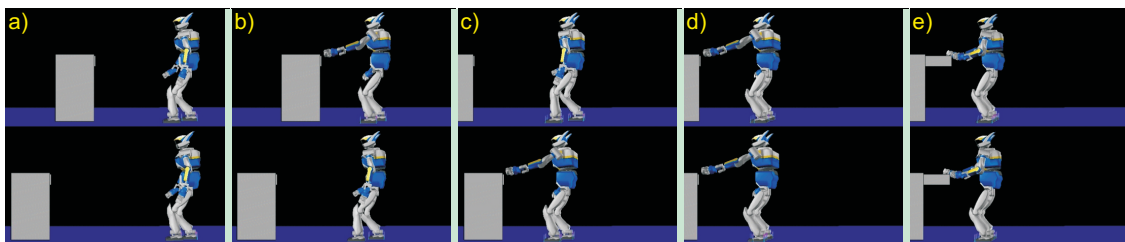


**Figure 3.45:** The snapshot sequences of two scenarios of drawer jumping, simulated in the OpenHRP environment. Two rows represent two different initial positions of the drawer, but the same final position of it. The snapshots are made at equal time intervals. Moment b) is when the drawer in the upper row jumps to its new position. Moment c) is when the drawer in the upper row jumps to its new position. Moment d) is the final reach with the left arm. e) is the reaching of the object inside drawer with the right hand.

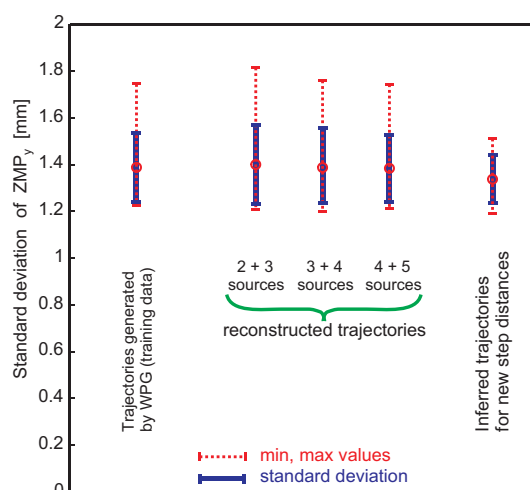


**Figure 3.46:** ZMP variability in the lateral plane (y-direction). See the text for more explanations. The figure is adopted from<sup>215</sup>.

line scenario of drawer jumping. The total kinematic trajectories were produced by the kinematic synthesis architecture based on learned representations of feasible elementary movements. The online-adaptive control was implemented at the kinematic level (Section 3.3.4). The resulting trajectories were sent in real time without closed-loop feedback to the robot control architecture (WPG+DF+SoT modules) controlling the robot in OpenHRP environment. The resulting animation can be found in the **movie**<sup>28</sup> and snapshots of the behavior for two different drawer jumping distances are presented in Fig. 3.45.

A more quantitative assessment of the performance is given in Fig. 3.46, which shows the variability of the ZMP in the lateral plane. The figure compares feasible trajectories,

<sup>28</sup><https://goo.gl/upHLsx> (tiny.cc/yt9l5y)

which are generated by the WPG from original trajectories without interpolation to novel step sizes or goal distances, with the behaviors of the system for novel goal distances that were not part of the training set and that required adaptation of the behavior using the online planning architecture. We compared again the behaviors for the different numbers of sources for the anechoic mixing model (in total between 5 and 9 sources). The analysis is based on 30 newly synthesized four-action sequences for novel goal distances.

The ZMP trajectory in the lateral plane was computed within all stance intervals, and the standard deviation (STD) of the difference between this trajectory and the reference ZMP trajectory was computed. The figure shows error bars with mean and variances as well as the maximum ranges of the variation. The ZMP variability is relatively independent of the number of sources for the reconstruction of trajectories and even for an inference of novel step distances the variability is not significantly higher than for the original trajectories generated with the WPG. This shows that the closed-loop system produces highly stable behaviors in terms of the variation of the ZMP.

#### **Comparison with simple machine learning approach**

One might ask if the proposed complex architecture is really necessary, and if one could not just learn dynamically feasible trajectories generated with the WPG and interpolate between the corresponding full-body kinematic angle trajectories using machine learning techniques. This approach would be based on the hope that the generated interpolations of the control signals also result in dynamically feasible behaviors when the training trajectories were dynamically feasible. We tested our method against such a simpler approach.

For this test we created training data consisting of 30 dynamically feasible walking-reaching trajectories, which were directly generated by the MPC-based WPG. Each of these trajectories results in dynamically stable behavior of the robot. The resulting full-body angle trajectories were again approximated with anechoic mixing models with different numbers of sources (between 5 and 9). Based on this training data 30 new trajectories for the new goal distances were computed, using either the simple machine learning approach discussed above, or with our method of learning upper-body and base trajectories separately.

The behaviors generated with the simple machine learning approach often resulted in falling of the robot, specifically during the last action (box opening and reaching for the object, where both arms are extended). The instability frequently also emerges earlier, already after the robot stops during the reaching step. A demonstration of this behavior is

given in **movie**<sup>29</sup>, which compares the behavior generated by the naïve machine learning approach with the stable behavior obtained with our method. The parameters of the target behaviors are exactly identical for the two simulations.

The distribution of falling events			
Algorithm	slow speed (tr.1-10)	middle speed (tr.11-20)	fast speed (tr.21-30)
"ML 3+2"	0	10	7
"ML 4+3"	1	0	2
"ML 5+4"	0	5	10
Our method	0	0	0

**Table 3.1:** Fraction of trials with falls of the robot within 30 test trials with novel goal distances that were not part of the training set. Simple interpolation using machine learning techniques, approximating the trajectories with different numbers of sources (ML) is compared with our method that integrates online planning with the MPC control system. (For the ML conditions, the first number indicates the number of sources for the approximation of the first action, and the second number the additional sources introduced for the approximation of the other steps).

A quantitative analysis is given in Tab. 3.1, that shows how often the robot fell down out of the 30 novel synthesized behaviors. The simulations are grouped according to the speed of the walks. In addition, we tested interpolations generated with different numbers of source functions for the machine learning approach, and compared this with our method using 4+3 sources. For the low speed behaviors the machine learning approach leads to stable behavior in some cases, and to falling in others, where the success of the method varies in a non-systematic manner with the number of source functions used for the approximation. For the fast speed movements the simple machine learning approach always results in falling in a significant number of cases. Contrary to this result, our method always results in stable behavior without falling.

The superiority of our approach is also confirmed by an additional analysis of the mechanical parameters that determine whether the behaviors can be realized on the real HRP-2 robot. Fig. 3.47.a shows the peak values of the ankle pitch torques for behaviors created directly using the MPC-based WPG, behaviors generated with the naïve machine learning approach (ML) of approximating the full body angle trajectories, and our method. For the naïve machine learning approach almost all torque peak values exceed 30 Nm, which is infeasible for the robot (red shaded region in Fig. 3.47.a). This is especially true if this approach is used for the learning-based inference of new trajectories. Contrasting with this result, the torques for behaviors generated directly with the WPG and the ones generated with our method are always in the feasible range. This is true both for the off-line

<sup>29</sup><https://goo.gl/6hbX6g> (tiny.cc/gu9l5y)

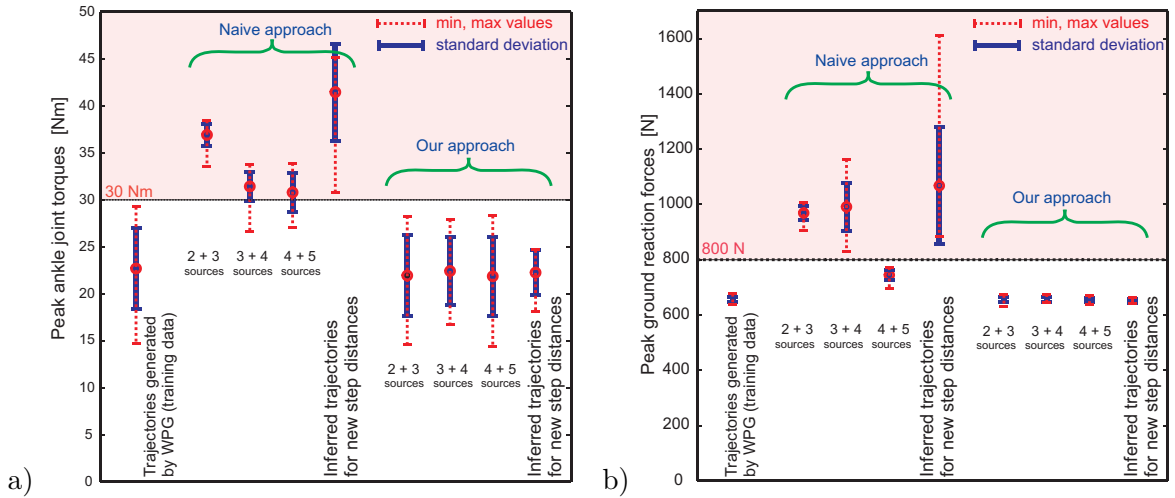


**Figure 3.47:** a) Peak ankle torques and b) peak ground reaction forces obtained for testing trials with different methods: WPG: trajectories generated with the WPG; naïve ML: interpolation of feasible control signals using machine learning methods; and with our method. We compare also resynthesis of training behaviors, using different numbers of sources for the approximation of the trajectories, and the synthesis of new trajectories for new target distances. (Blue error bars indicate mean and standard deviation. Red lines indicate the ranges between minimum and maximum value). The figure is adopted from<sup>215</sup>.

reconstruction and for the learning-based inference using our method, and independent of the number of source functions.

A similar result emerges for the analysis of the ground reaction forces (maximal normal force of the feet during the 4-action sequence). The maximum admissible force for the real HRP-2 is 800 N. Fig. 3.47.b shows that for the naïve ML approach in many cases the ground reaction force is larger than this limit, except for the reconstruction with 9 sources. Especially for the synthesis of new inferred behaviors, the peak ground reaction forces are always infeasible. This contrasts with the results obtained with our method. Here in all cases, for the off-line reconstruction and for the learning-based inference, the ground reaction forces are always in the feasible range and quite similar to the peak values that are obtained when the behavior is directly computed by the WPG using MPC.

These results convincingly show that the proposed architecture provides a significant benefit over simpler approaches that just interpolate between control signals obtained from training data that corresponds to stable behaviors of the robot. The integration of online planning with the MPC-based control architecture in combination with the Dynamic Filter always results in stable and robust behavior, even largely independently of the accuracy of the learned trajectory model (number of source functions).

## Chapter 4

# Contraction Theory and Self-organized Scenarios in Computer Graphics and Robotics

### 4.1 Introduction and Related Work

The online simulation of human behavior is a core problem in computer animation with important applications such as computer games. While the dominant approach for the generation of realistic human movements is based on off-line synthesis using motion capture, this approach cannot easily be transferred to real-time applications. Only recently, researchers have started to develop methods to learn models for online synthesis from motion capture data<sup>126,268,285</sup>. Dynamical systems derived, for example, from biomechanical or physical models seem particularly appropriate for real-time synthesis<sup>40,112,308</sup>. However, it has turned out that models for the generation of human movements with high degree of realism typically have to be rather detailed<sup>8,123,307</sup>, resulting in complex dynamical systems whose properties are difficult to control. Consequently, the dynamical stability properties of such systems have rarely been addressed, and given their complexity it is an open question whether they can be treated at all.

An important domain of the application of dynamical systems in computer animation is the simulation of autonomous and collective behavior of many characters, e.g. in crowd animation<sup>218,316</sup>. Some work in this domain has been inspired by observations in biology showing that coordinated behavior of large groups of agents, such as flocks of birds, can be modeled as an emergent behavior that results from the dynamic interactions between individual agents, without requiring a central mechanism that ensures coordination<sup>45,61</sup>. One example is the tendency of multiple agents to synchronize their behavior, for example

during walking or applauding. It is well-known that such behaviors can be analyzed efficiently within the framework of nonlinear dynamics<sup>243</sup>. This makes it interesting to exploit the underlying principles for the automatic synthesis of collective behavior in computer animation<sup>38,250,304</sup>.

The control of collective behavior of groups of agents has been treated in mathematical control theory<sup>232,274</sup>, typically assuming simplified often linear models for the agents. Group coordination and cooperative control have also been studied in robotics, e.g. in the context of the navigation of groups of vehicles<sup>137,249</sup>, or with the goal to generate collective behavior by self-organization. Examples are the spontaneous adaptation to perturbations of inter-agent communication or changes in the number of agents<sup>203,223</sup>. Many approaches have analyzed asymptotic stability for consensus scenarios, proposing quadratic Lyapunov functions and linear combinations of quadratic Lyapunov functions for systems with a switching structure of the interactions (e.g.<sup>182</sup>). But in the most interesting cases, quadratic Lyapunov functions for the switching systems did not exist<sup>137</sup>. This non-existence was demonstrated theoretically in<sup>225</sup>. See also<sup>179</sup> for a review of the general problems of stability of such systems. These problems drew attention towards tools derived from the concept of uniform exponential stability (cf.<sup>321</sup>), e.g. Contraction Theory<sup>183</sup>, which provides constructive ways for the design of switching interactions in complex nonlinear systems.

In the previous Chapter 3 I presented a new method that approximates complex human behavior by relatively simple nonlinear dynamical systems. Consistent with related approaches in robotics<sup>40,98,252,276</sup> and biology<sup>91</sup>, this method generates complex movements by combining learned movement primitives<sup>235</sup>. The resulting system architecture is simple and thus suitable for a treatment of its dynamical stability properties. In this chapter I present the development of a systematic method for the design of the dynamics of interactive crowds. For this purpose, I approximate human movements by relatively simple mathematical models, combining dynamical models with appropriate learning methods. In the following I also introduce a novel framework for the analysis and design of the stability properties of systems for interactive character animation. Exploiting models that are based on learned movement primitives, I obtain a system dynamics that can be analyzed, even for situations with multiple characters. I introduce *Contraction theory* as the new theoretical approach that permits a treatment of the dynamical properties of networks of coupled nonlinear dynamical elements. Previously, Contraction theory has been applied successfully to analyze other types of complex systems<sup>183,242,294,333</sup>. Contraction theory is a method to derive the conditions for uniform exponential convergence of complex nonlinear systems. Contraction theory is based on famous theorem of N. N. Krasovskii, proven

by means of functional analysis<sup>161</sup>. Contrary to classical stability analysis for nonlinear systems, Contraction theory permits to re-use stability results for system components in order to derive conditions that guarantee the stability of the overall system. It provides a useful tool specifically for modularity-based stability analysis and design. Contraction theory has been already successfully used for synchronization of DMPs (Dynamic Movement Primitives) controlling Unmanned Aerial Vehicles<sup>240</sup> and it also has been used for CPG-based closed-loop control of Autonomous Underwater Vehicles<sup>281</sup>. But the stability properties for crowd animation systems realizing human behaviors with realistic levels of complexity have never been treated before.

## 4.2 Contraction Theory for Analysis of Stability of Nonlinear Systems

Dynamical systems describing the behavior of autonomous characters are essentially nonlinear. This makes the analysis of their stability properties a difficult problem. A major difficulty of this analysis is that for nonlinear, as opposed to linear dynamical systems, stability properties of parts usually do not transfer to composite systems. Contraction theory<sup>183</sup> provides a general method for the analysis of nonlinear systems, which permits such a transfer, making it suitable for the analysis of complex systems with many components. The classical approach for stability analysis of nonlinear systems is to compute first the stationary solutions of the dynamics, and then to establish its *local stability* by linearization in the neighborhood of this solution. Already the computation of stationary solutions is often difficult or possible only numerically. Contraction theory takes a different approach and characterizes the system stability by the behavior of the differences between solutions with different initial conditions. If these differences vanish exponentially over time, and its solution converges towards a single trajectory, independent from the initial states, the system is called *globally asymptotically stable*. Interestingly, the analysis of such differences between solutions is often simpler than the classical linearization approach, making systems tractable that would be impossible to analyze with the classical approach.

In the following a single character will be described by a dynamical system of the form

$$\dot{\mathbf{x}} = \mathbf{f}(\mathbf{x}, t) \tag{4.1}$$

where the variable  $\mathbf{x}$  signifies the dynamical state of the character. For a walking avatar, this dynamics could be given by a limit cycle oscillator, whose periodic solution is mapped onto the joint angles of the character. The nonlinear mapping between dynamical state  $\mathbf{x}$

and the joint angles is learned using kernel methods (see Section 3.3.4 for details). The learned nonlinear mapping is bounded and acts as nonlinear observer of the state variable that does not modify the overall stability properties of the system, unless the joint angles are fed back into the dynamical state. The dynamics (4.1) can also be interpreted as describing a *Central Pattern Generator* (CPG) that drives the movement of the character.

In the following I present bounds for the convergence of solutions of the dynamical system of the form (4.1). These bounds depend on the eigenvalues of matrices that are derived from the *Jacobian* of the system  $\mathcal{J}(\mathbf{x}, t) = \frac{\partial \mathbf{f}(\mathbf{x}, t)}{\partial \mathbf{x}}$ . Given a square matrix  $\mathbf{A}$ , the matrix  $\mathbf{A}_s = (\mathbf{A} + \mathbf{A}^T)/2$  signifies its symmetric part. Lets also define the real-valued matrix functions  $\lambda_{\min}(\mathbf{A}_s)$  and  $\lambda_{\max}(\mathbf{A}_s)$  which correspond to the smallest, respectively largest, eigenvalue of the symmetric matrix  $\mathbf{A}_s$ . The matrix  $\mathbf{A}_s$  is positive definite (denoted by  $\mathbf{A}_s > \mathbf{0}$ ) if  $\lambda_{\min}(\mathbf{A}_s) > 0$ , and negative definite (denoted by  $\mathbf{A}_s < \mathbf{0}$ ) if  $\lambda_{\max}(\mathbf{A}_s) < 0$  (see the definitions in mathematical supplement - Appendix B). If the matrix is itself a function of state and time (i.e.,  $\mathbf{A}_s(\mathbf{x}, t)$ ) we say that it is *uniformly positive definite* if there exists a real  $\beta > 0$  such that  $\forall \mathbf{x}, \forall t : \lambda_{\min}(\mathbf{A}_s(\mathbf{x}, t)) \geq \beta$ . Likewise, we say it is *uniformly negative definite* if there exists a  $\beta > 0$  such that  $\forall \mathbf{x}, \forall t : \lambda_{\max}(\mathbf{A}_s(\mathbf{x}, t)) \leq -\beta$ .

#### 4.2.1 General Theorems of Contraction Analysis

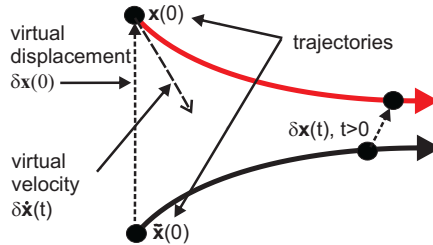


**Figure 4.1:** Two trajectories of a dynamical system and the virtual displacement.

Assume  $\mathbf{x}(t)$  is one solution of the system and  $\tilde{\mathbf{x}}(t) = \mathbf{x}(t) + \delta\mathbf{x}(t)$  a neighboring one. The function  $\delta\mathbf{x}(t)$  is also called a *virtual displacement* (see Fig. 4.1). If the virtual displacement is small enough the last equation together with equation (4.1) implies

$$\dot{\delta\mathbf{x}}(t) = \mathcal{J}(\mathbf{x}, t)\delta\mathbf{x}(t)$$

implying through  $\frac{d}{dt}\|\delta\mathbf{x}(t)\|^2 = 2\delta\mathbf{x}^T(t)\mathcal{J}_s(\mathbf{x}, t)\delta\mathbf{x}$  the inequality:

$$\|\delta\mathbf{x}(t)\| \leq \|\delta\mathbf{x}(0)\| e^{\int_0^t \lambda_{\max}(\mathcal{J}_s(\mathbf{x}, s)) ds} \quad (4.2)$$



If the Jacobian is uniformly negative definite this equation implies that any nonzero virtual displacement decays exponentially to zero over time. This decay occurs with a *convergence rate* (inverse timescale) that is bounded from below by  $\rho_c = -\sup_{\mathbf{x},t} \lambda_{\max}(\mathcal{J}_s(\mathbf{x},t))$ . By 'concatenating' such virtual displacements at fixed points in time one can show that any difference between the trajectories decays to zero with at least this time constant<sup>183</sup>. This has the consequence of all trajectories converging towards a single trajectory exponentially. Therefore, this motivates:

**Definition 1.** *With respect to the dynamical system  $\dot{\mathbf{x}} = \mathbf{f}(\mathbf{x},t)$ , the regions in state space for which the symmetrized Jacobian matrix  $\mathcal{J}_s = \frac{1}{2}(\frac{\partial \mathbf{f}}{\partial \mathbf{x}} + \frac{\partial \mathbf{f}^T}{\partial \mathbf{x}})$  is uniformly negative definite are called contracting regions. All solutions that start in these regions converge towards a single trajectory for  $t \rightarrow \infty$ .*

The previous argument can be extended by measuring the length of the virtual displacement using a different metric (coordinate system). By assuming a uniformly invertible square matrix  $\Theta(\mathbf{x},t)$ , which in most cases is state- and time-dependent, one can introduce the transformed displacement  $\delta \mathbf{z}(t) = \Theta(\mathbf{x},t)\delta \mathbf{x}(t)$ . Analogous to the previous case one finds:

$$\frac{d}{dt}(\delta \mathbf{z}^T \delta \mathbf{z}) = 2\delta \mathbf{z}^T \dot{\delta \mathbf{z}} = 2\delta \mathbf{z}^T \underbrace{(\dot{\Theta} + \Theta \frac{\partial \mathbf{f}}{\partial \mathbf{x}})}_{\mathbf{F}} \Theta^{-1} \delta \mathbf{z}$$

This implies the following general result:

**Theorem 1.** *Assume that for the system (4.1) it is possible to find a square matrix  $\Theta(\mathbf{x},t)$  such that  $\Theta(\mathbf{x},t)^T \Theta(\mathbf{x},t)$  is uniformly positive definite, and such that the generalized Jacobian*

$$\mathbf{F} = (\dot{\Theta} + \Theta \frac{\partial \mathbf{f}}{\partial \mathbf{x}}) \Theta^{-1} \quad (4.3)$$

*is uniformly negative definite, then all system trajectories converge exponentially to a single trajectory, and the system is called contracting. The rate of convergence of  $\|\delta \mathbf{z}(t)\|$  is at least  $\rho_c = -\sup_{\mathbf{x},t} \lambda_{\max}(\mathbf{F}_s(\mathbf{x},t))$ . The matrix  $\mathbf{M}(\mathbf{x},t) = \Theta(\mathbf{x},t)^T \Theta(\mathbf{x},t)$  is also called the contraction metric.*

*Conversely, the existence of a uniformly positive definite metric  $\mathbf{M}(\mathbf{x},t) = \Theta(\mathbf{x},t)^T \Theta(\mathbf{x},t)$  with respect to which the system is contracting is a necessary condition for the global exponential convergence of trajectories<sup>183</sup>. Furthermore, all transformations  $\Theta$  corresponding to the same  $\mathbf{M}$  result in the same eigenvalues for the symmetric part of  $\mathbf{F}$ <sup>294</sup>, and thus the same convergence rate. (The proofs can be found in<sup>183,294</sup>.)*

Contraction analysis can be applied to *hierarchically coupled systems* that are given by the dynamics

$$\frac{d}{dt} \begin{pmatrix} \mathbf{x}_1 \\ \mathbf{x}_2 \end{pmatrix} = \begin{pmatrix} \mathbf{f}_1(\mathbf{x}_1) \\ \mathbf{f}_2(\mathbf{x}_1, \mathbf{x}_2) \end{pmatrix} \quad (4.4)$$

where the first subsystem is not influenced by the state of the second. The corresponding Jacobian  $\mathbf{F} = \begin{bmatrix} \mathbf{F}_{11} & 0 \\ \mathbf{F}_{21} & \mathbf{F}_{22} \end{bmatrix}$  implies for the dynamics of the virtual displacements:  $\frac{d}{dt} \begin{pmatrix} \delta \mathbf{x}_1 \\ \delta \mathbf{x}_2 \end{pmatrix} = \begin{bmatrix} \mathbf{F}_{11} & 0 \\ \mathbf{F}_{21} & \mathbf{F}_{22} \end{bmatrix} \begin{pmatrix} \delta \mathbf{x}_1 \\ \delta \mathbf{x}_2 \end{pmatrix}$ . If  $\mathbf{F}_{21}$  is bounded, then the exponential convergence of the first subsystem, (following from  $[\mathbf{F}_{11}]_s < 0$ ), implies thus convergence of the whole system, if in addition  $[\mathbf{F}_{22}]_s < 0$ . This follows from the fact the term  $\mathbf{F}_{21}\delta\mathbf{x}_1$  is just an exponentially decaying disturbance for the second subsystem. (See<sup>183</sup> for proof).

#### 4.2.2 Partial Contraction and Flow-invariant Manifolds

Many systems are not contracting with respect to all dimensions of the state space, but show convergence with respect to a subset of dimensions. A typical example is an externally driven nonlinear oscillator. By its tendency to self-initiate oscillatory solutions it is unstable, and thus non-contracting, within a region around the the origin of state space. However, independent of the initial state, it might converge exponentially against a single trajectory that is determined by the external driving signal. Partial contraction<sup>333</sup> allows to capture this property in a mathematically well-defined manner. The key idea is to construct an auxiliary system that is contracting with respect to a subset of dimensions (or submanifold) in state space.

**Theorem 2.** *Consider a nonlinear system of the form*

$$\dot{\mathbf{x}} = \mathbf{f}(\mathbf{x}, \mathbf{x}, t) \quad (4.5)$$

*and assume that the auxiliary system*

$$\dot{\mathbf{y}} = \mathbf{f}(\mathbf{y}, \mathbf{x}, t) \quad (4.6)$$

*is contracting with respect to  $\mathbf{y}$  uniformly for all relevant  $\mathbf{x}$ . If a particular solution of the auxiliary system verifies a specific smoothness property, then all trajectories of the original system (4.5) verify this property with exponential convergence. The original system is then said to be partially contracting.*

A 'smooth property' is a property of the solution that depends smoothly on space and time, such as convergence to a particular solution or value. The proof of the theorem is immediate noticing that the observer-like system (4.6) has  $\mathbf{y}(t) = \mathbf{x}(t)$  for all  $t \geq 0$  as a particular solution. Since all trajectories of the  $\mathbf{y}$ -system converge exponentially to a single trajectory, this implies that also the trajectory  $\mathbf{x}(t)$  obeys this specific property with

exponential convergence.

Related to partial contraction are the following methods that will be crucial for the derivation of results on the synchronization of groups of avatars. Again starting from the equation (4.1), we assume the existence of a *flow-invariant linear subspace*  $\mathcal{M}$ , i.e. a linear subspace  $\mathcal{M}$  such that  $\forall t : \mathbf{f}(\mathcal{M}, t) \subset \mathcal{M}$ . This implies that any trajectory starting in  $\mathcal{M}$  remains in  $\mathcal{M}$ . Further, we assume that  $p = \dim(\mathcal{M})$  and consider an orthonormal basis  $(\mathbf{e}_1, \dots, \mathbf{e}_n)$  where the first  $p$  vectors form a basis of  $\mathcal{M}$  and the last  $n - p$  a basis of  $\mathcal{M}^\perp$ , the orthogonal space of  $\mathcal{M}$ . We define an  $n \times (n - p)$  matrix  $\mathbf{V}$  whose columns are  $\mathbf{e}_{p+1}^T, \dots, \mathbf{e}_n^T$ .  $\mathbf{V}^T$  can be regarded as projection on  $\mathcal{M}^\perp$ , which implies  $\mathbf{x} \in \mathcal{M} \Leftrightarrow \mathbf{V}^T \mathbf{x} = \mathbf{0}$ . It holds that  $\mathbf{V}^T \mathbf{V} = \mathbf{I}_{n-p}$  and  $\mathbf{V} \mathbf{V}^T + \mathbf{U} \mathbf{U}^T = \mathbf{I}_n$ , where  $\mathbf{U}$  is the matrix formed by the first  $p$  basis vectors as columns.

**Theorem 3.** *Assume that for the dynamical system (4.1) a flow-invariant linear subspace  $\mathcal{M}$  exists with the associated orthonormal projection matrix  $\mathbf{V}^T$ . A particular solution  $\mathbf{x}_p(t)$  of this system converges exponentially to  $\mathcal{M}$  if the auxiliary system*

$$\dot{\mathbf{y}} = \mathbf{V}^T \mathbf{f}(\mathbf{V} \mathbf{y} + \mathbf{U} \mathbf{U}^T \mathbf{x}_p(t), t) \quad (4.7)$$

*is contracting with respect to  $\mathbf{y}$  for all relevant  $\mathbf{x}_p$ , then starting from any initial condition, all trajectories of the original system will exponentially converge to the invariant subspace  $\mathcal{M}$ . If furthermore all the contraction rates for (4.7) are lower-bounded by some constant  $\lambda > 0$ , uniformly in  $\mathbf{x}_p$  and in a common metric, then the convergence to  $\mathcal{M}$  will be exponential with a minimum rate  $\lambda$ .*

The proof of this theorem can be found in<sup>242</sup>. It implies that a simple sufficient condition for global exponential convergence to  $\mathcal{M}$  is given by the following inequality that needs to hold uniformly:

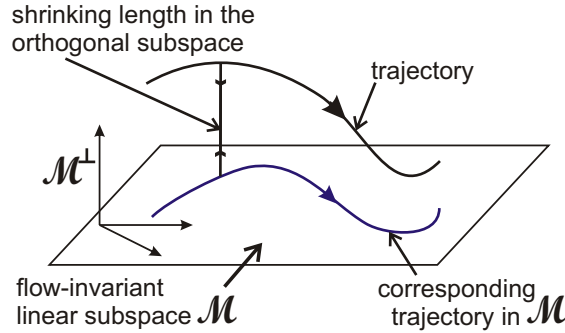
$$\boxed{\mathbf{V}^T \left[ \frac{\partial \mathbf{f}}{\partial \mathbf{x}} \right]_s \mathbf{V} < \mathbf{0}} \quad (4.8)$$

Fig. 4.2 schematically depicts a flow-invariant *linear subspace*  $\mathcal{M}$ . Such that any trajectory starting in  $\mathcal{M}$  remains in  $\mathcal{M}$ :  $\forall t, \mathbf{f}(\mathcal{M}, t) \subset \mathcal{M}$ .

An even more general condition can be derived if there exists a constant invertible transform  $\Theta$  on  $\mathcal{M}^\perp$  such that

$$\Theta \mathbf{V}^T \left[ \frac{\partial \mathbf{f}}{\partial \mathbf{x}} \right]_s \mathbf{V} \Theta^{-1} < \mathbf{0} \quad (4.9)$$

is fulfilled uniformly<sup>242</sup>.



**Figure 4.2:** Illustration of a flow-invariant *linear subspace*  $\mathcal{M}$  and a trajectory converging to this flow-invariant manifold  $\mathcal{M}$ .

Finally, we introduce here a theorem that provides sufficient conditions for synchronization of a network that is composed from  $N$  identical dynamical systems that communicate through a common medium or channel with state variable  $\chi$ . The relevant dynamics is given by

$$\begin{aligned}\dot{\mathbf{x}} &= \mathbf{f}(\mathbf{x}, \chi, t), \\ \dot{\chi} &= g(\chi, \Psi(\mathbf{x}), t)\end{aligned}\tag{4.10}$$

$\mathbf{x}$  containing the state variables of the individual systems and all components of  $\mathbf{f}$  having the same form  $f$ . Exploiting the Partial contraction theorem 2 the following result can be derived<sup>266</sup>:

**Theorem 4.** (*Quorum sensing*) *If the reduced order virtual system  $\dot{y} = f(y, \chi, t)$  is contracting for all relevant  $\chi$  then all solutions of the original system converge exponentially to a single trajectory, i.e.  $|x_i(t) - x_j(t)| \rightarrow 0$  as  $t \rightarrow +\infty$ .*

### 4.3 Linear Coupling of Nonlinear DMPs

Contraction analysis can be applied to guarantee the stability of networks of coupled dynamical elements, such as oscillators. The animation systems discussed in the following exploit character models whose behavior is driven by nonlinear limit cycle oscillators. The stationary solution of these oscillators is given by a sinusoidal oscillation with a constant equilibrium amplitude. Groups of interacting characters can be modeled by coupled networks of such nonlinear oscillators. In the following, we describe how methods from Contraction theory can be exploited to analyze the dynamics of such networks, providing mathematical results that help to design the behavior of animations of the collective behavior of such interacting characters.

The state feedback coupling term is called *diffusive*, when it is a linear function of differences of the corresponding state variables. We assume in the following  $n$  systems with linear *diffusive coupling* of the form (cf.<sup>333</sup>):

$$\dot{\mathbf{x}}_i = \mathbf{f}(\mathbf{x}_i, t) + \sum_{j \neq i} \mathbf{K}^{ij} (\mathbf{x}_j - \mathbf{x}_i) \quad \forall i = 1, \dots, n \quad (4.11)$$

Here if the dimensionality of each vector  $\mathbf{x}_i$  is  $N$ , then the dimensionality of each square matrix  $\mathbf{K}^{ij}$  is  $N \times N$ . In the case of diffusive coupling, after synchronisation, the dynamics of each subsystem is equivalent to the dynamics of uncoupled subsystem.

The matrix  $\mathbf{L}$  with the blocks ( $\mathbf{L}_{ii} = \sum_{j \neq i} \mathbf{K}^{ij}$  and  $\mathbf{L}_{ij} = -\mathbf{K}^{ij}$  for  $j \neq i$ ) is called the *Laplacian matrix* of the coupling (see<sup>333</sup>). With this matrix and the definitions  $\mathbf{x} = [\mathbf{x}_1^T, \dots, \mathbf{x}_n^T]^T$  and  $\mathbf{f}(\mathbf{x}_i, t) = [\mathbf{f}(\mathbf{x}_1, t)^T, \dots, \mathbf{f}(\mathbf{x}_n, t)^T]^T$  the equation system can be written in vector form:  $\dot{\mathbf{x}} = \mathbf{f}(\mathbf{x}, t) - \mathbf{L}\mathbf{x}$ . This implies that the Jacobian of the system is given by  $\mathcal{J}(\mathbf{x}, t) = \mathbf{D}(\mathbf{x}, t) - \mathbf{L}$ , where

$$\mathbf{D}(\mathbf{x}, t) = \begin{bmatrix} \frac{\partial \mathbf{f}}{\partial \mathbf{x}}(\mathbf{x}_1, t) & 0 & 0 \\ 0 & \ddots & 0 \\ 0 & 0 & \frac{\partial \mathbf{f}}{\partial \mathbf{x}}(\mathbf{x}_n, t) \end{bmatrix}. \quad (4.12)$$

For diffusive coupling, we assume again the existence of a flow-invariant linear subspace  $\mathcal{M}$  of the  $\mathbf{x}$  space that contains a particular solution of the form  $\mathbf{x}_1^* = \dots = \mathbf{x}_n^*$ . For this solution all state variables  $\mathbf{x}_i$  are identical and thus in synchrony. In addition, for this solution the coupling term in equation (4.11) vanishes so that the form of the solution is identical to the solution of the uncoupled systems  $\dot{\mathbf{x}}_i = \mathbf{f}(\mathbf{x}_i, t)$ .

Introducing  $\mathbf{V}^T$  as a projection matrix corresponding to the subspace  $\mathcal{M}^\perp$ , a sufficient condition for convergence to this solution is given by the matrix inequality  $\mathbf{V}^T (\mathbf{D}(\mathbf{x}, t) - \mathbf{L})_s \mathbf{V} < \mathbf{0}$ . From this inequality the following sufficient condition for exponential convergence can be derived<sup>242</sup>

$$\lambda_{\min}(\mathbf{V}^T \mathbf{L}_s \mathbf{V}) > \sup_{\mathbf{x}, t} \lambda_{\max} \left( \left[ \frac{\partial \mathbf{f}}{\partial \mathbf{x}}(\mathbf{x}, t) \right]_s \right) \quad (4.13)$$

which implies the following minimum convergence rate:

$$\rho_c = - \sup_{\mathbf{x}, t} \lambda_{\max}(\mathbf{V}^T (\mathbf{D}(\mathbf{x}, t) - \mathbf{L})_s \mathbf{V}).$$

### 4.3.1 The Andronov-Hopf Oscillator

The dynamics of an individual character is modeled by an Andronov-Hopf oscillator, a nonlinear oscillator that is characterized by a limit cycle that corresponds to a circular trajectory in phase space. After re-parametrization (rescaling of time and state-space axes) the dynamics of this oscillator is described by the differential equations<sup>11</sup>:

$$\begin{cases} \dot{x}(t) = (1 - (x^2(t) + y^2(t))) x(t) - \omega y(t) \\ \dot{y}(t) = (1 - (x^2(t) + y^2(t))) y(t) + \omega x(t) \end{cases} \quad (4.14)$$

which can be written in vector form (with  $\mathbf{x} = [x, y]^T$ ):

$$\dot{\mathbf{x}}(t) = \mathbf{f}(\mathbf{x}, t) \quad (4.15)$$

The Jacobian for a single Andronov-Hopf oscillator is given by

$$\mathcal{J}(\mathbf{x}) = \frac{\partial \mathbf{f}}{\partial \mathbf{x}} = \begin{bmatrix} -(x^2 + y^2 - 1) - 2x^2 & -2xy - \omega \\ -2xy + \omega & -(x^2 + y^2 - 1) - 2y^2 \end{bmatrix}$$

implying  $|\mathcal{J}_s(\mathbf{x}) - \lambda \mathbf{I}| = (1 - r^2 - \lambda)(1 - 3r^2 - \lambda)$  with  $r^2 = x^2 + y^2$ . The eigenvalues of the matrix  $\mathcal{J}_s(\mathbf{x})$  are thus bounded by 1 from above.

Introducing polar coordinates  $r(t) = \sqrt{x^2(t) + y^2(t)}$  and  $\phi(t) = \arctan(y(t)/x(t))$ , the system (4.14) can be rewritten:

$$\begin{cases} \dot{r}(t) = r(t) (1 - r^2(t)) \\ \dot{\phi}(t) = \omega \end{cases} \quad (4.16)$$

The symmetrized Jacobian in this coordinates is given by

$$\mathcal{J}_s = \begin{bmatrix} 1 - 3r^2 & 0 \\ 0 & 0 \end{bmatrix} \quad (4.17)$$

showing that, according to Definition 1, this system is semi-contracting<sup>242</sup> in the region  $|r| > 1/\sqrt{3}$  where its symmetrized Jacobian is uniformly negative definite. Introduction of the new variable  $\rho = 1/r^2 > 0$  transforms the dynamics into the form:

$$(\dot{r}^2) = 2r^2 (1 - r^2) \Rightarrow \dot{\rho} = 2(1 - \rho)$$

In these coordinates  $\rho$  and  $\phi$ , the eigenvalues of the symmetrized Jacobian are  $-2$  and  $0$ , so that the system is semi-contracting in the whole phase plane. The system is contracting

with respect to the variable  $\rho$ , while the dynamics of  $\phi$  is *indifferent*.

### 4.3.2 Symmetric Diffusive Coupling of Linear Phases of Multiple Oscillators

Given the decoupled  $r$  (radial) and  $\phi$  (phase) dynamics of the Andronov-Hopf oscillator we may separately couple the phases of such oscillators. As an example of phase coupling one may use symmetrical linear diffusive coupling, which results in uniformly exponentially convergent dynamics (in fact, partially contracting towards the manifold  $\phi_i = \phi_j, \forall i, j$ ). Thus, for *all-to-all* coupling, for every oscillator  $i$  ( $k > 0$  is the uniform coupling strength):

$$\frac{d}{dt}\phi_i = \omega + k \sum_j (\phi_j - \phi_i) \quad (4.18)$$

where all differences and sums are taken on the unitary circle (e.g. the circular mean average phase would be  $\hat{\phi} = \text{angle}(\sum_i \exp[\phi_i \sqrt{-1}])$ ). Instead of all-to-all coupling we may use a general symmetrical linear diffusive coupling, where the coupling network structure is described by an undirected single-connected coupling graph (e.g. with the equal weights of the bidirectional coupling links). With link weights  $k > 0$  and  $A_{ij}$  the adjacency matrix of the coupling graph (see A.1):

$$\dot{\phi}_i = \omega + k \sum_j A_{ij} (\phi_j - \phi_i) \quad (4.19)$$

In vector notation with  $\mathbf{L} \geq 0$  the Laplacian matrix of the coupling graph (A.1):

$$\dot{\phi} = \omega - k\mathbf{L}\phi \quad (4.20)$$

The Jacobian of this system is given by  $\mathcal{J}(\phi, t) = -k\mathbf{L}$ . If the coupling network is balanced and singly-connected (A.1), then the Laplacian matrix of the coupling graph is a symmetric positive definite matrix with a single zero eigenvalue corresponding to the eigenvector  $\bar{\mathbf{1}}/\sqrt{N}$  ( $\bar{\mathbf{1}}$  is the vector of  $N$  ones). The dynamics has a flow-invariant linear subspace  $\mathcal{M}$  that contains the particular solution  $\phi_1^* = \dots = \phi_n^*$ . For this solution all phase variables  $\phi_i$  are identical and thus in synchrony. In this case, the coupling term in equation (4.20) vanishes, so that the form of the solution is identical to the one of an uncoupled system. If  $\mathbf{V}^T$  is a projection matrix onto the invariant subspace  $\mathcal{M}^\perp$ , then by Eq.(4.8) the sufficient condition for convergence towards  $\mathcal{M}$  is given by  $\mathbf{V}^T(-k\mathbf{L})_s\mathbf{V} < \mathbf{0}$ . This implies  $\lambda_{\min}(\mathbf{V}^T(k\mathbf{L})_s\mathbf{V}) = k\lambda_{\mathbf{L}}^+ > 0$ , with  $\lambda_{\mathbf{L}}^+$  being the smallest non-zero eigenvalue of the symmetrical part of the Laplacian matrix  $\mathbf{L}_s$ . For singly-connected coupling graphs (with all the positive weights of the bidirectional links) all nonzero eigenvalues of  $\mathbf{L}_s$  are

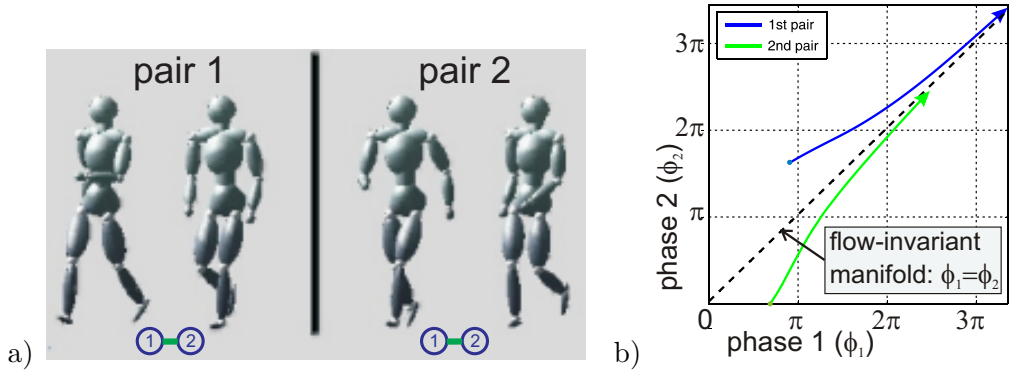


**Figure 4.3:** a) Two simulations (pair 1 and pair 2) of the same system of two paired avatars. In each simulation a pair of avatar synchronizes, but the synchronization moment is dependent on initial phases. b) The resulting trajectories are depicted as blue and green lines. See **Demo video** ([tiny.cc/zmdm5y](http://tiny.cc/zmdm5y)).

real positive, see A.1. Thus, this system is *partially contracting* (all oscillators converge towards the same linearly propagating phase, their differences computed by modulus  $2\pi$ ) for any  $k > 0$  with uniform contraction rate  $\rho_c = k\lambda_{\mathbf{L}}^+$ .

Fig. 4.3 and the associated video ([tiny.cc/zmdm5y](http://tiny.cc/zmdm5y)) illustrate the dynamics of the convergence towards the linear flow-invariant manifold in case of two paired linear phases:

$$\begin{cases} \dot{\phi}_1 = \omega + k(\phi_2 - \phi_1) \\ \dot{\phi}_2 = \omega + k(\phi_1 - \phi_2) \end{cases}$$

Fig. 4.3 depicts two simulations of the same system of two paired avatars, where in each simulation a pair of avatar synchronizes, but the synchronization moment is dependent on their initial phases.

### 4.3.3 All-to-all Symmetric Linear Diffusive Coupling of Multiple DMPs

#### The case of two Andronov-Hopf oscillators

The constraints that guarantee the synchronization of two symmetrically coupled oscillators can be proven following<sup>242</sup>. The dynamics of two Andronov-Hopf oscillators with symmetric diffusive linear coupling is given (using 4-dimensional state vector  $\mathbf{x} = [\mathbf{x}_1^T, \mathbf{x}_2^T]^T$ , with



$\mathbf{x}_i = [x_i, y_i]^T$ ,  $i = 1, 2$ , and the definition according to equation (4.15)) by:

$$\begin{aligned} \begin{pmatrix} \dot{\mathbf{x}}_1 \\ \dot{\mathbf{x}}_2 \end{pmatrix} &= \begin{pmatrix} \mathbf{f}(\mathbf{x}_1) \\ \mathbf{f}(\mathbf{x}_2) \end{pmatrix} - k \underbrace{\begin{bmatrix} \mathbf{I} & -\mathbf{I} \\ -\mathbf{I} & \mathbf{I} \end{bmatrix}}_{\mathbf{L}_{(2)}} \begin{pmatrix} \mathbf{x}_1 \\ \mathbf{x}_2 \end{pmatrix} \\ \Leftrightarrow \dot{\mathbf{x}} &= \mathbf{f}(\mathbf{x}) - k \mathbf{L}_{(2)} \mathbf{x} \end{aligned} \quad (4.21)$$

According to the corollary of Theorem 3, a flow-invariant manifold  $\mathcal{M}$  of this system is given by the linear 2-dimensional subspace (in the 4-dimensional state space of  $\mathbf{x}$ ) that is defined by the linear relationship  $\mathbf{x}_1 = \mathbf{x}_2$ . For points on this manifold the coupling term vanishes, and the solution of the coupled system coincides with the solutions of the uncoupled individual oscillators.

By interchanging the columns of the matrix  $\mathbf{L}_{(2)} - \lambda \mathbf{I}$  we compute  $\det(\mathbf{L}_{(2)} - \lambda \mathbf{I}) = \lambda^2(\lambda - 2)^2$ . This implies that the matrix  $\mathbf{L}_{(2)}$  has rank 2. Its nullspace is 2-dimensional and thus coincides with  $\mathcal{M}$ . If according to Theorem 3 the matrix  $\mathbf{V}^T$  is a projector onto  $\mathcal{M}^\perp$  this implies that the matrix  $\mathbf{V}^T \mathbf{L}_{(2)} \mathbf{V}$  has only eigenvalues equal to 2.

A sufficient condition for global exponential convergence of the coupled oscillator system can be derived from equation (4.13, Section 4.3):

$$\lambda_{\min} \left( \mathbf{V}^T (k \mathbf{L}_{(2)}) \mathbf{V} \right) = 2k > \sup_{\mathbf{x}, t} \lambda_{\max} \left( \left[ \frac{\partial \mathbf{f}}{\partial \mathbf{x}} \right]_s \right) = 1 \quad (4.22)$$

The equality on the right side states that the eigenvalues of the Jacobian matrix  $\mathcal{J}_s(\mathbf{x}_i)$  of a single Andronov-Hopf oscillator are bounded by 1 from above (see 4.3.1). This implies that a sufficiently strong coupling with  $k > 1/2$  guarantees the global exponential convergence to a stable behavior.

### The case of multiple Andronov-Hopf oscillators

The last analysis can be extended for to any number  $N$  of coupled oscillators. In this case, the  $2N$ -dimensional square matrix  $\mathbf{L}$  has the form:

$$\mathbf{L} = \begin{bmatrix} (N-1) & 0 & -1 & 0 & \dots \\ 0 & (N-1) & 0 & -1 & \dots \\ -1 & 0 & (N-1) & 0 & \dots \\ 0 & -1 & 0 & (N-1) & \dots \\ \dots & \dots & \dots & \dots & \dots \end{bmatrix}$$

i.e.,  $L_{ii} = N - 1$  and  $L_{ij} = -1$  if  $i \neq j$  and  $(i + j) \bmod 2 = 0$ , and  $L_{ij} = 0$  otherwise. By rearranging the columns and rows this matrix can be restructured in the form:

$$\mathbf{L} = \begin{bmatrix} \mathbf{L}_G & 0 \\ 0 & \mathbf{L}_G \end{bmatrix} \quad (4.23)$$

where  $\mathbf{L}_G$  is the Laplacian matrix of the complete graph with  $N$  vertices (A.2):

$$\mathbf{L}_G = \begin{bmatrix} (N-1) & -1 & -1 & \dots \\ -1 & (N-1) & -1 & \dots \\ -1 & -1 & (N-1) & \dots \\ \dots & \dots & \dots & \dots \end{bmatrix}$$

Note that  $\mathbf{L}_G = N\mathbf{I} - \bar{\mathbf{1}}\bar{\mathbf{1}}^T$ . The matrix  $\bar{\mathbf{1}}\bar{\mathbf{1}}^T$  has rank 1 and eigenvector  $\bar{\mathbf{1}}/\sqrt{N}$  with eigenvalue  $N$  ( $\bar{\mathbf{1}}$  is the vector of  $N$  ones), while all other eigenvalues are 0. From  $\det(\mathbf{L}_G - \lambda\mathbf{I}) = \det(-\mathbf{1}\mathbf{1}^T - (\lambda - N)\mathbf{I}) = 0$  follows that the matrix  $\mathbf{L}_G$  has one eigenvalue 0 and all other  $N - 1$  eigenvalues are  $N$ . From this follows with equation (4.23) that two eigenvalues of matrix  $\mathbf{L}$  are 0, while all non-zero eigenvalues are  $N$ .

For equation (4.22) one obtains the inequality  $Nk > \sup_{\mathbf{x}, t} \lambda_{\max} \left( \left[ \frac{\partial \mathbf{f}}{\partial \mathbf{x}} \right]_s \right) = 1$ . Global exponential convergence to a stable synchronized solution is thus guaranteed for  $k > 1/N$ .

#### 4.3.4 Symmetric Linear Diffusive Couplings with more General Structure

Following the procedure in<sup>333</sup>, we discuss next systems with more general symmetric coupling of  $N$  oscillators, where we assume equal coupling gains  $k$ . The corresponding dynamics is  $(\mathbf{x}_i = [x_i, y_i]^T, i = [1, \dots, N])$ :

$$\dot{\mathbf{x}}_i = \mathbf{f}(\mathbf{x}_i) + k \sum_{j \in \mathcal{N}_i} (\mathbf{x}_j - \mathbf{x}_i), \quad \forall i = 1, \dots, N \quad (4.24)$$

where  $\mathcal{N}_i$  denotes the set of indices of all oscillators that are coupled with oscillator  $i$ . The couplings are assumed to be bidirectional, defining an undirected coupling graph. This implies  $j \in \mathcal{N}_i$  iff  $i \in \mathcal{N}_j$ . By construction the coupling graph is *balanced*, i.e. the sum of the (weighted) connections towards each oscillator equals the sum of (weighted) connections away from this oscillator. The corresponding state-coupling matrix  $\mathbf{L}$  is symmetric and has a block structure:  $\mathbf{L} = \mathbf{L}_G \otimes I_p$ . It is derived from the *Laplacian matrix* of the coupling graph  $\mathbf{L}_G$  (cf. A.1), where  $p$  is the dimensionality of the individual sub-systems ( $I_p$  is the identity matrix of dimension  $p$ , and  $\otimes$  signifies the *Kronecker product*). The blocks of  $\mathbf{L}$  at positions  $(i, j)$  are given by  $-\mathbf{I}$  and the  $i$ -th diagonal block is given by  $n_i\mathbf{I}$ ,  $n_i$  signifying the number of elements in  $\mathcal{N}_i$ . Like in the previous sections, this matrix, by appropriate sorting of columns and rows, can be brought in the form  $\begin{bmatrix} \mathbf{L}_G & 0 \\ 0 & \mathbf{L}_G \end{bmatrix}$ . Since the network is balanced (A.1), the sum of the rows of the Laplacian matrix are zero and  $\bar{\mathbf{1}}/\sqrt{N}$  is an eigenvector with eigenvalue 0. Again, the block structure implies that all eigenvalues of  $\mathbf{L}_G$  appear twofold in the matrix  $\mathbf{L}$ . Consequently, two of its eigenvalues are zero, independently of the form of the sets  $\mathcal{N}_i$ .

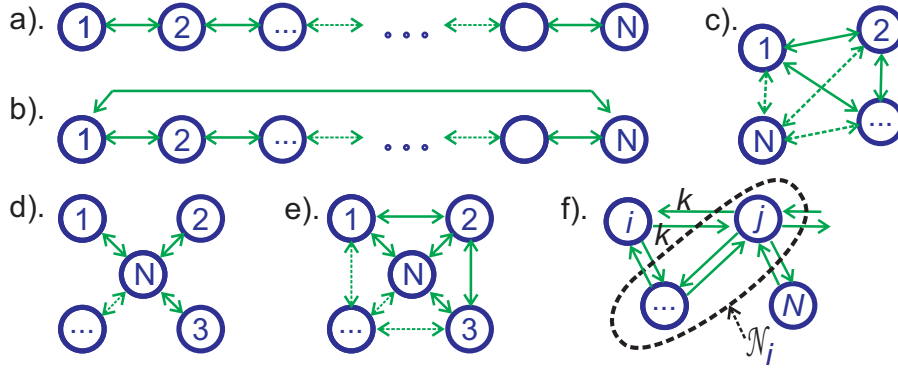


**Figure 4.4:** Examples of undirected coupling graphs with  $N$  nodes. a) *chain* (“path graph”); b) *ring*; c) *all-to-all* coupled network (complete graph); d) *star*; e) *wheel*; f) general symmetric coupling with link strength  $k$  (showing the neighborhood  $\mathcal{N}_i$  of the node  $i$ ).

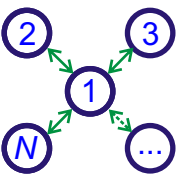
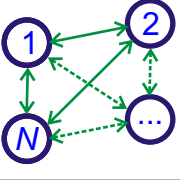
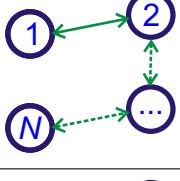
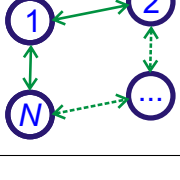
Following again the argumentation in the last sections one can derive a necessary condition for the exponential convergence from equation (4.13):

$$\lambda_{\min} \left( \mathbf{V}^T (k\mathbf{L})_s \mathbf{V} \right) = k\lambda_{\mathbf{L}}^+ > \sup_{\mathbf{x}, t} \lambda_{\max} \left( \left[ \frac{\partial \mathbf{f}}{\partial \mathbf{x}} \right]_s \right) = 1 \quad (4.25)$$

Here,  $\lambda_{\mathbf{L}}^+$  signifies the smallest non-zero eigenvalue of the matrix  $\mathbf{L}_G$  that depends on the form of the coupling. The matrix  $\mathbf{V}^T$  defines the projection to orthogonal complement of the flow invariant manifold  $\mathbf{x}_1 = \dots = \mathbf{x}_n$ . The condition for exponential convergence is thus  $k > 1/\lambda_{\mathbf{L}}^+$ .

Fig. 4.4 shows a number of coupling graphs that have been used in our animation system. Panel a shows a *symmetric chain* (or “path graph”) of a set of  $N$  oscillators. In this case, the first nonzero eigenvalue of the matrix  $\mathbf{L}_G$  can be shown to be  $\lambda_{\mathbf{L}}^+ = 2(1 - \cos(\pi/N))$ <sup>333</sup>. For a *symmetric ring* (panel b) one can show  $\lambda_{\mathbf{L}}^+ = 2(1 - \cos(2\pi/N))$  A.2. A *star coupling* of  $N > 2$  oscillators can be interpreted as a network, where  $N - 1$  oscillators are connected bidirectionally with the one in the center of the star, with the same weights, while they are not coupled with each other (Fig. 4.4.d). If the first oscillator is in the center this implies for the elements of the Laplacian matrix  $(L_G)_{1,1} = N - 1$ ,  $(L_G)_{1,i} = (L_G)_{i,1} = -1$ ,  $(L_G)_{i,i} = 1$ , for  $i > 1$ , while all other entries are zero. It can be shown that the eigenvalues of this matrix are 0, 1 (the last -  $(N - 2)$  times), and  $N$ , (see A.2). This implies  $\lambda_{\mathbf{L}}^+ = 1$  and thus the partial contraction condition is  $k > 1$ .

All these results for the star, ring, chain and all-to-all coupling networks are summarized in Table 4.1.

Type	$\lambda_{\mathbf{L}}^+$	stability condition	coupling scheme
<i>Star coupling</i>	1	$k > 1$	
<i>All-to-all coupling</i>	$N$	$k > 1/N$	
<i>Chain coupling</i>	$2(1 - \cos(\pi/N))$	$k > 1/\lambda_{\mathbf{L}}^+$	
<i>Ring coupling</i>	$2(1 - \cos(2\pi/N))$	$k > 1/\lambda_{\mathbf{L}}^+$	

**Table 4.1:** Different types of linear symmetric diffusive coupling of  $N$  Andronov-Hopf oscillators.  $\lambda_{\mathbf{L}}^+$  denotes the minimal non-zero eigenvalue of the Laplacian matrix of each coupling graph. The stability condition for the homogeneous interaction link strength  $k$  in the 3rd column is the sufficient condition for the partial contraction of the coupled DMPs. Section 4.3.4.

### 4.3.5 Simulations of Collective Behavior of the Networks of Coupled Oscillators

The following section presents a number of examples illustrating the behavior of groups of characters when the underlying dynamics fulfills or violates the bounds for contracting system behavior.

The individual dynamic primitives that control each individual character are given by Andronov-Hopf oscillators. The translation of the characters was computed by enforcing the kinematic constraints for the ground contact of the feet. Character speed was modulated by appropriate choice of the eigenfrequency  $\omega$  of the oscillators.

The first set of demonstrations shows synchronization between a group of three characters with all-to-all coupling, for different coupling strengths. As shown in Section 4.3.3 for three oscillators in this case the dynamics is contracting for  $k \geq 1/3$ .

**Movie**<sup>1</sup> shows a group of characters, starting with random initial step phases, for the case that the coupling strength  $k = 0.334$  fulfills this theoretical bound. In this case the dynamics quickly converges to a stable state, the characters walking in synchrony. Contrasting with this case, **Movie**<sup>2</sup> shows an example where the coupling strength  $k = 0.111$  violates the theoretical bound, resulting in very slow synchronization (reaching the equilibrium state only after hundreds of steps). The fact that the system still converges to a stable solution reflects that the bounds derived by Contraction theory define sufficient conditions for uniform exponential stability, but not necessary conditions for asymptotic stability. For an even stronger violation of the theoretical bound, as shown in **Movie**<sup>3</sup> for the choice  $k = -2.0$ , results in a system dynamics that does not result in the formation of a coordinated behavioral pattern anymore. But the strong coupling deforms the limit cycles in phase space, resulting in unnatural joint trajectories and very slow propagation of the characters in a transient period.

The following set of demonstrations was generated assuming a bidirectional chain ("path") coupling between the oscillators. As shown in Section 4.3.4 for three oscillators (characters) in this case the dynamics is contracting for  $k \geq 1$ . **Movie**<sup>4</sup> shows an example with  $k = 1.0$  that fulfills the theoretical bound, resulting in the quick synchronization of the characters. Contrasting with this example, **Movie**<sup>5</sup> shows the case  $k = 0.333$  that violates the contraction condition. In this case the characters do not realize coordinated behavior within the observed time interval.

<sup>1</sup><https://goo.gl/U9ZB1Q> (tiny.cc/nx9l5y)

<sup>2</sup><https://goo.gl/9XkVdN> (tiny.cc/7y9l5y)

<sup>3</sup><https://goo.gl/yR7UMv> (tiny.cc/u09l5y)

<sup>4</sup><https://goo.gl/ZkpB55> (tiny.cc/g19l5y)

<sup>5</sup><https://goo.gl/zRrFBG> (tiny.cc/319l5y)

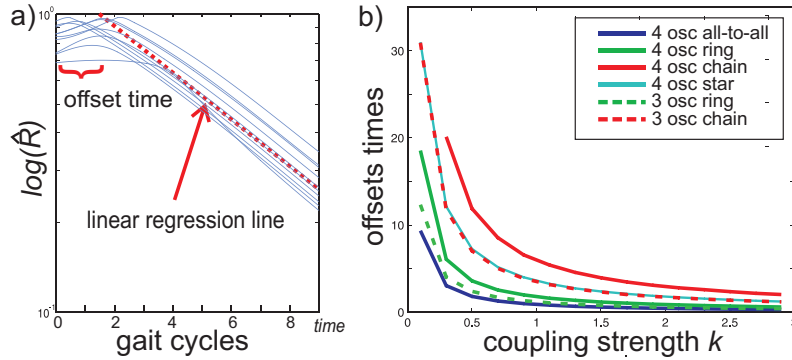


**Figure 4.5:** a) Dispersion of the phase of the oscillators, averaged over 100 simulations with random initial conditions, as function of time (gait cycles). After an offset time, during which the dispersion remains relatively constant, it decays exponentially. Convergence rates were estimated by fitting linear function to this decay. b) Offset times (in gait cycles) as function of the coupling strength. (End of offset time interval was defined by the point where the regression line crosses the level  $\hat{R} = 1$ .) The figure is adopted from<sup>237</sup>.

#### 4.3.6 Theoretical vs. Empirical Convergence Rates

As a more systematic validation of our theoretical bounds we also computed empirical convergence rates  $\lambda^{exper} = 1/\tau^{exper}$  for groups of characters of different size  $N$ . These rates were obtained assuming approximately exponential convergence of the sizes of virtual displacements:  $\|\delta x\| \sim e^{-t/\tau^{exper}}$ . The norm of the virtual displacements was approximated by the angular dispersion  $\hat{R} = (1 - \frac{1}{N} |\sum_j e^{i\phi_j}|)^{\frac{1}{2}}$  of the phases  $\phi_j$  of the oscillators (<sup>163</sup>), averaged over 100 simulations with random initial conditions.

Fig. 4.5a) shows the logarithm of this dispersion measure as a function of time (in gait cycles). It shows an initial constant segment (offset time), and after that a nearly linear decay with time, from which the time constant  $\tau^{exper}$  can be estimated by linear regression. Fig. 4.5b) shows the offset times as function of the coupling strength for different types of coupling.

Fig. 4.6a) shows the dependency between coupling strengths  $k$  and the convergence rate  $\lambda^{exper}$  as estimated from simulations in the regime of the exponential convergence. As derived from the theoretical bound, the convergence rate varies linearly with coupling strength. In case of three oscillators the ring coupling is equivalent to all-to-all coupling. Fig. 4.6b) shows the slope  $d\lambda^{exper}(k)/dk$  of this linear relationship as function of  $N$ , the number of oscillators in the network. We find a close similarity between the theoretically predicted relationship (dashed curves) and the results from the simulation (indicated by the stars). In addition, it is evident that for all-to-all coupling the convergence rate increases with the number of oscillators, while for chain or ring coupling the convergence speed decreases with the number of oscillators (for fixed coupling strength). These results

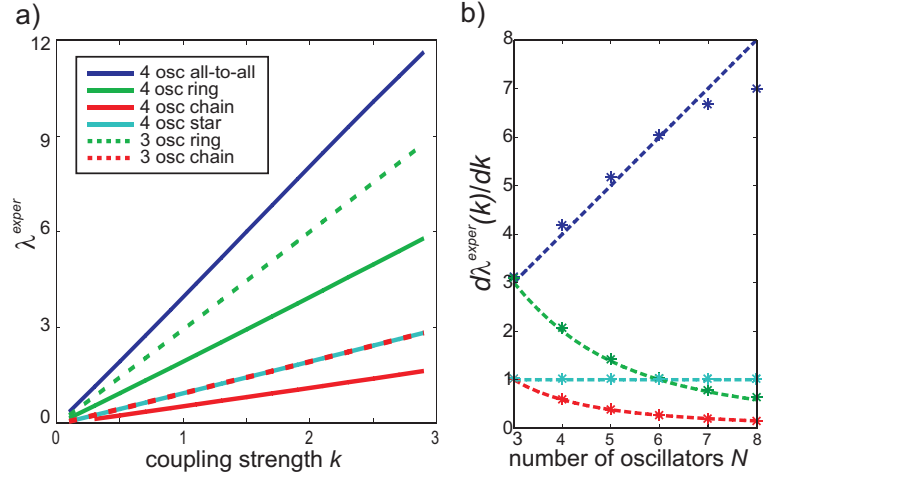


**Figure 4.6:** a) The relationship between convergence rate and coupling strength  $k$  for different types of coupling graphs. b) Slopes of this relationship as function of the number  $N$  of Andronov-Hopf oscillators, comparing simulation results (indicated by asterisks) and derived from the theoretical bounds (Section 4.3.4). The figure is adopted from<sup>237</sup>.

show in particular that the proposed theoretical framework is not only suitable for proving asymptotic stability, but also for guaranteeing the convergence speed of the system dynamics.

### 4.3.7 Leader-group Asymmetric Interaction

I also consider scenarios where multiple characters are coupled asymmetrically to a single one, which can act as a 'leader' that controls the pattern of the others. Assume first a follower scenario, where a single oscillator is coupled to the group of  $N$  identical oscillators that are already synchronized. The underlying dynamics is defined by:

$$\dot{\mathbf{x}}_0 = \mathbf{f}(\mathbf{x}_0) - k \left( N\mathbf{x}_0 - \sum_i \mathbf{x}_i \right) = \mathbf{f}(\mathbf{x}_0) - kN (\mathbf{x}_0 - \mathbf{x}_{\text{mean}})$$

A particular solution of this system is  $\mathbf{x}_0 = \mathbf{x}_{\text{mean}}$ . If the system is partially contracting in  $\mathbf{x}_0$  this implies the exponential convergence of the follower state  $\mathbf{x}_0$  to the equilibrium state  $\mathbf{x}_{\text{mean}}$  of the other oscillators. This condition is obviously fulfilled if  $kN > \sup_{\mathbf{x},t} \lambda_{\max} \left( \left[ \frac{\partial \mathbf{f}}{\partial \mathbf{x}} \right]_s \right) = 1$ .

In a leader scenario, the single oscillator feeds unidirectionally into all other  $N$  oscillators with the same coupling strength  $\alpha$ , but not vice versa. This situation is described by the



**Figure 4.7:** a) Scheme: single oscillator (Leader) feeds unidirectionally into each of  $N$  all-to-all coupled oscillators (Followers) with the same coupling strength  $\alpha$ . b) Scene view: the group of followers synchronize in gait phase with the leader. The progress bar below shows the periods of synchronization (green) and the period of perturbation (red) - see videos linked in main text.

dynamics (for  $1 \leq i \leq N$ ):

$$\begin{cases} \dot{\mathbf{x}}_0 = \mathbf{f}(\mathbf{x}_0) \\ \dot{\mathbf{x}}_i = \mathbf{f}(\mathbf{x}_i) + k\mathbf{I} \sum_{j \in \mathcal{N}_i} (\mathbf{x}_j - \mathbf{x}_i) + \alpha(\mathbf{x}_0 - \mathbf{x}_i) \end{cases} \quad (4.26)$$

The coupling scheme is depicted in Fig. 4.7. Since the leader oscillator does not receive external inputs it oscillates autonomously, and  $\mathbf{x}_0$  can be treated as external input. Denoting  $\tilde{\mathbf{x}}_0 = [\mathbf{x}_0^T, \dots, \mathbf{x}_0^T]^T$ , re-write the second equation as:

$$\dot{\mathbf{x}} = \mathbf{f}(\mathbf{x}) - k\mathbf{L}\mathbf{x} - \alpha\mathbf{x} + \alpha\tilde{\mathbf{x}}_0 \quad (4.27)$$

This implies  $\mathcal{J}(\mathbf{x}, t) = \mathbf{D}(\mathbf{x}, t) - k\mathbf{L} - \alpha\mathbf{I}$ , and the contraction conditions (see Section 4.3) are:  $\lambda_{\min}(k\mathbf{L}_G + \alpha\mathbf{I}) > \sup_{\mathbf{x}, t} \lambda_{\max}\left(\left[\frac{\partial \mathbf{f}}{\partial \mathbf{x}}\right]_s\right) = 1$ . For the special case that the  $N$  oscillators (except for the leader oscillator) are *all-to-all* symmetrically coupled this contraction condition becomes  $kN + \alpha > 1$ . This implies that for  $kN < 1$  contracting behavior can still be guaranteed when the coupling  $\alpha$  to the leader oscillator is sufficiently strong. The minimum convergence rate is then given by  $\rho_c = kN + \alpha$ .

### Simulations of leader-group scenarios

As discussed above, one can introduce a leader that can entrain all other characters in the scene by its own behavior. In addition, coupling with a leader can synchronize other characters in the scene that would not synchronize otherwise. We showed that, assuming  $k$  signifies the coupling strength between the members of the group and  $\alpha$  the strength of the coupling between the members and the leader, contracting behavior is obtained for  $kN + \alpha > 1$ .



Different behaviors are illustrated in the following movies, showing five characters. One of them is the leader (dark grey) that was coupled unidirectionally to all members of the of group. Without the leader the group ( $\alpha = 0$ ) shows exponential convergence for  $k > 1/4$ . **Movie**<sup>6</sup> shows a case with  $k = 0.01$ , i.e., the system is non-contracting and no coordinated behavior is reached in the simulation. If a leader with sufficiently strong coupling to the other group members ( $\alpha = 1$ ) is introduced the theoretical contraction bound is fulfilled. As shown in **Movie**<sup>7</sup>, in this case fast convergence to a coordinated behavior is observed even for small values of  $k$ . The next example shown in **Movie**<sup>8</sup> corresponds to the case  $k = 0.2$  and  $\alpha = 0.25$ , fulfilling also the theoretical bound for contraction. The characters converge very quickly to a coordinated behavior. This case shows an example where all characters are initially not coupled (yellow bar on time line) and start with random initial phases. After activation of the coupling (green bar) the leader experiences a phase perturbation. The group quickly adopts the behavior of the leader. **Movie**<sup>9</sup> shows a corresponding example where a perturbation of the same size is not applied to the state of the leader but to the one of a group member. In this case, the group member quickly adopts again a group's behavior.

## 4.4 Stability Conditions for Crowd Control

The previous sections described self-organized multi-agent behaviors achieved by synchronization of the underlying DMPs. This section introduces more complex scenarios of self-organized group behaviors, where each agent is described semi-empirically as a complex nonlinear dynamical system with non-smooth nonlinearities. Interactive behavior of multiple characters can be modelled by making the states of the oscillators and the mixing weights dependent on the explicit behavior of the other characters in the scene. Such couplings result in a highly nonlinear overall system dynamics.

The animation of each avatar is based on a learning-based approach for the modeling of human movements using DMPs as presented above: Ch. 3, Section 3.3.4. The DMP eigenfrequencies can be controlled online resulting in changes of the walking gait frequency. Then, by blending of the mixing weights  $w_{ij}$  and the phase delays  $\tau_{ij}$ , intermediate gait styles can be generated (Ch. 3, Section 3.4). This technique was applied to generate walking along paths with different curvatures (instantaneously controlling heading direction), changes in step length, and emotional gait styles. All these controls result in a complex nonlinear mapping from the state of the DMPs to the workspace parameters of each agent

<sup>6</sup><https://goo.gl/9Ydddf> (tiny.cc/z29l5y)

<sup>7</sup><https://goo.gl/mBpxC5> (tiny.cc/a39l5y)

<sup>8</sup><https://goo.gl/44vqn5> (tiny.cc/h39l5y)

<sup>9</sup><https://goo.gl/SvtZVC> (tiny.cc/l49l5y)

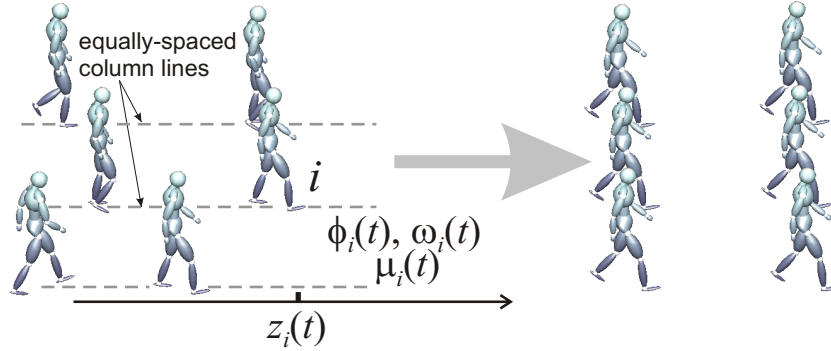


**Figure 4.8:** Variables exploited for speed and position control. Every character  $i$  is characterized by its position  $z_i(t)$ , phase  $\phi_i(t)$  and instantaneous eigenfrequency  $\omega_i(t) = \dot{\phi}_i(t)$  of the corresponding Andronov-Hopf oscillator, and a step-size scaling parameter  $\mu_i(t)$ .

(e.g. instantaneous position and orientation). The feedback loops are closed based on the resulting workspace parameters at each time instance. I run empirical estimations of the shape of the mapping function and its derivatives for different values of the control parameters. Using these estimates I propose sufficient conditions on the feedback parameters that guarantee the global exponential stability in simple scenarios and the partial contraction in consensus behavior of interacting crowds.

#### 4.4.1 Crowd Control Architecture

Flexible control of the locomotion of articulating agents requires the control of multiple variables, specifying a control dynamics with multiple coupled levels. For the examples discussed here below our system included the control of the following variables: 1) phase within the step cycle, 2) step length, 3) gait frequency, and 4) heading direction. The control of step phase was accomplished by linear phase coupling of the Andronov-Hopf oscillators (Section 4.3.1) that correspond to different agents, resulting in phase synchronization. These oscillators have a stable limit cycle that corresponds to an oscillation with constant amplitude and the (time-dependent) phase  $\phi(t)$ . In absence of external couplings the phase increases linearly, i.e.  $\phi(t) = \omega t + \phi(0)$ , where  $\omega$  is the stable eigenfrequency of the oscillator. Control of step frequency was accomplished by varying this parameter in a time-dependent manner in dependence of the behavior of the characters in the scene. Step-length and direction were controlled by morphing between gaits with different step lengths or path curvatures, blending the parameters of the anechoic mixing model (see above). In this case the controlled variables are the blending coefficient of these mixtures. (Ch. 3, Section 3.4).

The formulation of the system dynamics in terms of speed control is simplified by the introduction of the positions  $z_i$  for each individual character along its propagation path (see Fig. 4.8). This variable fulfills the differential equation  $\dot{z}_i(t) = \dot{\phi}_i g(\phi_i)$ , where the positive function  $g$  determines the instantaneous propagation speed of the character depending on the phase within the gait cycle. This nonlinear function was determined empirically from a kinematic model of a character. By integration of this propagation dynamics one obtains  $z_i(t) = G(\phi_i(t) + \phi_i^0) + c_i$ , with an initial phase shift  $\phi_i^0$  and some constant  $c_i$  depending on the initial position and phase of avatar  $i$ , and the monotonously increasing function  $G(\phi_i) = \int_0^{\phi_i} g(\phi) d\phi$ , where we assume  $G(0) = 0$ .

In the following we will analyze four different control rules, whose combination allows to generate flexible locomotion behavior of a crowd of characters:

**I) Control of step frequency:** A simple form of speed control results if the frequency of the oscillators  $\dot{\phi}_i$  is made dependent on the behavior of the other characters. Assuming that  $\omega_0$  is the equilibrium frequency of the oscillators without interaction, this can be accomplished by the control dynamics:

$$\dot{\phi}_i(t) = \omega_0 - m_d \sum_{j=1}^N A_{ij} [z_i(t) - z_j(t) - d_{ij}] \quad (4.28)$$

The constants  $d_{ij}$  specify the stable pairwise relative distances in the final formed order for each pair  $(i, j)$  of characters. The elements of the coupling graph's adjacency matrix  $A$  determine whether characters  $i$  and  $j$  are interacting and thus dynamically coupled. These parameters were set to  $A_{ij} = 1$ , if the characters were coupled, and they are zero otherwise (with  $A_{ii} = 0$ ). For example, we choose  $A_{ij} = 1, \forall i \neq j$  for *all-to-all coupling*, and  $A_{ij} = 1, \forall \text{ mod}(|i - j|, N) = 1$  for *ring coupling*. The constant  $m_d > 0$  determines the coupling strength.

With the Laplacian matrix  $\mathbf{L}^d$  of the coupling graph (that is assumed to be *strongly connected*<sup>237,242</sup>), defined by  $L_{ij}^d = -A_{ij}$  for  $i \neq j$  and  $L_{ii}^d = \sum_{j=1}^N A_{ij}$ , and the constants  $c_i = -\sum_{j=1}^N A_{ij} d_{ij}$ , the last equation system can be re-written in vector form:

$$\dot{\boldsymbol{\phi}} = \omega_0 \mathbf{1} - m_d (\mathbf{L}^d G(\boldsymbol{\phi} + \boldsymbol{\phi}^0) + \mathbf{c}) \quad (4.29)$$

**II) Control of step length:** Step length was varied by morphing between gaits with short and long steps. Detailed analysis showed that the influence of step length on propagation speed could be well approximated by simple linear rescaling. If the propagation velocity of character  $i$  is  $v_i(t) = \dot{z}_i(t) = \dot{\phi}_i(t) g(\phi_i(t)) = \omega_i(t) g(\phi_i(t))$  for the normal step size, then the velocity for modified step size could be approximated by  $v_i(t) = \dot{z}_i(t) = (1 + \mu_i) \omega_i(t) g(\phi_i(t))$  with morphing parameter  $\mu_i$ . The empirically measured propagation velocity as function of gait phase is shown in Fig. 4.9 a) for different values of the step

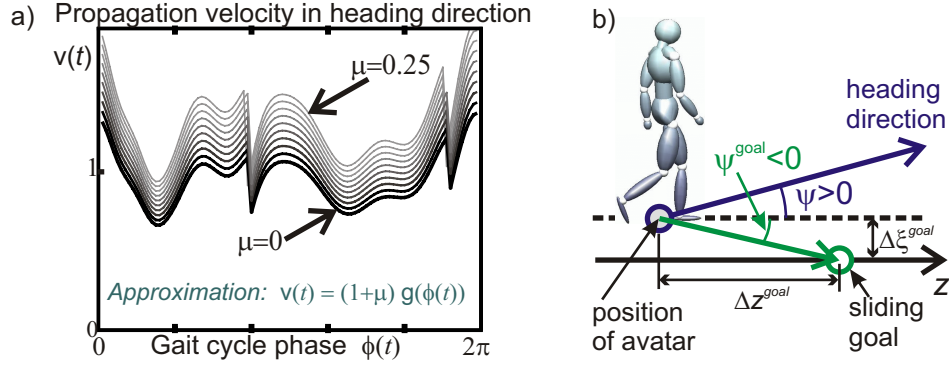


**Figure 4.9:** a) Propagation velocity for different values of the step-length morphing parameter ( $\mu = [0 \dots 0.25]$ ) as function of the gait cycle phase  $\phi$ . Empirical estimates are well approximated by a linear rescaling of the propagation speed function defined above  $\dot{z} \approx (1 + \mu)g(\phi)$ , for constant  $\omega = 1$ . b) The heading direction control depends on the difference between the actual heading direction  $\psi^{heading}$  and the goal direction  $\psi^{goal}$ . Movement along parallel lines was modelled by defining 'sliding goals' that moved along the lines. The figure is adopted from<sup>213</sup>.

length parameter  $\mu_i$ .

In order to realize speed control by step length the morphing parameter  $\mu_i$  was made dependent on the difference between actual and desired position differences  $d_{ij}$  between the agents  $\mu_i = -m_z \sum_{j=1}^N A_{ij}^z [z_i(t) - z_j(t) - d_{ij}]$ , resulting in the control rule:

$$\dot{z}_i(t) = \omega_i(t)g(\phi_i(t))(1 - m_z \sum_{j=1}^N A_{ij}^z [z_i(t) - z_j(t) - d_{ij}])$$

with the constant coupling strength  $m_z > 0$ . Here the adjacency matrix  $A^z$  of the coupling graph corresponds to the Laplacian matrix  $\mathbf{L}^z$  (according to the equivalent relationships as specified above). In vector notation the dynamics for the control of speed by step length can be written as:

$$\dot{\mathbf{z}} = \omega g(\phi + \phi^0)(1 - m_z(\mathbf{L}^z \mathbf{z} + \mathbf{c})) \quad (4.30)$$

**III) Control of step phase:** By defining separate controls for step length and step frequency the position and step phase of the characters can be varied independently. This makes it possible to simulate arbitrary spatial patterns of characters, at the same time synchronizing their step phases. The additional control of step phase can be accomplished by simple addition of a linear coupling term in equation (4.29):

$$\dot{\phi} = \omega_0 \mathbf{1} - m_d(\mathbf{L}^d G(\phi + \phi^0) + \mathbf{c}) - k \mathbf{L}^\phi \phi \quad (4.31)$$

with  $k > 0$  and the Laplacian  $\mathbf{L}^\phi$ . (All sums or differences of angular variables were

computed modulo  $2\pi$ ).

**IV) Control of heading direction:** The control of the heading directions  $\psi_i$  of the characters was based on differential equations that specify attractors for goal directions  $\psi_i^{goal}$ , which were computed from 'sliding goals' that were placed along straight lines at fixed distances in front of the characters (Fig. 4.9 b). The heading dynamics was given by a nonlinear differential equation, independently for every character:

$$\dot{\psi}_i = \omega_i(t)(-m_\psi \sin(\psi_i - \psi_i^{goal}) + g^\psi(\phi_i(t) + \phi_i^0)) \quad (4.32)$$

where  $\psi_i^{goal} = \arctan(\Delta\xi_i^{goal}/\Delta z_i^{goal})$ , with  $\Delta\xi_i^{goal}$  specifying the distance to the goal line orthogonal to the propagation direction and  $\Delta z_i^{goal}$  being a constant (Fig. 4.9 b). The first term describes a simple direction controller whose gain is defined by the constant  $m_\psi > 0$ . The second term approximates oscillations of heading direction, where  $g^\psi$  is again an empirically determined periodic function. Control is realized by making the morphing coefficients that determine the contributions of left vs. right-curved walking dependent on the change rate  $\dot{\psi}_i$  of the heading direction.

The mathematical results derived in the following sections apply to subsystems derived from the complete system dynamics defined by equations (4.30), (4.31) and (4.32). In addition, simulations will be presented that illustrate the range of behaviors that can be modelled by the full system dynamics.

#### 4.4.2 Analysis of Scenarios of Crowd Formation Control

In the following we derive stability conditions for the formation of coordinated behavior of crowds, providing contraction bounds for four scenarios corresponding to control problems with increasing levels of complexity. Corresponding crowd behaviors are illustrated by demo movies.

**1) Control of step phase without position control:** This simple control rule permits to simulate step synchronization, as in the case of a group of soldiers (Section 4.3.2). The dynamics is given by (4.31) with  $m_d = 0$  (omitting the position control term). In case of phase coupling the sufficient condition for partial contraction becomes  $k\lambda_{\mathbf{L}\phi}^+ > 0$  with the uniform contraction rate  $\rho_c = k\lambda_{\mathbf{L}\phi}^+$  for any  $k > 0$ . See **Movie**<sup>10</sup>.

**2) Speed control by variation of step frequency:**

The dynamics of this scenario is given by equations (4.29) and (4.30) with  $m_z = 0$ . Assuming arbitrary initial distances and phase offsets of different propagating characters, implying by  $G(\phi_i^0) = c_i$  that  $c_i \neq c_j$ , for  $i \neq j$ , we redefine  $d_{ij}$  as  $d_{ij} - (c_i - c_j)$  in (4.28), and accordingly  $\mathbf{c}$  in equation (4.29). Furthermore, we assume for this analysis a scenario where the characters follow one leading character whose dynamics does not receive input

<sup>10</sup><https://goo.gl/KA1BrD> (tiny.cc/r59l5y)

from the others. In this case all phase trajectories converge to a single unique trajectory only if  $c_i = c_j$  for all  $i, j$ , as consequence of the strict correspondence between gait phase and position that is given by equation (4.29). In all other cases the trajectories of the followers converge to one-dimensional, but distinct attractors that are uniquely defined by  $c_i$ . These attractors correspond to a behavior where the followers' positions oscillate around the position of the leader. The partial contraction of the dynamics with  $\mathbf{c} = 0$  guarantees that the resulting attractor area is bounded in phase space (cf. Ch.3.7.VII in<sup>183</sup>).

For the analysis of contraction properties lets consider an auxiliary system obtained from (4.29) by keeping only the terms that depend on  $\phi$ :  $\dot{\phi} = -m_d \mathbf{L}^d G(\phi + \phi^0)$ . According to Theorem 3 the symmetrized Jacobian of this system projected onto the orthogonal complement of the flow-invariant linear subspace  $\phi_1^* + \phi_1^0 = \dots = \phi_N^* + \phi_N^0$  determines whether this system is partially contracting. By virtue of a linear change of variables, the analysis of contraction properties of this system is equivalent to the analysis of the contraction properties of the dynamical system  $\dot{\phi} = -m_d \mathbf{L}^d G(\phi)$  on trajectories converging to the flow-invariant manifold  $\phi_1^* = \dots = \phi_N^*$ .

The sufficient conditions for (exponential) partial contraction towards the flow-invariant subspace are, (see equation (4.13)):  $\mathbf{V}^T \mathcal{J}_s(\phi) \mathbf{V} = -m_d \mathbf{V}^T \mathbf{B}(\phi) \mathbf{V} < 0$ , introducing  $\mathbf{B}(\phi) = \mathbf{L}^d \mathbf{D}_g + \mathbf{D}_g (\mathbf{L}^d)^T$  and  $\mathbf{V}^T$  signifying the projection matrix onto the orthogonal complement of the flow-invariant linear subspace. For diffusive coupling with a symmetric Laplacian the linear flow-invariant manifold  $\phi_1^* = \dots = \phi_N^*$  is also the null-space of the Laplacian. In this case, the eigenvectors of the Laplacian that correspond to nonzero eigenvalues can be used to construct the projection matrix  $\mathbf{V}^T$ .

For example, in the case of  $N$  characters with symmetrical *all-to-all coupling* with  $\mathbf{L}^d = N\mathbf{I} - \mathbf{1}\mathbf{1}^T \geq 0$  we obtain  $\frac{1}{2} \mathbf{V}^T (\mathbf{L}^d \mathbf{D}_g + \mathbf{D}_g (\mathbf{L}^d)^T) \mathbf{V} = N \mathbf{V}^T \mathbf{D}_g \mathbf{V} > 0$  for  $\mathbf{D}_g > 0$ . In this case, the contraction rate is given by  $\rho_{min} = m_d \min_{\phi} (g(\phi)) \lambda_{\mathbf{L}^d}^+$ , with  $\lambda_{\mathbf{L}^d}^+ = N$ .

For general symmetric coupling with positive links with equal coupling strength  $m_d > 0$  a weak sufficient contraction condition can be derived (see Appendix B.3.2):  $\lambda_{min}^+(\mathbf{L}^d) / \lambda_{max}^+(\mathbf{L}^d) > (\max_{\phi} (g(\phi)) - \min_{\phi} (g(\phi))) / (\max_{\phi} (g(\phi)) + \min_{\phi} (g(\phi)))$ . This condition was also presented (in a weaker form) in my work<sup>212</sup> as  $\lambda_{min}^+(\mathbf{L}^d) / \lambda_{max}^+(\mathbf{L}^d) > \max_{\phi} (|g(\phi) - \text{mean}(g(\phi))|) / \text{mean}(g(\phi))$ , with  $\text{mean}(g(\phi)) = 1/T \int_0^T g(\phi) d\phi$ . Appendix B in this Thesis presents the full derivation for the necessary and sufficient conditions for positive definiteness of anticommutators of two symmetric real matrices. Based on Theorem 6 (B.3.3), the strong sufficient conditions for the partial contraction of the system are:  $\boxed{(1-\alpha)^2/(1+\alpha)^2 + (1-\beta)^2/(1+\beta)^2 < 1}$  with  $\alpha = \lambda_{min}^+(\mathbf{L}^d) / \lambda_{max}^+(\mathbf{L}^d)$  and  $\beta = \min_{\phi} (g(\phi)) / \max_{\phi} (g(\phi))$ . This sufficient condition permits to constrain the admissible coupling topologies dependent on  $g(\phi)$ , see the discussion at the end of Appendix B.3.4. Alternatively, it is also possible to introduce low-pass filtering in the control dynamics to increase the smoothness of the function  $g(\phi)$ , see<sup>213</sup>.



**Figure 4.10:** Self-organized reordering of a crowd with 16 characters. Control dynamics affects simultaneously direction, distance and gait phase. See [Demo<sup>7</sup>].

These stability bounds are illustrated by **Movie**<sup>11</sup> that shows convergent behavior of the characters when the contraction condition  $m_d > 0$ ,  $(\mathbf{L}^d)_s \geq 0$  is satisfied for all-to-all coupling.

**Movie**<sup>12</sup> shows the divergent behavior of a group when this condition is violated when  $m_d < 0$ . In these and the next demonstrations the actual values of interaction parameters  $m_d, m_z, m_\psi > 0$  (in cases, when they additionally satisfy the sufficient contraction conditions) were obtained by matching the corresponding convergence rates to those of the real human behavior in crowds<sup>334</sup>.

**3) Step size control combined with control of step phase:** The dynamics is given by equations (4.30) and (4.31) with  $m_d = 0$ . This dynamics defines a *hierarchically coupled* nonlinear system (of Eq.(4.4) type). While the dynamics would be difficult to analyze with classical methods, the dynamics for  $\mathbf{z}(t)$  that is given by equation (4.30) is partially contracting in the case of all-to-all coupling for any bounded external input  $\phi(t)$  if  $m_z > 0$ ,  $\mathbf{L}^z \geq 0$ , and  $\omega(t) > 0$ . These sufficient conditions can be derived from the positive-definiteness of the symmetrized Jacobian applying similar techniques as above. The Jacobian of this subsystem is  $\mathcal{J}(\phi, \omega) = -m_z \mathbf{D}_g^z(\phi, \omega) \mathbf{L}^z$ , with diagonal matrix  $(\mathbf{D}_g^z(\phi, \omega))_{ii} = \omega_i g(\phi_i + \phi_i^0)$  that is positive definite since  $g(\phi) > 0$  and  $\omega > 0$ . In the case of *all-to-all* symmetric coupling this subsystem is (exponentially) contracting and its relaxation rate is determined by  $\rho_z = m_z \min_\phi (g(\phi)) \lambda_{\mathbf{L}^z}^+$  for any input from the dynamics of  $\phi(t)$ , see equation (4.31). The dynamics of  $\phi(t)$  is contracting when  $(\mathbf{L}^\phi)_s \geq 0$  and its relaxation rate is  $\rho_\phi = k \lambda_{\mathbf{L}^\phi}^+$ , where  $\lambda_{\mathbf{L}^\phi}^+$  is the smallest non-zero eigenvalue of  $(\mathbf{L}^\phi)_s$  (see Part 1 of this section). The effective relaxation time of the overall dynamics is thus determined by the minimum of the contraction rates  $\rho_\phi$  and  $\rho_z$ . For the cases of general symmetric coupling with a symmetric Laplacian matrix  $\mathbf{L}^z$ , the partial contraction sufficient conditions for the  $\mathbf{z}(t)$  subsystem are:  $(1-\alpha)^2/(1+\alpha)^2 + (1-\beta)^2/(1+\beta)^2 < 1$  with  $\alpha = \lambda_{min}^+(\mathbf{L}^z)/\lambda_{max}^+(\mathbf{L}^z)$  and  $\beta = \min_\phi(g(\phi))/\max_\phi(g(\phi))$ . The last inequality is the corollary of Theorem 6 (B.3.3).

Demonstrations of this control dynamics satisfying the contraction conditions are shown

<sup>11</sup><https://goo.gl/iLBk6h> (tiny.cc/w79l5y)

<sup>12</sup><https://goo.gl/PcKqRm> (tiny.cc/s89l5y)

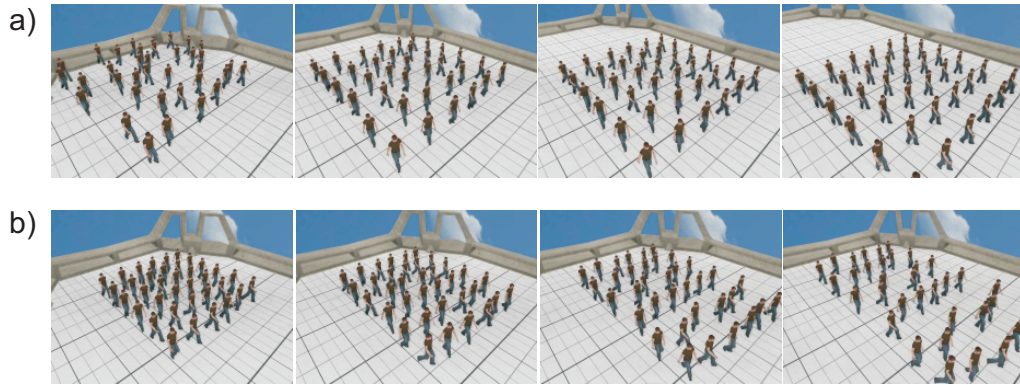


**Figure 4.11:** Control dynamics affects row distances via gait phase velocities. a) When the sufficient contraction conditions of the system dynamics are satisfied, the crowd organizes into an ordered formation where all agents synchronize their velocities. b) For a violation of the necessary contraction conditions the crowd formation behavior becomes unstable.

in **Movie**<sup>13</sup>, without control of step phase, and in **Movie**<sup>14</sup>, with control of step phase.

**4) Advanced scenarios:** A simulation of a system with stable dynamics including both types of speed control (via step size and step frequency) and step phase control is shown in **Movie**<sup>15</sup>. A larger crowd with 16 avatars simulated using the open-source animation engine **Horde3d**<sup>278</sup>, is shown in **Movie**<sup>16</sup>. In this simulation an additional dynamics for obstacle avoidance and control of heading direction was activated during the group formation period. Then this navigation dynamics was deactivated, and speed and position control according to the discussed principles result in the final coordinated behavior of the crowd. (For a larger crowd of 36 avatars see **Movie**<sup>17</sup>.) **Movie**<sup>18</sup> shows the divergence of the dynamics for  $m_d < 0$ , violating the necessary contraction condition for the step phase dynamics ( $\mathbf{L}^d \not\asymp 0$ ). The two simulations shown in **Movie**<sup>19</sup> and **Movie**<sup>20</sup> illustrate the convergence for a crowd with 49 avatars for two different values of the strength of the distance-to-step size coupling, the parameters of gait phase coupling remaining constant. Again, after a short initial period of speed control via step frequency, it is switched to speed control via step size, and at this moment the step synchronization based on direct phase coupling is switched on.

**5) Control of heading direction:** For the control of heading direction in the presence of couplings that affect the step phases, the contraction conditions can be derived from

<sup>13</sup><https://goo.gl/qzw7d4> (tiny.cc/489l5y)

<sup>14</sup><https://goo.gl/kHox6f> (tiny.cc/399l5y)

<sup>15</sup><https://goo.gl/AJmPaB> (tiny.cc/8aam5y)

<sup>16</sup><https://goo.gl/6Anoc8> (tiny.cc/qbam5y)

<sup>17</sup><https://goo.gl/dvJYss> (tiny.cc/ndam5y)

<sup>18</sup><https://goo.gl/fKqgKE> (tiny.cc/xeam5y)

<sup>19</sup><https://goo.gl/HJKUFp> (tiny.cc/ffam5y)

<sup>20</sup><https://goo.gl/6Jwgfp> (tiny.cc/hgam5y)



the result on *hierarchically coupled* systems discussed above in Part 3 of this section. For the analysis of the stability of the dynamics defined by equation (4.32) it is sufficient to analyze the contraction properties of the dynamics for the heading direction  $\psi$ , treating the additional term  $\omega(t)g^\psi(\phi(t))$  as an external input to the  $\psi$  subsystem.

Assuming a constant goal direction (see also the next Section 4.4.3), the uncoupled dynamics for one character, given by  $\dot{\psi} = -\omega(t)m_\psi \sin(\psi - \psi^{goal})$  is contracting in the intervals  $]\psi^{goal} - \pi + 2\pi n, \psi^{goal} + \pi + 2\pi n[$ ,  $n \in \mathbf{Z}$  for constant  $m_\psi > 0$ . (If  $\phi(t)$  is a smooth strictly increasing function of  $t$  with the substitution  $\psi(\phi(t)) = \psi(\phi)$  (and  $\omega(t) = d\phi/dt$ ) the last differential equation can be rewritten as:  $d\psi/d\phi = -m_\psi \sin(\psi(\phi) - \psi^{goal})$ ).

Another possibility to realize direction control is to feed back the circular mean average direction of all characters as joint control parameter  $\chi = \text{angle}(\frac{1}{N} \sum_i \exp[\psi_i \sqrt{-1}])$ . In this case the "quorum sensing" dynamics (cf.<sup>266</sup>) is given by

$$\dot{\psi}_i = \omega_i(t)(\sin(\chi - \psi_i) + g^\psi(\phi(t))), \forall i \in [1 \dots N], \quad (4.33)$$

which is suitable for the application of Theorem 4. This implies that the overall dynamics is contracting if the dynamics  $\dot{\psi}_i = \omega_i(t) \sin(\chi(t) - \psi_i)$  is contracting for any  $\chi(t)$ . The same Theorem guarantees contraction, when the consensus variable  $\chi$  is estimated by a low-pass filter (with time-constant  $\alpha > 0$ ):  $\alpha \dot{\chi} = -\chi + \text{angle}(\frac{1}{N} \sum_i \exp[\psi_i \sqrt{-1}])$ . The simulation shown in **Movie**<sup>21</sup> illustrates the consensus scenario defined by equation (4.33), (without a synchronization of gait cycles). In the next subsection I will present more detailed analysis of stability of Schöner-Dose navigational dynamics for crowds with more general coupling graphs, without introduction of a consensus signal.

### 4.4.3 Analysis of Schöner-Dose Dynamics of Heading Direction Control

#### Contraction properties for heading direction angle of a single agent

Lets consider first the single agent case  $\dot{\psi}(t) = f(\psi(t))$ , where the scalar  $\psi$  is the heading direction angle and in particular  $f(\psi) = -\sin(\psi)$ . This system has a stable stationary point at  $\psi = 0$  and unstable point at  $\psi = \pi$ . Following Ch. 3.9 in<sup>183</sup>, we find the local coordinate system  $\Theta(\psi)$  in the  $\psi$  domain, for which the resulting local symmetrized Jacobian  $\mathcal{J}_s(\psi) = (\mathcal{J}(\psi) + \mathcal{J}(\psi)^T)/2 < 0$  is negative in the new metric  $\mathbf{M}(\psi) = \Theta^T(\psi)\Theta(\psi)$  (and not explicitly dependent on time). The resulting PDE is:

$$\frac{\partial \Theta(\psi)}{\partial \psi} \cdot f(\psi) + \Theta(\psi) \frac{\partial f(\psi)}{\partial \psi} = \mathcal{J}(\psi)\Theta(\psi) \quad (4.34)$$

<sup>21</sup><https://goo.gl/PrCrAU> (tiny.cc/7gam5y)

Then, taking a constant desired  $\mathcal{J} = -\mathbf{I}$ , we need to solve (in our one dimensional case it is an ODE):

$$\frac{d\Theta(\psi)}{d\psi}f(\psi) + \Theta(\psi)\frac{df(\psi)}{d\psi} = -\Theta(\psi) \quad (4.35)$$

finding  $\Theta(\psi)$ , in our case, a scalar function of  $\psi$ . With  $f(\psi) = -\sin(\psi)$ :

$$\frac{d}{d\psi}(-\sin(\psi)\Theta(\psi)) = -\Theta(\psi) \quad (4.36)$$

Integrating with  $\Theta(0) = 1/2$  leads to  $\Theta(\psi) = 1/(1 + \cos(\psi))$ . The resulting metric is singular at  $\psi = \pi + 2\pi n$ ,  $n \in \mathbf{Z}$ , so that the contraction regions are  $]2n\pi - \pi, 2n\pi + \pi[$ . Schöner-Dose dynamics<sup>277</sup> uses  $f(\psi) = -\sin(\psi)\exp(-k\psi^2)$  for some  $k > 0$ , where the gaussian shunting term is evaluated for the main component part of  $\psi \in [-\pi, \pi]$ . If, in general, we have a dynamics in the form of  $f(\psi) = -\sin(\psi)g(\psi)$  for some periodic  $g(\psi) > 0$  with  $\psi \in [-\pi, \pi]$ , then:

$$\frac{d}{d\psi}(-\sin(\psi)g(\psi)\Theta(\psi)) = \mathcal{J}(\psi)\Theta(\psi) \quad (4.37)$$

Setting  $\tilde{\Theta}(\psi) = \Theta(\psi)g(\psi)$  and  $\mathcal{J}(\psi) = -g(\psi) < 0$ , we arrive at a similar equation as before:

$$\frac{d}{d\psi}(\sin(\psi)\tilde{\Theta}) = \tilde{\Theta} \quad (4.38)$$

with partial solution  $\tilde{\Theta}(\psi) = 1/(1 + \cos(\psi))$ , so that  $\Theta(\psi) = 1/(g(\psi)[1 + \cos(\psi)])$ , where the denominator has zeros only at  $\Theta(2n\pi + \pi) = 0$ , and the contracting regions are  $]2n\pi - \pi, 2n\pi + \pi[$  as before.

### Asymptotic stability of multi-agent heading direction angles coupling

We now consider multi-agent consensus dynamics for  $f(\psi) = -\sin(\psi)$ , for all-to-all symmetric coupling of  $N$  agents with constant strength  $k > 0$ :

$$\dot{\psi}_i = -\frac{k}{N} \sum_{j=1}^N \sin(\psi_i - \psi_j), \forall i, j \in [1 \dots N] \quad (4.39)$$

Introducing the potential function:

$$U(\boldsymbol{\psi}) = -\frac{k}{2N} \sum_{i=1}^N \sum_{j=1}^N \cos(\psi_i - \psi_j) \quad (4.40)$$

we obtain:  $\dot{\psi}_i = -\frac{\partial U}{\partial \psi_i}$  and the potential  $U(\boldsymbol{\psi})$  has minima at  $\forall i, j: \psi_i = \psi_j + 2n\pi, \forall n \in \mathbf{Z}$ . Since  $\frac{dU}{dt} = \sum_{j=1}^N \frac{\partial U}{\partial \psi_j} \frac{d\psi_j}{dt} = -k \sum_{j=1}^N \left(\frac{\partial U}{\partial \psi_j}\right)^2 \leq 0$  (with  $\frac{dU}{dt} = 0$  at prescribed minima and

strictly negative in some finite area around them), then  $U(\psi)$  plays the role of a *Lyapunov's function*. Next we consider Schöner-Dose type coupling:

$$\dot{\psi}_i = -k \sum_{j=1}^N \sin(\psi_i - \psi_j) g(\psi_i - \psi_j), \forall i, j \in [1 \dots N] \quad (4.41)$$

In case of  $g(\cdot) > 0$  the periodic function  $f(\Delta\psi) = \sin(\Delta\psi)g(\Delta\psi)$  has two zeros at  $\Delta\psi = 0$  and  $\Delta\psi = \pi$ . It may be regarded as  $f(\Delta\psi) = -F'(\Delta\psi)$ , a derivative of a smooth periodic function  $F(\Delta\psi)$ . This function has a maximum at  $\Delta\psi = 0$  and a minimum at  $\Delta\psi = \pi$ . Again, we construct  $U(\boldsymbol{\psi}) = -k \sum_{i=1}^N \sum_{j=1}^N F(\psi_i - \psi_j)$ , which has global marginally stable manifold of minima at  $\forall i, j: \psi_i = \psi_j + 2n\pi, \forall n \in \mathbf{Z}$ . And  $U(\boldsymbol{\psi})$  has saddle points where some  $\psi_i$  differ by  $\pi n$  from the others. But again,  $\dot{\psi}_i = -\frac{\partial U}{\partial \psi_i}$  with  $\frac{dU}{dt} = -k \sum_{j=1}^N (\frac{\partial U}{\partial \psi_j})^2 < 0$  (outside minima of  $U(\boldsymbol{\psi})$ ), and  $U(\boldsymbol{\psi})$  is Lyapunov function of the system, assuring global marginal stability of the stable manifold.

For general diffusive coupling with coupling graph Laplacian  $\mathbf{L}$ :

$$\dot{\psi}_i = -k \sum_{j=1}^N \mathbf{L}_{ij} f(\psi_i - \psi_j), \forall i, j \in [1 \dots N] \quad (4.42)$$

where  $f(\psi_i - \psi_j)$  the same as above, we have:  $U(\boldsymbol{\psi}) = -k \sum_{i=1}^N \sum_{j=1}^N \mathbf{L}_{ij} F(\psi_i - \psi_j)$ , and  $\frac{dU}{dt} = -[\dot{\boldsymbol{\psi}}]^T (\mathbf{L} + \mathbf{L}^T) [\dot{\boldsymbol{\psi}}]$ , so:  $\frac{dU}{dt} \leq 0$  for  $\mathbf{L}_s = (\mathbf{L} + \mathbf{L}^T)/2 \geq 0$ .

### Contraction properties of multi-agent heading direction angle coupling

While the demonstration of the global asymptotic stability for Schöner-Dose dynamics is straightforward and simple due to the existence of a global Lyapunov function, the proof of contraction can be obtained (if not using nonlinear coordinate change) for a limited area around the stable stationary fixed point. Contraction analysis can also be done relative to other norms (see Lohmiller and Slotine 1998, Ch.3.7(II),<sup>183</sup>), such as  $\|\delta\mathbf{z}\|_{\text{inf}} = \max_i |\delta z_i|$  and  $\|\delta\mathbf{z}\|_1 = \sum_i |\delta z_i|$ , with associated balls defined accordingly. Using the same reasoning as in standard matrix measure results (see for details<sup>266</sup>), the corresponding convergence results are:

$$\frac{d}{dt} \|\delta\mathbf{z}\|_{\text{inf}} \leq \max_i (\mathcal{J}_{ii} + \sum_{j \neq i} |\mathcal{J}_{ij}|) \|\delta\mathbf{z}\|_{\text{inf}} \quad (4.43)$$

$$\frac{d}{dt} \|\delta\mathbf{z}\|_1 \leq \max_j (\mathcal{J}_{jj} + \sum_{i \neq j} |\mathcal{J}_{ij}|) \|\delta\mathbf{z}\|_1 \quad (4.44)$$

so that, to guarantee contraction we need diagonal dominance of the Jacobian matrix. Consider diffusive coupling with coupling graph Laplacian  $\mathbf{L}$  ( $\mathbf{L}_{ij} > 0, \forall i \neq j$ ) and  $k > 0$ :

$$\dot{\psi}_i = -k \sum_j \mathbf{L}_{ij} \sin(\psi_i - \psi_j) \quad (4.45)$$

The non-diagonal elements of the Jacobian matrix for this dynamics are  $\mathcal{J}_{ij} = k\mathbf{L}_{ij} \cos(\psi_i - \psi_j)$ , and the diagonal elements are:  $\mathcal{J}_{ii} = -k \sum_{j \neq i} \mathbf{L}_{ij} \cos(\psi_i - \psi_j)$ . The Jacobian is row-wise diagonally dominant when  $\sum_{j \neq i} \mathbf{L}_{ij} \cos(\psi_i - \psi_j) \geq \sum_{j \neq i} \mathbf{L}_{ij} |\cos(\psi_i - \psi_j)|$ , which is true if  $\forall(i, j) : |\psi_i - \psi_j| < \pi/2$ . Thus, the dynamics is *partially contracting* with respect to  $\|\cdot\|_{\text{inf}}$  norm in the area where  $|\psi_i - \psi_j| < \pi/2, \forall(i, j)$ . In case of a symmetric coupling graph Laplacian  $\mathbf{L} = \mathbf{L}^T > 0$  the resulting Jacobian is also column-wise diagonally dominant, and the dynamics is *partially contracting* with respect to the  $\|\cdot\|_1$  norm. The *partial contraction* with respect to the  $\|\cdot\|_2$  norm can be demonstrated (after change of variables) using the tools presented in Appendix B, Section B.3.

## 4.5 Warped Limit Cycle Attractors for Robotics Applications

A single Andronov-Hopf oscillator in polar coordinates ( $r^2 = x^2 + y^2, \phi = \arctan(y/x)$ ) is given by (Section 4.3.1):

$$\begin{cases} \dot{r} = r(1 - r^2) \\ \dot{\phi} = \omega \end{cases} \quad (4.46)$$

Changing the radial variable in polar coordinates to  $\rho = 1/r^2 > 0$ :

$$\begin{cases} \dot{\rho} = 2(1 - \rho) \\ \dot{\phi} = \omega \end{cases} \quad (4.47)$$

The stable attractor solution is a circle  $\rho = \text{const} = 1$ , but we can morph the limit cycle shape by making  $\rho$  dependent on  $\phi$ . In morphing we should preserve the limit cycle to be homotopically equivalent to the circle by looping around zero just once. In case of our autonomous (time-invariant) system, the corresponding vector field of tangential vectors for the trajectories in the phase plane must be aligned with the tangent vectors on the limit cycle. Let  $f(\phi) = \rho^*(\phi)$  be the desired new shape, with  $f$  a periodic continuous function of  $\phi$ . The tangent vector field on the limit cycle has a radial component with length proportional to  $f'_\phi = df/d\phi$ , while the orthogonal component is proportional to  $d\phi/d\phi \equiv 1$ . The tangent vector field for all trajectories in the phase plane must have the

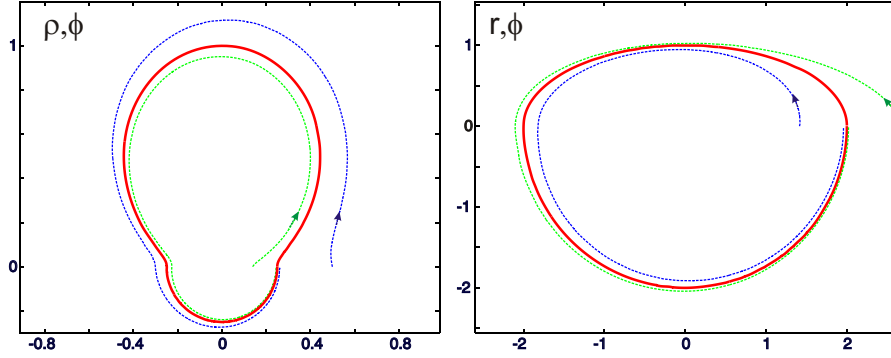


**Figure 4.12:** Demonstration of limit cycle attractor shape morphing. The attractor (depicted in red) is the concatenation of a half-ellipse and a half circle. Left panel shows the dynamics in the phase plane using polar coordinates  $(\rho, \phi)$ . The resulting phase space with polar coordinates  $(r, \phi)$  is at the right. See explanation of the variables in the text.

same directions to be locally “parallel” to the attractor line if translated along the radial rays, and in addition the dynamics must have the contracting component. The simplest form of warped shape attractor preserving the autonomy of the  $\phi$ -dynamics ( $\dot{\phi} = const = \omega$ ) is, with some  $\alpha > 0$ :

$$\frac{d\rho}{d\phi} = \alpha[f(\phi) - \rho] + \omega f'_{\phi} \quad (4.48)$$

where we made a linear change of variables, since  $\phi(t) = \omega t + \phi_0$ , making  $\phi$  our scaled time coordinate, (e.g. with  $\phi_0 = 0$ ).

The example of morphing the limit cycle shape is presented on Fig. 4.12, where we used half of a circle for the lower half-plane ( $r^* = 2$ , for  $\phi \in [\pi; 2\pi[$ ) and half of an ellipsoid for the upper half-plane in polar coordinates of  $(r, \phi)$ , appropriately translated into  $f(\phi)$  in polar coordinates of  $(\rho, \phi)$ . In  $(r, \phi)$  coordinates for  $\phi \in [0; \pi[$  the desired half-ellipsoid is defined by:  $r^* = 2/\sqrt{\cos^2(\phi) + 4\sin^2(\phi)}$  (vertical half-axis is equal to 1, and horizontal one is equal to 2), and the desired  $\rho^* = 1/(r^*)^2$ . The new convergence rate was made proportional to a constant  $\alpha > 0$ . The system is contracting for  $\rho$  in the whole phase space excluding the zero-point, since its Jacobian is  $\mathcal{J}_{\rho} = -\alpha < 0$ .

In the second example we preserve the circular shape of the limit cycle attractor (for  $\rho^* = 1/4$ ,  $r^* = 1/\sqrt{\rho^*} = 2$ ), but we morph the convergence rate coefficient  $\alpha(\phi) > 0$ , which is a periodic function of  $\phi$ , taking a small value of  $\alpha = 0.04$  for upper hemiplane (which is  $\phi \in [0; \pi[$ ) and large value of  $\alpha = 0.8$  for lower half-plane ( $\phi \in [\pi; 2\pi[$ ), see Fig. 4.13. Thus (now  $f'_{\phi} = 0$ ):

$$\frac{d\rho}{d\phi} = \alpha(\phi)[1/4 - \rho] \quad (4.49)$$

The system is contracting as its Jacobian is  $\mathcal{J}_{\rho} = -\alpha(\phi) < 0$  for any  $\alpha(\phi) > 0$ . Thus, we can establish any desired varying convergence rate  $\alpha(\phi) > 0$  for the system in  $(\rho, \phi)$

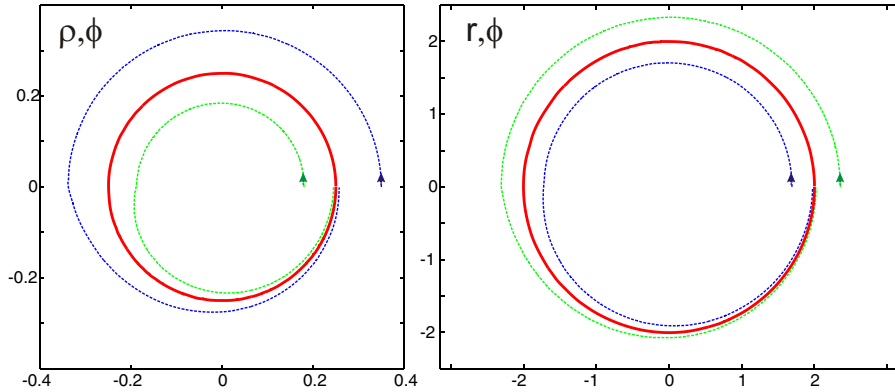


**Figure 4.13:** Demonstration of warping of the convergence dynamics by variable contraction rates in upper and lower hemiplanes of the phase space. The attractor is the circle ( $r = \text{const} = 2$ ,  $\phi \in ]0, 2\pi[$ ) depicted in red. Left panel shows the dynamics in the phase plane using polar coordinates  $(\rho, \phi)$ , the resulting phase space with polar coordinates  $(r, \phi)$  is at the right.

coordinates, or derive it from the desired varying convergence rate in  $(r, \phi)$  coordinates, while the dynamics remains contracting.

We saw that by decoupling the  $\phi$  and  $r$  dynamics of the Andronov-Hopf oscillator we have an opportunity to morph its shape and convergence rate as functions of phase. Thus, when we couple such warped oscillators by their phases (Section 4.3.2), assuming that the coupling results in partial contraction of phase dynamics, the overall system is partially contracting. The last is due to the system’s hierarchical coupling structure (Section 4.2.1, Ch.3.8.3 in<sup>183</sup>): the phase dynamics is not affected by the radial dynamics, and the radial dynamics is contracting for any phase dynamics regarded as external input.

We designed a general family of warped Andronov-Hopf oscillators in collaboration with colleagues from EPFL, Lausanne<sup>5</sup>. The family of warped Andronov-Hopf oscillators was used as DMPs<sup>132</sup> in a general architecture of interconnected CPGs (similar to<sup>130</sup>). We used the linear symmetric diffusive coupling between the phases of CPGs, with the linear phase dynamics of each component (see Section 4.3.2).

#### 4.5.1 Equi-affine Transform Preserving “Power Laws” and Partial Contraction for the Modeling and Control of Walking

In this section I present the work done in collaboration with LAAS/CNRS in Toulouse, France and the Weizmann Institute of Science in Rehovot, Israel. The task is to design a kinematic pattern synthesis architecture to control humanoid robot navigation behavior, varying its walking speed and velocity. The kinematic pattern consists of a predefined walking trajectory and velocity along this trajectory. This pattern must satisfy the desired

kinematic properties - the different “*power laws*”, which constrain the propagation velocities as a specific function of the path curvature. In order to control the real humanoid biped online, the kinematic policy must be defined for the whole phase space - i.e. it is a vector field defined at each position of the biped in the 2D workspace plane where the navigation path is defined. Thus, the vector field dictates the desired velocity at every point of the workspace plane, and drives the biped back towards the prescribed path in a stable way.

The main idea is to build the vector field from a kinematic policy that is uniformly stably convergent towards the desired trajectory for all perturbations experienced by biped. The work is presented in conference proceedings<sup>148</sup>. The walking paths, which we tested in this work are ellipses of different shapes. We design the policy vector field to be uniformly partially contracting in some neighborhoods of these elliptic paths. Thus, every trajectory which converges to the nominal elliptic path, is exponentially stable in its neighborhood. On the other hand every such transient trajectory must satisfy the power law prescribed uniformly for any trajectory in some finite region of the workspace including attractor. We solve the task by using the canonical dynamical system, the Andronov-Hopf oscillator, which has a circular limit cycle attractor trajectory. Using the circular symmetry of the phase portrait of this dynamical system we re-scale the velocity vector field, using a scaling factor dependent only on the distance to the center of the phase plane, which guarantees the desired power law. We prove that such rescaled velocity vector field remains uniformly contracting with respect to the radial variable in a circular strip around the circle attractor of the Andronov-Hopf oscillator. As a next step we introduce the equi-affine transform mapping the phase plane dynamics onto the workspace plane. By doing this we create any elliptic shape of the desired path in the workspace plane and simultaneously preserve the desired power law along every trajectory dictated by the vector field policy. This *power law preservation* property is substantial for equi-affine transforms of the Euclidean plane<sup>24,90,244</sup>. Thus, using the equi-affine transformed Andronov-Hopf oscillators with radially rescaled velocities, we guarantee that the power law is enforced for every trajectory, (not only on the attractor trajectory), and simultaneously we guarantee the partial contraction property of the image of the equi-affine map of the vector field, since the designed underlying canonical system is made uniformly partially contracting.

### **Power laws observed in human motion analysis**

The speed of human motion is characterized by the *one-third power law* as the movement speed  $v$  decreases when curvature  $\kappa$  increases, following the quantitative relation  $v = \gamma\kappa^{-\beta}$ , with  $\gamma$  the piecewise constant velocity gain factor and  $\beta = 1/3$  the power law exponent. It appears for different end effectors under general settings: for drawing<sup>164</sup> and pointing<sup>283</sup> hand motion, smooth pursuit eye movements<sup>71</sup>, leg motions<sup>136</sup>. For locomotion along

elliptic trajectories, it was found that the center of the head obeyed the one-third power law<sup>326</sup>. Power law behaviors appear to emerge from jerk minimization<sup>251,328</sup>, cf. also<sup>32,128</sup>. Alternatively, the specific one-third power law, which is equivalent to moving with a constant equi-affine speed<sup>244</sup>, may result from equi-affine metrics used by the human brain<sup>90</sup>, possibly in a mixture with Euclidean and full affine metrics<sup>24</sup>.

The goal of the study with a humanoid biped robot was to investigate experimentally the different walking gaits derived from different power laws in order to compare the resulting dynamic properties and power consumption of the robot and to optimize the kinematic driving policies for the gait pattern generations regarding the effectiveness of the resulting performance. The Walking Pattern Generator used in this research is described in detail in Chapter 3 before.

### Polar morphed Andronov-Hopf oscillator

The Andronov-Hopf oscillator in inverted polar coordinates is given as:

$$\begin{cases} \dot{\phi} = \omega \\ \dot{\rho} = \alpha(1 - \rho) \end{cases} \quad (4.50)$$

Here  $\rho = \frac{1}{r^2} = \frac{1}{x^2+y^2}$ ,  $\phi = \tan^{-1}(\frac{y}{x})$ , where  $x, y$  are Cartesian coordinates of the point in the phase plane.  $\rho$  and  $\phi$  are describing the radial (inverted squared radius) and the angular dynamics correspondingly, and  $\omega, \alpha > 0$  positive constants. For any reference path of the limit cycle attractor,  $r_0(\phi)$ , given in polar coordinates, this oscillator can be morphed as shown above:

$$\begin{cases} \dot{\phi} = \omega \\ \dot{\rho} = \alpha(F(\phi) - \rho) + \omega \frac{dF}{d\phi} \end{cases} \quad (4.51)$$

This is still partially contracting with respect to  $\rho$ , with  $F(\phi) = \frac{1}{r_0^2(\phi)}$  depending on the limit cycle shape.

Next we focus on regularization of the phase portrait with a power law  $v = h(\kappa) = \gamma\kappa^{-\beta}$ , with  $\gamma$  a global constant and  $\beta$  the exponent value. We constrain the power law application to the ring area of the phase plane around the circle attractor of the Andronov-Hopf oscillator, where all trajectories have positive curvature, guaranteeing that the regularization process will result in finite speeds, see details in<sup>148</sup>. The phase plane portraits of equi-affine transformed oscillators with different power law regularization are depicted on Fig. 4.14.



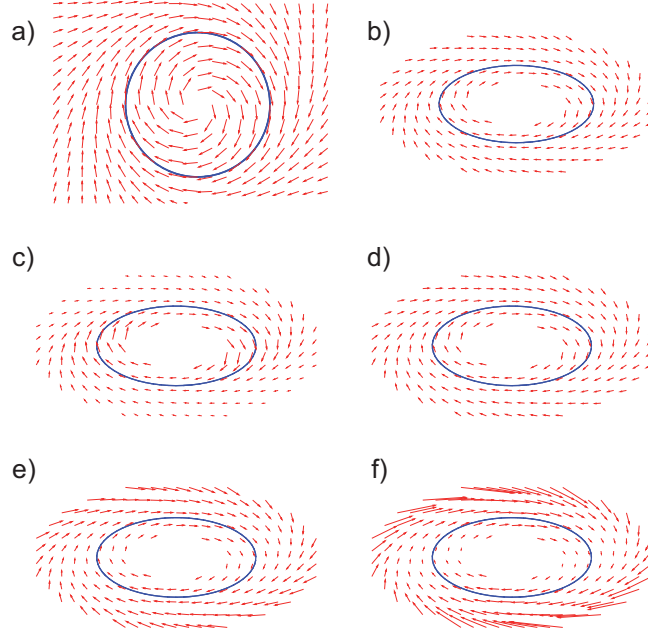


**Figure 4.14:** Morphing and regularization of an Andronov-Hopf oscillator. a) The unit cycle oscillator, b) an elliptic morphing by equi-affine transform of the phase plane, and c)-f) four power law regularizations according to  $\beta = -1/3, 0, 1/3, 2/3$  power laws. The figure is adopted from<sup>148</sup>.

### The power law circularly regularized Andronov-Hopf oscillator is radially contracting

For the unit circle Andronov-Hopf oscillator, the power law function depends on curvature which is independent of  $\phi$ . Denote  $\tilde{\rho} = \rho - 1 = \frac{1}{r^2} - 1$  and  $h(\tilde{\rho}) \geq C > 0$  a constant times the regularization power law function. Since  $h(\tilde{\rho}) > 0$  in the area where the curvature is strictly positive, the regularized dynamics are:

$$\begin{cases} \dot{\phi} = \omega g(\tilde{\rho}) \\ \dot{\tilde{\rho}} = -\tilde{\rho} h(\tilde{\rho}) \end{cases} \quad (4.52)$$

With  $g(\rho) = \frac{h(\tilde{\rho})}{r}$ . The  $\tilde{\rho}$  dynamics are independent of  $\phi$ . The Jacobian of the  $\tilde{\rho}$  subsystem is  $\mathcal{J} = -(h(\tilde{\rho}) - \tilde{\rho}h'(\tilde{\rho}))$ , and after the coordinate change  $\Theta(\tilde{\rho}) = \frac{1}{h(\tilde{\rho})}$  (see<sup>183</sup>) it is:

$$\begin{aligned} \mathcal{J}_\Theta &= (\dot{\Theta} + \Theta \mathcal{J}) \Theta^{-1} = \\ &= \left( \frac{h' \tilde{\rho}}{h} + \frac{1}{h} (-h - \tilde{\rho} h') \right) h \\ &= -h \leq -C < 0 \end{aligned} \quad (4.53)$$

The dynamics of  $\tilde{\rho}$  are therefore contracting. The dynamics of  $\phi$  are bounded in  $\tilde{\rho}$  and therefore it admits the nonlinear local  $\tilde{\rho}$  dependent coordinate system where  $\phi$  is indifferent, similar to the original oscillator. The method of coordinate transform used here is similar to the one presented in Section 4.4.3.

## Chapter 5

# Conclusions and Outlook

The presented PhD thesis addresses topics in learning of motor features from examples of human behavior. The challenge is to generate complex and structured human motion online and in an adaptive manner. For applications in robotics, the problem emerges that human motion typically violates the geometrical and physical constraints of humanoid robot systems. In this case, it is a nontrivial problem to decide which aspects of human motion should be reproduced by the robot system, while guaranteeing the robustness of the performance in the face of perturbations.

The problems treated in Chapter 2 of the thesis include the task of imitation learning of motor features at the level of individual motor acts and of their elementary combinations. The proposed approach combines ideas of optimal path planners in configurational space (*C-space*) with ideas of pre-selection of action sub-goals and motor means. The proposed hierarchical representation of observable and executable motion features (together with motion subgoals) allows for the learning of robot-specific motor actions. The top levels of motion feature selection are realized by interconnected Neural Fields, building up a hierarchy of coupled sensor and motor representations of actions. Such architecture is suitable for a conditioned imitation of motion and for the imitative learning of new motor skills from observing human actions. The employed imitation paradigm puts the highest preference on reproducing the goal of an observed action. The primacy of the goal over the action means allows coping with differences in embodiments and task constraints known as the 'correspondence problem' in robot imitation. Also, learning to understand an observed behavior as a goal-directed action enables the robot to reuse the stored information in new contexts and to acquire more abstract knowledge associated with that action. As a part of general architecture, I also described the real-time capable module for the kino-dynamic motion planning of goal-directed reaching movements with a robot arm of 7-8 degrees of freedom (*DoF*). This low level path planning and obstacle avoidance subsystem is uni-

versal for the very different geometry of an anthropomorphic robot arm, and it employs a version of a probabilistic roadmap path planner in adaptively re-sampled C-space. In this chapter I presented techniques of offline and online re-sampling of the posture spaces, which accelerate substantially the computation time needed for the solution of the path planning problem for 7-8 degrees of freedom robot arms. I also describe the extension of the high levels of proposed architecture exploiting the neural fields with transient excitatory dynamics and the augmented correlation-based learning rule, which is dependent on the activation level of postsynaptic neuron.

Chapter 3 of the thesis considers the motion transfer problem at the level of learning and synthesis of motor synergies, which define spatio-temporal combinations of motor features. The representation of spatio-temporal synergies of motion kinematics is based on unsupervised learning techniques, dimensionality reduction methods, including unconstrained and constrained anechoic mixture models, which can be considered shift-invariant generalizations of ICA and PCA. The problems considered in this chapter include those of synthesis of sequential multi-action behavior, both in goal-directed and spontaneous activities, and those of task-related action transitions. Here I describe the online reactive kinematic synthesis algorithm for complex full body motion, which is based on learned Dynamic Movement Primitives (*DMPs*), and which is implemented in two ways: as generative architecture for motion in a computer animation system, and as a part of a general control architecture for the humanoid biped robot HRP-2. For the last case, the approach integrates the kinematic synthesis algorithm in the full control architecture that guarantees dynamic balance of the biped during walking. Also, a number of machine learning techniques are described which establish online control of the motion by external variables. These methods include the learning of mappings from task parameters of goal-directed actions onto the manifold of weights and delays of kinematic motion primitives. The technique of semi-supervised learning in style-preserving bilinear regression is developed for the tasks of structural learning in motor control. The proposed solutions were tested successfully on a robot physics simulator as well as on the real HRP-2 humanoid robot, realizing the online control of walking combined with arm reaching and other tasks performed with the upper body. I demonstrate the feasibility of the proposed embedded kinematic control not only for flexible instantaneous behaviors, but also for online control of transitional multi-action sequences.

The next problem treated in Chapter 4 of this thesis is the implementation of multi-agent control strategies for crowds of agents that realize human full-body motion, and which are characterized by highly nonlinear agent models. I propose a number of control scenarios for crowds of walking avatars, including multiple-feedback controls for the

---

individual avatars based on their instantaneous positions, velocities, walking directions and gait phases. Basic control strategies for navigation of individual agents are derived from simplified models of human navigation. The flexible synthesis of complex transient behaviors requires elaborate tools from modern theories of nonlinear control in order to guarantee stable system behavior. Here, the framework of Contraction Theory was used as a new approach to nonlinear stability analysis and as the control synthesis tool. Contraction theory applied as a synthesis principle, allows the composability of control blocks in parallel or hierarchical schemes. I present a number of mathematical tools guaranteeing the sufficient contraction conditions for composite nonlinear systems. The derivations of these tools are presented in the main text and in the appendix of this thesis. The mathematical results obtained were successfully implemented for the control of interacting crowds of multiple agents driven by nonlinear dynamic motion primitives (DMPs, or networks of interconnected DMPs). The results are illustrated by a number of videos, while performance measures are evaluated and compared with the theoretical results. Additionally, the concept of a morphable oscillator and its applications are introduced in this chapter.

All the chapters are considering the problems of robust motion transfer from humans to artefacts.

The first Chapter 2 proposes a solution for goal-directed imitative motion planning based on a pre-learned repertoire of robot-specific motor acts, represented as pre-selections of subsets of arm configurations in C-space. For motion planning in new environment, those pre-selections are activated from the higher decision-making levels of the motor features hierarchy, where those activations can be triggered by environmental context cues or by the motor features cues demonstrated by human subject (teacher). On the lower level of motion planning, the pre-selection technique accelerates the planning process by means of a reduction of the search space. Nevertheless, when the online refinement of C-space is combined with iterative re-planning, the resulting planned trajectory is optimal, while staying close to the pre-selected trajectories bundle. This architecture provides the mechanism of copying action sub-goals and motion features on an abstract higher level, and allows the robot to re-use (and re-learn if necessary) its own repertoire of obstacle-avoiding arm reaches. Thus the architecture provides the solution to the 'geometric correspondence problem' in imitation of the arm reaching, transporting, placing acts and their simple combinations.

The next Chapter 3 focuses on transfer of the fine-structure of features of kinematic trajectories. The proposed approach reproduces the kinematic motion patterns very close to those demonstrated by a human actor, while providing superior naturalness of the motion in transitions between motor actions. The key solution proposed here, which ad-

addresses those two challenges simultaneously, is the use of an anechoic mixture model as a dimensionality reduction technique. The anechoic source signals represent spatio-temporal motion primitives. For some applications of computer animation those extracted primitives approximate the full body motion in a holistic manner. For applications in humanoid robotics I exploited the modular approximation by estimation of full body motion primitives, controlled by gait parameters, superimposed with upper body motion primitives, controlled by the parameters of arm reaching motion and by the reaching target position with respect to the trunk. The proposed modular step-wise approximation approach allows flexible control of arm reaching in any phase of the gait cycle. It allows a further extension of the architecture by introducing filtering of the lower body motion, in order to provide stability and robustness of the bipedal walking. The approach is implemented on the humanoid robot HRP-2, where the lower body motion (represented as Centre of Mass (*CoM*) and feet trajectories) is modified online using NMPC architecture<sup>220,221</sup>. This architecture provides dynamic stability of locomotion while taking into account the desirable upper-body motion as well. In this framework, the learning of the associations between gait and arm reaching parameters and the parameters of kinematic generative model is done using a set of trial trajectories generated by the whole architecture implemented on the OpenHRP physics simulator. This set of trial trajectories is generated to cover all combinations of different step sizes of sequentially adjacent steps in double-gait-cycle sequences (as for example in the drawer reaching task). Thus, this approach of controlling goal-specific spatio-temporal kinematic motion primitives in modular fashion has demonstrated an advantage in the architecture where the primal goal of stability of bipedal gait cycle should be achieved together with the robust reproduction of arm reaching movements during walking. The robustness of the total synthetic architecture has been demonstrated in several experiments described in this chapter.

The last Chapter 4 deals with the problems of imitation of collective motion of crowds of artificial agents. The individual navigation strategies of artificial agents are mimicked based on human examples, while the interactive and collective control strategies satisfy global stability properties. Again, the modular approach is shown to be advantageous here and is implemented in a hierarchical control architecture. The motion of the individual agents and their navigation strategy is generated using the kinematic motion synthesis architecture proposed in the previous chapter. The collective crowd control is based on Contraction Theory. This theory provides the tools of modular compositional control for ensembles of inter-connected non-linear dynamical systems. I derived the conditions for the stable combinations of step-size with gait phase synchronisation control and for other compositional schemes, while implementing a variable topology of agents' interactions. Here, the derived sufficient conditions for the uniform exponential stability of the com-

---

posite non-linear system guarantees the global exponential convergence of the total crowd behavior, while taking into account the wide range of variability of agents' behavior in different phases of motion.

The modularity-based approaches to complex full-body motion synthesis as proposed in this thesis can be extended in several ways.

The subsumption architecture proposed in Chapter 2 admits interesting extensions. First, the higher level planners, modelled as networks of interconnected Neural Fields, may be extended to represent the semantic networks of inter-dependent motor acts as coupled to the corresponding motor subgoals networks. During the execution of multi-action sequences some planned motor acts may possibly fail. In such scenarios error-correcting re-planning can be performed online by such an extended bi-layered architecture as was shown in pilot experiments. A second possible direction of research is distributed multi-agent planners. In cases when agents participating in a single collaborative task have the same configuration state space planners, the agents may still have limited individual information about the global environment. The information exchange and update takes place only during the execution. Here, the update of a global value-function of the task results from an active inference during execution, similar to so-called 'inverse reinforcement learning'. Such distributed planners need an extensive analysis of convergence and stability properties of the online updating-and-replanning algorithms.

Similar future research directions can be proposed for the DMP-based online kinematic planners of Chapter 3. E.g. for the problem of mutual interaction of separate controllers for the lower and the upper body parts in walking and arm-reaching tasks. Here, the arm reaching controller that affects the upper-body DoFs, operates in a trunk-related local coordinate frame. But the arm configuration changes due to this control, and also influences the CoM dynamics, which is overcompensated by WPG control. The last, in its turn, affects the trunk position and tilt. For the proposed architecture for the HRP-2 humanoid, the instantaneous agreement between controllers is achieved via the hierarchical framework of Stack-of-Tasks, using a QP-solver<sup>221,300</sup>, such that the performed goal-related arm reaching stays as precise as possible in global task-related coordinates. However, the problem of stable synthesis of spatial and temporal superpositions of versatile behaviors in changing environment remains unsolved for more general scenarios.

The Contraction Theory methods developed in the last Chapter 4 need to be extended for scenarios involving modular controllers of non-linearly interacting body parts, as described above. As next possible extensions, Contraction Theory methods could also be developed for new multi-agent scenarios, involving the delayed communication between

## 5. Conclusions and Outlook

---

the agents and for cases when the agents are dynamically controlled robots interacting in joint collaborative tasks in shared workspace.



# Appendix A

## Some Facts from Algebraic Graph Theory

### A.1 Definitions and Facts from Algebraic Graph Theory

For a graph  $\mathbf{G} = \mathbf{G}(V, E)$  we have:  $V$  is a non-empty *vertex* (node) set and  $E$  is an *edge* (link) set. If there is a direction of flow associated with each edge,  $\mathbf{G}$  is called a directed graph, otherwise it is undirected. If positive weights are associated with the directed or undirected edges, the graph is called weighted. The *adjacency matrix* of a non-weighted graph of order  $n$  is defined as

$$\mathbf{A}(\mathbf{G}) = [a_{ij}] \in R^{n \times n}$$

where  $a_{ij} = 1$  for all  $i \neq j$  if  $(i, j) \in E$ , otherwise  $a_{ij} = 0$ . For weighted undirected graphs  $a_{ij} = a_{ji} \geq 0$ .

The *vertex degree matrix* (also called *valency matrix*):

$$\mathbf{D}(\mathbf{G}) = \text{diag}(d_1, \dots, d_n) \in R^{n \times n}$$

is a diagonal matrix with  $d_i = \sum_j a_{ij}$ .

The matrix

$$\mathbf{L}(\mathbf{G}) = \mathbf{D} - \mathbf{A} \tag{A.1}$$

is defined as *Laplacian matrix* of the graph  $\mathbf{G}$  (sometimes called *admittance matrix*, *Kirchhoff matrix* or *discrete Laplacian*). For an undirected graph  $\mathbf{G}$  with order  $n$ ,  $\mathbf{L}$  is symmetric and positive semi-definite. The first eigenvalue is always zero, corresponding to the eigenvector  $1/\sqrt{n}[1, 1, \dots, 1]^T = \frac{1}{\sqrt{n}}\bar{\mathbf{1}}$  - since all the row-sums of  $\mathbf{L}(\mathbf{G})$  are 0s (as  $d_i = \sum_j a_{ij}$ ).

Denoting  $c$  as the number of connected components of  $\mathbf{G}$ ,

$$\text{rank}(\mathbf{L}) = n - c$$

The second minimum eigenvalue of the graph Laplacian,  $\lambda_2 = \lambda_2(\mathbf{L})$  is called the *algebraic connectivity*, which is zero if and only if the graph is not connected<sup>108</sup>. The multiplicity of the zero eigenvalue equals the number of connected components of the graph<sup>10</sup>.

An orientation of an undirected graph is an assignment of a direction to each edge. Assign an arbitrary orientation  $\sigma$  to an undirected graph  $\mathbf{G}$ . We get the *incidence matrix*:

$$\mathbf{Q} = \mathbf{Q}(\mathbf{G}^\sigma) = [q_{ij}] \in R^{n \times \tau} \quad (\text{A.2})$$

where  $\tau$  is the number of the links in  $E$ . For each oriented link  $k$  which starts from node  $i$  and ends at node  $j$ , we have  $q_{ik} = 1$  and  $q_{jk} = -1$ . All the other entries of  $\mathbf{Q}$  are equal to 0. Moreover,

$$\mathbf{L} = \mathbf{Q}\mathbf{Q}^T \quad (\text{A.3})$$

which holds for any choice of the orientation  $\sigma$ . Two non-isomorphic graphs might have the same eigenvalue spectrum of their Laplacian matrices<sup>72,110,196</sup>.

If the graph is weighted, we have the weighted Laplacian matrix:

$$\mathbf{L} = \mathbf{Q}\mathbf{W}\mathbf{Q}^T$$

where  $\mathbf{W} \in R^{\tau \times \tau}$  is a diagonal matrix with the  $k^{\text{th}}$  diagonal entry corresponding to the weight of the  $k^{\text{th}}$  link. For non-weighted graphs, from (A.3), the inner product  $(\mathbf{L}x, x) = (\mathbf{Q}\mathbf{Q}^T x, x) = (\mathbf{Q}^T x, \mathbf{Q}^T x) = \sum_{[ij] \in E} (x_i - x_j)^2$  (summation for all the edges  $[ij]$ ), and for the weighted case:

$$(\mathbf{L}x, x) = \sum_{[ij] \in E} a_{ij} (x_i - x_j)^2 \quad (\text{A.4})$$

We consider  $n$  coupled dynamical systems, each described by a first-order ODE:

$$\begin{cases} \dot{x}_1(t) = f_1(x_1, \dots, x_n) + \sum_{j \neq i} a_{1j} (x_j - x_1) \\ \dots \\ \dot{x}_n(t) = f_n(x_1, \dots, x_n) + \sum_{j \neq i} a_{nj} (x_j - x_n) \end{cases} \quad (\text{A.5})$$

where all  $a_{ij} = a_{ji} \geq 0$  - this is the case of *symmetric diffusive coupling*. Then the Jacobian matrix of the system is  $\mathcal{J} = \left[ \frac{\partial f_i(\mathbf{x})}{\partial x_j} \right] - \mathbf{L}(\mathbf{G})$ , with  $\mathbf{L}(\mathbf{G})$  the symmetric Laplacian matrix of the undirected coupling graph  $\mathbf{G}$ .

For non-symmetric diffusive coupling:  $a_{ij} \neq a_{ji}$ . This is the case of a *directed* diffusive coupling network. The coupling is called *balanced* if the weights of incoming links are equal to the weights of outgoing links at every vertex:  $\sum_{j \neq i} a_{ij} = \sum_{j \neq i} a_{ji}$ , the corresponding row-sums and column-sums of the adjacency matrix of the weighted coupling graph are equal. But the matrix  $\mathbf{L}$  in the Jacobian of the network dynamics  $\mathcal{J} = \left[ \frac{\partial f}{\partial \mathbf{x}} \right] - \mathbf{L}$  is not symmetric, though its row-sums as well as its column-sums are all zeros. We will call it the *Laplacian matrix of a directed graph*. In *Contraction Theory* we are interested in symmetrized Jacobians. If we symmetrize the corresponding Laplacian matrix of the directed balanced graph, we obtain a symmetric positive semidefinite matrix  $(\mathbf{L} + \mathbf{L}^T)/2$ , which is symmetric and has all properties of a graph Laplacian with the same number of nodes, but with the links weights the averaged weights of the forward and backward links connecting a pair of nodes<sup>242</sup>.

In the remainder of this Appendix we will consider only finite, undirected and non-weighted graphs. According to **Weyl's Theorem**, (Theorem 4.3.1 in<sup>125</sup>), if square matrices  $\mathbf{A}$  and  $\mathbf{B}$  are Hermitian and the eigenvalues  $\lambda_i(\mathbf{A})$ ,  $\lambda_i(\mathbf{B})$  and  $\lambda_i(\mathbf{A} + \mathbf{B})$  are arranged in increasing order, for each  $k = 1, 2, \dots, n$ , we have (as corollary to the *Courant-Fisher Min-max Theorem*, e.g. Ch.2, §44 in<sup>339</sup>)

$$\lambda_k(\mathbf{A}) + \lambda_1(\mathbf{B}) \leq \lambda_k(\mathbf{A} + \mathbf{B}) \leq \lambda_k(\mathbf{A}) + \lambda_n(\mathbf{B}) \quad (\text{A.6})$$

If  $\mathbf{L}$  is the Laplacian matrix of a connected undirected graph  $\mathbf{G}$ , then matrix  $\mathbf{L}$  has only one zero eigenvalue  $\lambda_1(\mathbf{L})$ . Let us add an undirected link to  $\mathbf{G}$  between the nodes  $i$  and  $j$ . Then the Laplacian matrix of the new graph becomes  $\mathbf{L} + \mathbf{E}^{[ij]}$ , where symmetric matrix  $\mathbf{E}^{[ij]}$  has ones in two places on the diagonal  $\mathbf{E}_{ii}^{[ij]} = \mathbf{E}_{jj}^{[ij]} = 1$  and minus ones at the corresponding off-diagonal positions  $\mathbf{E}_{ij}^{[ij]} = \mathbf{E}_{ji}^{[ij]} = -1$ , while all other entries of matrix  $\mathbf{E}^{[ij]}$  are zeros.  $\mathbf{E}^{[ij]}$  is a rank-1 matrix, and its first  $n - 1$  eigenvalues are zeros, the last and the largest one is equal to 2. Nevertheless, the first (the smallest) eigenvalue of new Laplacian matrix remains zero. But the second eigenvalue, the algebraic connectivity, is non-decreasing when adding the new link, according to Weyl's Theorem (A.6):  $\lambda_2(\mathbf{L}) \leq \lambda_2(\mathbf{L} + \mathbf{E}^{[ij]}) \leq \lambda_2(\mathbf{L}) + 2$ .

The last result can be improved based on the fact that the addition of matrix  $\mathbf{E}^{[ij]}$  is a rank-1 modification. In this case we have *interlacing* of the resulting eigenvalues, (Th.8.1.5

in<sup>109</sup>, Ch.2, §40-41 in<sup>339</sup>, Theorem 4.3.4 in<sup>125</sup>):

$$0 = \lambda_1(\mathbf{L}) = \lambda_1(\mathbf{L} + \mathbf{E}^{[ij]}) \leq \lambda_2(\mathbf{L}) \leq \lambda_2(\mathbf{L} + \mathbf{E}^{[ij]}) \leq \lambda_3(\mathbf{L}) \leq \dots \leq \lambda_n(\mathbf{L}) \leq \lambda_n(\mathbf{L} + \mathbf{E}^{[ij]}) \quad (\text{A.7})$$

which is Theorem 3.2 in<sup>199</sup>. Notice that the sum of eigenvalues of the Laplacian  $\sum_{i=1}^n \lambda_i(\mathbf{L}) = \text{trace}(\mathbf{Q}\mathbf{Q}^T) = \text{trace}(\mathbf{Q}^T\mathbf{Q})$  is equal on one hand to the twice number of edges of the unweighted graph and on the other hand (by the trace formula) equal to the sum of the degrees of all vertices of the graph:

$$\sum_{i=1}^n \lambda_i(\mathbf{L}) = 2|E| = \sum_i d_i \quad (\text{A.8})$$

Thus, in our case of adding one link to  $\mathbf{G}$ , we have  $\sum_{i=1}^n (\lambda_i(\mathbf{L} + \mathbf{E}^{[ij]}) - \lambda_i(\mathbf{L})) = 2$ , and at least one inequality  $\lambda_i(\mathbf{L}) \leq \lambda_i(\mathbf{L} + \mathbf{E}^{[ij]})$  in (A.7) must be strict<sup>199</sup>.

Dropping a link from an undirected graph results in nullifying the corresponding column of the incidence matrix  $\mathbf{Q}$ . The nonzero eigenvalues of  $\mathbf{L} = \mathbf{Q}\mathbf{Q}^T$  are the same as the nonzero eigenvalues of  $\mathbf{Q}^T\mathbf{Q}$ <sup>10</sup>. Further, nullifying a single column from the incidence matrix  $\mathbf{Q}$  results in reducing the rank of  $\mathbf{Q}^T\mathbf{Q}$  by 1, so that the new reduced matrix  $\mathbf{Q}^T\mathbf{Q}$  can be regarded as a principle submatrix of the old one. We have the following result concerning  $(n-1)$ -by- $(n-1)$  principle submatrices of a symmetric matrix of size  $n$ -by- $n$  (*Cauchy interlacing property*, as corollary to the *Courant-Fisher Min-max Theorem*, see: Th.4.3.8 in<sup>125</sup>):

**Cauchy's Interlacing Theorem:** If  $\mathbf{A}$  is a Hermitian matrix and  $\mathbf{B}$  is a principle submatrix of  $\mathbf{A}$ , then the eigenvalues of  $\mathbf{B}$  interlace the eigenvalues of  $\mathbf{A}$ .

Due to this theorem, by deleting a link from a graph, the new nonzero eigenvalues of the Laplacian matrix  $\mathbf{L}$  interlace the old ones, see<sup>322 54</sup>. This theorem also provides the interlacing property (A.7) for connected graphs.

**Generalized Cauchy's Interlacing Theorem:** Let  $\mathbf{A}$  be an  $n \times n$  real symmetric matrix and  $\mathbf{B}$  be an  $r \times r$ ,  $1 \leq r \leq n$ , principal submatrix of  $\mathbf{A}$ , obtained by deleting  $n-r$  rows and the corresponding columns from  $\mathbf{A}$ . If  $\lambda_1(\mathbf{A}) \leq \lambda_2(\mathbf{A}) \leq \dots \leq \lambda_n(\mathbf{A})$  and  $\lambda_1(\mathbf{B}) \leq \lambda_2(\mathbf{B}) \leq \dots \leq \lambda_r(\mathbf{B})$  are the eigenvalues of  $\mathbf{A}$  and  $\mathbf{B}$ , respectively, then for each integer  $k$  such that  $1 \leq k \leq r$ :  $\lambda_k(\mathbf{A}) \leq \lambda_k(\mathbf{B}) \leq \lambda_{k+n-r}(\mathbf{A})$ .

This generalized interlacing theorem is also corollary to the *Courant-Fisher Min-max Theorem*, see: Th.4.3.15 in<sup>125</sup>). The corollary from this generalized interlacing theorem is known as the *Poincaré separation theorem*, see<sup>125</sup>.

The last theorem established the interlacing property for the Laplacian eigenvalues of

two graphs, where one is obtained from another by dropping one vertex of degree  $n - r$ , see Th.3.1 in<sup>116</sup>.

The *Cartesian product* of two graphs  $\mathbf{G}_1 = (V_1, E_1)$  and  $\mathbf{G}_2 = (V_2, E_2)$  is the graph denoted as  $\mathbf{G}_1 \square \mathbf{G}_2 = (V_1 \times V_2, E)$ , such that  $((v_1, v_2), (w_1, w_2)) \in E$  if and only if either  $v_1 = w_1$  and  $v_2, w_2 \in E_2$  **or**  $v_1, w_1 \in E_1$  and  $v_2 = w_2$ . The Laplacian eigenvalues of the Cartesian product  $\mathbf{G}_1 \square \mathbf{G}_2$  of graphs  $\mathbf{G}_1$  and  $\mathbf{G}_2$  are equal to all the possible sums of eigenvalues of the two factors:  $\lambda_i(\mathbf{L}(\mathbf{G}_1)) + \lambda_j(\mathbf{L}(\mathbf{G}_2))$ ,  $i = 1, \dots, |V(\mathbf{G}_1)|$ ,  $j = 1, \dots, |V(\mathbf{G}_2)|$ ,<sup>88</sup>. And  $\lambda_2(\mathbf{L}(\mathbf{G}_1 \square \mathbf{G}_2)) = \min[\lambda_2(\mathbf{L}(\mathbf{G}_1)), \lambda_2(\mathbf{L}(\mathbf{G}_2))]$ . The adjacency matrix of the Cartesian product graph  $\mathbf{G}_1 \square \mathbf{G}_2$  is the *Kronecker sum* of their adjacency matrices:  $\mathbf{A}(\mathbf{G}_1 \square \mathbf{G}_2) = \mathbf{A}(\mathbf{G}_1) \otimes \mathbf{I}_{n_2} + \mathbf{I}_{n_1} \otimes \mathbf{A}(\mathbf{G}_2)$ , where  $\otimes$  is *Kronecker product* ( $\mathbf{A} \otimes \mathbf{B} = [a_{ij}\mathbf{B}]$ ), and the diagonal size of square matrix  $\mathbf{A}(\mathbf{G}_k)$  is denoted as  $n_k$ . The Laplacian matrix of the Cartesian product of two graphs is the Kronecker sum of their Laplacians.

The *tensor product* of two graphs  $\mathbf{G}_1 = (V_1, E_1)$  and  $\mathbf{G}_2 = (V_2, E_2)$  is the graph denoted as  $\mathbf{G}_1 \times \mathbf{G}_2 = (V_1 \times V_2, E)$ , such that  $((v_1, v_2), (w_1, w_2)) \in E$  if and only if  $v_1, w_1 \in E_1$  **and**  $v_2, w_2 \in E_2$ . The tensor product of two connected graphs is not always connected, it is connected if and only if both factors are connected and at least one factor is nonbipartite<sup>133</sup>. The adjacency matrix of the tensor product of two graphs  $\mathbf{G}_1 \times \mathbf{G}_2$  is the tensor product (Kronecker product) of their adjacency matrices  $\mathbf{A}(\mathbf{G}_1 \times \mathbf{G}_2) = \mathbf{A}(\mathbf{G}_1) \otimes \mathbf{A}(\mathbf{G}_2)$ , and its eigenvalues are all the pairwise products of the eigenvalues of those two adjacency matrices of factors. General solution for obtaining Laplacian eigenvalues of graphs tensor product in terms of eigenvalues of two Laplacians of the factors is not known, but a good approximation is given by<sup>273</sup>.

In<sup>88</sup> the important results on algebraic connectivity bounds are derived:

$$\lambda_2(\mathbf{L}(\mathbf{G})) \leq \frac{n}{n-1} \min \{d(i); i \in V(\mathbf{G})\},$$

$$\lambda_n(\mathbf{L}(\mathbf{G})) \geq \frac{n}{n-1} \max \{d(i); i \in V(\mathbf{G})\},$$

If  $\mathbf{G}_1$  is a spanning subgraph of  $\mathbf{G}_2$  then  $\lambda_2(\mathbf{L}(\mathbf{G}_1)) \leq \lambda_2(\mathbf{L}(\mathbf{G}_2))$ .

Another important inequality for the algebraic connectivity is obtained in<sup>198</sup>:

$$\lambda_2(\mathbf{L}(\mathbf{G})) \geq \frac{4}{n \text{diam}(\mathbf{G})}, \text{ where } \text{diam}(\mathbf{G}) \text{ is the diameter of } \mathbf{G}.$$

## A.2 Some Examples

Let  $K_n$  denote the complete graph on  $n$  vertices. Lemma 2 in<sup>10</sup> states: The eigenvalues of  $\mathbf{L}(K_n)$  are 0, with multiplicity 1, and  $n$ , with multiplicity  $n - 1$ . Indeed,  $\mathbf{L}(K_n) = n\mathbf{I}_n - \mathbf{J}_n$ , where  $\mathbf{I}_n$  is identity matrix of size  $n$ -by- $n$  and  $\mathbf{J}_n$  is the square matrix of all ones, of size

$n$ -by- $n$ . Thus, the vector  $\mathbf{1}_n$  of size  $n$  with all the components equal to 1 is the eigenvector with eigenvalue 0, and for all the other vectors  $\mathbf{u}$  orthogonal to it:  $\mathbf{J}_n \mathbf{u} = 0$ .

Let  $\bar{\mathbf{G}}$  denote the graph complimentary to  $\mathbf{G}$ . That is,  $\bar{\mathbf{G}}$  has the same set of vertices as  $\mathbf{G}$ , and the two vertices are joined by an edge in  $\bar{\mathbf{G}}$  if and only if they are not joined in  $\mathbf{G}$ . For graph  $\mathbf{G}$  with  $n$  vertices:  $\mathbf{L}(\mathbf{G}) + \mathbf{L}(\bar{\mathbf{G}}) = \mathbf{L}(K_n)$ . Vector  $\mathbf{1}_n$  is a zero-eigenvalue eigenvector for all these Laplacian matrices. If  $\mathbf{u}$  orthogonal to  $\mathbf{1}_n$  is the eigenvector of  $\mathbf{L}(\mathbf{G})$  with the eigenvalue  $\lambda$ ,  $\mathbf{L}(\mathbf{G})\mathbf{u} = \lambda\mathbf{u}$ , then  $\mathbf{L}(\bar{\mathbf{G}})\mathbf{u} = \mathbf{L}(K_n)\mathbf{u} - \mathbf{L}(\mathbf{G})\mathbf{u} = (n - \lambda)\mathbf{u}$ . Since the eigenvalues of  $\mathbf{L}(\bar{\mathbf{G}})$  are also non-negative, one must have  $\lambda \leq n$ .  $\lambda = n$  if and only if  $\mathbf{L}(\bar{\mathbf{G}})\mathbf{u} = 0$ , and the dimension of the space of such vectors  $\mathbf{u}$  is one less than the nullity of  $\mathbf{L}(\bar{\mathbf{G}})$ . Thus, the multiplicity of eigenvalue  $n$  of  $\mathbf{L}(\mathbf{G})$  is equal to one less than the number of connected components of  $\bar{\mathbf{G}}$ , see<sup>10</sup>.

The eigenvalues of standard Laplacian of the complete bipartite graph  $K_{m,n}$  on  $m + n$  vertices are:  $\{m + n, m, n, 0\}$  with multiplicities  $\{1, n - 1, m - 1, 1\}$  respectively<sup>10</sup>.

Consider the *star graph* of  $n + 1$  vertices and  $n$  edges  $\mathbf{G}$ , where the single central vertex is connected to all the other  $n$  vertices. Orient all the links towards central vertex, then the matrix  $\mathbf{Q}^T \mathbf{Q} = \mathbf{I}_n + \mathbf{J}_n$  has size  $n$ -by- $n$  and it has no zero eigenvalues (like any such matrix for a connected graph with tree structure, where the number of links is one less than the number of vertices). One eigenvalue of  $\mathbf{Q}^T \mathbf{Q}$  (which corresponds to the eigenvector  $\mathbf{1}_n$ ) equals to  $n + 1$  and the other  $n - 1$  eigenvalues equal 1 (they correspond to the eigenvectors orthogonal to  $\mathbf{1}_n$ ). Also, those are the  $n$  non-zero eigenvectors of Laplacian of the star graph of  $n + 1$  vertices.

If  $\mathbf{G}$  is the *cycle* (ring network) with  $n$  vertices, then the eigenvalues of  $\mathbf{L}(\mathbf{G})$  are  $4\sin^2(\pi k/n)$ ,  $k = 1, 2, \dots, n$ . The smallest non-zero eigenvalue is  $\lambda_2 = 4\sin^2(\pi/n) = 2(1 - \cos(2\pi/n))$ . The eigenvectors and eigenvalues of the cycle graph are computed in<sup>298</sup>, Lecture 2, Lemma 2.4.4. If  $\mathbf{G}$  is the *path* (chain network) with  $n$  vertices, the eigenvalues of  $\mathbf{L}(\mathbf{G})$  are  $4\sin^2(\pi k/(2n))$ ,  $k = 0, 1, \dots, n - 1$ . The smallest non-zero eigenvalue is  $\lambda_2 = 4\sin^2(\pi/(2n)) = 2(1 - \cos(\pi/n))$ . If  $\mathbf{G}$  is the *wheel* with  $n + 1$  vertices, the eigenvalues of  $\mathbf{L}(\mathbf{G})$  are  $n + 1, 1, 1 + 4\sin^2(\pi k/n)$ ,  $k = 1, 2, \dots, n - 1$ . The eigenvalues of the wheel graph can be computed by considering its complement, while taking into account the eigenvalues of the cycle graph with  $n$  vertices.

## Appendix B

# Stability Conditions for Non-linear Dynamical Systems

### B.1 Some Definitions and Facts from Matrix Analysis

A square matrix  $\mathbf{H} \in \mathbb{C}^{n \times n}$  is called *Hermitian* if  $\mathbf{H}^* = \mathbf{H}$ , where  $\mathbf{H}^*$  denotes the transposed and complex conjugate matrix. The real Hermitian matrix  $\mathbf{S} \in \mathbb{R}^{N \times N}$  is symmetric when  $\mathbf{S}^T = \mathbf{S}$ , where  $\mathbf{S}^T$  denotes matrix transpose. The eigenvalues of Hermitian matrices are real numbers <sup>(23,125)</sup>.

For the square, nonsingular and invertible matrix  $\mathbf{X}$ , the square matrices  $\mathbf{A}$  and  $\mathbf{B} = \mathbf{X}^{-1}\mathbf{A}\mathbf{X}$  are *similar*, and the conjugation by  $\mathbf{X}$  is called a *similarity transformation*. A similarity transformation preserves the eigenvalue spectrum.

The *inertia* of a Hermitian or real symmetric matrix is a triplet of the numbers of negative, zero and positive eigenvalues. Two real square matrices  $\mathbf{A}$  and  $\mathbf{B}$  are called *congruent* if there exists a real invertible matrix  $\mathbf{X}$ :  $\mathbf{B} = \mathbf{X}^T\mathbf{A}\mathbf{X}$ . *Sylvester's law of inertia* states that two congruent real symmetric matrices have the same inertia <sup>125</sup>.

A Hermitian (or real symmetric) matrix  $\mathbf{H}$  is called *positive definite* if for any non-zero complex vector  $\mathbf{x}$ :  $\mathbf{x}^*\mathbf{H}\mathbf{x} > 0$  (denoted as  $\mathbf{H} > 0$ ).  $\mathbf{H}$  is *positive semi-definite* (denoted as  $\mathbf{H} \geq 0$ ) if  $\mathbf{x}^*\mathbf{H}\mathbf{x} \geq 0, \forall \mathbf{x} \neq 0 \in \mathbb{C}^N$ . A Hermitian (or real symmetric) matrix  $\mathbf{H}$  is called *negative definite* if for any non-zero complex vector  $\mathbf{x}$ :  $\mathbf{x}^*\mathbf{H}\mathbf{x} < 0$  (denoted as  $\mathbf{H} < 0$ ).  $\mathbf{H}$  is *negative semi-definite* (denoted as  $\mathbf{H} \leq 0$ ) if  $\mathbf{x}^*\mathbf{H}\mathbf{x} \leq 0, \forall \mathbf{x} \neq 0 \in \mathbb{C}^N$ .

*Loewner order* <sup>184</sup> is the partial order defined by the convex cone of positive semi-definite matrices: if  $\mathbf{A}$  and  $\mathbf{B}$  are two Hermitian matrices,  $\mathbf{A} \geq \mathbf{B}$  if  $(\mathbf{A} - \mathbf{B})$  is positive semi-definite.

$\mathbf{A} > \mathbf{B}$  if  $(\mathbf{A} - \mathbf{B})$  is positive definite. In the following we denote  $\lambda_{min}(\mathbf{A})$  the minimal real eigenvalue of a Hermitian matrix  $\mathbf{A}$  and  $\lambda_{max}(\mathbf{A})$  is its maximal real eigenvalue. For two Hermitian matrices  $\mathbf{A}$  and  $\mathbf{B}$  we will use the sign  $\succ$  if the minimum eigenvalue of one matrix exceeds the maximum eigenvalue of another:  $\mathbf{A} \succ \mathbf{B}$  if  $\lambda_{min}(\mathbf{A}) > \lambda_{max}(\mathbf{B})$ , similarly  $\mathbf{A} \succeq \mathbf{B}$  if  $\lambda_{min}(\mathbf{A}) \geq \lambda_{max}(\mathbf{B})$ .

By definition, the positive definiteness must be tested with respect to non-zero complex vectors. The positivity of  $\mathbf{x}^T \mathbf{S} \mathbf{x}$  with respect to real vectors  $\forall \mathbf{x} \neq 0 \in \mathbb{R}^n$  does not suffice to guarantee positive definiteness with respect to any non-zero complex vector. But, for the specific case of real symmetric matrices ( $\mathbf{S} = \mathbf{S}^T$ ) we have for  $\forall \mathbf{x}, \mathbf{y} \in \mathbb{R}^N$ :

$$(\mathbf{x} - i\mathbf{y})^T \mathbf{S} (\mathbf{x} + i\mathbf{y}) = \mathbf{x}^T \mathbf{S} \mathbf{x} + \mathbf{y}^T \mathbf{S} \mathbf{y}$$

Thus,  $\mathbf{S} = \mathbf{S}^T > 0$  iff  $\mathbf{x}^T \mathbf{S} \mathbf{x} > 0, \forall \mathbf{x} \neq 0 \in \mathbb{R}^n$ . This means, that for real symmetric matrices we may test positive definiteness using real vectors only.

The principle of *biorthogonality*: if a square matrix  $\mathbf{M}$  has two different eigenvalues  $\lambda$  and  $\mu$ , then any left eigenvector of  $\mathbf{M}$  corresponding to  $\mu$  ( $\mathbf{y}$ , such that  $\mathbf{y}^* \mathbf{M} = \mu \mathbf{y}^*$ ) is orthogonal to any right eigenvector of  $\mathbf{M}$  corresponding to  $\lambda$  ( $\mathbf{x}$ , such that  $\mathbf{M} \mathbf{x} = \lambda \mathbf{x}$ ). On one hand:  $\mathbf{y}^* \mathbf{M} \mathbf{x} = \mathbf{y}^* (\lambda \mathbf{x}) = \lambda (\mathbf{y}^* \mathbf{x})$ , on the other hand:  $\mathbf{y}^* \mathbf{M} \mathbf{x} = (\mu \mathbf{y}^*) \mathbf{x} = \mu (\mathbf{y}^* \mathbf{x})$ , so that, if  $\lambda \neq \mu$ , then necessarily:  $\mathbf{y}^* \mathbf{x} = 0$ . If a square matrix of size  $N$  is real symmetric, and all its eigenvalues are distinct, then it has  $N$  pairwise orthogonal eigenvectors. In this case of a real symmetric matrix  $\mathbf{S}$  a decomposition can be written as  $\mathbf{S} = \sum_{i=1}^N \lambda_i \mathbf{v}_i \mathbf{v}_i^T$ , where  $\mathbf{v}_i$  are real eigenvectors corresponding to distinct real eigenvalues  $\lambda_i$  of  $\mathbf{S}$ .

For the symmetric real invertible matrices  $\mathbf{L}$  and  $\mathbf{D}$ , the spectra of the eigenvalues of  $\mathbf{LD}$  and  $\mathbf{DL}$  are the same. And if  $\mathbf{W}$  is a matrix whose columns are right eigenvectors of  $\mathbf{LD}$ , then  $\mathbf{DW}$  is a matrix whose columns are right eigenvectors of  $\mathbf{DL}$ .

**Remark 1.** For two symmetric real matrices  $\mathbf{S}_1 \succ \mathbf{S}_2$  ( $\lambda_{min}(\mathbf{S}_1) > \lambda_{max}(\mathbf{S}_2)$ ): from  $\mathbf{x}^T \mathbf{S}_1 \mathbf{x} > \mathbf{y}^T \mathbf{S}_2 \mathbf{y}, \forall \mathbf{x} \in \mathbb{R}^N, \|\mathbf{x}\|_2 = 1$ , and  $\forall \mathbf{y} \in \mathbb{R}^N, \|\mathbf{y}\|_2 = 1$  it follows  $\mathbf{x}^T (\mathbf{S}_1 - \mathbf{S}_2) \mathbf{x} > 0 \forall \mathbf{x} \neq 0 \in \mathbb{R}^N$  ( $\mathbf{S}_1 - \mathbf{S}_2$  is positive definite). And if  $\lambda_{min}(\mathbf{S}_1) > \max_i (|\lambda_i(\mathbf{S}_2)|)$ , then  $\mathbf{x}^T (\mathbf{S}_1 \pm \mathbf{S}_2) \mathbf{x} > 0 \forall \mathbf{x} \neq 0 \in \mathbb{R}^N$  ( $\mathbf{S}_1 \pm \mathbf{S}_2$  are positive definite).

When all the eigenvalues of a matrix  $\mathbf{A}$  have *negative* (*positive*) real part, such a matrix is said to be *negative* (*positive*) *stable*. The theorem of Lyapunov (<sup>186</sup>) states that  $\mathbf{A}$  is negative (*positive*) stable if and only if there exists a real symmetric positive definite matrix  $\mathbf{H}$ , such that  $\mathbf{A}^T \mathbf{H} + \mathbf{H} \mathbf{A}$  is negative (*positive*) definite. A stable matrix  $\mathbf{A}$  is said to be *diagonally stable* if there exists a full rank diagonal matrix  $\mathbf{D} > 0$ , for which  $\mathbf{A}^T \mathbf{D} + \mathbf{D} \mathbf{A} > 0$ . If  $\mathbf{A}$  is diagonally stable, then for each positive diagonal matrix  $\tilde{\mathbf{D}} > 0$ ,



the matrices  $\mathbf{A}\tilde{\mathbf{D}}$  and  $\tilde{\mathbf{D}}\mathbf{A}$  are also diagonally stable<sup>(19)</sup>. (The definitions for *D-stable* (14,104) and *S-stable* matrices and their relations to diagonally stable matrices (27) can be found elsewhere, e.g. see<sup>141</sup>).

## B.2 Lur'e-Persidskii Systems

Consider a system of  $N$  coupled dynamical systems, each one described by a first order ODE:

$$\dot{\phi}_i(t) = \sum_{j=1}^N A_{ij}(G(\phi_j(t)) - G(\phi_i(t))), \quad \forall i \in [1 \dots N] \quad (\text{B.1})$$

with  $A_{ij} = A_{ji} \geq 0$ ,  $A_{ii} = 0, \forall i, j \in [1 \dots N]$  time-constant coefficients. This form of coupling is called *symmetric diffusive* coupling with  $A$  the adjacency matrix of the coupling graph. Assume that the nonlinear function  $G(\phi)$  is differentiable and invertible with  $dG(\phi)/d\phi = g(\phi) > 0, \forall \phi$ . We also assume that it satisfies the conditions:  $G(0) = 0$ ,  $G(\phi)\phi > 0$ . Using  $\phi(t)$ , the vector with components  $\phi_i(t)$  we write the dynamics in vector notation as:

$$\dot{\phi} = -\mathbf{L}G(\phi) \quad (\text{B.2})$$

with time-constant matrix  $\mathbf{L}$  the Laplacian of the coupling graph, corresponding to the adjacency matrix  $A$ ,  $\mathbf{L}_{ij} = -A_{ij}$  for  $i \neq j$  and  $\mathbf{L}_{ii} = \sum_{j=1}^N A_{ij}$ .  $\mathbf{L}$  is a symmetric positive semi-definite matrix. In the following we consider connected coupling graph, in this case the single zero eigenvalue of  $\mathbf{L}$  corresponds to the eigenvector  $\bar{\mathbf{1}}/\sqrt{N}$ .

Next, I prove the asymptotic Lyapunov-type stability (cf.<sup>166</sup>) of the equilibrium consensus manifold, where  $\phi_i = \phi_j, \forall i, j$ , exploiting the *Diagonal Stability* approach (e.g.<sup>150</sup>). It is based on pioneering work of A.I. Lur'e<sup>(185)</sup>, E.A. Barbashin<sup>(18)</sup> and Persidskii<sup>(241)</sup> on Lyapunov's asymptotic and absolute stability for nonlinear systems.

**Lemma 1.** *The consensus manifold  $\phi_1 = \phi_2 = \dots = \phi_N$  of system (B.2) is asymptotically stable.*

Lemma 1 is proven by explicit construction of a Lyapunov function. For the function  $G(\tau)$  with properties as listed above, a *Persidskii-type integral*  $\int_0^t G(\tau)d\tau$  is a nonnegative convex function of  $t$ , and it equals zero only for  $t = 0$ . The average  $\bar{\phi}(t) = \frac{1}{N} \sum_i \phi_i(t)$  is constant in time  $\dot{\bar{\phi}}(t) = 0$  (due to  $A_{ij} = A_{ji}, \forall i, j$  in (B.1) and  $\mathbf{L}\bar{\mathbf{1}} = 0$  in (B.2)). Thus, we can introduce a *Persidskii-type* Lyapunov function  $V(\phi)$ , which equals zero  $V(\phi) = 0$  if and only if  $\phi_i = \phi_j = \bar{\phi}, \forall i, j$  (cf.<sup>150</sup>):

$$V(\phi) = \sum_i \Delta_{ii} \int_0^{\phi_i - \bar{\phi}} G(\tau)d\tau > 0 \quad (\text{B.3})$$

where  $\mathbf{\Delta} > 0$  is some full rank positive diagonal matrix. Taking into account  $\frac{d\bar{\phi}}{dt} = 0$  on each trajectory, compute  $\dot{V}(\phi) = dV(\phi)/dt = \sum_i [\partial V(\phi)/\partial(\phi_i - \bar{\phi})] \frac{d(\phi_i - \bar{\phi})}{dt}$ :

$$\dot{V}(\phi) = -G(\phi - \bar{\phi})^T (\mathbf{L}^T \mathbf{\Delta} + \mathbf{\Delta} \mathbf{L}) G(\phi - \bar{\phi}) \quad (\text{B.4})$$

$\dot{V}(\phi) \leq 0$ , if there exists such a full rank diagonal  $\mathbf{\Delta} > 0$ , that  $(\mathbf{L}^T \mathbf{\Delta} + \mathbf{\Delta} \mathbf{L}) \geq 0$  <sup>(150)</sup>. And  $\dot{V}(\phi) = 0$  only for  $\phi_i = \phi_j = \bar{\phi}, \forall i, j$ , exactly at the points where  $V(\phi) = 0$ . With our positive semi-definite symmetric  $\mathbf{L}$ , we may choose  $\mathbf{\Delta} = \mathbf{I}$ , which gives us the Lyapunov function B.3 and proves the asymptotic stability of the consensus manifold  $\forall i, j : \phi_i = \phi_j = \bar{\phi}$ .  $\square$

### B.3 Partial Contraction and its Necessary and Sufficient Stability Conditions

In this part I consider the necessary and sufficient conditions for positive definiteness of Lyapunov-Volterra type matrices, which are the anticommutators of two full rank real symmetric matrices. (The anticommutator of two square matrices  $\mathbf{A}$  and  $\mathbf{B}$  is defined as  $\mathbf{AB} + \mathbf{BA}$ .) Consider again the dynamical system of Persidskii-type (B.5). The *contraction analysis* of this system (see Ch. 4, Section 4.4.2) is the core of our analysis of stability of different scenarios of multi-agent self-organized behavior presented in this thesis.

$$\dot{\phi} = -\mathbf{L}G(\phi) \quad (\text{B.5})$$

Here, as above the time-constant square matrix  $\mathbf{L} \in \mathbb{R}^{N \times N}$  is the Laplacian of the coupling graph, and the nonlinear function  $G(\phi)$  is differentiable and invertible with  $dG(\phi)/d\phi = g(\phi) > 0$ , and it satisfies the conditions:  $G(0) = 0$ ,  $G(\phi)\phi > 0$ , as in the previous section.

In the framework of *Contraction theory* we analyse the sufficient conditions which guarantee the symmetrized Jacobian of the dynamical system to be uniformly strictly negative definite. In case of *partial contraction* towards a linear flow invariant manifold, which is a linear subspace of the whole phase space, (see Ch. 4, Section 4.2.2), we are interested in negative definiteness conditions for the Jacobian locally projected onto the orthogonal complement to this linear manifold. With the symmetric constant matrix  $\mathbf{L}$ , the symmetrized Jacobian matrix of (B.5) is

$$\mathcal{J}_s(\phi) = -(\mathbf{L}\mathbf{D}(\phi) + \mathbf{D}(\phi)\mathbf{L}) \quad (\text{B.6})$$

where matrix  $\mathbf{D}(\phi)$  is dependent on the current configuration, the point in phase space  $\phi$ . In the following part of this Appendix we denote this matrix as  $\mathbf{D} \in \mathbb{R}^{N \times N}$  (keeping in mind its variability). It is a full-rank diagonal matrix with strictly positive diagonal elements  $\mathbf{D}_{ii} = g(\phi_i) > 0, \forall i \in [1 \dots N]$ . In all the problems that we address,  $g(\phi)$  is a continuous function with values bounded to a positive interval  $0 < g_{min}(\phi) \leq g(\phi) \leq g_{max}(\phi)$ .

The sufficient stability conditions for the exponential convergence towards the flow-invariant manifold (the line subspace  $\phi_1 = \dots = \phi_N$ ) is:

$$\mathbf{V}^T(\mathbf{LD} + \mathbf{DL})\mathbf{V} > 0 \quad (\text{B.7})$$

where  $\mathbf{V}$  is a matrix whose columns are eigenvectors of  $\mathbf{L}$  corresponding to non-zero eigenvalues of the Laplacian  $\mathbf{L}$  and the single zero eigenvalue corresponds to the eigenvector  $\bar{\mathbf{1}}/\sqrt{N}$  in linear subspace of  $\phi_1 = \dots = \phi_N$ . Lets denote the minimal zero eigenvalue of  $\mathbf{L}$  as  $\lambda_1$  and all other positive eigenvalues of  $\mathbf{L}$  as  $0 < \lambda_2 = \lambda_{min} \leq \dots \leq \lambda_i \leq \dots \leq \lambda_N = \lambda_{max}$ . The sufficient stability conditions (B.7) must hold for any admissible matrix  $\mathbf{D}$ . In transient states of the convergence towards the flow-invariant manifold this diagonal matrix may take all the values of admissible interval  $g(\phi)$ :  $0 < g_{min}(\phi) \leq \mathbf{D}_{ii} \leq g_{max}(\phi)$ , with minimal and maximal values denoted as  $d_{min}$  and  $d_{max}$ .

The problem is to find the relations between  $d_{min}, d_{max}, \lambda_{min}, \lambda_{max}$ , which guarantee  $\mathbf{V}^T(\mathbf{LD} + \mathbf{DL})\mathbf{V} > 0$ , for the fixed constant matrix  $\mathbf{L} = \mathbf{L}^T > 0$ ; and for all possible distributions of  $\mathbf{D}_{ii}$  in the positive interval  $[d_{min}; d_{max}]$ .

$\mathbf{V}$  is the matrix, whose columns are normalized eigenvectors of  $\mathbf{L}$  corresponding to non-zero eigenvalues.  $\mathbf{V}$  has a size of  $N$  by  $N - 1$ . Thus,  $\mathbf{V}^T\mathbf{V} = \mathbf{I}_{(N-1)}$  and  $\mathbf{V}\mathbf{V}^T = \mathbf{I}_{(N)} - \frac{1}{N}\bar{\mathbf{1}}_{(N)}\bar{\mathbf{1}}_{(N)}^T$  has rank  $(N - 1)$ . In the following we omit the dimensionality notations for  $\mathbf{I}_{(N)}$  and  $\bar{\mathbf{1}}_{(N)}$  since the sizes of the identity matrices (denoted as  $\mathbf{I}$ ) and unit vectors (denoted as  $\bar{\mathbf{1}}$ ) will be clear.

Lets introduce a diagonal positive matrix  $\mathbf{\Lambda}$  of non-zeros eigenvalues of  $\mathbf{L}$ :  $\mathbf{\Lambda} = \mathbf{V}^T\mathbf{L}\mathbf{V}$ . Moreover, we have:  $\mathbf{V}^T\mathbf{DLV} = \mathbf{V}^T\mathbf{D}(\mathbf{V}\mathbf{V}^T + \frac{1}{N}\bar{\mathbf{1}}\bar{\mathbf{1}}^T)\mathbf{LV} = (\mathbf{V}^T\mathbf{D}\mathbf{V})(\mathbf{V}^T\mathbf{L}\mathbf{V}) = \tilde{\mathbf{D}}\mathbf{\Lambda}$ , due to  $\bar{\mathbf{1}}^T\mathbf{L} = 0$ . We denote  $\tilde{\mathbf{D}} = \mathbf{V}^T\mathbf{D}\mathbf{V} > 0$ . Thus, we have  $\mathbf{V}^T(\mathbf{LD} + \mathbf{DL})\mathbf{V} = \mathbf{\Lambda}\tilde{\mathbf{D}} + \tilde{\mathbf{D}}\mathbf{\Lambda}$  for the symmetric real, strictly positive definite full rank matrices  $\mathbf{\Lambda}$  and  $\tilde{\mathbf{D}}$ .

The minimal and maximal diagonal values of  $\mathbf{\Lambda}$  are the minimal and maximal non-zero eigenvalues of  $\mathbf{L}$ , denoted as  $\lambda_{min}$  and  $\lambda_{max}$ . The matrix  $\tilde{\mathbf{D}}$  corresponds to the quadratic form of  $\mathbf{D}$  restricted to the  $N - 1$ -dimensional subspace (which is orthogonal to the vector

$\bar{\mathbf{1}}$ ).  $\mathbf{V}$  is the orthogonal projection. In this case, the eigenvalues of  $\tilde{\mathbf{D}}$  (denoted below as  $\tilde{d}_i$ ,  $i \in [1 \dots N - 1]$ ) *interlace* the eigenvalues of  $\mathbf{D}$  ( $d_i$ ,  $i \in [1 \dots N]$ ) due to *Cauchy's Interlacing Theorem* (Th.4.3.8 in<sup>125</sup>, see also Appendix on Graphs). So, arranging all of them in increasing order:  $d_{min} = d_1 \leq \tilde{d}_{min} = \tilde{d}_1 \leq d_2 \leq \tilde{d}_2 \leq \dots \leq \tilde{d}_{N-2} \leq d_{N-1} \leq \tilde{d}_{max} = \tilde{d}_{N-1} \leq d_{max} = d_N$ .

The bounds for  $\tilde{d}_{min}$  and  $\tilde{d}_{max}$  can be tight:  $\tilde{d}_{min} = d_{min}$  and  $\tilde{d}_{max} = d_{max}$  simultaneously. E.g. for  $N = 4$  take  $\mathbf{D}$  with the diagonal values  $\{2; 2; 1; 1\}$ , then for the vector  $\mathbf{u} \in Range(\mathbf{V})$ ,  $\mathbf{u} = [0 \ 0 \ 1 \ 1]^T / \sqrt{2}$  ( $\|\mathbf{u}\|_2^2 = 1$ ) we have  $\mathbf{u}^T \mathbf{D} \mathbf{u} = 1$  and for the vector  $\mathbf{v} \in Range(\mathbf{V})$ ,  $\mathbf{v} = [1 \ 1 \ 0 \ 0]^T / \sqrt{2}$  ( $\|\mathbf{v}\|_2^2 = 1$ ) we have  $\mathbf{v}^T \mathbf{D} \mathbf{v} = 2$ . Since the orthogonal projection  $\mathbf{V}$  preserves 2-norm, ( $\|\mathbf{V}x\|_2^2 = \|x\|_2^2$ ), we have  $\tilde{d}_{min} = d_{min} = 1$  and  $\tilde{d}_{max} = d_{max} = 2$ . For the problems of stability analysis considered in this Appendix, the diagonal values  $\mathbf{D}$  might be any combination of the values in the positive interval  $[d_{min}; d_{max}]$ . In these cases,  $\tilde{d}_{min}$  might take its minimal value  $d_{min}$ , whenever  $\tilde{d}_{max}$  takes its maximal value  $d_{max}$ . Then, we are interested in such conditions of positive definiteness of  $\Lambda \tilde{\mathbf{D}} + \tilde{\mathbf{D}} \Lambda$ , whenever the eigenvalue spectrum of  $\tilde{\mathbf{D}}$  is contained within the positive interval  $[d_{min}; d_{max}]$ .

For a positive definite matrix, the *inverted condition number* (in 2-norm) is the ratio between its minimal and maximal non-zero eigenvalues. In our case, we denote the inverted condition number of matrix  $\Lambda$  as  $\alpha = \lambda_{min} / \lambda_{max}$ ,  $0 < \alpha \leq 1$  and  $\beta = d_{min} / d_{max}$ ,  $0 < \beta \leq 1$  is the inverted condition number of matrix  $\mathbf{D}$ . Denoting  $\tilde{\beta} = \tilde{d}_{min} / \tilde{d}_{max}$ , we have (due to the eigenvalues interlacing property):  $\tilde{\beta} \geq \beta > 0$ .

Using an orthogonal transform with orthonormal matrix  $\mathbf{O}$  ( $\mathbf{O}^T = \mathbf{O}^{-1}$ ) the symmetric matrix  $(\Lambda \tilde{\mathbf{D}} + \tilde{\mathbf{D}} \Lambda)$  can be transformed to  $(\mathbf{A} \mathbf{B} + \mathbf{B} \mathbf{A})$ , with symmetric full rank matrices  $\mathbf{A} = \mathbf{O}^T \Lambda \mathbf{O}$  and  $\mathbf{B} = \mathbf{O}^T \tilde{\mathbf{D}} \mathbf{O}$  having the same real eigenvalues spectra as matrices  $\Lambda$  and  $\tilde{\mathbf{D}}$  respectively. Thus the problem of positive definiteness of  $(\Lambda \tilde{\mathbf{D}} + \tilde{\mathbf{D}} \Lambda)$  is equivalent to the positive definiteness conditions for any  $(\mathbf{A} \mathbf{B} + \mathbf{B} \mathbf{A})$ , where full rank symmetric real matrices  $\mathbf{A}$  and  $\mathbf{B}$  have the same eigenvalue spectra as  $\Lambda$  and  $\tilde{\mathbf{D}}$ . More generally, we may reformulate our problem as:

**Problem 1.** *In terms of the inverted condition numbers  $\alpha$  and  $\beta$  for a pair of symmetric real matrices  $\mathbf{A} > 0$  and  $\mathbf{B} > 0$ , find the necessary and sufficient conditions for  $\mathbf{A} \mathbf{B} + \mathbf{B} \mathbf{A} > 0$ .*

Regarding the equivalent roles of the symmetric positive definite matrices  $\mathbf{A}$  and  $\mathbf{B}$  in anticommutator  $(\mathbf{A} \mathbf{B} + \mathbf{B} \mathbf{A})$ , the necessary and sufficient conditions must be symmetric with respect to  $0 < \alpha \leq 1$  and  $0 < \beta \leq 1$ . We may also rescale the matrices  $\mathbf{A}$  and

$\mathbf{B}$  by multiplying them with some positive scalars, setting the minimum and maximum eigenvalues of  $\mathbf{A}$  to  $(1 - \zeta)$  and  $(1 + \zeta)$ ,  $0 \leq \zeta < 1$ , and the minimum and maximum eigenvalues of  $\mathbf{B}$  to  $(1 - \eta)$  and  $(1 + \eta)$ ,  $0 \leq \eta < 1$ . Thus, after rescaling:  $\zeta = \frac{1-\alpha}{1+\alpha}$  and  $\eta = \frac{1-\beta}{1+\beta}$ . Reversing:  $\alpha = \frac{1-\zeta}{1+\zeta}$  and  $\beta = \frac{1-\eta}{1+\eta}$ .

If, e.g.  $\alpha = 1$ , then  $\mathbf{A} = \lambda_{\max}(\mathbf{A})\mathbf{I}$  and  $\mathbf{AB} + \mathbf{BA} = 2\lambda_{\max}(\mathbf{A})\mathbf{B} > 0$ , because  $\mathbf{B} > 0$ . Similarly,  $\mathbf{AB} + \mathbf{BA} > 0$  when  $\beta = 1$  and  $\mathbf{A} > 0$ . Thus, one obvious *sufficient condition* for the positive definiteness of the anticommutator of two positive definite symmetric matrices is that at least one of them is a positive scalar multiplied by identity matrix.

**Remark 2.** For two positive definite symmetric real matrices  $\mathbf{A} > 0$  and  $\mathbf{B} > 0$ , the matrix  $\mathbf{AB} + \mathbf{BA}$  is not always positive definite (or positive semi-definite), and may have eigenvalues of different signs. (E.g. see<sup>338</sup>).

In the next paragraphs I demonstrate this property by some examples. Consider a similarity transform with *full rank* orthogonal matrix  $\mathbf{O}$  which diagonalizes a matrix  $\mathbf{A}$ :  $\mathbf{O}^T\mathbf{A}\mathbf{O} = \mathbf{\Lambda}$  and  $\mathbf{O}^T\mathbf{B}\mathbf{O} = \tilde{\mathbf{D}}$ . This transform preserves the eigenvalue spectra of the transformed  $\mathbf{A}$  and  $\mathbf{B}$  and  $\mathbf{O}^T(\mathbf{AB} + \mathbf{BA})\mathbf{O} = \mathbf{\Lambda}\tilde{\mathbf{D}} + \tilde{\mathbf{D}}\mathbf{\Lambda}$  for some diagonal matrix  $\mathbf{\Lambda} > 0$ .

$\mathbf{\Lambda}\tilde{\mathbf{D}} + \tilde{\mathbf{D}}\mathbf{\Lambda}$  can be represented as a *Hadamard product* ( $\circ$ ), an element-wise product (for two matrices  $\mathbf{X}$  and  $\mathbf{Y}$ ,  $[\mathbf{X} \circ \mathbf{Y}]_{ij} = \mathbf{X}_{ij}\mathbf{Y}_{ij}$ ):  $\tilde{\mathbf{D}} \circ (\bar{\mathbf{1}}\bar{\lambda}^T + \bar{\lambda}\bar{\mathbf{1}}^T)$ , where the column vector  $\bar{\lambda} = \text{diag}(\mathbf{\Lambda})$ ,  $\bar{\lambda}_i = \Lambda_{ii}$ . By the famous *Schur's Theorem* the Hadamard product of two positive definite matrices is positive definite,<sup>279</sup>. But in our case, the rank-1 matrix  $\mathbf{M} = \bar{\mathbf{1}}\bar{\lambda}^T + \bar{\lambda}\bar{\mathbf{1}}^T$  is not positive definite. For some  $\varepsilon > 0$  introduce the decomposition:

$$\bar{\mathbf{1}}\bar{\lambda}^T + \bar{\lambda}\bar{\mathbf{1}}^T = \frac{1}{2\varepsilon}((\bar{\lambda} + \varepsilon\bar{\mathbf{1}})(\bar{\lambda} + \varepsilon\bar{\mathbf{1}})^T - (\bar{\lambda} - \varepsilon\bar{\mathbf{1}})(\bar{\lambda} - \varepsilon\bar{\mathbf{1}})^T) \quad (\text{B.8})$$

So,

$$\tilde{\mathbf{D}} \circ (\bar{\mathbf{1}}\bar{\lambda}^T + \bar{\lambda}\bar{\mathbf{1}}^T) = \frac{1}{2\varepsilon}(\mathbf{\Lambda}^+\tilde{\mathbf{D}}\mathbf{\Lambda}^+ - \mathbf{\Lambda}^-\tilde{\mathbf{D}}\mathbf{\Lambda}^-) \quad (\text{B.9})$$

where the diagonal matrix  $\mathbf{\Lambda}^+$  has elements  $(\mathbf{\Lambda}^+)_{ii} = (\bar{\lambda} + \varepsilon\bar{\mathbf{1}})_i$  and  $(\mathbf{\Lambda}^-)_{ii} = (\bar{\lambda} - \varepsilon\bar{\mathbf{1}})_i$ . E.g. if  $\tilde{\mathbf{D}}$  has zero eigenvalue, we can choose  $\mathbf{x}$  for  $(\mathbf{\Lambda}^+)^{-1}\mathbf{x}$  to be equal to an eigenvector of  $\tilde{\mathbf{D}}$  corresponding to a zero eigenvalue and get:  $\mathbf{x}^T(\tilde{\mathbf{D}} \circ (\bar{\mathbf{1}}\bar{\lambda}^T + \bar{\lambda}\bar{\mathbf{1}}^T))\mathbf{x} = -\frac{1}{2\varepsilon}\mathbf{x}^T(\mathbf{\Lambda}^-\tilde{\mathbf{D}}\mathbf{\Lambda}^-)\mathbf{x} < 0$ . It follows that, a *necessary condition* for the positive definiteness of the anticommutator of two positive semi-definite symmetric matrices is that both of them must be strictly positive definite.

For the decomposition (B.8) above we can choose  $\varepsilon = \sqrt{(\bar{\lambda}^T\bar{\lambda})/N}$  (here  $N$  is the diagonal size of  $\mathbf{\Lambda}$ ) in order to get an orthogonal decomposition with  $\mathbf{l}_+ = \bar{\lambda} + \bar{\mathbf{1}}\sqrt{\frac{(\bar{\lambda}^T\bar{\lambda})}{N}}$  (and  $\mathbf{\Lambda}^+ = \text{diag}(\mathbf{l}_+)$ ) orthogonal to  $\mathbf{l}_- = \bar{\lambda} - \bar{\mathbf{1}}\sqrt{\frac{(\bar{\lambda}^T\bar{\lambda})}{N}}$  (and  $\mathbf{\Lambda}^- = \text{diag}(\mathbf{l}_-)$ ), cf. Eq. (B.9). Notice, that  $\mathbf{l}_-^T\mathbf{M}\mathbf{l}_- = \mathbf{l}_-^T(\bar{\mathbf{1}}\bar{\lambda}^T + \bar{\lambda}\bar{\mathbf{1}}^T)\mathbf{l}_- < 0$ . Then, for a symmetric real  $\tilde{\mathbf{D}} > 0$ :

$\mathbf{l}_-^T(\tilde{\mathbf{D}} \circ \mathbf{M})\mathbf{l}_- = \text{trace}(\tilde{\mathbf{D}}\mathbf{\Lambda}^{-}\mathbf{M}\mathbf{\Lambda}^{-}) = \text{trace}(\tilde{\mathbf{D}}^{1/2}\mathbf{\Lambda}^{-}\mathbf{M}\mathbf{\Lambda}^{-}\tilde{\mathbf{D}}^{1/2})$ , which is the trace of a matrix congruent to the matrix  $\mathbf{\Lambda}^{-}\mathbf{M}\mathbf{\Lambda}^{-}$ . The congruence transform preserves inertia, but  $\mathbf{\Lambda}^{-}\mathbf{M}\mathbf{\Lambda}^{-}$  is not positive definite:  $\bar{\mathbf{l}}^T(\mathbf{\Lambda}^{-}\mathbf{M}\mathbf{\Lambda}^{-})\bar{\mathbf{l}} = \mathbf{l}_-^T\mathbf{M}\mathbf{l}_- < 0$ . Thus, we might choose a (non-diagonal)  $\tilde{\mathbf{D}}$  to obtain  $\mathbf{l}_-^T(\tilde{\mathbf{D}} \circ \mathbf{M})\mathbf{l}_- < 0$ . (See also Ch.3.4 in<sup>124</sup>). This shows that even strict positive definiteness of the matrices  $\mathbf{\Lambda}$  and  $\tilde{\mathbf{D}}$  is not sufficient to guarantee the positive definiteness of the anticommutator  $\mathbf{\Lambda}\tilde{\mathbf{D}} + \tilde{\mathbf{D}}\mathbf{\Lambda}$ . For example, if  $\tilde{\mathbf{D}} = \begin{bmatrix} 1 & 1 \\ 1 & 1.02 \end{bmatrix}$ , with  $\text{eigenvalues}(\tilde{\mathbf{D}}) \approx \{2.01005; 0.00995\} > 0$  and  $\mathbf{\Lambda} = \begin{bmatrix} 3 & 0 \\ 0 & 2 \end{bmatrix}$ , then  $\text{eigenvalues}(\mathbf{\Lambda}\tilde{\mathbf{D}} + \tilde{\mathbf{D}}\mathbf{\Lambda}) \approx \{10.1313; -0.0513\}$ . The derivation of the worst case for 2-by-2 matrices follows in the next subsection B.3.1.

### B.3.1 The Necessary Conditions for Positive Definiteness of the Anticommutator of two Positive Definite Symmetric Real Matrices

Consider a general 2-by-2 symmetric real matrix  $\tilde{\mathbf{D}} = V^T \begin{bmatrix} 1+\zeta & 0 \\ 0 & 1-\zeta \end{bmatrix} V$ , ( $0 < \zeta < 1$ ), where  $V$  is an orthogonal matrix  $V^T V = \mathbf{I}$ . An orthogonal rotation in 2D real plane can be parameterized by a single parameter - the rotation angle. Varying this parameter, we find that the minimum of the minimal eigenvalue of  $(\mathbf{\Lambda}\tilde{\mathbf{D}} + \tilde{\mathbf{D}}\mathbf{\Lambda})$  is achieved when  $V = \begin{bmatrix} 1 & 1 \\ -1 & 1 \end{bmatrix} / \sqrt{2}$ . For this  $V$  and for a diagonal matrix  $\mathbf{\Lambda} = \begin{bmatrix} 1+\eta & 0 \\ 0 & 1-\eta \end{bmatrix}$ , ( $0 < \eta < 1$ ), we have  $\mathbf{\Lambda}\tilde{\mathbf{D}} + \tilde{\mathbf{D}}\mathbf{\Lambda} = 2 \begin{bmatrix} 1+\eta & \zeta \\ \zeta & 1-\eta \end{bmatrix}$ , with characteristic polynomial:  $\mu^2 - 2\mu + (1 - \eta^2 - \zeta^2)$ . The minimal eigenvalue  $\mu$  is negative, when  $\boxed{\eta^2 + \zeta^2 > 1}$ . In terms of the previously defined  $\alpha$  and  $\beta$ : the minimal eigenvalue of  $\mathbf{\Lambda}\tilde{\mathbf{D}} + \tilde{\mathbf{D}}\mathbf{\Lambda}$  is negative, when  $(1-\alpha)^2/(1+\alpha)^2 + (1-\beta)^2/(1+\beta)^2 > 1$ . The borderline of this inequality is depicted as a red line in Fig. B.1.

Suppose we have two general  $N$ -by- $N$  dimensional positive symmetric real matrices, where one matrix is fixed and the system of eigenvectors of the second variable matrix may be rotated (but its the eigenvalue spectrum stays preserved). Then, choose the two-dimensional linear subspace spanned by two eigenvectors of the fixed matrix corresponding to its minimal and maximal eigenvalues. For some variation of directions of the eigenvectors of the variable matrix we may get them laying in our chosen two-dimensional linear subspace rotated by  $\pi/4$  with respect to the eigenvectors of the fixed matrix laying in this subspace. Then, in this 2-dimensional subspace, we have the worst case analyzed above for the case of two general 2-by-2 positive symmetric real matrices. Thus, we have the following theorem:

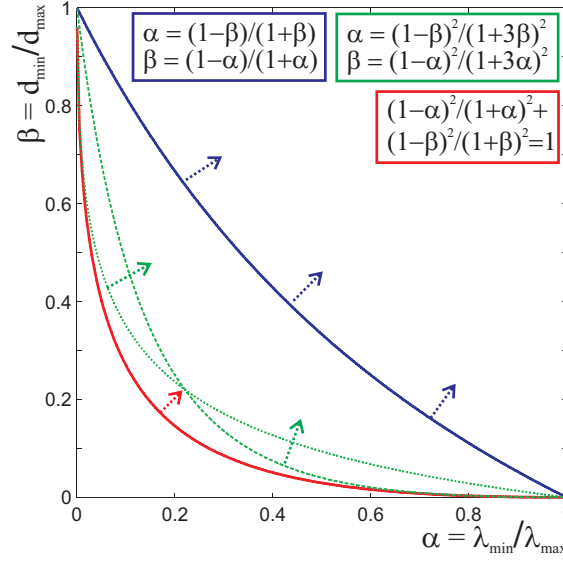


**Figure B.1:** Red line (cf. Eq. (B.10)): the *necessary and sufficient conditions* of positive definiteness of anticommutator of two positive definite symmetric real matrices. Blue line: weak *sufficient conditions*, Eq. (B.13-B.14). Green lines: stronger *sufficient conditions*, Eq. (B.18-B.19). On the axes are the inverted condition numbers of the two matrices. The arrows point inside the area of stability.

**Theorem 5.** For two positive definite symmetric real matrices  $\mathbf{A} > 0$  and  $\mathbf{B} > 0$ ,  $\alpha = \lambda_{\min}(\mathbf{A})/\lambda_{\max}(\mathbf{A})$ ,  $\beta = \lambda_{\min}(\mathbf{B})/\lambda_{\max}(\mathbf{B})$ , the **necessary condition** for positive definiteness of  $\mathbf{AB} + \mathbf{BA}$  is:

$$\boxed{(1-\alpha)^2/(1+\alpha)^2 + (1-\beta)^2/(1+\beta)^2 < 1} \quad (\text{B.10})$$

It means that we can always find symmetric real matrices  $\mathbf{A} > 0$  and  $\mathbf{B} > 0$ , with  $\alpha$  and  $\beta$  violating (B.10), to obtain  $\mathbf{AB} + \mathbf{BA}$  that is not positive definite.

### B.3.2 The *Sufficient Conditions* for Positive Definiteness of the Anticommutator of two Positive Definite Symmetric Real Matrices

**Weak sufficient conditions.**

For two positive definite matrices  $\tilde{\mathbf{D}} > 0$  with minimal and maximal eigenvalues  $d_{\min}$  and  $d_{\max}$ , and diagonal  $\mathbf{\Lambda} > 0$  with minimal and maximal eigenvalues (diagonal elements)  $\lambda_{\min}$  and  $\lambda_{\max}$ , we analyse the sufficient conditions for positive definiteness of the matrix  $\mathbf{\Lambda}\tilde{\mathbf{D}} + \tilde{\mathbf{D}}\mathbf{\Lambda}$ .

Lets use the following separation of terms:  $\mathbf{\Lambda}\tilde{\mathbf{D}}+\tilde{\mathbf{D}}\mathbf{\Lambda} = 2m\tilde{\mathbf{D}}+[\tilde{\mathbf{D}}(\mathbf{\Lambda}-m\mathbf{I})+(\mathbf{\Lambda}-m\mathbf{I})\tilde{\mathbf{D}}]$ , for a positive  $m = \min_i (\mathbf{\Lambda})_{ii} = \lambda_{min}$ . Lets also denote the maximal residual of the diagonal elements of  $\mathbf{\Lambda}$  as  $M = \max_i (\mathbf{\Lambda} - m\mathbf{I})_{ii} = \lambda_{max} - \lambda_{min}$ . Denote the two terms in this decomposition as  $\mathbf{S}_1 = 2m\tilde{\mathbf{D}}$  and  $\mathbf{S}_2 = \tilde{\mathbf{D}}(\mathbf{\Lambda} - m\mathbf{I}) + (\mathbf{\Lambda} - m\mathbf{I})\tilde{\mathbf{D}}$ . Then  $\mathbf{S}_2$  is not positive definite in general (see **Remark 2** above).

For the matrices  $\mathbf{S}_1$  and  $\mathbf{S}_2$  we may apply the argument stated in **Remark 1** by testing their 2-norms. The 2-norm of  $\mathbf{S}_2$  is dominated by  $2d_{max}M$ . The sufficient condition for positive definiteness of matrix  $\mathbf{\Lambda}\tilde{\mathbf{D}} + \tilde{\mathbf{D}}\mathbf{\Lambda}$  is:  $2d_{min}m > 2d_{max}M$ , (where on the left side is the minimum 2-norm of  $\mathbf{S}_1$  and on the right side is the maximum 2-norm of  $\mathbf{S}_2$ ):

$$\frac{d_{min}}{d_{max}} > \frac{\lambda_{max} - \lambda_{min}}{\lambda_{min}} \quad (\text{B.11})$$

In terms of the inverted condition numbers  $\alpha = \lambda_{min}/\lambda_{max}$  and  $\beta = d_{min}/d_{max}$ :  $\beta > 1/\alpha - 1$ ,  $\alpha > 1/(1+\beta)$ .

In order to obtain better sufficient conditions, take  $m = (\lambda_{min} + \lambda_{max})/2$  and the residual  $M = (\lambda_{max} - \lambda_{min})/2$ , then the limiting inequality is:

$$\frac{d_{min}}{d_{max}} > \frac{\lambda_{max} - \lambda_{min}}{\lambda_{max} + \lambda_{min}} \quad (\text{B.12})$$

In terms of  $\alpha$  and  $\beta$ :

$$\boxed{\beta > \frac{1 - \alpha}{1 + \alpha}} \quad (\text{B.13})$$

inverting leads to:

$$\boxed{\alpha > \frac{1 - \beta}{1 + \beta}} \quad (\text{B.14})$$

In terms of the previously introduced  $\zeta$  and  $\eta$  these conditions are:  $\eta < (1-\zeta)/(1+\zeta)$  or  $\zeta < (1-\eta)/(1+\eta)$ . I also re-write the last inequality using new variable  $d_{mean} = (d_{min} + d_{max})/2$  as:

$$\boxed{\frac{\lambda_{min}}{\lambda_{max}} > \frac{d_{max} - d_{mean}}{d_{mean}}} \quad (\text{B.15})$$

These weak sufficient conditions were first presented in<sup>212</sup>. In Fig. B.1 this condition borderline is depicted as a blue continuous line.

### Stronger sufficient conditions.

Now consider again the matrix  $\mathbf{\Lambda}\tilde{\mathbf{D}}+\tilde{\mathbf{D}}\mathbf{\Lambda} = \tilde{\mathbf{D}} \circ (\bar{\mathbf{1}}\bar{\lambda}^T + \bar{\lambda}\bar{\mathbf{1}}^T)$ , where  $\mathbf{\Lambda} > 0$  a is diagonal



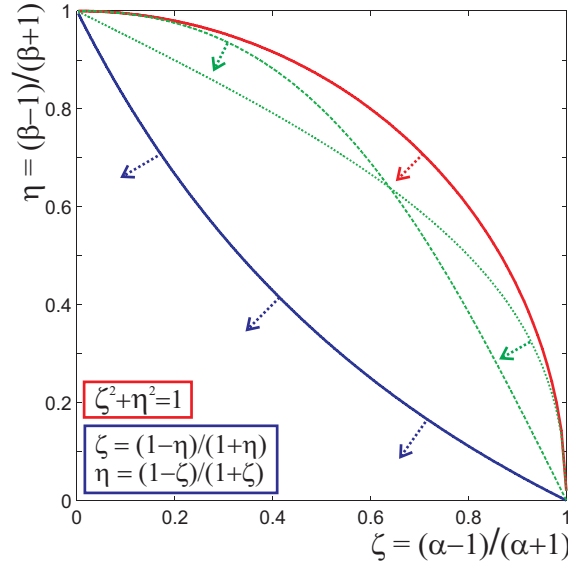


**Figure B.2:** Figure plots results presented in Fig. B.1 but in parameters  $\zeta$  and  $\eta$ . Red line, Eq. (B.10): the *necessary and sufficient conditions* of positive definiteness of anticommutator of two positive definite symmetric real matrices. Blue line: *weak sufficient conditions*, Eq. (B.13-B.14). Green lines: *stronger sufficient conditions*, Eq. (B.18-B.19). The arrows point inside the area of stability.

matrix of real positive values,  $\tilde{\mathbf{D}} > 0$  is a real symmetric strictly positive-definite matrix and the column vector  $\bar{\lambda} = \text{diag}(\mathbf{\Lambda})$ ,  $\bar{\lambda}_i = \mathbf{\Lambda}_{ii}$ . Use the decomposition as in **Remark 2**:

$$\bar{\mathbf{1}}\bar{\lambda}^T + \bar{\lambda}\bar{\mathbf{1}}^T = \frac{1}{2\varepsilon}((\bar{\lambda} + \varepsilon\bar{\mathbf{1}})(\bar{\lambda} + \varepsilon\bar{\mathbf{1}})^T - (\bar{\lambda} - \varepsilon\bar{\mathbf{1}})(\bar{\lambda} - \varepsilon\bar{\mathbf{1}})^T) \quad (\text{B.16})$$

and

$$\tilde{\mathbf{D}} \circ (\bar{\mathbf{1}}\bar{\lambda}^T + \bar{\lambda}\bar{\mathbf{1}}^T) = \frac{1}{2\varepsilon}[(\mathbf{\Lambda} + \varepsilon\mathbf{I})\tilde{\mathbf{D}}(\mathbf{\Lambda} + \varepsilon\mathbf{I}) - (\mathbf{\Lambda} - \varepsilon\mathbf{I})\tilde{\mathbf{D}}(\mathbf{\Lambda} - \varepsilon\mathbf{I})] \quad (\text{B.17})$$

Choose  $\varepsilon$  in order to maximize the minimal value of the first term in square brackets and respectively minimize the absolute value of the maximal value of the second term. Choosing  $\varepsilon = (\lambda_{max} + \lambda_{min})/2$ , we get the sufficient condition for positive definiteness as:  $(\lambda_{max} + 3\lambda_{min})^2 d_{min} > (\lambda_{max} - \lambda_{min})^2 d_{max}$ , which is:

$$\beta > \left( \frac{1 - \alpha}{1 + 3\alpha} \right)^2 \quad (\text{B.18})$$

or  $\alpha > (1 - \sqrt{\beta})/(1 + 3\sqrt{\beta})$ . Due to the symmetry of the roles of  $\alpha$  and  $\beta$ , we also have:

$$\alpha > \left( \frac{1 - \beta}{1 + 3\beta} \right)^2 \quad (\text{B.19})$$

or  $\beta > (1-\sqrt{\alpha})/(1+3\sqrt{\alpha})$ . In the Fig. B.1 these condition borderlines are depicted as green dotted and dashed lines.

### B.3.3 The *Necessary and Sufficient Conditions* for Positive Definiteness of the Anticommutator of two Positive Definite Symmetric Real Matrices

I now give the proof that the necessary conditions for positive definiteness of anticommutator of two positive definite symmetric real matrices as derived above [B.3.1] are *the sufficient conditions* for positive definiteness of the anticommutator. The proof sketch is from Dr. Fedor V. Petrov from St. Petersburg conveyed by personal communication.

**Theorem 6.** *Assume two real symmetric positive definite matrices  $\mathbf{A}$  and  $\mathbf{B}$ , with the range of eigenvalues of  $\mathbf{A}$  as  $[1 - \zeta; 1 + \zeta]$ ,  $0 \leq \zeta < 1$ , and the range of eigenvalues of  $\mathbf{B}$  as  $[1 - \eta; 1 + \eta]$ ,  $0 \leq \eta < 1$ , Then,  $\mathbf{AB} + \mathbf{BA} > 0$ , iff  $\boxed{\zeta^2 + \eta^2 < 1}$ .*

The proof is as follows.

$\mathbf{AB} + \mathbf{BA} > 0$  can be written as  $((\mathbf{AB} + \mathbf{BA})\mathbf{u}, \mathbf{u}) > 0$  for a real vector  $\mathbf{u}$ . Further,  $((\mathbf{AB} + \mathbf{BA})\mathbf{u}, \mathbf{u}) = 2(\mathbf{Au}, \mathbf{Bu})$ . Represent  $\mathbf{A} = \mathbf{I} + \mathbf{X}$ ,  $\mathbf{B} = \mathbf{I} + \mathbf{Y}$ , where matrices  $\mathbf{X}$ ,  $\mathbf{Y}$  are such, that their 2-norms are less or equal than  $\zeta$ ,  $\eta$  correspondingly. Then, the angle between  $\mathbf{Au}$  and  $\mathbf{u} \neq 0$  takes all the values between 0 and  $\arcsin(\zeta)$ , and the angle between  $\mathbf{Bu}$  and  $\mathbf{u}$  takes all the values between 0 and  $\arcsin(\eta)$ .

*Sufficiency:* If  $\zeta^2 + \eta^2 < 1$ , then the sum  $\arcsin(\zeta) + \arcsin(\eta) < \pi/2$ , and by the triangle inequality of the two planar angles (the 1st is between  $\mathbf{u}$  and  $\mathbf{Au}$  and the 2nd is between  $\mathbf{u}$  and  $\mathbf{Bu}$ ) the angle between  $\mathbf{Au}$  and  $\mathbf{Bu}$  is less than  $\pi/2$ .

*Necessity* (see Th. 5 in B.3.1): If  $\zeta^2 + \eta^2 > 1$ , one may find the 2-dimensional subspace embedding  $\mathbf{u}$ ,  $\mathbf{Au}$ ,  $\mathbf{Bu}$ , where the angle between  $\mathbf{Au}$ ,  $\mathbf{Bu}$  is greater than  $\pi/2$ .  $\square$

This proof is based on the *Kantorovich inequality*<sup>145,180</sup>. V.L. Kantorovich attributed this type of inequality to G. Pólya's and G. Szegő's book "Problems and Theorems in Analysis I. Series. Integral Calculus. Theory of Functions." (<sup>245</sup>, Ch.2 "Inequalities", §1, Problem #92). The Kantorovich inequality establishes the relation between the minimal  $\lambda_{min}(\mathbf{A}) > 0$  and the maximal  $\lambda_{max}(\mathbf{A})$  eigenvalues of a positive definite symmetric real matrix  $\mathbf{A}$  and the maximal angle between two real vectors  $\mathbf{x} \neq 0$  and  $\mathbf{Ax}$ . The *Kantorovich inequality* is:

$$\frac{(\mathbf{x}, \mathbf{x})^2}{(\mathbf{x}, \mathbf{Ax})(\mathbf{x}, \mathbf{A}^{-1}\mathbf{x})} \geq \frac{4\lambda_{max}\lambda_{min}}{(\lambda_{max} + \lambda_{min})^2} \quad (\text{B.20})$$

For the angle  $\angle(\mathbf{y}, \mathbf{A}\mathbf{y})$  between  $\mathbf{y} \neq 0$  and  $\mathbf{A}\mathbf{y}$  we have:  $\cos^2 \angle(\mathbf{y}, \mathbf{A}\mathbf{y}) = \frac{(\mathbf{y}, \mathbf{A}\mathbf{y})^2}{(\mathbf{A}\mathbf{y}, \mathbf{A}\mathbf{y})(\mathbf{y}, \mathbf{y})} \leq 1$  by the *Cauchy-Schwarz inequality*, which states for two vectors:  $(\mathbf{x}, \mathbf{y})^2 \leq (\mathbf{x}, \mathbf{x})(\mathbf{y}, \mathbf{y})$ . Then,  $\sin^2 \angle(\mathbf{y}, \mathbf{A}\mathbf{y}) = 1 - \frac{(\mathbf{y}, \mathbf{A}\mathbf{y})^2}{(\mathbf{A}\mathbf{y}, \mathbf{A}\mathbf{y})(\mathbf{y}, \mathbf{y})}$ . Changing the variable to  $\mathbf{x} = \mathbf{A}^{1/2}\mathbf{y}$ :  $\sin^2 \angle(\mathbf{y}, \mathbf{A}\mathbf{y}) = 1 - \frac{(\mathbf{A}^{-1/2}\mathbf{x}, \mathbf{A}^{1/2}\mathbf{x})^2}{(\mathbf{A}^{1/2}\mathbf{x}, \mathbf{A}^{1/2}\mathbf{x})(\mathbf{A}^{-1/2}\mathbf{x}, \mathbf{A}^{-1/2}\mathbf{x})} = 1 - \frac{(\mathbf{x}, \mathbf{x})}{(\mathbf{x}, \mathbf{A}\mathbf{x})(\mathbf{x}, \mathbf{A}^{-1}\mathbf{x})}$ . And  $\frac{(\mathbf{x}, \mathbf{x})}{(\mathbf{x}, \mathbf{A}\mathbf{x})(\mathbf{x}, \mathbf{A}^{-1}\mathbf{x})} \geq \frac{4\lambda_{max}\lambda_{min}}{(\lambda_{max} + \lambda_{min})^2}$  by the Kantorovich inequality. Then,  $\sin^2 \angle(\mathbf{y}, \mathbf{A}\mathbf{y}) \leq \frac{(\lambda_{max} + \lambda_{min})^2 - 4\lambda_{max}\lambda_{min}}{(\lambda_{max} + \lambda_{min})^2} = \left(\frac{\lambda_{max} - \lambda_{min}}{\lambda_{max} + \lambda_{min}}\right)^2$ . Finally,  $\angle(\mathbf{y}, \mathbf{A}\mathbf{y}) \leq \arcsin(\zeta)$  in terms of the previously defined  $0 \leq \zeta < 1$ :  $\lambda_{max} = 1 + \zeta$  and  $\lambda_{min} = 1 - \zeta$ . Related problems were also analyzed in<sup>21</sup> (cf.<sup>337</sup>).

The geometric proof of sufficient conditions along the lines of Theorem 6 can be extended for the case of a general non-symmetric real square matrix  $\mathbf{A}$  and a real symmetric positive definite matrix  $\mathbf{B}$ . Lets denote  $\mathbf{A}^+ = (\mathbf{A} + \mathbf{A}^T)/2$ ,  $\mathbf{A}^- = (\mathbf{A} - \mathbf{A}^T)/2$  for a real square matrix  $\mathbf{A} = \mathbf{A}^+ + \mathbf{A}^-$ . For the following we assume  $\mathbf{A}^+$  is positive definite with  $\lambda_{max}(\mathbf{A}^+) > \lambda_{min}(\mathbf{A}^+) > 0$  the maximal and minimal eigenvalues of  $\mathbf{A}^+$ . (Positive definiteness of  $\mathbf{A}^+$  implies also  $\Re(\lambda(\mathbf{A})) > 0$ , Bendixson-Hirsch theorem:<sup>23</sup>, p.217). Denote  $\zeta = \frac{\lambda_{max}(\mathbf{A}^+) - \lambda_{min}(\mathbf{A}^+)}{\lambda_{max}(\mathbf{A}^+) + \lambda_{min}(\mathbf{A}^+)}$ . And for a real symmetric positive definite  $\mathbf{B}$  denote  $\eta = \frac{\lambda_{max}(\mathbf{B}) - \lambda_{min}(\mathbf{B})}{\lambda_{max}(\mathbf{B}) + \lambda_{min}(\mathbf{B})}$ . Introduce  $\nu = \frac{2\|\mathbf{A}^-\|_2}{\lambda_{max}(\mathbf{A}^+) + \lambda_{min}(\mathbf{A}^+)}$ . Then, the sufficient conditions for positive definiteness of  $\mathbf{A}^T\mathbf{B} + \mathbf{B}\mathbf{A} > 0$  are  $\eta^2 < \left[\frac{\zeta\nu - \sqrt{1 + \nu^2 - \zeta^2}}{1 + \nu^2}\right]^2$ . When  $\nu \rightarrow 0$  the conditions approximate those of Theorem 6 as  $\zeta^2 + \eta^2 < 1$ .

### B.3.4 The Role of the Sufficient Conditions for Partial Contraction in Design of Convergent Multi-agent Behavior

All the derived sufficient conditions and the tight necessary and sufficient conditions from this subsection play an important role in establishing the sufficient conditions for contraction, for the positive definiteness of equation B.7. Indeed, for any variable  $\mathbf{D}(\phi) > 0$  we may choose such a connected coupling graph for diffusive symmetric coupling, so its Laplacian matrix  $\mathbf{L}$  will have non-zero eigenvalues satisfying the necessary and sufficient conditions for the positive definiteness of Eq. B.7). We can always choose *all-to-all* coupling, for which  $\mathbf{L} = N\mathbf{I} - \bar{\mathbf{1}}\bar{\mathbf{1}}^T$  and  $\mathbf{A} = \mathbf{V}^T\mathbf{L}\mathbf{V} = N\mathbf{I}$ , where the columns of  $\mathbf{V}$  are orthogonal eigenvectors of  $\mathbf{L}$  corresponding to  $N - 1$  of its non-zero eigenvalues (A.2). And  $\mathbf{V}^T(\mathbf{L}\mathbf{D} + \mathbf{D}\mathbf{L})\mathbf{V} = \mathbf{A}\tilde{\mathbf{D}} + \tilde{\mathbf{D}}\mathbf{A} = 2N\tilde{\mathbf{D}} > 0$ ,  $\forall \mathbf{D} > 0$ , where  $\tilde{\mathbf{D}} = \mathbf{V}^T\mathbf{D}\mathbf{V} > 0$ .

If we drop a single symmetric bidirectional link from an all-to-all coupled graph, then the non-zero eigenvalues of  $\mathbf{L}$  (and the eigenvalues of  $\mathbf{A}$ ) will be:  $N$  ( $N - 2$  times) and  $N - 2$  (once). If we drop  $k$  such bidirectional links which have no common vertex at their ends, then the non-zero eigenvalues of  $\mathbf{L}$  (and the eigenvalues of  $\mathbf{A}$ ) will be:  $N$  ( $N - k - 1$  times) and  $N - 2$  ( $k$  times), see App. A. Thus, the inverted condition number of  $\mathbf{A}$  changes from 1 (for all-to-all coupling graph) down to  $(N - 2)/N = 1 - 2/N$ . Dependent on the ratio

$d_{min}/d_{max}$  (the limiting inverted condition number for  $\tilde{\mathbf{D}}$ ), this provides an estimate of how robust the coupling scheme is (e.g. all-to-all coupling) to dropouts of symmetrical links. Similar estimates for the Laplacian inverted condition number changes can also be made for dropouts of symmetrical links, whenever they might have a common vertex, while the total graph connectivity is still preserved. This has practical value for designing interaction networks of agents possessing individual non-linear dynamics. The aim of this design is to preserve the contraction properties of the group dynamics in cases of communication link dropouts.

# Bibliography

- [1] Y. Abe, M. Da Silva, and J. Popović. Multiobjective control with frictional contacts. *ACM SIGGRAPH/Eurograph. Symp. on Comp. Anim.*, 2007. 53
- [2] P. K. Agarwal, H. Edelsbrunner, O. Schwarzkopf, and E. Welzl. Euclidean minimum spanning trees and bichromatic closest pairs. *Discrete & Computational Geometry*, 6(3):407–422, 1991. 28
- [3] J. K. Aggarwal and M. S. Ryoo. Human activity analysis: A review. *ACM Comput. Surv.*, 43(3):16:1–16:43, 2011. 1
- [4] M. Aitken, G. Butler, D. Lemmon, E. Saindon, D. Peters, and G. Williams. The Lord of the Rings: The visual effects that brought middle earth to the screen. In *ACM SIGGRAPH 2004 Course Notes*, number 11 in SIGGRAPH’04, New York, NY, USA, 2004. ACM. 1
- [5] M. Ajallooeian, J. van den Kieboom, A. Mukovskiy, M. A. Giese, and A. J. Ijspeert. A general family of morphed nonlinear phase oscillators with arbitrary limit cycle shape. *Physica D: Nonlinear Phenomena*, 263:41–56, 2013. 7, 55, 84, 156
- [6] A. Ajoudani, J. Lee, A. Rocchi, M. Ferrati, E. M. Hoffman, A. Settini, D. G. Caldwell, A. Bicchi, and N. G. Tsagarakis. A manipulation framework for compliant humanoid COMAN: Application to a valve turning task. In *14th IEEE-RAS Int. Conf. On Humanoid Robots (Humanoids, 2014)*, pages 664–670, 2014. 55
- [7] B. Akgun and M. Stilman. Sampling heuristics for optimal motion planning in high dimensions. In *2011 IEEE/RSJ Int. Conf. on Intelligent Robots and Systems*, pages 2640–2645, 2011. 20
- [8] I. Albrecht, J. Haber, and H. P. Seidel. Construction and animation of anatomically based human hand models. *Proc. ACM SIGGRAPH/Eurographics Symposium on Computer Animation (SCA 2003)*, pages 98–109, 2003. 123
- [9] S.-i. Amari. Dynamics of pattern formation in lateral-inhibition type neural fields. *Biological Cybernetics*, 27(2):77–87, 1977. 10, 15, 16
- [10] W. N. Anderson Jr. and T. D. Morley. Global convergence of quorum sensing networks. *Lin. and Multilin. Alg.*, 18:141–145, 1985. 168, 170, 171, 172
- [11] A. A. Andronov, A. A. Vitt, and S. E. Khaikin. *Theory of Oscillators*. Dover Publ. Inc., New York, 1987. 84, 132

- [12] O. Arikan, D. A. Forsyth, and J. F. O'Brien. Motion synthesis from annotations. *ACM Trans. on Graphics, SIGGRAPH '03*, 22(3):402–408, 2003. 2, 53
- [13] Ronald C. Arkin. *Behavior-Based Robotics*. The MIT Press, Cambridge, MA, 1998. 19
- [14] Kenneth J. Arrow and Maurice McManus. A note on dynamic stability. *Econometrica*, 26(3):448–454, 1958. 175
- [15] H. Asada and J.-J. E. Slotine. *Robot Analysis and Control*. John Wiley & Sons, Inc., New York, NY, USA, 1st edition, 1992. 96
- [16] C. G. Atkeson, A. W. Moore, and S. Schaal. Locally weighted learning for control. *A.I. Review*, 11:75–113, 1997. 88, 93
- [17] P. Baerlocher and R. Boulic. An inverse kinematic architecture enforcing an arbitrary number of strict priority levels. *The Visual Computer*, 20(6):402–417, 2004. 25, 89, 90
- [18] E. A. Barbashin. The construction of Lyapunov functions. *Differential Equations*, 4:1097–1112, 1968. Transl. of 'Differentsial'nye Uravneniya', 4 (1968), 2127–2158. 175
- [19] G. P. Barker, A. Berman, and R. J. Plemmons. Positive diagonal solutions to the Lyapunov equations. *Linear and Multilinear Algebra*, 5(4):249–256, 1978. 175
- [20] J. Barraquand and J.-C. Latombe. Robot Motion Planning: A distributed representation approach. *The Int. J. of Robotics Research*, 10(6):628–649, 1991. 19
- [21] F. L. Bauer and A. S. Householder. Some inequalities involving the euclidean condition of a matrix. *Numerische Mathematik*, 2(1):308–311, 1960. 185
- [22] H. Bekkering, A. Wohlschläger, and M. Gattis. Imitation of gestures in children is goal-directed. *The Quarterly Journal of Experimental Psychology. A, Human Experimental Psychology*, 53(1):153–164, 2000. 9
- [23] R. Bellman. *Introduction to Matrix Analysis*. McGraw-Hill, 1960. 173, 185
- [24] D. Bennequin, R. Fuchs, A. Berthoz, and T. Flash. Movement timing and invariance arise from several geometries. *PLoS Computational Biology*, 5(7):e1000426, 2009. 157, 158
- [25] J. L. Bentley. Multidimensional binary search trees used for associative searching. *Comm. of the ACM*, 18(9):509–517, 1975. 27
- [26] M. B. Berkinblit, I. M. Gelfand, and A. G. Feldman. A model for the control of multi-joint movements. *Biofizika*, 31(1):136–146, 1986. 25
- [27] A. Berman and D. Hershkowitz. Matrix diagonal stability and its implications. *SIAM J. on Algebraic Discrete Methods*, 4(3):377–382, 1983. 175
- [28] N. A. Bernstein. *The Coordination and Regulation of Movements*. Pergamon Press, N.Y., Oxford, 1967. 54, 89

- 
- [29] R. Bhatia. *Matrix Analysis. Graduate texts in mathematics. 169.* Springer-Verlag, Berlin Heidelberg, 1997. 64
- [30] E. Bicho, P. Mallet, and G. Schöner. Target representation on an autonomous vehicle with low level sensors. *The Int. J. of Robotics Research*, 19(5):424–447, 2000. 10
- [31] Z. Z. Bien and D. Stefanov, editors. *Advances in Rehabilitation Robotics. Human-friendly Technologies on Movement Assistance and Restoration for People with Disabilities*, volume 306. Springer, Berlin, 2004. 1
- [32] A. Biess. Shaping of arm configuration space by prescription of non-Euclidean metrics with applications to human motor control. *Physical Review E*, 87(1):012729, 2013. 158
- [33] A. Billard, Y. Epars, S. Calinon, G. Cheng, and S. Schaal. Discovering optimal imitation strategies. *Robotics and Autonomous Systems*, 47(2-3):68–77, 2004. 41
- [34] M. Brandao, L. Jamone, P. Kryczka, N. Endo, K. Hashimoto, and A. Takanishi. Reaching for the unreachable: Integration of locomotion and whole-body movements for extended visually guided reaching. In *Proc. of 13th IEEE-RAS Int. Conf. on Humanoid Robots (Humanoids)*, pages 28–33, 2013. 55
- [35] D. Braun. Structural learning. *Scholarpedia*, 8(10):12312, 2013. 89
- [36] D. A. Braun, C. Mehring, and D. M. Wolpert. Structural learning in action. *Behavioural Brain Research*, 206:157–165, 2010. 89
- [37] D. A. Braun, P. A. Ortega, E. Theodorou, and S. Schaal. Path Integral Control and Bounded Rationality. In *IEEE Symposium on Adaptive Dynamic Programming and Reinforcement Learning (ADPRL)*, 2011. 20
- [38] D. C. Brogan and J. K. Hodgins. Group behaviors for systems with significant dynamics. *Autonomous Robots*, 1997. 124
- [39] R. A. Brooks. Intelligence without reason. *Proc. of the 12th Int. Joint Conf. on A.I., IJCAI'91*, 1:569–595, 1991. 3
- [40] J. Buchli, L. Righetti, and A. J. Ijspeert. Engineering entrainment and adaptation in limit cycle systems - from biological inspiration to applications in robotics. *Biol. Cyb.*, 95(6):645–664, 2006. 79, 123, 124
- [41] M. Buehler, K. Iagnemma, and S. Singh, editors. *The DARPA Urban Challenge. Autonomous Vehicles in City Traffic*, volume 56. Springer-Verlag, Berlin Heidelberg, 2009. 1
- [42] G. Bugmann, J. G. Taylor, and M. J. Denham. *Route finding by neural nets*, pages 217–230. Alfred Waller Ltd., Henley-on-Thames, 1995. 20
- [43] E. Burdet, D. W. Franklin, and T. E. Milner. *Human Robotics. Neuromechanics and Motor Control*. MIT Press, 2013. 1

- [44] J. C. Butcher. *Numerical Methods for Ordinary Differential Equations*. John Wiley, 2003. 80, 84
- [45] S. Camazine, J. L. Deneubourg, N. R. Franks, J. Sneyd, G. Theraulaz, and E. Bonabeau. *Self-organization in biological systems*. Princeton University Press, New Jersey, 2001. 123
- [46] S. Cambon, R. Alami, and F. Gravot. A hybrid approach to intricate motion, manipulation and task planning. *The Int. J. of Robotics Research*, 28(1):104–126, 2009. 19
- [47] S. Cambon, F. Gravot, and R. Alami. A robot task planner that merges symbolic and geometric reasoning. In *Proc. of the 16th European Conf. on A.I., ECAI'04*, Valencia, Spain, pages 895–899, Amsterdam, The Netherlands, The Netherlands, 2004. IOS Press. 19
- [48] J. F. Canny. *The Complexity of Robot Motion Planning*. MIT Press, Cambridge, MA, USA, 1988. 19
- [49] J. F. Canny and M. C. Lin. An opportunistic global path planner. *Algorithmica*, 10:102–120, 1993. 19
- [50] D. P. Carey, D. I. Perrett, and M. W. Oram. Recognizing, understanding and reproducing action. In M. Jeannerod, editor, *Handbook of Neuropsychology Vol.11, Action and Cognition*, pages 111–129. Elsevier (incl. Pergamon), 1997. F. Boller J. Grafman (Series Eds). 14
- [51] H. Carnahan, B. J. McFadyen, D. L. Cockell, and A. H. Halverson. The combined control of locomotion and prehension. *Neurosci. Res. Comm.*, 19:91–100, 1996. 54
- [52] C.-C. Chang and C.-J. Lin. *LIBSVM: a Library for Support Vector Machines*, 2001. 82, 83, 85
- [53] L. Y. Chang and N. S. Pollard. Constrained least-squares optimization for robust estimation of center of rotation. *Journal of Biomechanics*, 40(6):1392–1400, 2007. 63
- [54] G. Chen, G. Davis, F. Hall, Z. Li, K. Patel, and M. Stewart. An interlacing result on normalized laplacians. *SIAM J. Discrete Math.*, 18:353–361, 2004. 170
- [55] E. Chiovetto, A. d’Avella, and M. A. Giese. A unifying framework for the identification of motor primitives. *eprint arXiv:1603.06879*, 2016. 70, 71
- [56] E. Chiovetto and M. A. Giese. Kinematics of the coordination of pointing during locomotion. *Plos One*, 8(11), 2013. 54, 59, 70, 75
- [57] P. Comon and C. Jutten. *Handbook of Blind Source Separation. ICA and Applications*. Academic Press, 1 edition, 2010. 51, 68
- [58] C. I. Connolly and J. B. Burns. A model for the functioning of the striatum. *Biol. Cybern.*, 68(6):535–544, 1993. 20
- [59] C. I. Connolly and J. B. Burns. A new striatal model and its relationship to basal ganglia diseases. *Neuroscience Research*, 16(4):271–274, 1993.



- 
- [60] C. I. Connolly and J. B. Burns. *A State-Space Striatal Model*, pages 163–177. MIT Press, Cambridge MA, 1995. 20
- [61] I. D. Couzin. Collective cognition in animal groups. *Trends in Cogn. Sci.*, 13(1):1–44, 2009. 123
- [62] S. Dalibard, A. El Khoury, F. Lamiroux, A. Nakhaei, M. Täix, and J.-P. Laumond. Dynamic walking and whole-body motion planning for humanoid robots: An integrated approach. *Int. Journal of Robotics Research*, 32(9-10):1089–1103, 2013. 55
- [63] A. d’Avella and E. Bizzi. Shared and specific muscle synergies in neural motor behaviours. *Proc. Natl. Acad. Sci. USA*, 102(8):3076–3081, 2005. 67
- [64] A. d’Avella, A. Portone, L. Fernandez, and F. Lacquaniti. Control of fast-reaching movements by muscle synergy combinations. *J. Neurosci.*, 26(30):7791–7810, 2006. 70
- [65] A. d’Avella, P. Saltiel, and E. Bizzi. Combinations of muscle synergies in the construction of a natural motor behavior. *Nature Neurosci.*, 6(3):300–308, 2003. 67, 70
- [66] E. Dayan, I. Sella, A. Mukovskiy, Y. Douek, M. A. Giese, R. Malach, and T. Flash. The Default Mode Network differentiates biological from non-biological motion. *Cerebral Cortex*, 26(1):234–245, 2016. 63
- [67] P. Dayan and L. F. Abbott. *Theoretical Neuroscience: Computational and Mathematical Modeling of Neural Systems*. MIT Press, Cambridge, Mass., revised. edition, 2005. 16
- [68] S. Dehaene, J. P. Changeux, and J. P. Nadal. Neural networks that learn temporal sequences by selection. *Proc. Natl. Acad. Sci. USA*, 84(9):2727–2731, 1987. 44
- [69] I. Delis, S. Panzeri, T. Pozzo, and B. Berret. A unifying model of concurrent spatial and temporal modularity in muscle activity. *J. Neurophysiol.*, 111(3):675–693, 2014. 70
- [70] Y. Demiriz and G. Hayes. Imitation as a dual-route process featuring predictive and learning components: A biologically plausible computational model. In K. Dautenhahn and C. L. Nehaniv, editors, *Imitation in Animals and Artifacts*, pages 327–361. MIT Press, 2002. 41
- [71] C. de’Sperati and P. Viviani. The relationship between curvature and velocity in two-dimensional smooth pursuit eye movements. *The Journal of Neuroscience*, 17(10):3932–3945, 1997. 157
- [72] E. A. Dinic, A. K. Kelmans, and M. A. Zaitsev. Nonisomorphic trees with the same T-polynomial. *Inform. Process. Lett.*, 6:73–76, 1977. 168
- [73] Boston Dynamics. Backflipping Atlas, Video Friday. IEEE Spectrum, 2017. 2
- [74] D. W. Eggert, A. Lorusso, and R. B. Fisher. Estimating 3-d rigid body transformations: a comparison of four major algorithms. *Machine Vision and Applications*, 9(5-6):272–290, 1997. 63

- [75] C. Engels and G. Schöner. Dynamic fields endow behavior-based robots with representations. *Robotics and Autonomous Systems*, 14(1):55–77, 1995. 10
- [76] W. Erlhagen, A. Mukovskiy, and E. Bicho. A dynamic model for action understanding and goal-directed imitation. *Brain Research*, 1083(1):174–188, 2006. 4, 14, 17, 36, 39, 43
- [77] W. Erlhagen, A. Mukovskiy, E. Bicho, and H. Bekkering. Development of action understanding in imitation tasks. In *Proc. IEEE Int. Conf. on Robotics and Automation, ICRA '2005*, Barcelona, Spain, April 2005. 4
- [78] W. Erlhagen, A. Mukovskiy, E. Bicho, G. Panin, C. Kiss, A. Knoll, H. van Schie, and H. Bekkering. Action understanding and imitation learning in a robot-human task. In W. Duch, J. Kacprzyk, E. Oja, and S. Zadróžny, editors, *Artificial Neural Networks: Biological Inspirations, ICANN, 2005*, volume LNCS 3696, pages 261–268, Berlin, Heidelberg, 2005. Springer-Verlag. 4, 13
- [79] W. Erlhagen, A. Mukovskiy, E. Bicho, G. Panin, C. Kiss, A. Knoll, H. van Schie, and H. Bekkering. Goal-directed imitation for robots: A bio-inspired approach to action understanding and skill learning. *J. Robotics and Autonomous Systems*, 54(5):353–360, 2006. 4, 12, 16, 21, 22, 32, 34, 38, 39
- [80] W. Erlhagen, A. Mukovskiy, F. Chersi, and E. Bicho. On the development of intention understanding for joint action tasks. In *IEEE 6th Int. Conf. on Development and Learning, ICDL 2007*, pages 140–145, 2007. 4, 44, 45, 46
- [81] W. Erlhagen and G. Schöner. Dynamic field theory of movement preparation. *Psychological Review*, 109(3):545–572, 2002. 15, 16
- [82] A. Escande, N. Mansard, and P. Wieber. Fast resolution of hierarchized inverse kinematics with inequality constraints. In *IEEE Int. Conf. on Robotics and Automation (ICRA 2010, Anchorage, USA)*, pages 3733–3738, 2010. 90
- [83] A. Esposito and L. C. Jain, editors. *Toward Robotic Socially Believable Behaving Systems - Volume I, Modeling Emotions*, volume 105. Springer-International Publishing, 2016. 1
- [84] A. Esposito and L. C. Jain, editors. *Toward Robotic Socially Believable Behaving Systems - Volume II, Modeling Social Signals*, volume 106. Springer-International Publishing, 2016. 1
- [85] A. Fang and N. S. Pollard. Efficient synthesis of physically valid human motion. *ACM Trans. on Graphics*, 22(3):417–426, 2003. 53
- [86] A. A. Fel'dbaum. *Optimal Control Systems*. Academic Press, New York, 1965. 54
- [87] A. W. Feng, Y. Xu, and A. Shapiro. An example-based motion synthesis technique for locomotion and object manipulation. *Proc. of ACM SIGGRAPH I3D*, pages 95–102, 2012. 54
- [88] M. Fiedler. Algebraic connectivity of graphs. *Czech. Math. J.*, 23(98):298–305, 1973. 171

- 
- [89] A. Finn and S. Scheding, editors. *Developments and Challenges for Autonomous Unmanned Vehicles*, volume 3. Springer-Verlag, Berlin Heidelberg, 2010. 1
- [90] T. Flash and A.A. Handzel. Affine differential geometry analysis of human arm movements. *Biological Cybernetics*, 96(6):577–601, 2007. 157, 158
- [91] T. Flash and B. Hochner. Motor primitives in vertebrates and invertebrates. *Curr. Opin. Neurobiol.*, 15(6):660–666, 2005. 54, 124
- [92] A. Fod, M. J. Mataric, and O. C. Jenkins. Automated derivation of primitives for movement classification. *Autonomous Robots*, 12(1):39–54, 2002. 54, 79
- [93] L. Fogassi, P. F. Ferrari, B. Gesierich, S. Rozzi, F. Chersi, and G. Rizzolatti. Parietal lobe: From action organization to intention understanding. *Science*, 308(5722):662–667, 2005. 3, 14
- [94] J. H. Friedman, J. L. Bentley, and R. A. Finkel. An algorithm for finding best matches in logarithmic expected time. *ACM Trans. of Mathematical Software*, 3(3):209–226, 1977. 27
- [95] J. M. Fuster. Temporal processing. *Annals of the New York Academy of Sciences*, 769(1):173–182, 1995. 19
- [96] Joaquin M. Fuster. *Memory in the Cerebral Cortex: An Empirical Approach to Neural Networks in the Human and Nonhuman Primate*. MIT Press, Cambridge, MA, 1994. 19
- [97] A. Gams, B. Nemeč, L. Zlajpah, M. Wächter, A. J. Ijspeert, T. Asfour, and A. Ude. Modulation of motor primitives using force feedback: Interaction with the environment and bimanual tasks. In *Proc. IEEE/RSJ Int. Conf. on Intelligent Robots and Systems (IROS 2013)*, pages 5629–5635, 2013. 55
- [98] A. Gams, L. Righetti, A. J. Ijspeert, and J. Lenařćić. A dynamical system for online learning of periodic movements of unknown waveform and frequency. *Proc. of the IEEE-RAS/EMBS Int. Conf. on Biomed. Robotics and Biomechanics*, pages 85–90, 2008. 55, 124
- [99] F. R. Gantmacher. *The Theory of Matrices, Vol.2*. AMS Chelsea Publishing, 1959. 64
- [100] M. Gienger, B. Bolder, M. Dunn, H. Sugiura, H. Janssen, and C. Goerick. Predictive behavior generation - a sensor-based walking and reaching architecture for humanoid robots. In K. Berns and T. Luksch, editors, *Informatik Aktuell (AMS)*, pages 275–281. Springer-Verlag, 2007. 55
- [101] M. Gienger, M. Toussaint, and C. Goerick. Whole-body motion planning - building blocks for intelligent systems. In K. Harada, editor, *Motion Planning for Humanoid Robots*, pages 67–98. Springer, 2010. 20
- [102] M. Gienger, M. Toussaint, N. Jetchev, A. Bendig, and C. Goerick. Optimization of fluent approach and grasp motions. In *Proc. of 8th IEEE-RAS Int. Conf. on Humanoid Robots (Humanoids 2008)*, pages 111–117, 2008. 55

- [103] M. A. Giese, A. Mukovskiy, A. Park, L. Omlor, and J. J. E. Slotine. Real-time synthesis of body movements based on learned primitives. In D. Cremers, editor, *Stat. and Geom. Approaches to Visual Motion Analysis, LNCS 5604*, pages 107–127. Springer-Verlag, Berlin/Heidelberg, 2009. 6, 51, 67, 70, 79, 82, 86, 100, 101
- [104] G. Giorgi and C. Zuccotti. An overview on D-stable matrices. DEM Working Papers Series 097, University of Pavia, Dept. of Econ., 2015. 175
- [105] M. Gleicher. Retargetting motion to new characters. *Proc. ACM SIGGRAPH, Int. Conf. on Comp. Graph. and Interactive Techniques*, pages 33–42, 1998. 53, 98
- [106] M. Gleicher. Motion Path Editing. *Proc. of 2001 ACM Symp. on Interactive 3D Graphics*, pages 195–202, 2001. 2
- [107] M. Gleicher, H. J. Shin, L. Kovar, and A. Jepsen. Snap-together motion: Assembling run-time animation. *Proc. the Symp. on Interactive 3D Graphics*, Apr 2003. 2, 53
- [108] C. Godsil and G. Royle. *Algebraic Graph Theory*. Springer, 2001. 168
- [109] G.H. Golub and C.F. Van Loan. *Matrix Computations*. The Johns Hopkins University Press, 1989. 170
- [110] C. Gordon, D.L. Webb, and S. Wolpert. One cannot hear the shape of a drum. *Bull. Amer. Math. Soc.*, 27:134–138, 1992. 168
- [111] F. Gravot, S. Cambon, and R. Alami. *aSyMov: A Planner That Deals with Intricate Symbolic and Geometric Problems*, pages 100–110. Springer, Berlin, Heidelberg, 2005. 19
- [112] R. Grzeszczuk, D. Terzopoulos, and G. Hinton. NeuroAnimator: Fast neural network emulation and control of physics based models. *Proc. ACM SIGGRAPH'98, Int. Conf. on Comp. Graph. and Interactive Techniques*, pages 9–20, 1998. 123
- [113] M. A. Gutiérrez, F. Vexo, and D. Thalmann. *Stepping into Virtual Reality*. Springer Science & Business Media, 2008. 1
- [114] F. O. Hadlock. A shortest path algorithm for grid graphs. *Networks*, 7(4):323–334, 1977. 20
- [115] E. Hairer, S. P. Nørsett, and G. Wanner. *Solving ordinary differential equations I: Nonstiff problems*. Berlin: Springer Verlag, 2 edition, 1993. 80
- [116] F. J. Hall. The adjacency matrix, standard laplacian, and normalized laplacian, and some eigenvalue interlacing results. *Tech.Rep.*, 2010. 171
- [117] C. M. Harris and D. M. Wolpert. Signal-dependent noise determines motor planning. *Nature*, 394:780–784, 1998. 89
- [118] K. Hauser and Y. Zhou. Asymptotically optimal planning by feasible kinodynamic planning in a state-cost space. *IEEE Trans. on Robotics*, 32(6):1431–1443, 2016. 20

- 
- [119] O. Herbort, M. V. Butz, and G. Pedersen. *The SURE-REACH Model for Motor Learning and Control of a Redundant Arm: From Modeling Human Behavior to Applications in Robotics*, pages 85–106. Springer Berlin Heidelberg, Berlin, Heidelberg, 2010. 20
- [120] Oliver Herbort and Martin V. Butz. Planning and control of hand orientation in grasping movements. *Exper. Brain Res.*, 202(4):867–878, 2010. 20
- [121] A. Herdt, H. Diedam, P.-B. Wieber, D. Dimitrov, K. Mombaur, and M. Diehl. Online walking motion generation with automatic foot step placement. *Advanced Robotics*, 24(5-6):719–737, 2010. 56, 113
- [122] G. E. Hinton. Parallel computations for controlling an arm. *J. Mot. Behav.*, 16(2):171–194, 1984. 25
- [123] J. K. Hodgins, W. L. Wooten, D. C. Brogan, and J. F. O’Brien. Animating human athletics. *Proc. ACM SIGGRAPH’95*, pages 7–78, 1995. 123
- [124] R. A. Horn. The Hadamard product. In C. R. Johnson, editor, *Proc. of Symposia in Applied Mathematics*, volume 40, pages 87–169, AMS, Providence, Rhode Island, USA, 1990. AMS Short Course Lecture Notes. 180
- [125] R. A. Horn and C. R. Johnson. *Matrix Analysis*. Cambridge University Press, Cambridge, 1985. 169, 170, 173, 178
- [126] E. Hsu, K. Pulli, and J. Popović. Style translation for human motion. *ACM Trans. on Graphics, SIGGRAPH’05*, 24(3):1082–1089, 2005. 53, 123
- [127] Y. Huang and M. Kallmann. Planning motions for virtual demonstrators. In *Intelligent Virtual Agents*, pages 190–203. Springer, 2014. 54
- [128] D. Huh and T.J. Sejnowski. Spectrum of power laws for curved hand movements. *Proceedings of the National Academy of Sciences*, 112(29):E3950–E3958, 2015. 158
- [129] Connolly C. I., Grupen R. A., and Souccar K. A hamiltonian framework for kinodynamic planning and control. In *IEEE Conf. On Robotics and Automation*, volume 3, pages 2746–2751, 1995. 20
- [130] A. J. Ijspeert, A. Crespi, D. Ryczko, and J.-M. Cabelguen. From swimming to walking with a salamander robot driven by a spinal cord model. *Science*, 315(5817):1416–1420, 2007. 156
- [131] A. J. Ijspeert, J. Nakanishi, H. Hoffmann, P. Pastor, and S. Schaal. Dynamical movement primitives: Learning attractor models for motor behaviors. *Neural Computation*, 25(2):328–373, 2013. 55
- [132] A. J. Ijspeert, J. Nakanishi, and S. Schaal. Learning attractor landscapes for learning motor primitives. *Adv. in NIPS*, 15:1547–1554, 2002. 52, 55, 79, 156
- [133] W. Imrich and S. Klavžar. *Product Graphs: Structure and Recognition*. Wiley, 2000. 171

- [134] S. Intille and A. Bobick. Recognizing planned multi-person action. *J. of Computer Vision and Image Understanding*, 3:414–445, 2001. 1
- [135] Y. Ivanenko, R. Poppele, and F. Lacquaniti. Five basic muscle activation patterns account for muscle activity during human locomotion. *Journal Of Physiology*, 556:267–282, 2004. 67
- [136] Y.P. Ivanenko, R. Grasso, V. Macellari, and F. Lacquaniti. Two-thirds power law in human locomotion: role of ground contact forces. *Neuroreport*, 13(9):1171–1174, 2002. 157
- [137] A. Jadbabaie, J. Lin, and A. S. Morse. Coordination of groups of mobile autonomous agents using nearest neighbour rules. *IEEE Trans. On Automatic Control*, 48(6):988–1001, 2003. 124
- [138] L. Jaillet, J. Cortés, and T. Siméon. Transition-based RRT for path planning in continuous cost spaces. In *2008 IEEE/RSJ Int. Conf. on Intelligent Robots and Systems*, pages 2145–2150, 2008. 20
- [139] D. Jancke, W. Erlhagen, H. R. Dinse, A. C. Akhavan, M. Giese, A. Steinhage, and G. Schöner. Parametric population representation of retinal location: Neuronal interaction dynamics in cat primary visual cortex. *Journal of Neuroscience*, 19(20):9016–9028, 1999. 15
- [140] A. M. Johnson, J. King, and S. Srinivasa. Convergent Planning. *IEEE Robotics and Automation Letters*, 1(2):1044–1051, 2016. 20
- [141] C. R. Johnson. Sufficient conditions for  $d$ -stability. *Journal of Economic Theory*, 9(1):53–62, 1974. 175
- [142] I. T. Jolliffe. *Principal Component Analysis*. Springer Series in Statistics. Springer-Verlag, New York, 2 edition, 2002. 51
- [143] S. Kajita, F. Kanehiro, K. Kaneko, K. Fujiwara, K. Harada, K. Yokoi, and H. Hirukawa. Biped walking pattern generation by using preview control of zero-moment point. *Proc. of Int. Conf. on Robotics and Autom.*, pages 1620–1626, 2003. 55, 56, 112, 113
- [144] O. Kanoun, J.-P. Laumond, and E. Yoshida. Planning foot placements for a humanoid robots: A problem of inverse kinematics. *The Int. J. of Robotics Research*, 30:476–485, 2011. 55
- [145] V. L. Kantorovich. Functional analysis and applied mathematics (in russian). *Uspekhi Mat. Nauk*, 3:89–185, 1948. English transl.: National Bureau of Standards Report 1509, Washington, 1952. 184
- [146] H. J. Kappen. Linear theory for control of nonlinear stochastic systems. *Phys. Rev. Lett.*, 95(20):200–204, 2005. 20
- [147] H. J. Kappen. Path integrals and symmetry breaking for optimal control theory. *Journal of Statistical Mechanics: Theory and Experiment*, 11:P11011, 2005. 20

- 
- [148] M. Karklinsky, M. Naveau, A. Mukovskiy, O. Stasse, T. Flash, and P. Souères. Robust human-inspired power law trajectories for humanoid HRP-2 robot. *Biomedical Robotics and Biomechanics, 6th IEEE Conf.*, pages 106–113, 2016. 7, 84, 157, 158, 159
- [149] A. A. Kassim and B. V. K. V. Kumar. The wave expansion neural network. *Neurocomputing*, 16(3):237–258, 1997. 20
- [150] E. Kaszkurewicz and A. Bhaya. Robust stability and diagonal Liapunov functions. *SIAM. J. Matrix Analysis and Appl.*, 14(2):508–520, 1993. 175, 176
- [151] L. Kavraki and J.-C. Latombe. Randomized Preprocessing of Configuration Space for Path Planning: Articulated Robots. *Proc. of the IEEE/RSJ/GI Int. Conf. on Intelligent Robots and Systems '94. 'Adv. Robotic Systems and the Real World', IROS '94*, 3:1764–1771, 1994. 19
- [152] L. E. Kavraki, P. Svestka, J. C. Latombe, and M. H. Overmars. Probabilistic roadmaps for path planning in high-dimensional configuration spaces. *IEEE Trans. on Robotics and Automation*, 12(4):566–580, 1996. 20
- [153] C. Keysers and D. I. Perrett. Demystifying social cognition: A Hebbian perspective. *Trends in Cognitive Sciences*, 8(11):501–507, 2004. 16
- [154] C. A. Klein and C.-H. Huang. Review of pseudoinverse control for use with kinematically redundant manipulators. *IEEE Trans. on Systems, Man and Cybernetics*, 13:245–250, 1983. 90
- [155] M. Kleiner, D. Brainard, D. Pelli, A. Ingling, R. Murray, and C. Broussard. What's new in Psychtoolbox-3. *Perception*, 36(14):1–16, 2007. 65
- [156] J. Koenemann, A. Del Prete, Y. Tassa, E. Todorov, O. Stasse, M. Bennewitz, and N. Mansard. Whole-body model-predictive control applied to the HRP-2 humanoid. In *IEEE/RSJ Int. Conf. on Intelligent Robots and Systems (IROS)*, pages 3346–3351, 2015. 55
- [157] Y. Koga, K. Kondo, J. Kuffner, and J.-C. Latombe. Planning Motions with Intentions. In *Proc. of the 21st Ann. Conf. on Computer Graphics and Interactive Techniques, SIGGRAPH '94*, pages 395–408, New York, NY, USA, 1994. ACM. 19, 21
- [158] J. Koschorreck and K. Mombaur. Modeling and optimal control of human platform diving with somersaults and twists. *Optimization and Engineering*, 13(1):29–56, 2012. 55, 111
- [159] L. Kovar, M. Gleicher, and F. Pighin. Motion graphs. *Proc. of SIGGRAPH 2002*, pages 473–482, 2002. 54
- [160] L. Kovar, J. Schreiner, and M. Gleicher. Footskate cleanup for motion capture editing. In *Proceedings of the ACM SIGGRAPH Symposium on Computer Animation*, pages 97–104, San Antonio, Texas, 2002. ACM Press. 98
- [161] N.N. Krasovskii. *Problems of the Theory of Stability of Motion*. Mir, Moscow, 1959. 125

- [162] S. Kuindersma, R. Deits, M. Fallon, A. Valenzuela, H. Dai, F. Permenter, T. Koolen, P. Marion, and R. Tedrake. Optimization-based locomotion planning, estimation, and control design for the Atlas humanoid robot. *Autonomous Robots*, pages 1–27, 2015. 55
- [163] Y. Kuramoto. *Chemical Oscillations, Waves and Turbulence*. Springer, 1984. 140
- [164] F. Lacquaniti, C. Terzuolo, and P. Viviani. The law relating the kinematic and figural aspects of drawing movements. *Acta Psychologica*, 54(1-3):115–130, 1983. 157
- [165] W. M. Land, D. A. Rosenbaum, S. Seegelke, and T. Schack. Whole-body posture planning in anticipation of a manual prehension task: Prospective and retrospective effects. *Acta Psychologica*, 114:298–307, 2013. 54, 61, 89
- [166] J. P. LaSalle and S. Lefschetz. *Stability by Liapunov’s direct method with applications*. Academic Press, N.Y., 1964. 175
- [167] Jean-Claude Latombe. *Robot Motion Planning*. Springer US, Boston, MA, 1991. 19
- [168] A. M. Laursen. Movements evoked from the region of the caudate nucleus in cats. *Acta Physiol. Scand.*, 54(2):175–184, 1962. 20
- [169] S. M. LaValle. Rapidly-exploring random trees: A new tool for path planning. TR 98-11, Computer Science Dept., Iowa State University, October 1998. 20
- [170] S. M. LaValle. *Planning Algorithms*. Cambridge University Press, 2006. 20
- [171] S. M. LaValle and J. J. Kuffner Jr. Randomized kinodynamic planning. *The Int. J. of Robotics Research*, 20(5):378–400, 2001. 20
- [172] D. V. Lebedev, J. J. Steil, and H. J. Ritter. The dynamic wave expansion neural network model for robot motion planning in time-varying environments. *Neural Networks*, 18(3):267–285, 2005. 20
- [173] C. Y. Lee. An algorithm for path connections and its applications. *IRE Trans. on Electronic Computers*, EC-10(3):346–365, 1961. 20
- [174] D. D. Lee and H. S. Seung. Learning the parts of objects by Non-negative Matrix Factorization. *Nature*, 401(6755):788–791, 1999. 69
- [175] D. D. Lee and H. S. Seung. Algorithms for Non-negative Matrix Factorization. In T. K. Leen, T. G. Dietterich, and V. Tresp, editors, *Adv. in Neural Inform. Proc. Syst., 13. NIPS’2000*, pages 556–562. MIT Press, 2001. 69
- [176] M. Lemmon. 2-Degree-of-freedom Robot Path Planning using Cooperative Neural Fields. *Neural Computation*, 3(3):350–362, 1991. 20
- [177] M. Lemmon. Real-time optimal path planning using a distributed computing paradigm. In *American Control Conference*, pages 2062–2063, 1991. 20



- 
- [178] Y. Li, T. Wang, and H. Y. Shum. Motion texture: A two level statistical model for character motion synthesis. *Proc. of SIGGRAPH 2002*, pages 465–472, 2002. 53
- [179] D. Liberzon and A. S. Morse. Basic problems in stability and design of switched systems. *IEEE Control Systems*, 19(5):59–70, 1999. 124
- [180] V. B. Lidskii. On the characteristic numbers of the sum and product of symmetric matrices. *Doklady Akad. Nauk SSSR (N.S.)*, 75:769–772, 1950. 184
- [181] K. Liu, A. Hertzmann, and Z. Popovic. Learning physics-based motion style with nonlinear inverse optimization. *ACM Trans. on Graphics*, 23(3):1071–1081, 2005. 53
- [182] R.-W. Liu. Convergent systems. *IEEE Trans. on Automatic Control*, 13(4):384–391, 1968. 124
- [183] W. Lohmiller and J. J. E. Slotine. On Contraction Analysis for Nonlinear Systems. *Automatica*, 34(6):683–696, 1998. 6, 124, 125, 127, 128, 148, 151, 153, 156, 159
- [184] K. Löwner. Über monotone Matrixfunktionen. *Math. Zeit.*, 38:177–216, 1934. 173
- [185] A. I. Lur’e and V. N. Postnikov. On the theory of stability of control systems. *Prikl. Mat. I Mekh.*, 8(3):246–248, 1944. 175
- [186] A. Lyapunov. Problemes Général de la Stabilité du mouvement. *Communications of the Math. Soc. of Kharkow*, 1892. Republished in Annals of Math. Studies, no. 17, Princeton Press, Princeton, 1947. 174
- [187] A. A. Maciejewski and C. A. Klein. Obstacle avoidance for kinematically redundant manipulators in dynamically varying environments. *The Int. J. of Robotics Research*, 4(3):109–117, 1985. 90
- [188] N. Mansard, O. Khatib, and A. Kheddar. A unified approach to integrate unilateral constraints in the stack of tasks. *IEEE Trans. on Robotics*, 25(3):670–685, 2009. 89, 90
- [189] S. L. Marple. *Digital Spectral Analysis: With Applications*. Prentice-Hall Series in Signal Processing. Prentice Hall, Inc, Englewood Cliffs, NJ, 1987. 68
- [190] R. G. Marteniuk and C. P. Bertram. Contributions of gait and trunk movement to prehension: Perspectives from world- and body centered coordinates. *Motor Control*, 5:151–164, 2001. 54
- [191] J. P. Martin. *The basal ganglia and posture*. Pitman Medical, London, 1967. 20
- [192] W. Martin. Time-frequency analysis of random signals. *Proc. IEEE Int. Conf. on Acoustics, Speech, Signal Proc.*, 82:1325–1328, 1982. 68
- [193] G. Matz and F. Hlawatsch. Wigner distributions (nearly) everywhere: Time-frequency analysis of signals, systems, random processes, signal spaces and frames. *Signal Processing*, 83(7):1355–1378, 2003. 68

- [194] B.L. McNaughton, F.P. Battaglia, O. Jensen, E.I. Moser, and M.-B. Moser. Path integration and the neural basis of the 'cognitive map'. *Nature Reviews Neuroscience*, 7(8):663–678, 2006. 20
- [195] Bartlett W. Mel. *Connectionist Robot Motion Planning: A Neurally-Inspired Approach to Visually-Guided Reaching*. Academic Press, 1990. 19
- [196] R. Merris. Laplacian matrices of graphs: A survey. *Lin. Alg. and Appl.*, 197–198:143–176, 1994. 168
- [197] Michael John Milford. *Robot Navigation from Nature. Simultaneous Localisation, Mapping, and Path Planning Based on Hippocampal Models*. Springer Tracts in Advanced Robotics, 41. Springer-Verlag, Berlin Heidelberg, 2008. 20
- [198] B. Mohar. Eigenvalues, Diameter, and Mean Distance in Graphs. *Graphs and Combinatorics*, 7:53–64, 1991. 171
- [199] B. Mohar. The Laplacian spectrum of graphs. In Y. Alavi, G. Chartrand, O. R. Oellermann, and A. J. Schwenk, editors, *Graph Theory, Combinatorics, and Applications*, volume 2, pages 871–898. Wiley, 1991. 170
- [200] A. W. Moore. Variable resolution Dynamic Programming: Efficiently learning action maps in multivariate real-valued state-spaces. In *Machine Learning Proceedings, 1991*, pages 333–337. Morgan Kaufmann, San Francisco (CA), 1991. 20
- [201] A. W. Moore and C. G. Atkeson. The parti-game algorithm for variable resolution reinforcement learning in multidimensional state-spaces. *Machine Learning*, 21(3):199–233, 1995. 20, 25
- [202] P. Morasso. Spatial control of arm movements. *Experimental Brain Research*, 42(2):223–227, 1981. 80
- [203] L. Moreau. Stability of continuous-time distributed consensus algorithms. *Proc. 43rd IEEE Conf. on Decision and Control*, 4:3998–4003, 2004. 124
- [204] J. Morimoto and C. G. Atkeson. Minimax differential dynamic programming: An application to robust biped walking. In *Adv. in Neural Information Processing Systems (NIPS)*, pages 1539–1546, 2002. 20
- [205] M. Mørup, K. H. Madsen, and L. K. Hansen. Shifted Independent Component Analysis. In *7th Int. Conf. on Independent Component Analysis and Signal Separation*, volume ICA'07, pages 89–96, 2007. 71, 72, 74
- [206] M. Mørup, K. H. Madsen, and L. K. Hansen. Shifted Non-negative Matrix Factorization. In *2007 IEEE Workshop on Machine Learning for Signal Processing*, pages 139–144, 2007. 70
- [207] M. Mühlig, M. Gienger, and J.J. Steil. Human-robot interaction for learning and adaptation of object movements. In *Proc. of IEEE/RSJ Int. Conf. on Intelligent Robots and Systems (IROS 2010)*, pages 4901–4907, 2010. 55

- 
- [208] U. Muico, Y. Lee, J. Popovic, and Z. Popović. Contact-aware nonlinear control of dynamic characters. *ACM Trans. on Graphics*, 28(3):Art.No.81., 2009. 53
- [209] A. Mukovskiy, W. Land, T. Schack, and M. A. Giese. Modeling of predictive human movement coordination patterns for applications in computer graphics. *Journal of WSCG*, 23(2):139–146, 2015. 6, 52, 61, 62, 76, 78, 84, 87, 88
- [210] A. Mukovskiy, A. Park, L. Omlor, J. J. E. Slotine, and M. A. Giese. Self-organization of character behavior by mixing of learned movement primitives. *Proc. of the 13th Fall Workshop on Vision, Modeling, and Visualization (VMV 2008)*, pages 121–130, 2008. 6, 51, 52, 67, 70, 71, 79, 81, 86, 104
- [211] A. Mukovskiy, J. J. E. Slotine, and M. A. Giese. Analysis and design of the dynamical stability of collective behavior in crowds. *Journal of WSCG*, 19(1–3):69–76, 2011. 7, 84
- [212] A. Mukovskiy, J. J. E. Slotine, and M. A. Giese. Dynamically stable control of articulated crowds. *Journal of Computational Science*, 4(4):304–310, 2013. 7, 148, 182
- [213] A. Mukovskiy, J.J.E. Slotine, and M.A. Giese. Design of the dynamic stability properties of the collective behavior of articulated bipeds. *Proc. of 10th IEEE-RAS Int. Conf. on Humanoid Robots, Humanoids, 2010. Dec.6-8, 2010, Nashville, TN, USA*, pages 66–73, 2010. 7, 84, 146, 148
- [214] A. Mukovskiy, N. Taubert, D. Endres, C. Vassallo, M. Naveau, O. Stasse, P. Souères, and M. A. Giese. *Modeling of coordinated human body motion by learning of structured dynamic representations*, volume 117 of *Springer STAR Series*, pages 237–267. Springer Int. Publ., Berlin, Heidelberg, 2017. 6, 51, 52, 84
- [215] A. Mukovskiy, C. Vassallo, M. Naveau, O. Stasse, P. Souères, and M. A. Giese. Adaptive synthesis of dynamically feasible full-body movements for the humanoid robot HRP-2 by flexible combination of learned dynamic movement primitives. *Journal of Robotics and Autonomous Systems*, 91:270–283, 2017. 6, 52, 53, 67, 84, 112, 115, 116, 117, 118, 119, 122
- [216] P. Muraca, G. Raiconi, and T. Varone. Cooperative neural field for the path planning of a robot arm. *Journal of Intelligent and Robotic Systems*, 15(1):11–18, 1996. 20
- [217] F. A. Mussa-Ivaldi, P. Morasso, and R. Zaccaria. Kinematic networks. a distributed model for representing and regularizing motor redundancy. *Biological Cybernetics*, 60:1–16, 1988. 25
- [218] S. R. Musse and D. Thalmann. A behavioral model for real time simulation of virtual human crowds. *IEEE Trans. on Visualization and Comp. Graph.*, 7(2):152–164, 2001. 123
- [219] H. Nagai. Bellman equations of risk-sensitive control. *SIAM Journal on Control and Optimization*, 34(1):74–101, 1996. 20

- [220] M. Naveau, J. Carpentier, S. Barthelemy, O. Stasse, and P. Souères. METAPOD - Template META-PrOgramming applied to Dynamics: CoP-CoM trajectories filtering. In *2014 IEEE-RAS Int. Conf. on Humanoid Robots (Humanoids)*. IEEE, 2014. 52, 53, 56, 111, 112, 113, 164
- [221] M. Naveau, M. Kudruss, O. Stasse, C. Kirches, K. Mombaur, and P. Souères. A reactive Walking Pattern Generator based on Nonlinear Model Predictive Control. *IEEE Robotics and Automation Letters*, 2(1):10–17, 2017. 52, 56, 111, 112, 113, 164, 165
- [222] C. L. Nehaniv and K. Dautenhahn. The correspondance problem. In K. Dautenhahn and C. L. Nehaniv, editors, *Imitation in Animals and Artifacts*, pages 41–61. MIT Press, Cambridge, MA, USA, 2002. 3, 9, 19, 41
- [223] P. Ögren, M. Egerstedt, and X. Hu. A control Lyapunov function approach to multi-agent coordination. *IEEE Trans. on Robotics and Automatation*, 18(5):847–851, 2002. 124
- [224] J. O’Keefe and J. Dostrovsky. The hippocampus as a spatial map. preliminary evidence from unit activity in the freely-moving rat. *Brain Research*, 34(1):171–175, 1971. 20
- [225] A. Olshevsky and J. N. Tsitsiklis. On the nonexistence of quadratic Lyapunov functions for consensus algorithms. *IEEE Transactions on Automatic Control*, 53(11):2642–2645, 2008. 124
- [226] L. Omlor. *New Methods for Anechoic Demixing with Application to Shift Invariant Feature Extraction. PhD Thesis*. University of Tübingen, 2011. 63
- [227] L. Omlor and M. A. Giese. Blind source separation for over-determined delayed mixtures. *Adv. in NIPS*, 19:1049–1056, 2006. 69
- [228] L. Omlor and M. A. Giese. Extraction of spatio-temporal primitives of emotional body expressions. *Neurocomputing*, 70:10–12, 2007.
- [229] L. Omlor and M. A. Giese. Anechoic blind source separation using Wigner marginals. *J. of Machine Learning Res.*, 12:1111–1148, 2011. 69, 78
- [230] H. M. Ozaktas and D. Mendlovic. Fourier transforms of fractional orders and their optical interpretation. *Opt. Commun.*, 110:163–169, 1993. 69
- [231] H. M. Ozaktas, Z. Zalevsky, and M. A. Kutay. *The Fractional Fourier Transform*. Wiley, England, 2001. 69
- [232] D. A. Paley, N. E. Leonard, R. Sepulchre, D. Grunbaum, and J. K. Parrish. Oscillator models and collective motion: Spatial patterns in the dynamics of engineered and biological networks. *IEEE Control Systems Magazine*, 27:89–105, 2007. 124
- [233] Y. Pan, K. Bakshi, and E.A. Theodorou. Robust trajectory optimization: A cooperative stochastic game theoretic approach. In *Robotics: Science and Systems*, Rome, Italy, July 2015. 20

- 
- [234] S. Paris, J. Pettré, and Donikian S. Pedestrian reactive navigation for crowd simulation: A predictive approach. *Proc. Eurographics 2007*, 26(3):665–674, 2007. 99
- [235] A. Park, A. Mukovskiy, L. Omlor, and M. A. Giese. Self-organized character animation based on learned synergies from full-body motion capture data. *Proc. of Int. Conf. on Cognitive Systems, CogSys 2008*, 2008. 6, 52, 67, 70, 71, 79, 99, 101, 124
- [236] A. Park, A. Mukovskiy, L. Omlor, and M. A. Giese. Synthesis of character behaviour by dynamic interaction of synergies learned from motion capture data. *The 16-th Int. Conf. in Central Europe on Comp. Graphics, Visualization and Computer Vision 2008, WSCG'08*, pages 9–16, 2008. 5, 51, 52, 70, 71, 79, 105, 107
- [237] A. Park, A. Mukovskiy, J. J. E. Slotine, and M. A. Giese. Design of dynamical stability properties in character animation. *Proc. of VRIPHYS'09*, pages 85–94, 2009. 7, 84, 85, 140, 141, 145
- [238] S.I. Park, H.J. Shin, and S.Y. Shin. On-line locomotion generation based on motion blending. *Proc. of the 2002 ACM SIGGRAPH/Eurographics Symp. on Comp. Animation*, pages 105–111, 2002. 54
- [239] A. Perez, R. Platt, G. Konidaris, L. Kaelbling, and T. Lozano-Perez. LQR-RRT\*: Optimal sampling-based motion planning with automatically derived extension heuristics. In *2012 IEEE Int. Conf. on Robotics and Automation*, pages 2537–2542, 2012. 20
- [240] B. E. Perk and J. J. E. Slotine. Motion Primitives for Robotic Flight Control. *CoRR*, abs/cs/0609140, 2006. 125
- [241] S. K. Persidskii. Concerning problem of absolute stability. *Automat. Remote Control*, 30(12):1889–1895, 1970. 175
- [242] Q. C. Pham and J. J. E. Slotine. Stable concurrent synchronization in dynamic system networks. *Neural Networks*, 20(3):62–77, 2007. 124, 129, 131, 132, 134, 145, 169
- [243] A. Pikovsky, M. Rosenblum, and J. Kurths. *Synchronization, A Universal Concept in Nonlinear Sciences*. Cambridge Univ. Press, Cambridge, 2003. 124
- [244] F.E. Pollick and G. Sapiro. Constant affine velocity predicts the 1/3 power law of planar motion perception and generation. *Vision Research*, 37(3):347–353, 1997. 157, 158
- [245] G. Pólya and G. Szegő. *Problems and Theorems in Analysis I*. Springer-Verlag Berlin Heidelberg, 1998. 184
- [246] S. Quinlan and O. Khatib. Elastic bands: connecting path planning and control. In *Proc. IEEE Int. Conf. on Robotics and Automation*, volume 2, pages 802–807, 1993. 32
- [247] M. Quoy, S. Moga, and P. Gaussier. Dynamical neural networks for planning and low-level robot control. *IEEE Trans. on Systems, Man, and Cybernetics - Part A: Systems and Humans*, 33(4):523–532, 2003. 10

- [248] C. E. Rasmussen and C. K. I. Williams. *Gaussian Processes for Machine Learning*. The MIT Press, 2005. 93
- [249] W. Ren, R. W. Beard, and E. M. Atkins. A survey of consensus problems in multiagent coordination. *Proc. of the American Control Conference*, ThA04.2:1859–1864, 2005. 124
- [250] C. W. Reynolds. Flocks, herds, and schools: A distributed behavioral model. *Computer Graphics*, 21(4):25–34, 1987. 124
- [251] M. J. E. Richardson and T. Flash. Comparing smooth arm movements with the two-thirds power law and the related segmented-control hypothesis. *The Journal of Neuroscience*, 22(18):8201–8211, 2002. 158
- [252] L. Righetti and A. J. Ijspeert. Programmable Central Pattern Generators: An application to biped locomotion control. *Proc. of the 2006 IEEE Int. Conf. on Robotics and Automation*, pages 1585–1590, 2006. 124
- [253] G. Rizzolatti, L. Fogassi, and V. Gallese. Neurophysiological mechanisms underlying the understanding and imitation of action. *Nature Reviews. Neuroscience*, 2(9):661–670, 2001. 3, 9, 14, 37
- [254] O. Rodrigues. Des lois géométriques qui regissent les déplacements d’un système solide dans l’ espace, et de la variation des coordonnées provenant de ces déplacement considérées indépendant des causes qui peuvent les produire. *J. Math. Pures Appl.*, 5:380–440, 1840. 64
- [255] C. Rose, M. Cohen, and B. Bodenheimer. Verbs and Adverbs: Multidimensional motion interpolation. *IEEE Comp. Graphics and Appl.*, 18(5):32–40, 1998. 53
- [256] C. Rose, B. Guenter, B. Bodenheimer, and M. Cohen. Efficient generation of motion transitions using spacetime constraints. *Int. Conf. on Comp. Graph. and Interactive Techniques, Proc. ACM SIGGRAPH’96*, 30:147–154, 1996. 2, 53
- [257] D. A. Rosenbaum. Reaching while walking: Reaching distance costs more than walking distance. *Psych. Bull. Rev.*, 15:1100–1104, 2008. 54, 111
- [258] D. A. Rosenbaum. *Human Motor Control*. Academic Press, 2 edition, 2010. 3
- [259] D. A. Rosenbaum, S. E. Engelbrecht, M. M. Bushe, and L. D. Loukopoulos. A model for reaching control. *Acta Psychol.*, 82(1-3):237–250, 1993. 20
- [260] D. A. Rosenbaum, L. D. Loukopoulos, R. G. J. Meulenbroek, J. Vaughan, and S. E. Engelbrecht. Planning reaches by evaluating stored postures. *Psychological Review*, 102(1):28–67, 1995.
- [261] D. A. Rosenbaum, R. J. Meulenbroek, and J. Vaughan. Remembered positions: Stored locations or stored postures? *Experimental Brain Research*, 124(4):503–512, 1999.

- 
- [262] D. A. Rosenbaum, R. J. Meulenbroek, J. Vaughan, and C. Jansen. Coordination of reaching and grasping by capitalizing on obstacle avoidance and other constraints. *Experimental Brain Research*, 128(1):92–100, 1999.
- [263] D. A. Rosenbaum, R. J. Meulenbroek, J. Vaughan, and C. Jansen. Posture-based motion planning: Applications to grasping. *Psychological Review*, 108(4):709–734, 2001. 19, 20
- [264] N. Roy and S. Thrun. Motion Planning through Policy Search. In *IEEE/RSJ Int. Conf. on Intelligent Robots and Systems*, volume 3, pages 2419–2424, 2002. 20, 25
- [265] F. Rubin. The Lee path connection algorithm. *IEEE Trans. Comput.*, 23(9):907–914, 1974. 20
- [266] G. Russo and J. J. E. Slotine. Global convergence of quorum sensing networks. *Physical Review E*, 82(4):041919, 1–17, 2010. 130, 151, 153
- [267] D. Mendlovic S. Karako-Eilon, A. Yeredor. Blind source separation based on the fractional Fourier transform. In *4th Int. Symp. on ICA and BSS*, volume ICA’2003, pages 615–620, 2003. 69
- [268] A. Safonova, J. Hodgins, and N. Pollard. Synthesizing physically realistic human motion in low-dimensional, behavior-specific spaces. *ACM Trans. on Graphics*, 23(3):514–521, 2004. 52, 53, 67, 123
- [269] Y. Sakaguchi and S. Ikeda. Motor planning and sparse motor command representation. *Neurocomputing*, 70:1748–1752, 2007. 89
- [270] A. Samsonovich and B. L. McNaughton. Path integration and cognitive mapping in a continuous attractor neural network model. *The Journal of Neuroscience: The Official Journal of the Society for Neuroscience*, 17(15):5900–5920, 1997. 20
- [271] M. Santello, M. Flanders, and J. F. Soechting. Postural hand synergies for tool use. *Journal of Neuroscience*, 18(23):10105–15, 1998. 67
- [272] A. Savitzky and M. J. E. Golay. Smoothing and differentiation of data by simplified least squares procedures. *Analytical Chemistry*, 36(8):1627–1639, 1964. 76
- [273] H. Sayama. Estimation of Laplacian spectra of direct and strong product graphs. *Discrete Applied Math.*, 205(C):160–170, 2016. 171
- [274] L. Scardovi and R. Sepulchre. Collective optimization over average quantities. *Proc. of the 45th IEEE Conf. on Decision and Control, San Diego, California*, pages 3369–3374, 2006. 124
- [275] S. Schaal. Is imitation learning the route to humanoid robots? *Trends in Cognitive Sciences*, 3(6):233–242, 1999. 9, 14

- [276] S. Schaal, A. Ijspeert, and A. Billard. Computational approaches to motor learning by imitation. *Philosophical Transactions of the Royal Society B: Biological Sciences*, 358(1431):537–547, 2003. 9, 41, 52, 55, 79, 124
- [277] G. Schöner, M. Dose, and C. Engels. Dynamics of behavior: Theory and applications for autonomous robot architectures. *Robotics and Autonomous Systems*, 16(2-4):213–245, 1995. 99, 152
- [278] N. Schulz. Horde3D. <http://www.horde3d.org/>, 2006–2009. 65, 96, 150
- [279] J. Schur. Bemerkungen zur Theorie der beschränkten Bilinearformen mit unendlich vielen Veränderlichen. *Journal für die Reine und Angewandte Mathematik*, 140:1–28, 1911. 179
- [280] R. Scott. Sparking Life: Notes on the performance capture sessions for the Lord of the Rings: The Two Towers. *SIGGRAPH Comput. Graph.*, 37(4):17–21, 2003. 1
- [281] K. Seo, S.-J. Chung, and J. J. E. Slotine. CPG-based Control of a Turtle-like Underwater Vehicle. *Autonomous Robots, Special Issue on Control of Locomotion: From Animals to Robots*, 28(3):247–269, 2010. 125
- [282] R. Shadmehr. *Actuator and Kinematic Redundancy in Biological Motor Control*, pages 239–254. Springer Berlin Heidelberg, Berlin, Heidelberg, 1991. 25
- [283] R. Shadmehr and S. P. Wise. *Computational Neurobiology of Reaching and Pointing*. MIT Press, 2004. 157
- [284] W. Shao and D. Terzopoulos. Artificial intelligence for animation: Autonomous pedestrians. *Proc. ACM SIGGRAPH '05*, 69(5-6):19–28, 2005. 53
- [285] H. J. Shin, J. Lee, S. Y. Shin, and M. Gleicher. Computer puppetry: An importance-based approach. *ACM Transactions on Graphics*, 20(2):67–94, 2001. 123
- [286] A. Shoulson, N. Marshak, M. Kapadia, and N. I. Badler. ADAPT: The agent development and prototyping testbed. *IEEE Trans. on Visualiz. and Comp. Graphics (TVCG)*, 99:1–14, 2014. 54
- [287] B. Siciliano and O. Khatib. *Springer Handbook of Robotics, 2nd Ed.* Springer International Publishing, Switzerland, 2016. 64
- [288] B. Siciliano and J.-J. Slotine. A general framework for managing multiple tasks in highly redundant robotic systems. *Proc. of ICAR'91*, 2:1211–1215, 1991. 90
- [289] O. Sigaud and J. Peters, editors. *From Motor Learning to Interaction Learning in Robots*, volume 264. Springer-Verlag, Berlin Heidelberg, 2010. 1
- [290] T. Siméon, J.-P. Laumond, and C. Nissoux. Visibility-based probabilistic roadmaps for motion planning. *Advanced Robotics*, 14(6):477–493, 2000. 20



- 
- [291] S. Skiena. Ranger - Nearest Neighbor search in Higher dimensions. In *The Stony Brook Algorithm Repository*. Stony Brook University, Dept. of Computer Science, 2008. <http://www3.cs.stonybrook.edu/~algorithm/>. 27
- [292] S. S. Skiena. *The Algorithm Design Manual*. Springer, 2nd. edition, 2011. 27
- [293] J. J. Slotine and S. S. Sastry. Tracking control of non-linear systems using sliding surfaces, with application to robot manipulators. *Int. J. of Control*, 38(2):465–492, 1983. 96
- [294] J. J. E. Slotine. Modular stability tools for distributed computation and control. *Int. J. Adaptive Control and Signal Processing*, 17(6):397–416, 2003. 124, 127
- [295] J. F. Soechting and F. Lacquaniti. Invariant characteristics of a pointing movement in man. *Journal of Neuroscience*, 1:710–720, 1981. 80
- [296] M. Song, S. A. Mokhov, S. P. Mudur, and P. Grogono. Rapid interactive real-time application prototyping for media arts and stage performance. In *SIGGRAPH Asia 2015 Courses*, SA'15, pages 14:1–14:11, New York, NY, USA, 2015. ACM. 1
- [297] M. T. J. Spaan. *Partially Observable Markov Decision Processes*, pages 387–414. Springer, Berlin, Heidelberg, 2012. 20
- [298] D. A. Spielman. *Lecture Notes on 'Spectral Graph Theory'*, 2009. 172
- [299] M. Sreenivasa, P. Souères, and J.-P. Laumond. Walking to Grasp: Modeling of Human Movements as Invariants and an application to humanoid robotics. *IEEE Trans. on System, Man and Cybernetic Part A: Systems and Humans*, 42(4):880–893, 2012. 55
- [300] O. Stasse. *Habilitation Thesis*. Paul Sabatier University, CNRS, Toulouse, 2013. 53, 56, 112, 113, 165
- [301] O. Stasse, B. Verelst, A. Davison, N. Mansard, F. Saidi, B. Vanderborght, C. Esteves, and K. Yokoi. Integrating walking and vision to increase humanoid autonomy. *Int. Journal of Humanoid Robotics, Special Issue on Cognitive Humanoid Robots*, 5:287–310, 2008. 55
- [302] A. L. Swindlehurst. Time delay and spatial signature estimation using known asynchronous signals. *IEEE Trans. on Signal Processing*, 46(2):449–462, 1998. 69, 73
- [303] M. Täix, M. T. Tran, P. Souères, and E. Guigon. Generating human-like reaching movements with a humanoid robot: A computational approach. *J. of Computational Science*, 4:269–284, 2013. 54
- [304] W. Tang, T. R. Wan, and S. Patel. Real-time crowd movement on large scale terrains. *Theory and Practice of Computer Graphics*, pages 146–153, 2003. 124
- [305] Y. Tassa, T. Erez, and E. Todorov. Synthesis and stabilization of complex behaviors through online trajectory optimization. In *IEEE/RSJ Int. Conf. On Intelligent Robots and Systems (IROS)*, pages 4906–4913, 2012. 55

- [306] J. B. Tenenbaum and W. T. Freeman. Separating style and content with bilinear models. *Neural Comput.*, 12(6):1247–1283, 2000. 93, 94
- [307] D. Terzopoulos. Artificial Life and biomechanical simulation of humans. *Digital Human Symposium, 2009*, pages 8–13, 2009. 123
- [308] D. Terzopoulos and K. Waters. Physically-based facial modelling, analysis, and animation. *J. Visualization and Computer Animation*, 1(2):73–80, 1990. 123
- [309] F. J. Theis and Y. Inouye. On the use of joint diagonalization in blind signal processing. In *2006 IEEE Int. Symp. on Circuits and Systems*, volume ISCAS’2006, 2006. 73
- [310] G. Theodorou, K. Murphy, and L. P. Kaelbling. Representing hierarchical POMDPs as DBNs for multi-scale robot localization. In *Proc. IEEE Int. Conf. on Robotics and Automation, ICRA ’04*, volume 1, pages 1045–1051, 2004. 20
- [311] E. A. Theodorou, J. Buchli, and S. Schaal. A generalized Path Integral control approach to Reinforcement Learning. *Journal of Machine Learning Research*, 11:3137–3181, 2010. 20
- [312] E. A. Theodorou and E. Todorov. Relative entropy and free energy dualities: Connections to Path Integral and KL control. In *Proc. IEEE 51st Conf. on Decision and Control (CDC)*, pages 1466–1473, 2012. 20
- [313] L. Tian-He and G. Qiong. Image recovery from double amplitudes in fractional Fourier domain. *Chinese Physics*, 15(2):347–352, 2006. 69
- [314] E. Todorov and M. I. Jordan. Optimal feedback control as a theory of motor coordination. *Nature Neuroscience*, 5(11):1226–1235, 2002. 89
- [315] M. Toussaint and A. Storkey. Probabilistic inference for solving discrete and continuous state markov decision processes. In *Proc. of the 23rd Int. Conf. on Machine Learning, ICML’06*, pages 945–952, New York, NY, USA, 2006. ACM. 20
- [316] A. Treuille, S. Cooper, and Z. Popović. Continuum Crowds. *Proc. ACM SIGGRAPH’06*, 25(3):1160–1168, 2006. 123
- [317] N. Turner, L. Besson, J. Letteri, M. Hill, E. Reynolds, and P. Story. Weta Digital VFX: Valerian and the City of a Thousand Planets. In *ACM SIGGRAPH 2017 Computer Animation Festival, SIGGRAPH’17*, pages 26–26, New York, NY, USA, 2017. ACM. 1
- [318] M. A. Umiltà, E. Kohler, V. Gallese, L. Fogassi, L. Fadiga, C. Keysers, and G. Rizzolatti. I Know What You Are Doing: A Neurophysiological Study. *Neuron*, 31(1):155–165, 2001. 3, 37
- [319] Y. Uno, M. Kawato, and R. Suzuki. Formation and control of optimal trajectory in human multijoint arm movement: minimum torque-change model. *Biol. Cybern.*, 61:89–101, 1989. 89

- 
- [320] N. Vahrenkamp, D. Berenson, T. Asfour, J. Kuffner, and R. Dillmann. Humanoid motion planning for dual-arm manipulation and re-grasping tasks. In *2009 IEEE/RSJ Int. Conf. on Intelligent Robots and Systems*, pages 2464–2470, 2009. 20
- [321] N. van de Wouw, E. Lefeber, and I. L. Arteaga, editors. *Nonlinear Systems*, volume LNCIS 470. Springer Int. Publ., Switzerland, 2017. 124
- [322] J. van den Heuvel. Hamiltonian cycles and eigenvalues of graphs. *Lin. Alg. Appl.*, 226–228:723–730, 1995. 170
- [323] B. van der Pol and J. van der Mark. Frequency demultiplication. *Nature*, 120:363–364, 1927. 79
- [324] Hein T. van Schie and Harold Bekkering. Neural mechanisms underlying immediate and final action goals in object use reflected by slow wave brain potentials. *Brain Research*, 1148:183–197, 2007. 11
- [325] N. V. Vapnik. *Statistical Learning Theory*. Wiley-Interscience, 1998. 82
- [326] S. Vieilledent, Y. Kerlirzin, S. Dalbera, and A. Berthoz. Relationship between velocity and curvature of a human locomotor trajectory. *Neuroscience Letters*, 305(1):65–69, 2001. 158
- [327] P. Viola and W. M. Wells, III. Alignment by Maximization of Mutual Information. *Int. J. Comput. Vision*, 24(2):137–154, 1997. 13
- [328] P. Viviani and T. Flash. Minimum-jerk, two-thirds power law, and isochrony: converging approaches to movement planning. *Journal of Experimental Psychology. Human Perception and Performance*, 21(1):32–53, 1995. 158
- [329] R. Vuga, M. Ogrinc, A. Gams, T. Petric, N. Sugimoto, A. Ude, and J. Morimoto. Motion capture and reinforcement learning of dynamically stable humanoid movement primitives. In *Proc. of IEEE Int. Conf. on Robotics and Autom. (ICRA '2013)*, pages 5284–5290, 2013. 55
- [330] M. Vukobratovic and Yu. Stepanenko. On the stability of anthropomorphic systems. *Mathematical Biosciences*, 15:1–37, 1972. 53, 55, 111
- [331] J. M. Wang, D. J. Fleet, and A. Hertzmann. Multifactor Gaussian Process models for style-content separation. In *Proc. of the 24th Int. Conf. on Machine Learning, ICML '07*, pages 975–982, New York, NY, USA, 2007. ACM. 53
- [332] J. M. Wang, D. J. Fleet, and A. Hertzmann. Gaussian Process Dynamical Models for human motion. *IEEE Trans. on Pattern Analysis and Machine Intelligence*, 30(2):283–298, 2008. 53
- [333] W. Wang and J. J. E. Slotine. On partial contraction analysis for coupled nonlinear oscillators. *Biological Cybernetics*, 92(1):38–53, 2005. 79, 80, 81, 124, 128, 131, 136, 137
- [334] William H. Warren. The dynamics of perception and action. *Psychological Rev.*, 113(2):358–389, 2006. 99, 149

- [335] M. Weigelt and T. Schack. The development of End-State comfort planning in preschool children. *Exper. Psych.*, 57(6):476–782, 2010. 54, 111
- [336] P.-B. Wieber. Trajectory free linear model predictive control for stable walking in the presence of strong perturbations. *Proc. of IEEE Int. Conf. Humanoids'06*, pages 137–142, 2006. 56, 113
- [337] H. Wielandt. An extremum property of sums of eigenvalues. *Proc. Amer. Math. Soc.*, 6:106–110, 1955. 185
- [338] E. P. Wigner. On weakly positive matrices. *Canadian Journal of Mathematics*, 15:313–317, 1963. 179
- [339] J. H. Wilkinson. *Algebraic Eigenvalue Problem*. Clarendon Press, Oxford, 1965. 169, 170
- [340] A. Witkin and Z. Popović. Motion warping. *Proc. ACM SIGGRAPH'95*, 29:105–108, 1995. 2, 53
- [341] A. Wohlschläger, M. Gattis, and H. Bekkering. Action generation and action perception in imitation: An instance of the ideomotor principle. *Philosophical Transactions of the Royal Society B: Biological Sciences*, 358(1431):501–515, 2003. 9
- [342] C.-C. Wu and V. Zordan. Goal-directed stepping with momentum control. *ACM SIGGRAPH/Eurographics Symp. on Comp. Animation (SCA, 2010)*, 2010. 53
- [343] K. Yamane and Y. Nakamura. Dynamics Filter - Concept and implementation of on-line motion generator for human figures. In *Proc. of IEEE Int. Conf. on Robotics and Autom.*, pages 688–695, 2000. 52
- [344] A. Yeredor. Time-delay estimation in mixtures. In *Proc. (ICASSP'03). 2003 IEEE Int. Conf. on Acoustics, Speech, and Signal Processing*, volume 5, pages V–237–240, 2003. 72, 73
- [345] A. Yeredor. Blind source separation in the presence of doppler frequency shifts. In *Proc. (ICASSP'05). 2005 IEEE Int. Conf. on Acoustics, Speech, and Signal Processing*, volume 5, pages V–277–280, 2005. 72, 73
- [346] E. Yoshida, A. Mallet, F. Lamiraux, O. Kanoun, O. Stasse, M. Poirier, P-F. Dominey, J.-P. Laumond, and K. Yokoi. 'Give Me the Purple Ball' – He Said to HRP-2 N.14. *Proc. of IEEE-RAS Int. Conf. on Humanoid Robots (Humanoids'07)*, 2007. 55
- [347] V. B. Zordan and J. K. Hodgins. Motion capture-driven simulations that hit and react. *ACM SIGGRAPH/Eurographics Symp. on Comp. Animation*, pages 89–96, 2002. 53